UNCLASSIFIED

AD NUMBER
AD878075

LIMITATION CHANGES

TO:

Approved for public release; distribution is unlimited.

FROM:

Distribution authorized to U.S. Gov't. agencies and their contractors; Administrative/Operational Use; OCT 1970. Other requests shall be referred to Army Aviation Materiel Labs., Fort Eustis, VA 23604.

AUTHORITY

AMRDL ltr 11 Aug 1971

AD878075

AD

USAAVLABS TECHNICAL REPORT 70-33A

EFFECTS OF HIGH-LIFT DEVICES ON V/STOL AIRCRAFT PERFORMANCE
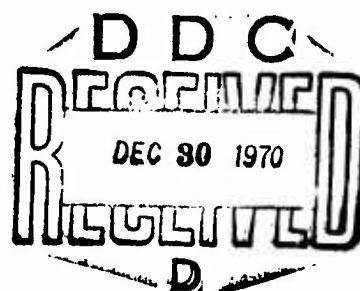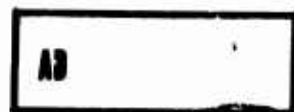
VOLUME I
Final Report

By

J. Hebert
et al

October 1970

DDC

RECEIVED

DEC 30 1970

D

U. S. ARMY AVIATION MATERIEL LABORATORIES
FORT EUSTIS, VIRGINIA

185

DISCLAIMERS

DISPOSITION INSTRUCTIONS

DEPARTMENT OF THE ARMY
HEADQUARTERS US ARMY AVIATION MATERIEL LABORATORIES
FORT EUSTIS. VIRGINIA 23604

This report has been reviewed by the U. S. Army
Aviation Materiel Laboratories and is considered
to be technically sound. The report is published
for the exchange of information and the stimu-
lation of ideas.

EFFECTS OF HIGH-LIFT DEVICES ON V/STOL

AIRCRAFT PERFORMANCE

VOLUME I

Final Report

By

J. Hebert
et al

Prepared by

Convair Division of General Dynamics
San Diego, California

for

U. S. ARMY AVIATION MATERIEL LABORATORIES
FORT EUSTIS, VIRGINIA

SUMMARY

The evaluation of any propeller-driven V/STOL configuration requires analytical methods that adequately assess the aerodynamic characteristics and the forces arising from the propeller and the slipstream.

This study was to develop a unified analytical procedure to evaluate the effects of passive high-lift devices on deflected-slipstream or tilt-wing V/STOL configurations. Methods were developed to predict the two-dimensional flapped airfoil characteristics to be used in a span load program. The span load results are used in procedures for estimating the coefficients of lift, longitudinal force, and moment for a wing partially immersed in a propeller slipstream. These characteristics can then be used in a performance program developed to calculate the takeoff, landing and transition maneuvers. In addition to these tasks, investigations were made into downwash characteristics, wind tunnel wall corrections, and correlations of flight test data with theory. An analysis of the effects of high-lift devices on the performance of a tilt-wing V/STOL configuration is included in the appendix.

The procedures to predict the two-dimensional aerodynamic characteristics of high-lift devices furnish reasonable estimates, generally within 10 percent of experimental results, that can be used in the span load program. The trend from General Dynamics experimental data indicates that the maximum lift levels from NACA data are approximately 10 to 20 percent lower. This may be attributed to the General Dynamics testing technique which utilizes side-wall blowing to eliminate adverse wall boundary layer interference effects.

The program initiated at Convair to develop a more basic approach to the problem of estimating the lift and longitudinal force coefficients was well justified. It is considerably less limited than existing empirical methods in that it requires only two-dimensional data for application to general configurations. The procedures for predicting lift and longitudinal force coefficients of a wing-flap combination give satisfactory results at all thrust coefficients. However, the procedures for predicting pitching moment coefficients result in erratic correlations for cases with flaps deflected.

The entire task of correlating wind tunnel data that has been corrected for wall effects with actual flight test conditions could not be accomplished due to the lack of a good set of flight test data for comparison. The evaluation of tunnel wall effects indicated that currently available correction procedures for lift and drag yield erroneous results and should not be applied.

The complexity of the performance program made numerous assumptions and capability restrictions desirable. For example, the equations of motion were reduced to two dimensions (i.e., no pitch dynamics), and several terms, such as pitch rates, wing tilt angular rates and pilot braking response time, were used as predetermined inputs. These assumptions were made to expedite the development of the system; however, the accuracy of the methods employed is sufficient to reflect the impact of high-lift devices on V/STOL aircraft. The program is a viable tool for performance estimation.

The problems associated with predicting the aerodynamic forces acting on a wing immersed in a slipstream should be investigated further. To improve the basic procedures, it is necessary that (1) additional correlations of pitching moments be made with experimental data to develop improved empirical factors for large chord ratio flaps, (2) methods be developed to incorporate the pronounced nonlinear characteristics of leading edge devices at low angles of attack, (3) the downwash estimating procedure be programmed for digital computer application and correlations be made with experimental data, and (4) tilt-prop configuration methodology be developed and incorporated into the aerodynamic and performance programs.

Jet flap and boundary layer control devices should be investigated so that methods could be developed to describe the effects of these devices on a wing immersed in a slipstream.

A study should be performed to define a wind tunnel/flight test program to correlate V/STOL vehicle aerodynamic characteristics.

FOREWORD

This report presents the results of an investigation of the effects of high-lift devices on V/STOL aircraft performance and stability and control.

TABLE OF CONTENTS

viii

LIST OF ILLUSTRATIONS

xiii

LIST OF SYMBOLS

A_M	model momentum area, sq ft
A_T	wind tunnel cross-sectional area, sq ft
A_X	horizontal acceleration, ft/sec^2
A_Z	vertical acceleration, ft/sec^2
A_n	nth term in series
A_o	first term in series
AR	wing aspect ratio
AR_{EQ}	equivalent aspect ratio of slipstream segment of the wing
AR_{FS}	effective geometric aspect ratio of free-stream segment of the wing
AR_H	effective geometric aspect ratio of slipstream segment of the wing in the hover condition
AR_{HS}	effective geometric aspect ratio of slipstream segment of the wing in the high-speed flight condition
a_{EQ}	equivalent lift curve slope of slipstream segment of the wing
a_{FS}	lift curve slope of free-stream segment of the wing
a_H	lift curve slope of slipstream segment of the wing in hover
a_o	two-dimensional lift curve slope
a_{SS}	lift curve slope of slipstream segment of the wing
a_w	three-dimensional lift curve slope
B	width of wind tunnel test section, ft
b	wing span, ft

b_e	effective vortex span, ft
b_v	vortex span downstream of model, ft
C	area of wind tunnel test section, sq ft
CG	center of gravity
C_D	drag coefficient
C_{D_C}	drag coefficient corrected for wall effects
$C_{D_{FS}}$	total drag coefficient on free-stream segment of the wing
C_{D_i}	induced drag coefficient
ΔC_{D_i}	change in induced drag caused by the boundary induced upwash
C_{D_N}	drag coefficient of nacelle based on slipstream dynamic pressure
$C_{D_{o_{NAC}}}$	drag coefficient of nacelle based on free-stream dynamic pressure
C_f	skin friction coefficient
$C_D(\alpha)$	body drag at angle of attack
$\Delta C_{D_{\alpha=0}}$	increment of drag at $\alpha = 0$ for deflected flaps
$C_{D_{i_{FS}}}$	induced drag coefficient on free-stream segment of the wing
$C_{D_{i_{SS}}}$	induced drag coefficient on slipstream segment of the wing
$C_{D_{P_{FS}}}$	profile drag coefficient on free-stream segment of the wing
$C_{D_{P_{SS}}}$	profile drag coefficient on slipstream segment of the wing
$C_{D_{SS}}$	total drag coefficient on slipstream segment of the wing
$C_{L_{DT}}$	lift coefficient due to direct thrust
$C_{L_{FS}}$	lift coefficient on the free-stream segment of the wing

$\Delta C_{L_{FS}}$ change in lift coefficient on the free-stream segment of the wing

C_L lift coefficient

C_{L_C} lift coefficient corrected for wall effects

C_{L_H} lift coefficient on slipstream segment of wing in hover

$C_{L_{HS}}$ lift coefficient on slipstream segment of wing in high-speed flight

$C_{L_{MAX}}$ total maximum lift of the interacting wing/propeller configuration

$\left(C_{L_{MAX}}\right)_{SS}$ maximum lift coefficient on the slipstream segment of the basic clean or flapped wing

$\left(C_{L_{MAX}}\right)_{FS}$ maximum lift coefficient on the free-stream segment of the basic clean or flapped wing

C_{L_N} lift coefficient of nacelle

C_{L_S} total lift coefficient on the slipstream segment of the wing

$C_{L_{SS}}$ lift coefficient on the slipstream segment of the wing

$\Delta \dot{C}_{L_{SS}}$ lift coefficient increment of slipstream segment of the wing

C_{L_T} total lift coefficient of the interacting wing/propeller configuration

C_{L_U} uncorrected lift coefficient

C_{m_o} zero lift pitching moment of the interacting wing/propeller flap configuration

C_{m_T} total pitching moment coefficient of the interacting wing/propeller configuration

$C_{m_{DT}}$ pitching moment coefficient due to the direct thrust term

$C_{N_{FS}}$ normal force coefficient on the free-stream segment of a stalled wing

$C_{N_{SS}}$ normal force coefficient on the slipstream segment of a stalled wing

C_T	thrust coefficient
C_{T_S}	thrust coefficient based on slipstream dynamic pressure
$C_{T_{S_C}}$	thrust coefficient corrected for wall effects
C_{X_S}	total drag coefficient on the slipstream segment of the wing
$C_{X_{DT}}$	longitudinal force coefficient on the free-stream segment of the interacting wing/propeller configuration
C_{X_N}	longitudinal force coefficient due to the nacelle
C_{X_T}	total longitudinal force coefficient on the interacting wing/propeller configuration
$\left(C_{L_\alpha}\right)_{DT}$	lift curve slope contribution (per deg) due to the direct thrust term
$\left(C_{L_\alpha}\right)_{EQ}$	equivalent lift curve slope (per deg) for slipstream segment of the wing
$\left(C_{L_\alpha}\right)_{FS}$	lift curve slope (per deg) for the free-stream segment of the basic clean wing, also $(C_{L_\alpha})_{PO}$
$C_{L_{\alpha_H}}$	lift curve slope (per deg) of the slipstream segment of the wing in the hover condition
$\left(C_{L_\alpha}\right)_{LA}$	lift curve slope contribution (per deg) due to the lift augmentation from the slipstream
$C_{L_{\alpha_N}}$	lift curve slope (per deg) due to the nacelle
$\left(C_{L_\alpha}\right)_{SS}$	lift curve slope (per deg) of the slipstream segment of the basic clean wing
$\left(C_{L_\alpha}\right)_T$	total lift curve slope (per deg) of the interacting wing/propeller configuration
$C_{L_{\alpha_W}}$	lift curve slope (per deg) of the basic clean wing
$\left(C_{m_{C_L}}\right)_N$	stability contribution of the nacelle

$\left(C_{m_{C_L}}\right)_{SS}$ stability of the slipstream segment of the basic clean wing

$\left(\Delta C_{m_o}\right)_F$ zero lift pitching moment coefficient due to flaps of the basic flapped wing

$\Delta C_{m_{o_F}}$ zero lift pitching moment coefficient due to flaps of the basic flapped interacting wing/propeller configuration

$C_{m_{o_W}}$ zero lift pitching moment coefficient of the basic clean wing

$\left(\Delta C_{m_o}\right)_{DT}$ zero lift pitching moment coefficient increment of the direct slipstream thrust on segment of the basic flapped wing

$\left(\Delta C_{m_o}\right)_{LA}$ zero lift pitching moment coefficient increment due to lift augmentation

$\left(\Delta C_{m_o}\right)_{PO}$ zero lift power-off pitching moment coefficient increment of the basic flapped wing

$\left(\Delta C_{m_o}\right)_{SS}$ zero lift pitching moment coefficient increment of the slipstream segment of the basic flapped wing

C_{m_α} total pitching moment curve slope (per deg) of the interacting wing/propeller configuration

$\left(C_{m_\alpha}\right)_B$ pitching moment curve slope (per deg) due to the fuselage

$\left(C_{m_\alpha}\right)_{DT}$ pitching moment curve slope due to the direct thrust term

$\left(C_{m_\alpha}\right)_{LA}$ pitching moment curve slope (per deg) due to the lift augmentation from the slipstream

$\left(C_{m_\alpha}\right)_N$ pitching moment curve slope (per deg) due to nacelles

$\left(C_{m_\alpha}\right)_P$ pitching moment curve slope (per deg) due to one propeller

$\left(C_{m_\alpha}\right)_{PO}$ power-off pitching moment curve slope (per deg) of the basic flapped wing

$\left(C_{m_\alpha}\right)_{SS}$	pitching moment curve slope (per deg) of the slipstream segment of the basic clean wing
$C_{m_{\alpha_W}}$	pitching moment curve slope (per deg) of the basic clean wing
c	airfoil chord, ft
$\bar{c}$	wing mean aerodynamic chord, ft
$\left(\dfrac{\bar{c}}{4}\right)_W$	quarter chord of wing MAC, ft
$\left(\dfrac{\bar{c}}{4}\right)_H$	quarter chord of horizontal tail MAC, ft
c_d	two-dimensional drag coefficient
c_{EXT}	extended chord
c_f	trailing edge flap chord
c_f'	leading edge flap chord
c_ℓ	two-dimensional lift coefficient
$\Delta c_{\ell_{\alpha=0}}$	increment of lift at $\alpha = 0$
c_{ℓ_δ}	theoretical lift effectiveness for trailing edge flap
$c_{\ell_{\delta if}}$	contribution to flap maximum lift from ideal angle of attack
$\Delta c_{\ell_{MAX}}$	increment of maximum lift
$\Delta c_{\ell_{MAX_{TH}}}$	theoretical increment in maximum lift due to plain flap
c_{ℓ_α}	lift curve slope of airfoil
$c_{\ell_{\alpha_{EXT}}}$	lift curve slope of airfoil with flap chord extension
$\Delta c_{\ell_{\alpha_{EXT}}}$	lift curve slope increment due to flap chord extension

c_{ℓ_δ}'	theoretical lift effectiveness for leading edge flap
$c_{\ell_{\delta_{MAX}}}'$	theoretical maximum lift effectiveness
Δc_m	moment increment for lift at $\alpha = 0$
$\dfrac{\Delta c_m}{\Delta c_\ell}$	slope of pitching moment curve
c_{m_δ}	theoretical moment effectiveness term
c_N	wing chord at nacelle location, ft
c_r	wing root chord, ft
c_1	extended flap chord for single-slotted flap
c_2	extended flap chord for double-slotted flap
D	drag force, lb
D_B	body diameter, ft
D_C	drag corrected for wall effects
D_N	nacelle diameter, ft
D_P	propeller diameter, ft
D_i	induced drag force, lb
d	contracted slipstream diameter, ft
EQ	flight condition index
g	acceleration due to gravity, ft/sec^2
H_B	fuselage height, ft
h	vertical distance from wake to trailing edge of wing, measured at quarter chord of horizontal tail MAC, ft

h_o	vertical distance from fuselage center line to quarter chord of wing, ft
h_T	tunnel height, ft
i_T	incidence angle between geometric thrust line and wing root chord, deg
i_W	angle between fuselage reference line and wing chord plane, deg
K_{ac}	empirical factor to account for chord extension
K_B	fuselage stability coefficient
K_E	flap chord extension factor
K_F	planform area factor
K_m	empirical factor for moment
K_N	nacelle stability coefficient
K_P	pressure term for airfoil
K_S	supervelocity term for airfoil
K_T	empirical factor for maximum lift
K_1	wing-body interference factor
K_2	horizontal tail-body interference factor
K_3	factor for horizontal position of nacelle
K_4	factor for vertical position of nacelle
K_δ	empirical factor for flap deflection
k	constant for calculation of induced upwash velocity at a model in a wind tunnel
k_R	roughness factor, mil

k_v	ratio of effective vortex span to vortex downstream of the model
L	lift force, lb
L_B	fuselage length, ft
L_C	lift corrected for wall effects
L_P	moment arm from quarter chord of the mean aerodynamic chord to the propeller plane, ft
L_c	characteristic length, ft
L_{DT}	lift force due to direct thrust, lb
LER	leading edge radius
L_H	lift on slipstream segment of wing in hover, lb
ℓ_B	body length, ft
ℓ_a	fuselage afterbody length, ft
ℓ_N	nacelle length, ft
ℓ_H	distance from quarter chord of wing MAC (mean aerodynamic chord) to quarter chord of horizontal tail MAC, ft
ℓ_H'	distance from wing root quarter chord to quarter chord of horizontal tail MAC, ft
ℓ_H''	distance with wing tilt from wing root quarter chord to quarter chord of horizontal tail MAC, ft
N	number of propellers
n	ratio of final induced velocities
q	free-stream dynamic pressure, lb/sq ft
q_c	free-stream dynamic pressure corrected for wall effects
q_p	total tangential velocity component induced by vortex element

q_S	slipstream dynamic pressure, lb/sq ft
R	distance from point P to downwash element, ft
r	distance from model, ft
S	wing area, sq ft
S_B	frontal area, sq ft
S_{FS}	free-stream wing area, sq ft
S_P	propeller disk area, sq ft
S_{SS}	slipstream wing area, sq ft
S_{TOP}	area of top of fuselage, sq ft
S_{WET}	wetted area, sq ft
S_{SIDE}	area of side of fuselage, sq ft
T	thrust vector, lb
t/c	thickness ratio
Δu	change in longitudinal velocity, ft/sec
Δu_D	longitudinal velocity induced by the longitudinal doublet, ft/sec
Δu_L	longitudinal velocity induced by the vertical doublet, ft/sec
u_o	longitudinal induced velocity, ft/sec
V	free-stream velocity, ft/sec
V_c	wind tunnel velocity corrected for wall effects, ft/sec
V_S	resultant slipstream velocity, ft/sec
W	weight, lb

W_B	fuselage width, ft
W_N	nacelle width, ft
w	upwash velocity at the model, ft/sec
Δw_D	vertical velocity induced by the longitudinal doublet, ft/sec
Δw_L	vertical velocity induced by the vertical doublet, ft/sec
w_h	reference velocity, ft/sec
w_o	vertical induced velocity, ft/sec
w_P	downwash velocity component, ft/sec
X_{DT}	longitudinal force due to direct thrust, lb
x	distance behind wing root chord trailing edge, ft
x_N	horizontal position of forward end of nacelle from wing leading edge, ft
x_f	distance from leading edge of airfoil to flap hinge line, percent of airfoil chord
x_o	distance from quarter chord of wing root to trailing edge of wing, ft
x_{PIV}	distance from wing pivot point to quarter chord of wing mean aerodynamic chord, ft
y	spanwise distance measured from the wing root section, ft
y_a	vertical distance of apex of afterbody from fuselage center line, ft
y_N	vertical position of nacelle center line from wing chord, ft
y_n	spanwise distance from wing root chord to nacelle center line, ft
z_H	vertical distance from fuselage center line to quarter chord of tail MAC, ft

z'_H	vertical distance from quarter chord of wing MAC to quarter chord of tail MAC, ft
z''_H	vertical distance from wake to quarter chord of horizontal tail, ft
z_{PIV}	distance from fuselage center line to wing pivot, ft
α	angle of attack of airfoil or wing, deg
α'	angle of attack of airfoil with leading edge flap deflected, deg
α_b	angle from tail of vortex element to point P, deg
α_c	corrected angle of attack, deg
α_{EFF}	effective angle of attack of thin flapped airfoil, deg
α_{FS}	angle of attack on free-stream segment of the wing, deg
α_{FUS}	fuselage angle of attack, deg
α_g	geometric angle of attack, deg
α_i	induced upwash angle, deg
$\Delta\alpha_i$	boundary induced upwash angle of the model, deg
α_{ic}	ideal angle of attack due to camber, deg
α_{if}	ideal angle of attack for flapped airfoil, deg
α_{o_L}	angle between the local wing chord and wing zero lift line, deg
α_s	stall angle of attack for symmetrical airfoil, deg
α_{sc}	stall angle of attack for cambered airfoil, deg
α_{sf}	stall angle of attack for flapped airfoil, deg
α_{SS}	angle of attack on slipstream segment of the wing, deg
α_T	angle of attack between geometric thrust line and the free-stream velocity vector, deg

α_u	uncorrected angle of attack, deg
α_W	angle of attack between wing zero lift line and the free-stream velocity vector, deg
α_{2-D}	effective section angle of attack, deg
α_{2-D_i}	induced section angle of attack, deg
α_δ	rate of change of zero-lift angle of attack with flap deflection, deg
$\Delta\alpha$	change in angle of attack due to wall corrections, deg
β	angle from nose of vortex element to point P, deg
Γ	circulation
$\Delta\Gamma$	vortex element strength
γ	flight path angle, deg
δ	correction factor
δ_f	trailing edge flap deflection angle, deg
$\delta_f{}'$	leading edge flap deflection angle, deg
δ_K	Krueger flap deflection angle, deg
δ_{LE}	leading edge device deflection angle, deg
δ_{NF}	nose flap deflection angle, deg
δ_S	slat deflection angle, deg
$\delta_{u,L}$	interference factor associated with the longitudinal velocity induced by the vertical doublet
$\delta_{u,D}$	interference factor associated with the longitudinal velocity induced by the longitudinal doublet
δ_V	vane deflection angle, deg

xxvi

$\delta_{w,L}$	interference factor associated with the vertical velocity induced by the vertical doublet
$\delta_{w,D}$	interference factor associated with the vertical velocity induced by the longitudinal doublet
ϵ	downwash angle, deg
ϵ_o	downwash angle with zero inclination of the wing, deg
ϵ_{b_i}	downwash contribution of two elemental bound vortices at equivalent spanwise stations, deg
ϵ_{o_i}	downwash contribution from elemental and trailing vortices, deg
ϵ_{t_i}	downwash contribution of trailing vortices at equivalent spanwise stations, deg
η	spanwise location, percent of wing semi-span
$\Delta\eta$	bound vortex span of each elemental horseshoe vortex system, percent of wing semi-span
η_{MAX}	empirical factor for maximum lift of a leading edge device
η_P	lifting efficiency of plain flap
η_i	spanwise location of bound vortex, percent of wing semi-span
η_1	lifting efficiency of single-slotted flap
η_ι	spanwise location of inboard tip of propeller, percent of wing semi-span
η_2	lifting efficiency of double-slotted flap
η_{2S}	factor to account for reduced effectiveness of aft flap
η_o	spanwise location of outboard end of flap, percent of wing semi-span
η_δ	factor accounting for change in deflection of leading edge device from optimum position

θ	wake deflection angle, deg
θ_f	defined by $\cos^{-1}(1 - \dfrac{x_f}{c/2})$
$\Lambda_{c/4}$	sweep of wing quarter chord, deg
λ	taper ratio of wing
λ_T	ratio of tunnel height to tunnel width
μ	coefficient of friction
ν	kinematic viscosity, ft^2/sec
ρ	density, $slugs/ft^3$
ϕ	angle through which thrust line is rotated due to superposition of slipstream and free-stream velocity, deg
Φ	effective turning angle, deg
Φ_{TE}	trailing edge angle of airfoil, deg
χ	wake skew angle, deg
χ_{EFF}	effective wake skew angle, deg
ω	angle between tangential and downwash velocity component, deg

1.0 INTRODUCTION

Interest in V/STOL aircraft has emphasized the need to improve the methods of predicting the aerodynamic characteristics of these vehicles at very low forward flight velocities. A general understanding of the high-lift characteristics of certain configurations exists because of the amount of available experimental data. However, reliable analytical methods of predicting the high-lift characteristics over a full range of variables, i.e., angle of attack, flap angle, thrust coefficient, etc., are not available.

A comprehensive literature search on V/STOL high-lift devices was conducted and is documented in Volume II of this report. The available two-dimensional experimental data were reviewed, and selected NACA test data and data developed by General Dynamics were used in developing a procedure to predict the two-dimensional characteristics of the following passive high-lift devices:

Trailing Edge Flaps	Leading Edge Devices
Plain Flaps	Nose Flaps
Single-Slotted Flaps	Slats
Double-Slotted Flaps	Kruegers

These characteristics, along with experimental clean airfoil data from Reference 1, are used in a span load program to predict the three-dimensional characteristics of an arbitrary configuration.

The limitations imposed by the available semiempirical methods for estimating the forces on a wing immersed in a propeller slipstream indicated the requirement for a more basic approach to the problem. The approach developed at Convair depends entirely on the availability of two-dimensional data and was first conceived by Canadair Limited in the early 1960's. Thrust, free-stream, and slipstream effects on the unpowered lift, drag, and pitching moment are predicted by the theory discussed in this report.

These data are then trimmed and used in the performance program to integrate two-degree-of-freedom equations of motion to predict vertical or rolling takeoff, landing, and transition maneuvers.

This report describes the study effort and the development of a methodology to evaluate the effects of high-lift devices on V/STOL aircraft performance.

2.0 TWO-DIMENSIONAL AERODYNAMIC CHARACTERISTICS OF HIGH-LIFT DEVICES

The design of V/STOL aircraft requires procedures that adequately predict the aerodynamic characteristics of high-lift devices. These devices are usually movable portions of the leading or trailing edge of the wing that are deflected to increase the maximum lift coefficient.

Considerable data are available from NACA sources on two-dimensional tests that were conducted during the 1930's. Unfortunately, these tests were not planned to investigate systematic parameters on high-lift airfoils. Several attempts have been made, such as References 2, 3, and 4, to organize the available data in a useable form. The above references either treated the increment in lift below stall or attempted to handle the complete lift curve.

This section summarizes a procedure (based on thin airfoil theory where possible) from Reference 5 that predicts the two-dimensional aerodynamic characteristics of the following high-lift devices:

Trailing Edge Flaps	Leading Edge Devices
Plain Flaps	Nose Flaps
Single-Slotted Flaps	Kruegers
Double-Slotted Flaps	Slats

Selected NACA test data, mainly the 23 series flapped airfoils, and data developed by General Dynamics were utilized in developing the procedure to predict incremental effects of high-lift devices. The predicted increments are added to the clean airfoil characteristics determined either from the experimental data in Reference 1 or predicted with the method of Reference 2.

2.1 TRAILING EDGE FLAPS

2.1.1 Theory

Descriptions of the basic theoretical treatment of the effects of flaps on the characteristics of airfoils, using an extension to thin airfoil theory, are given in References 6, 7, and 8. These analyses lead to expressions by which lift and pitching moment could be calculated. A further refinement of the theory, in References 9 and 10, shows equations relating maximum lift increment to lift increment at $\alpha = 0$. These equations are based on the assumption that leading edge separation is dependent only on the additional "angle of attack" loading.

2

Only a cursory description of thin airfoil theory is included since it is adequately covered in a number of references. Consider the flapped airfoil shown below:
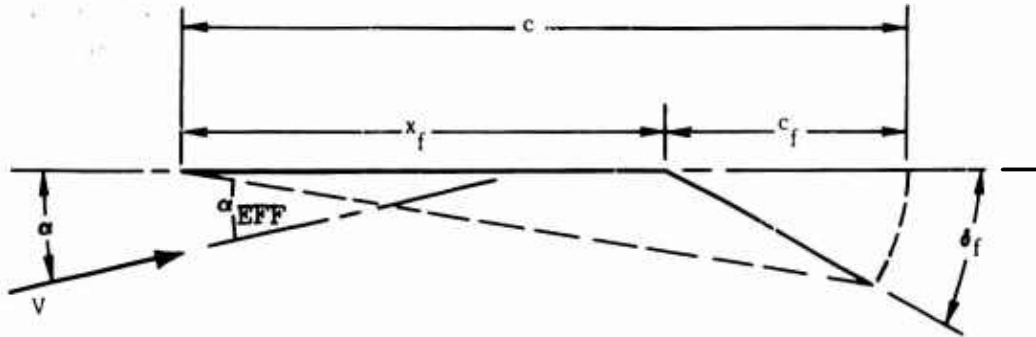
Flapped Airfoil Geometry

The angle of attack of the chord line with the flap deflected is

$$\alpha_{EFF} = \alpha + \delta_f \left(\frac{c_f}{c} \right) \tag{1}$$

From thin airfoil theory, the lift coefficient is

$$c_\ell = 2\pi A_0 + \pi A_1 \tag{2}$$

where

$$A_0 = \alpha + \frac{\pi - \theta_f}{\pi} \delta_f$$

$$A_1 = \frac{2\delta_f}{\pi} \sin \theta_f \tag{3}$$

and

$$\theta_f = \cos^{-1} \left(1 - \frac{x_f}{c/2} \right)$$

The equation for the lift coefficient of a flapped airfoil may be written as

$$c_\ell = 2\pi \left(\alpha + \frac{\pi - \theta_f}{\pi} \delta_f \right) + 2\delta_f \sin \theta_f \tag{4}$$

3

or

$$c_\ell = 2\pi \alpha + 2 \, (\pi - \theta_f + \sin \theta_f) \, \delta_f \qquad (5)$$

The two-dimensional lift coefficient can then be written as

$$c_\ell = 2\pi\alpha + c_{\ell_\delta} \delta_f = 2\pi \, (\alpha - \alpha_\delta \, \delta_f) \qquad (6)$$

where

$$c_{\ell_\delta} = 2 \, (\pi - \theta_f + \sin \theta_f) \qquad (7)$$

$$\alpha_\delta = -\frac{c_{\ell_\delta}}{2\pi} \qquad (8)$$

The theoretical lift effectiveness, c_{ℓ_δ}, is given in Figure 1. The rate of change of zero-lift angle with flap deflection, α_δ, may readily be obtained from c_{ℓ_δ}.

In thin airfoil theory the ideal angle of attack, α_i, can be defined as the angle of attack where lift is obtained from camber alone with no suction peak at the nose. This definition results by considering the aerodynamic loading over a thin cambered airfoil in two parts. One part, the basic load distribution, is characteristic of the camber-line shape. The other part, the additional load distribution, is due only to angle of attack.

The suction peak then depends on angle of attack, and for the symmetrical airfoil, $\alpha_{ic} = 0$. The symmetrical airfoil stalls at α_s and the cambered airfoil would stall at α_{sc}, where

$$\alpha_s = \alpha_{sc} - \alpha_{ic}$$

It follows that for the flapped airfoil, an ideal angle of attack may be defined such that

$$\alpha_s = \alpha_{sf} - \alpha_{if}$$

The ideal angle of attack for the flapped airfoil must be such that the A_o in Equation (3) goes to zero. It follows that for the flapped airfoil,

4
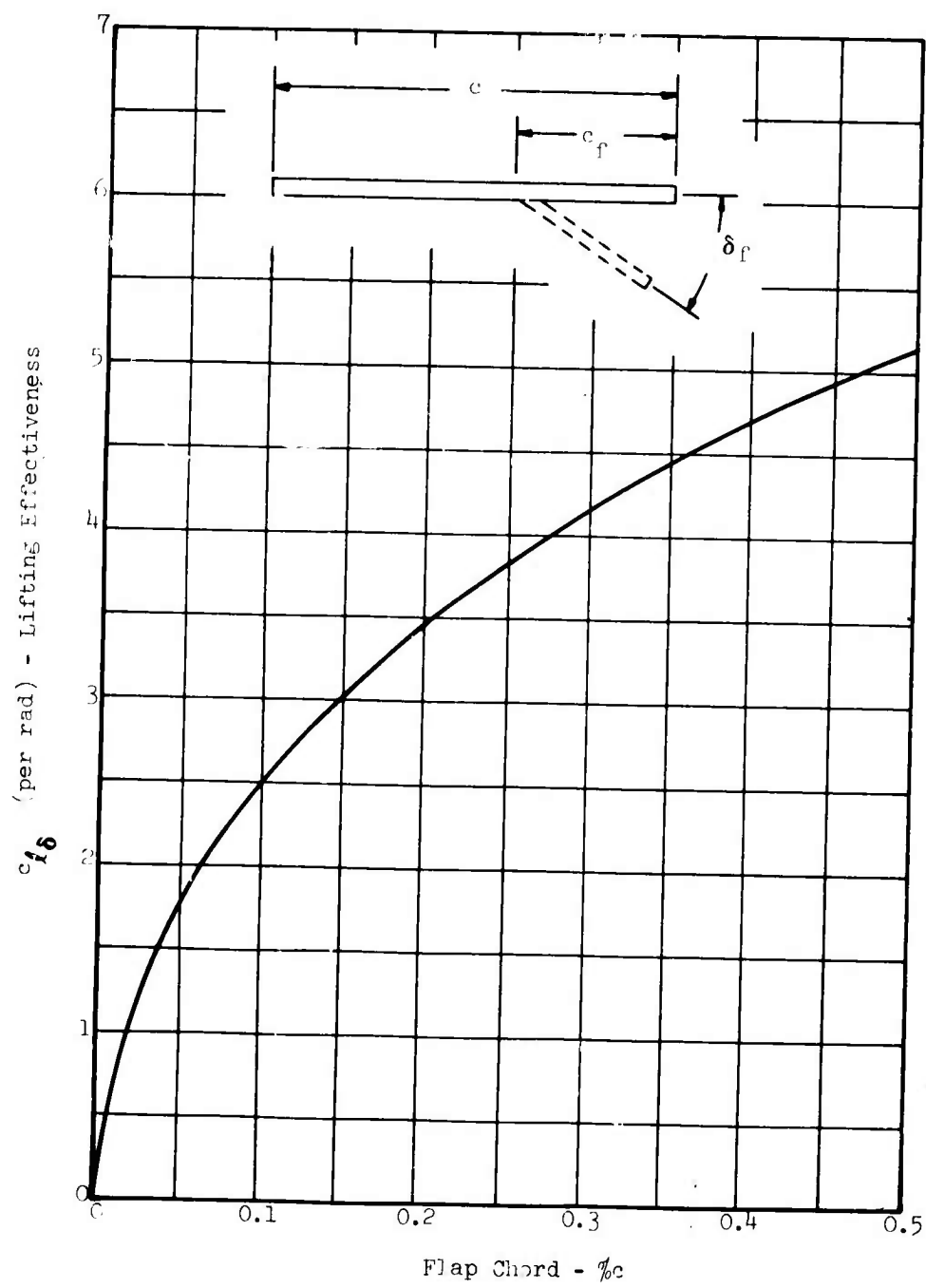
Figure 1. Theoretical Lifting Effectiveness Versus Flap Chord.

$$\alpha_{if} = -\left(\frac{\pi - \theta_f}{\pi}\right) \delta_f = -\left(1 - \frac{\theta_f}{\pi}\right)\delta_f \tag{9}$$

The increment of maximum lift can then be expressed as

$$\Delta c_{\ell_{max}} = \left(c_{\ell_\delta} + c_{\ell_{\delta_{if}}}\right)\delta_f \tag{10}$$

where

$$c_{\ell_{\delta_{if}}} = -2\pi\left(1 - \frac{\theta_f}{\pi}\right)$$

Substituting the $c_{\ell_{\delta_{if}}}$ term in Equation (10) results in the following equation:

$$\Delta c_{\ell_{max}} = \left(c_{\ell_\delta} - 2\pi + 2\theta_f\right)\delta_f \tag{11}$$

An expression can then be written in terms of the lift increment at $\alpha = 0$ which is useful in correlating data:

$$\frac{\Delta c_{\ell_{max}}}{\Delta c_{\ell_{\alpha=0}}} = \frac{c_{\ell_\delta} - 2\pi + 2\theta_f}{c_{\ell_\delta}} \tag{12}$$

The theoretical values for $\Delta c_{\ell_{max}}/\Delta c_{\ell_{\alpha=0}}$ are plotted in Figure 2.

The pitching moment increment about the quarter chord according to thin airfoil theory (References 1, 5, and 6) for a flapped airfoil is given by the following expression:

$$\Delta c_m = -\frac{\pi}{4}(A_1 - A_2) \tag{13}$$

where

$$A_1 = \frac{2\delta_f}{\pi}\sin\theta_f$$

$$A_2 = \frac{\delta_f}{\pi}\sin 2\theta_f \tag{14}$$

6
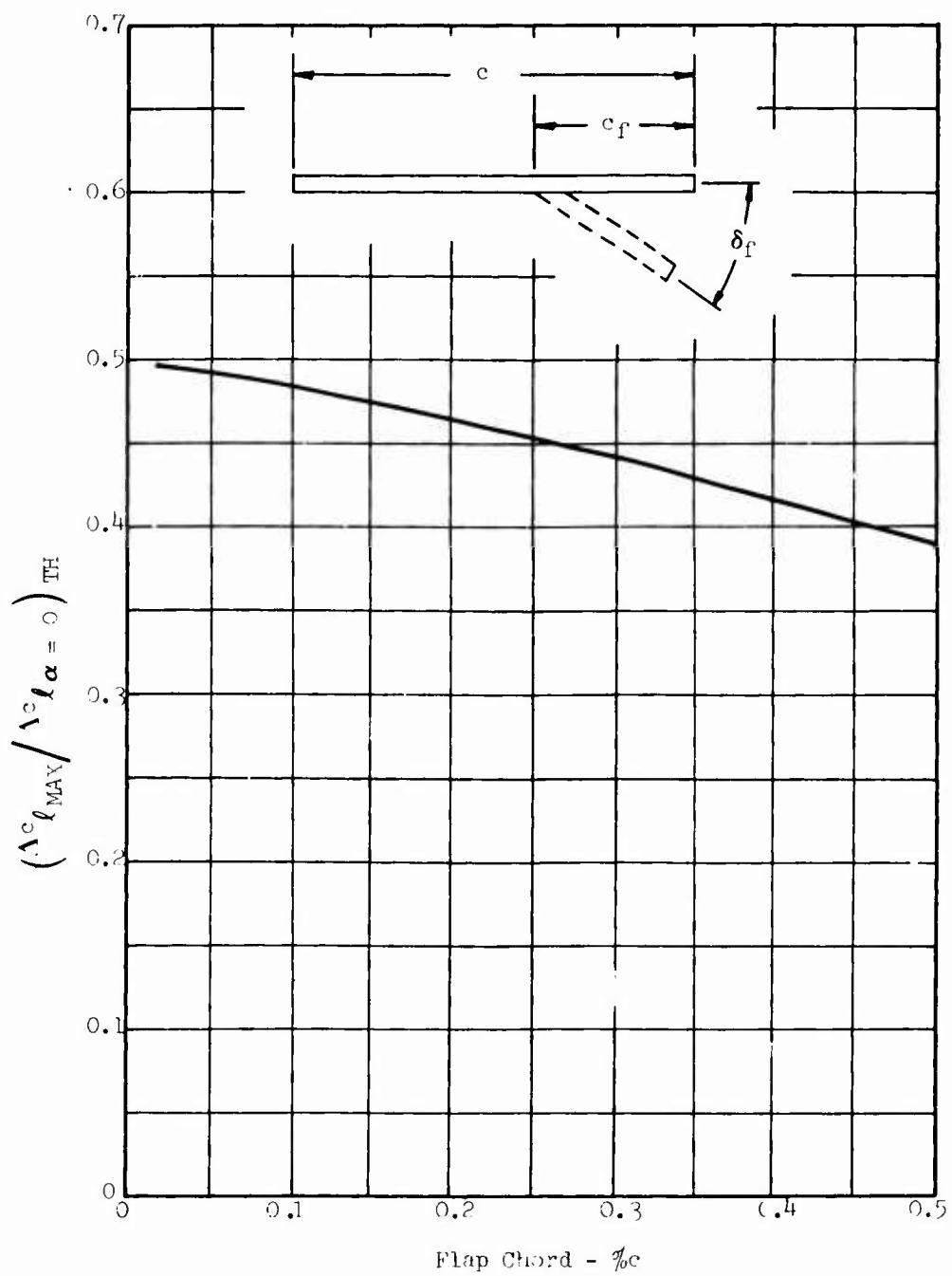
Figure 2. Theoretical Values of the Ratio of the Increment of Maximum Lift to the Increment of Lift at $\alpha = 0$ Versus Flap Chord.

Substituting in Equation (13), we may write

$$\Delta c_m = -1/2 \ (\sin \theta_f - 1/2 \sin 2\theta_f) \ \delta_f$$

$$= -1/2 \ (\sin \theta_f - \sin \theta_f \cos \theta_f) \ \delta_f \qquad (15)$$

where

$$\cos \theta_f = -\left(1 - 2 \frac{x_f}{c}\right)$$

The increment of moment due to flap deflection can now be expressed as

$$\Delta c_m = -\left(1 - \frac{x_f}{c}\right) \sin \theta_f \ \delta_f$$

$$= -\frac{x_f}{c} \sin \theta_f \ \delta_f = c_{m_\delta} \ \delta_f \qquad (16)$$

where $\quad c_{m_\delta}$ = the moment effectiveness parameter.

For convenience in analysis, the pitching moment increment caused by flap deflection can be expressed as the following ratio:

$$\frac{\Delta c_m}{\Delta c_{\ell_{\alpha=0}}} = \frac{c_{m_\delta}}{c_{\ell_\delta}} \qquad (17)$$

The theoretical values for $c_{m_\delta}/c_{\ell_\delta}$ are given in Figure 3.

2.1.2 Lift Increment at $\alpha = 0$ Degrees

The lift effectiveness of simple trailing edge flaps can be defined from thin airfoil theory. The rate of change of lift with flap deflection at constant angle of attack as given by Equation (7) is

$$c_{\ell_\delta} = 2 \ (\pi - \theta_f + \sin \theta_f) = \left(\frac{\partial c_\ell}{\partial \delta}\right)_\alpha$$

8
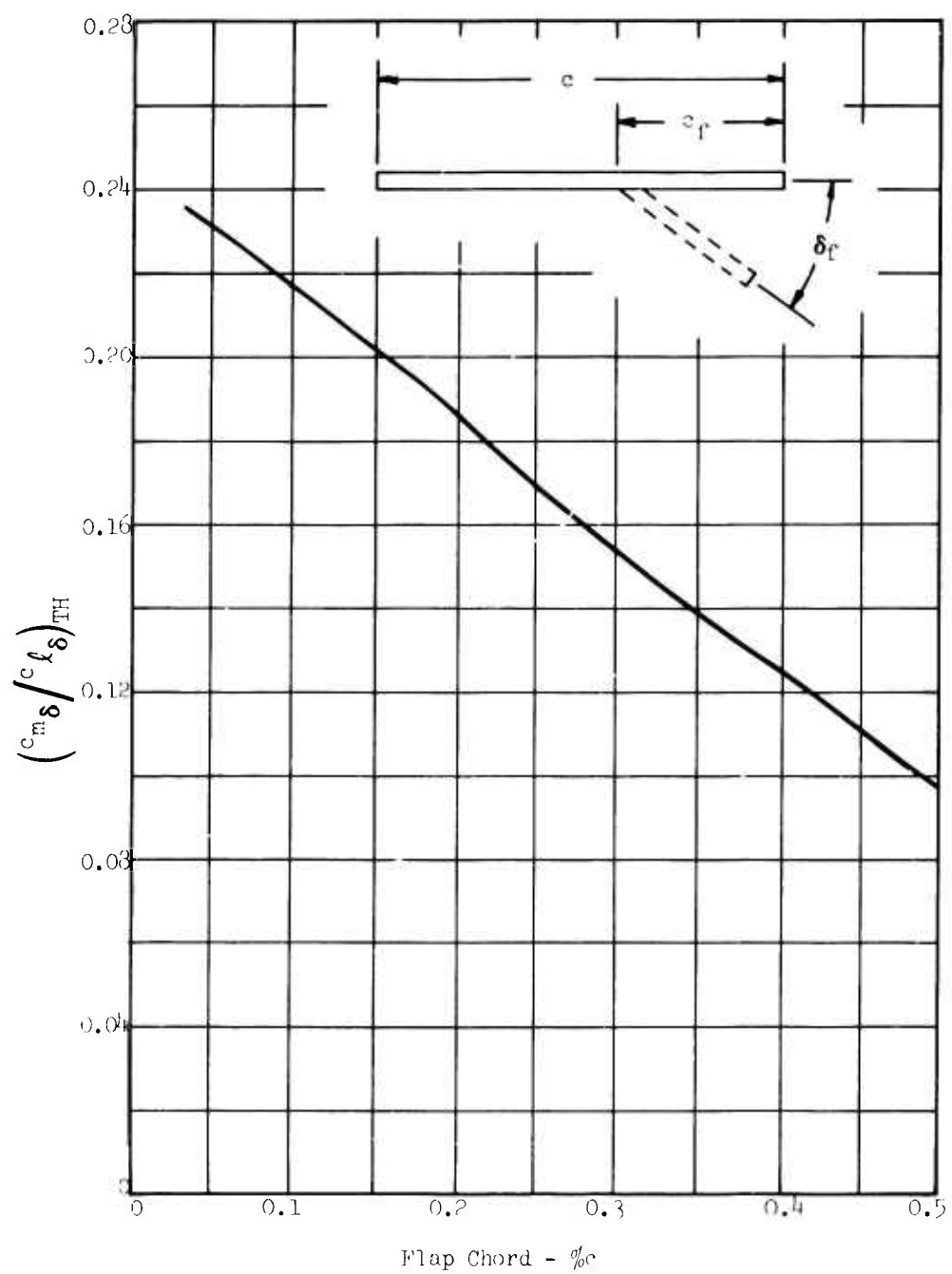
Figure 3. Theoretical Values of the Ratio of the Moment Effectiveness to Lifting Effectiveness Versus Flap Chord.

9

The lift of the flapped airfoil is related directly to the effective airfoil angle of attack for the linear lift range.

The theoretical lift effectiveness (c_{ℓ_δ}) is primarily a function of flap chord and airfoil thickness ratio. Any increase in airfoil thickness should increase the theoretical lift effectiveness term. However, it has been shown experimentally that the boundary layers on thick airfoils have a larger effect than on thin airfoils and cause a reduction in lift effectiveness. This reduction in lift effectiveness due to viscous effects is greater than the theoretical increases due to thickness.

Since the major effects are from the boundary layer, an empirical correlation parameter has been developed which relates the lifting characteristics of various trailing edge flaps to the theoretical lifting values for a flat plate.

This parameter, the effective turning angle, is defined by the following equation:

$$\Phi = \delta_f + \Phi_{TE} \tag{18}$$

where

$$\Phi_{TE} = TAN^{-1}\left(\frac{Y_{90} - Y_{100}}{0.10}\right)$$
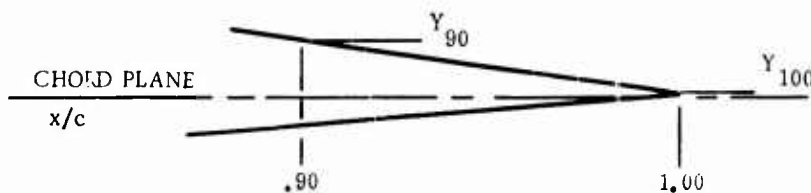
Airfoil Trailing Edge

The effective turning angle is used to relate the lifting efficiency of the flap to the theoretical thin airfoil lift values. The lifting efficiency is determined for plain, single- and double-slotted flaps shown in Figure 4.

The procedure assumes no compressibility or Reynolds number effects. The Reynolds number effect is accounted for in predicting the characteristics of the clean airfoil. Reference 11 indicates that the lift increment due to flaps is essentially constant with Reynolds number. The data used in developing the procedure was generally taken from two-dimensional tests conducted at Reynolds numbers of the order of 3.0×10^6.
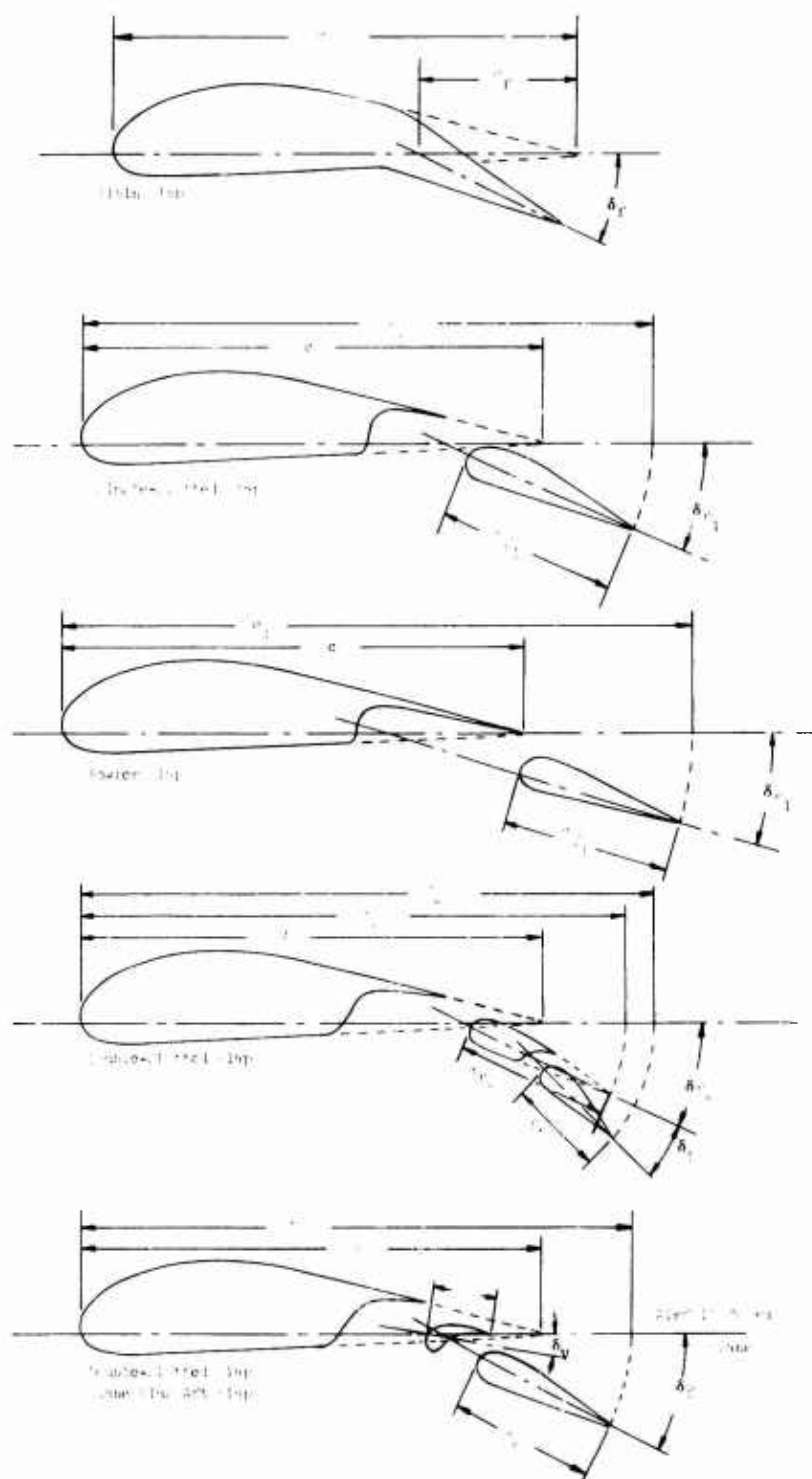
Figure 4. Trailing Edge Flap Geometry.

11

The lift increment at $\alpha = 0$ can then be calculated for plain flaps by using the following expression:

$$\Delta c_{\ell_{\alpha=0}} = \eta_P \, c_{\ell_\delta} \, \delta_f \tag{19}$$

where η_P is the lifting efficiency of the plain flap developed from data in References 12 through 17 (from Figure 5).

c_{ℓ_δ} is the theoretical lifting effectiveness (from Figure 1).

δ_f is the flap deflection angle.

Comparisons of low-speed test data with predicted $\Delta c_{\ell_{\alpha=0}}$ show that the correlations generally were within plus or minus 10 percent of the experiment values.*

The introduction of a slot to the plain flap creates slot flow that energizes the boundary layer over the flap. This flow at the slot lip decreases the viscous effects present on the plain flap and therefore increases the lifting efficiency of the single-slotted flap for deflections greater than 15 degrees. The lift increment at $\alpha = 0$ due to flap deflection for the single-slotted flap is given by the following expression:

$$\Delta c_{\ell_{\alpha=0}} = \eta_1 \, c_{\ell_\delta} \, \delta_f \tag{20}$$

Since most slotted flaps extend the airfoil chord, the equation is further modified as follows:

$$\Delta c_{\ell_{\alpha=0}} = \eta_1 \, c_{\ell_{\delta_1}} \, \delta_{f_1} \left(\frac{c_1}{c} \right) \tag{21}$$

where η_1 is the lifting efficiency of the single-slotted flap developed from data in References 18 through 27 (from Figure 5).

$c_{\ell_{\delta_1}}$ is the theoretical lifting effectiveness based on flap chord (from Figure 1).

δ_{f_1} is the single-slotted flap deflection.

$\left(\dfrac{c_1}{c} \right)$ is the ratio of extended chord to airfoil chord (from geometry in Figure 4).

*Note: All data correlations are shown in Reference 5.

12
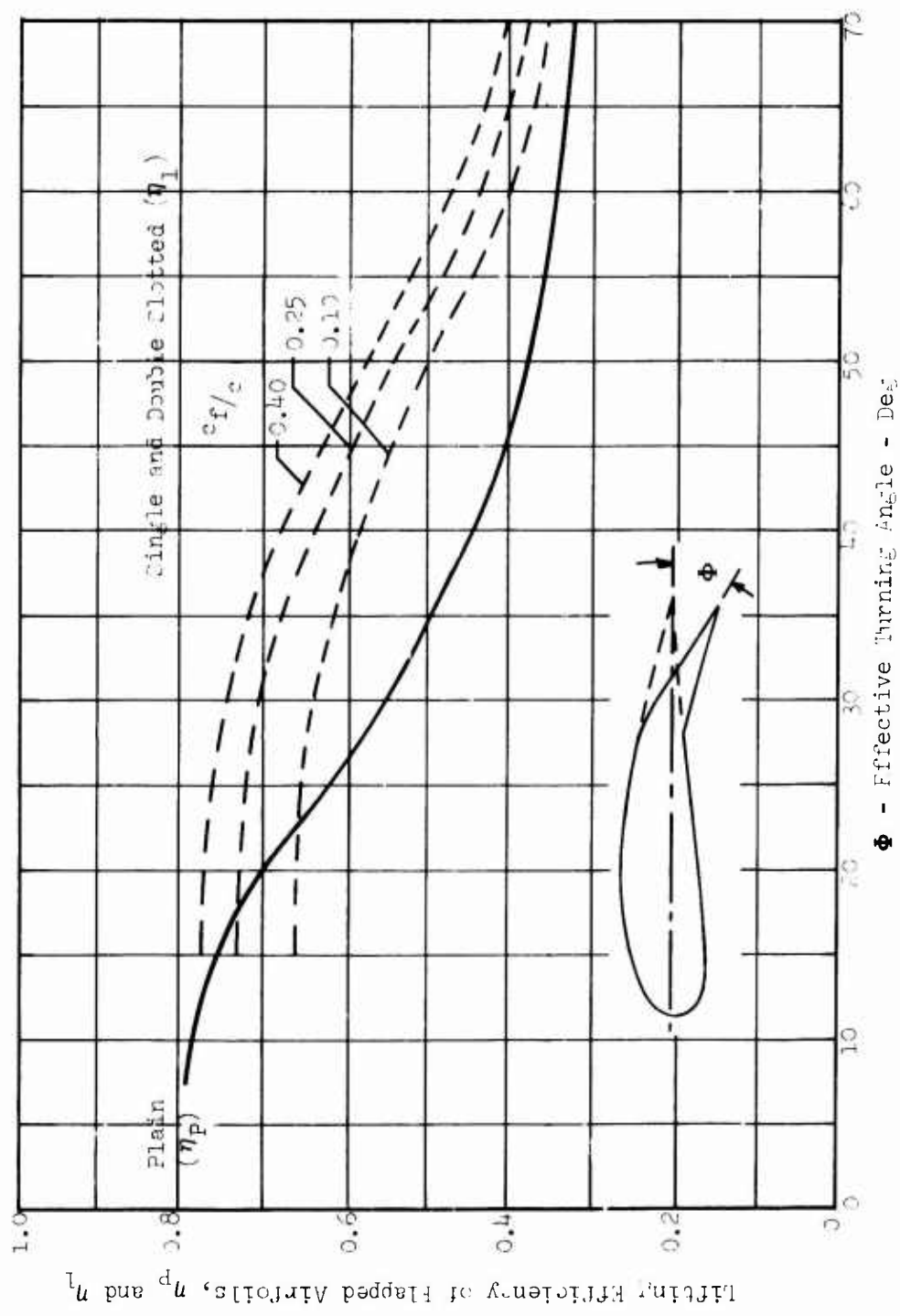
Figure 5. Turning Efficiency of Flaps.

13

All of the flaps analyzed incorporated chord extension which varied from 0 to approximately 10 percent. The procedure described above showed very good results for the single-slotted flaps at any arbitary deflection and chord extension. In addition, single-slotted flaps with 100 percent flap chord extension (chord extension equal to flap chord) were analyzed.

Because of the lack of systematic NACA experimental data for the various geometric and aerodynamic variables involved, it is very difficult to arrive at a more accurate data correlation basis. The data correlation for single-slotted flaps relied heavily on systematic comparisons of data from References 18 through 27. The correlations were generally within plus or minus 10 percent of the experimental values.

The introduction of a secondary slot to the flaps is handled by adding a term to Equation (21). The lift increment at $\alpha = 0$ due to flap deflection for double-slotted flaps is then given by the following expression:

$$\Delta c_{\ell_{\alpha=0}} = \eta_1 c_{\ell_{\delta_1}} \delta_{f_1} \left(\frac{c_1}{c}\right) + \eta_2 c_{\ell_{\delta_2}} \delta_{f_2} \left(1 + \frac{c_2 - c_1}{c}\right) \tag{22}$$

where   subscripts 1 and 2 refer to the primary and secondary flap, respectively.

$\left(\dfrac{c_1}{c}\right)$ is the ratio of extended chord to airfoil chord resulting from deflection of the primary flap.

$\left(1 + \dfrac{c_2 - c_1}{c}\right)$ is the ratio of extended chord to airfoil chord resulting from deflection of the secondary flap.

The flap geometry is from Figure 4.

The secondary slot caused by deflecting the aft flap is not as effective in creating lift as the primary slot. As a consequence, an additional empirical correlation parameter η_{2S} was developed. Values of η_{2S} versus aft flap deflection are shown in Figure 6. As the forward flap deflection is increased to approximately 20 degrees, the efficiency of the aft flap decreases for aft flap deflection greater than 15 degrees. The lifting effectiveness for the aft flap, η_2, is defined as

$$\eta_2 = \eta_1 \eta_{2S} \tag{23}$$

where η_1 is determined from the aft flap deflection and chord (from Figure 5).

η_{2S} accounts for reduced effectiveness of the aft flap (from Figure 6).

14
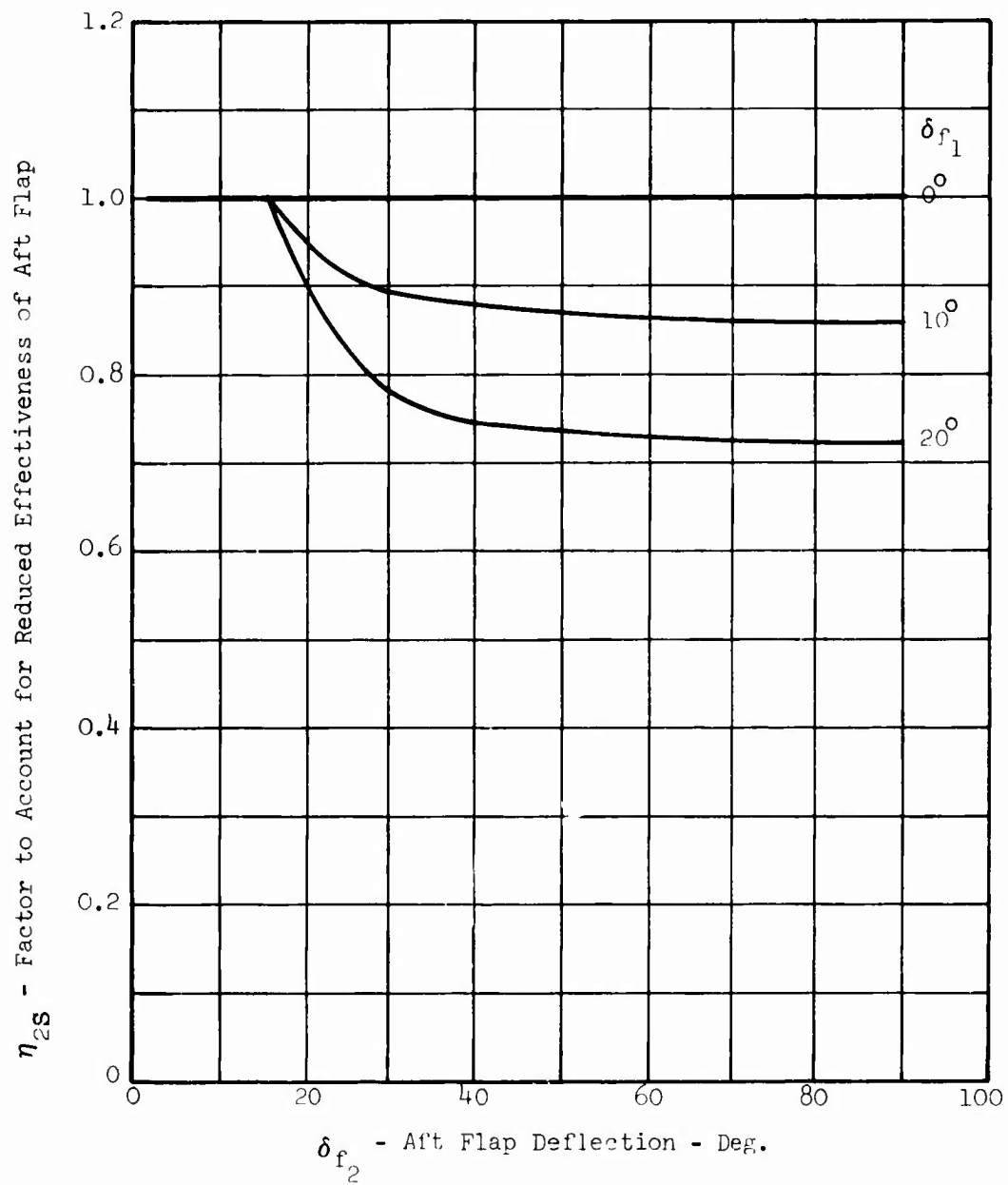
Figure 6. Turning Efficiency of Aft Flaps.

15

A similar procedure was also developed to analyze the double-slotted flap that has a vane and aft flap. The vane is contoured to produce slot flow at the forward slot lip and at a forward secondary slot. This type of double-slotted flap is shown in Figure 4. The available data indicated that the aft flap for this configuration does operate at full efficiency. The lift increment at $\alpha = 0$ due to flap deflection for a vane and aft flap combination is given below:

$$\Delta c_{\ell_{\alpha=0}} = \tau_1 \, c_{\ell_{\delta_v}} \, \delta_v \left(\frac{c + c_v}{c} \right) + \eta_1 \, c_{\ell_{\delta_2}} \, \delta_{f_2} \left(1 + \frac{c_2 - c_v}{c} \right) \tag{24}$$

where   subscripts v and 2 refer to the vane and secondary flap, respectively.

η_1 is the turning efficiency presented in Figure 5.

$\left(\dfrac{c + c_v}{c} \right)$ is the ratio of extended chord to airfoil chord resulting from deflection of the vane.

$\left(1 + \dfrac{c_2 - c_v}{c} \right)$ is the ratio of extended chord to airfoil chord resulting from deflection of the secondary flap.

The comparisons of experimental data from References 18, 24, and 27 through 33 with predicted values for the double-slotted flaps indicated correlations within plus or minus 10 percent of the experimental values.

2.1.3   Lift Curve Slope Increment

The theories for thin airfoils indicate that the lift curve slopes of a flat or cambered airfoil are the same, $c_{\ell_\alpha} = 2\pi$. The camber term simply shifts the lift curve upward by a constant increment. The experimental lift curve slopes for the unflapped and flapped airfoils without chord extension generally verify the theory. This assumption is valid up to the point where the flow separates from the airfoil or flap. After the flow separates, the lift curve slope of the flapped airfoil decreases to a value below that of the basic airfoil.

The effect of flap extension is determined by simply considering the change in effective chord. For a flapped airfoil with chord extension, the lift curve slope is then directly related to the airfoil chord increase.

16

$$c_{\ell_{\alpha_{EXT}}} = c_{\ell_{\alpha_{AIRFOIL}}} \left(\frac{c_{EXT}}{c} \right) \qquad (25)$$

This procedure assumes that (1) the lift curve slope for plain flaps is that of the unflapped airfoil, and (2) the change in lift curve slope for flaps that extend the airfoil chord is given by

$$\Delta c_{\ell_{\alpha_{EXT}}} = c_{\ell_{\alpha_{AIRFOIL}}} \left(\frac{c_{EXT} - c}{c} \right) \qquad (26)$$

where c_{ℓ_α} is the lift curve slope of the unflapped airfoil (from Reference 1).

c_{EXT} is the extended chord and is defined as c_1 for the single-slotted flap and c_2 for the double-slotted flap (from Figure 4).

2.1.4 Maximum Lift Increment

The maximum lift increments obtained from thin airfoil theory for flapped airfoils are strongly dependent on the flow characteristics of the unflapped airfoil at maximum lift. The phenomena for conventional airfoils are directly related to the airfoil leading edge radius and trailing edge angle. These parameters are determined by the airfoil family and thickness distribution (see References 1 and 2).

Basically, the deflection of the trailing edge introduces camber to the airfoil and results in a lift increase. Thin airfoil theory indicates a basic load distribution from angle of attack and an incremental load distribution due to camber or flap deflection, as shown in the following sketch.
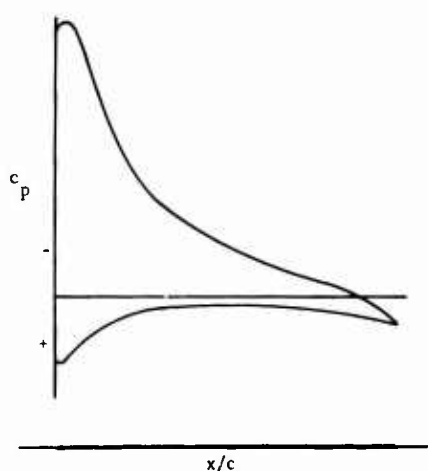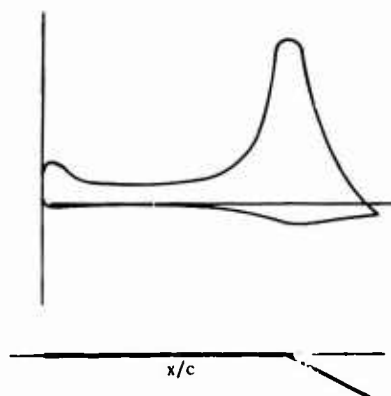
Basic Load Distribution   Load Distribution Due to Flap Deflection

17

The loading caused by flap deflection has a peak at the flap hinge line that diminishes to zero near the flap trailing edge and reduces to a much lower value at the leading edge. Nominally, the forward pressure gradient is relieved and the gradient over the flap is increased, causing separation even at low flap deflection. This trend is noticeable in Figure 5, which indicates the turning efficiency of plain flaps at $\alpha = 0$. The efficiency is reduced by separation and begins to fall off at flap deflections above 15 degrees. The flow separation is confined aft of the hinge line and does not spread forward until the flap deflection becomes increasingly large or the flapped airfoil reaches a maximum angle of attack and stalls. Maximum lift can then be defined as the lift limited by either flow separation that progresses forward of the flap or flow separation from the leading edge.

The theoretical relationship from thin airfoil theory was applied to the available maximum lift data on trailing edge flaps. The theoretical ratio of the maximum lift increment to the lift increment developed at $\alpha = 0$ is based on a criterion of leading edge separation on thin airfoils. As a consequence, empirical factors were required to correlate the experimental data on airfoils with finite thickness. The correlation parameters account for leading edge radius, thickness, flap chord, and flap deflection.

The resulting expression for maximum lift increment for plain, single- and double-slotted flaps uses the lift increment at $\alpha = 0$ from Section 2.1.2 and is given by the following expression:

$$\Delta c_{\ell_{max}} = \Delta c_{\ell_{\alpha=0}} \left(\frac{\Delta c_{\ell_{max}}}{\Delta c_{\ell_{\alpha=0}}} \right)_{TH} K_T K_\delta \tag{27}$$

where $\Delta c_{\ell_{\alpha=0}}$ is the predicted lift increment (from Section 2.1.2).

$\left(\dfrac{\Delta c_{\ell_{max}}}{\Delta c_{\ell_{\alpha=0}}} \right)_{TH}$ is the theoretical relationship accounting for flap chord (from Figure 2).

K_T is the empirical factor developed from experimental data for a flap at an optimum deflection angle (from Figures 7 and 8).

K_δ is the factor accounting for changes in flap deflection from the optimum deflection (from Figure 9).

18
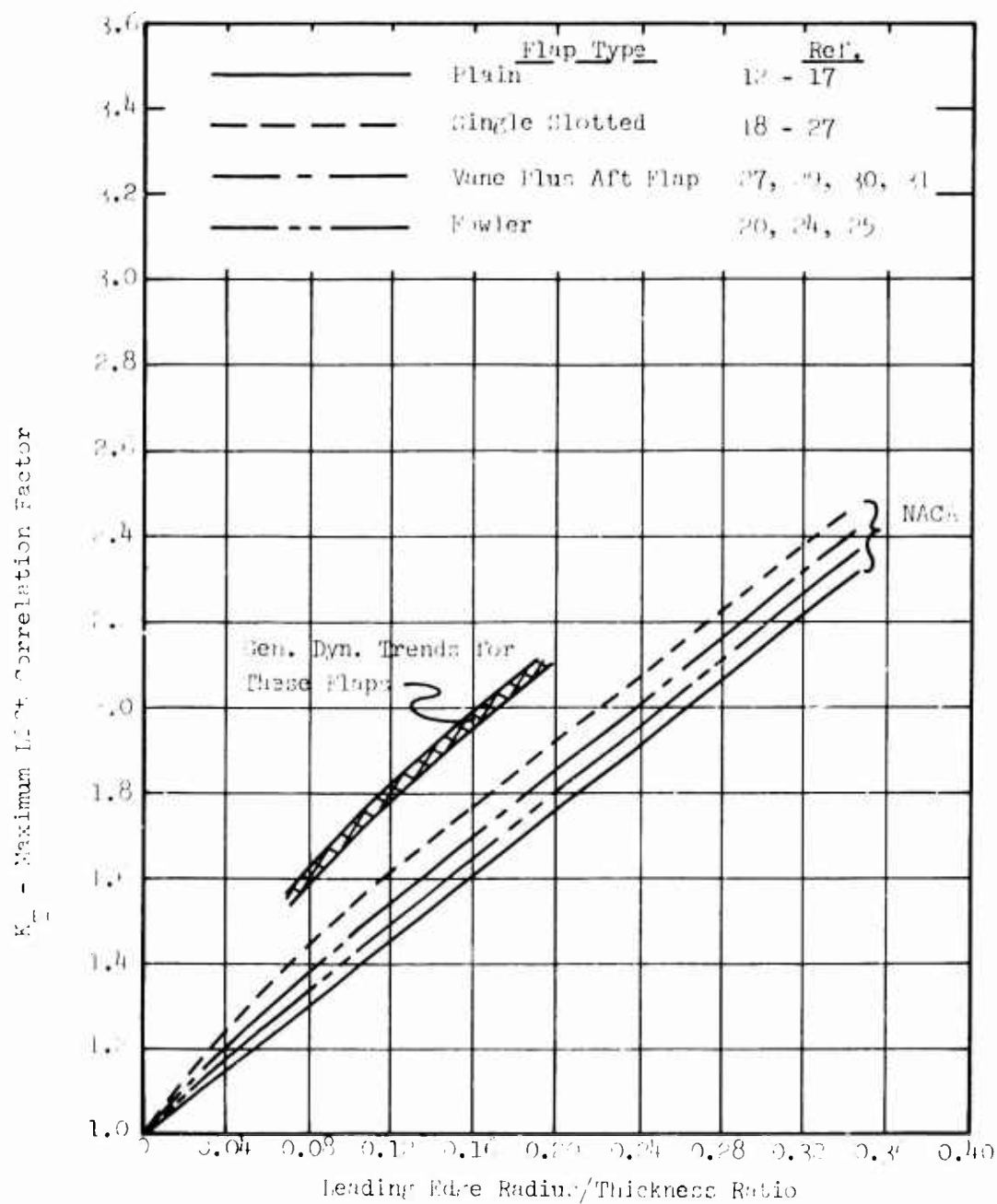
Figure 7. Maximum Lift Correlation Factor for Trailing Edge Flaps
Versus Leading Edge Radius/Thickness Ratio.

19
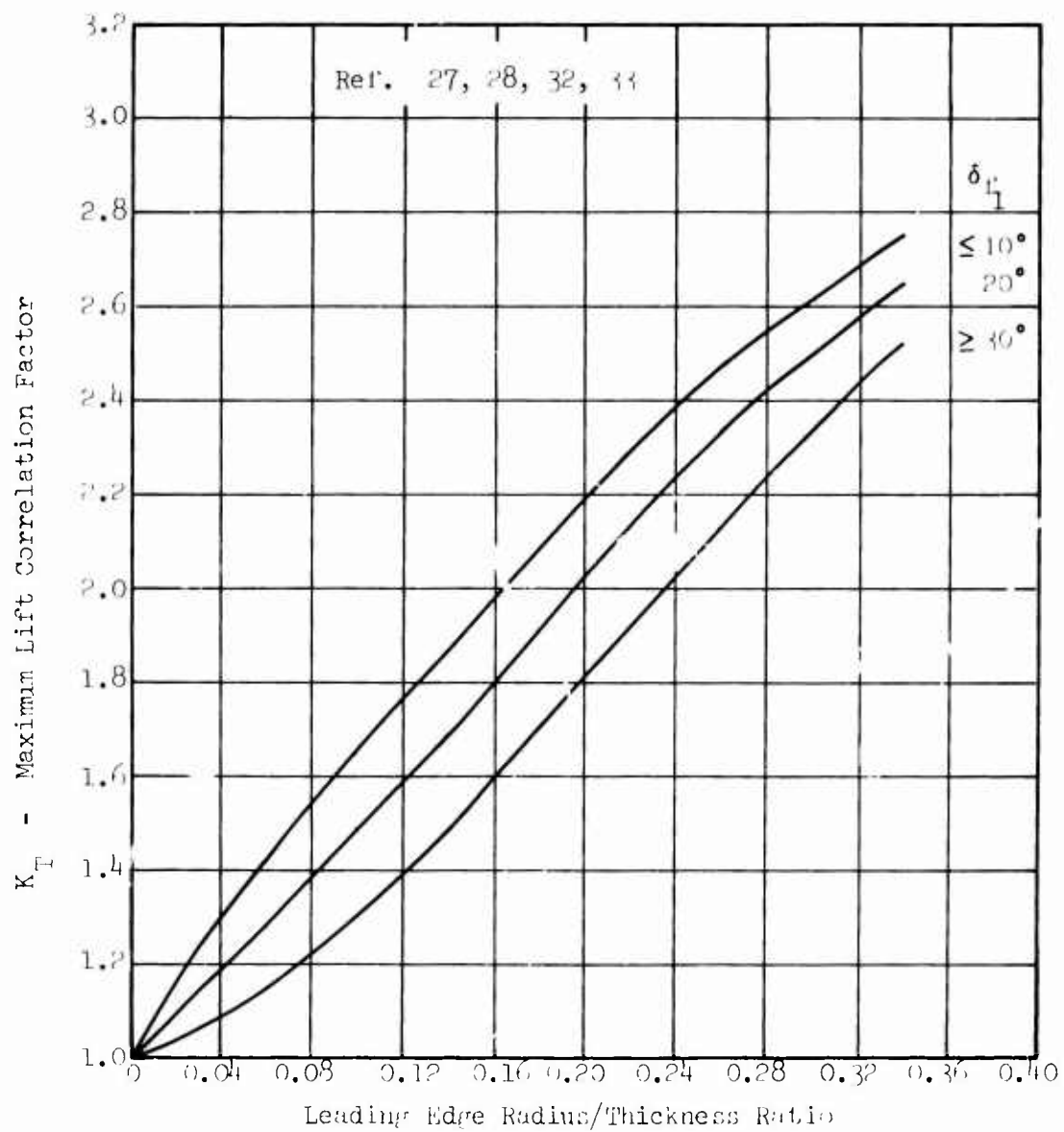
Figure 8. Maximum Lift Correlation Factor for Double-Slotted Trailing
Edge Flaps Versus Leading Edge Radius/Thickness Ratio.

20

The factor K_T was developed to account for flow separation from either the leading or trailing edge on airfoils with finite thickness.

The parameter, leading edge radius/thickness ratio, shown in Figures 7 and 8 is based on leading edge radius and thickness ratio of the basic airfoil. These terms correlate the data and give an adequate description of maximum lift increment for the trailing edge flaps considered. The data trends from recent General Dynamics two-dimensional tests are also shown in Figures 7 and 9. These tests were conducted in a facility that uses blowing slots on the walls to reduce separation effects.

Prediction of the maximum lift of single-slotted flaps with full chord extension requires an additional factor. This term, K_E, is shown in Figure 9.

2.1.5 Pitching Moment Increment

The equations developed from thin airfoil theory, Section 2.1.1, show that the pitching moment increment due to flap deflection is

$$\Delta c_m = c_{m_\delta} \delta$$

The moment was then directly related to the lift increment at $\alpha = 0$ by the following expression:

$$\frac{\Delta c_m}{\Delta c_{\ell_{\alpha=0}}} = \frac{c_{m_\delta}}{c_{\ell_\delta}}$$

The resulting values for the theoretical term are given in Figure 3. These values are used in conjunction with the predicted lift increment at $\alpha = 0$ to develop empirical factors and correlate experimental data. The expression for the pitching moment increment becomes

$$\Delta c_m = \Delta c_{\ell_{\alpha=0}} \left(\frac{c_{m_\delta}}{c_{\ell_\delta}} \right)_{TH} K_m \tag{28}$$

where $\Delta c_{\ell_{\alpha=0}}$ is the predicted lift increment (from Section 2.1.2).

21
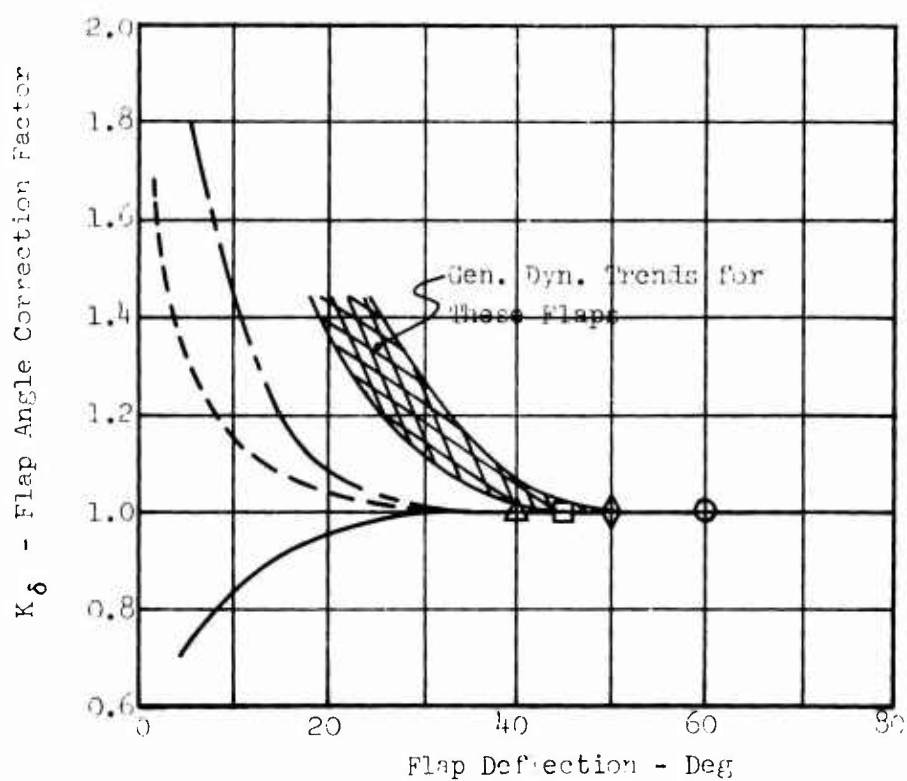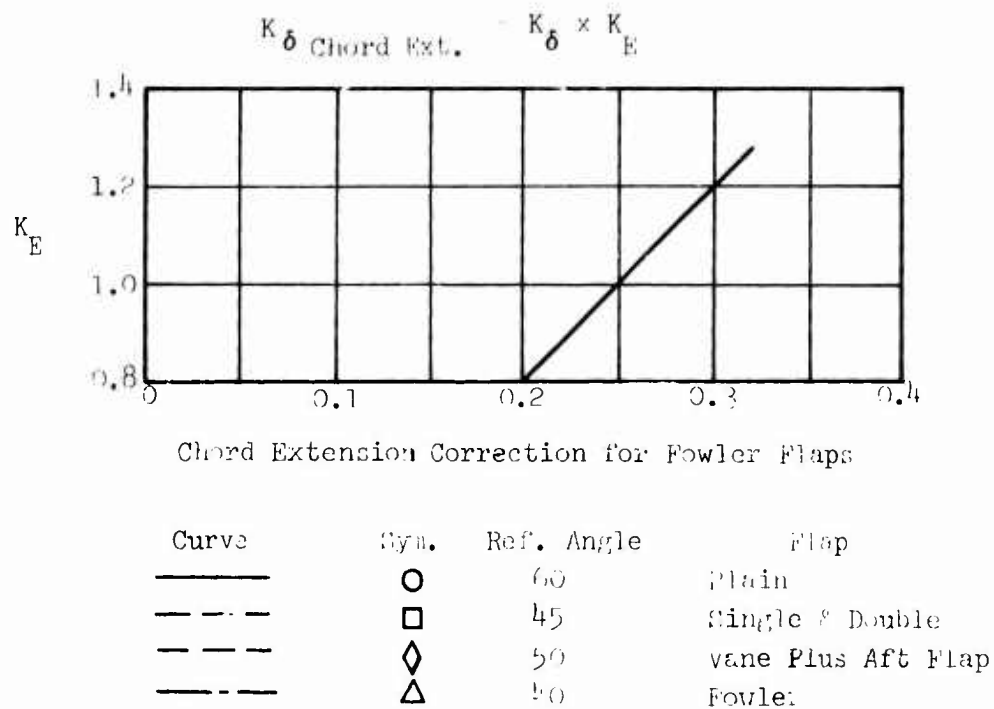
Figure 9. Flap Angle Correction Factor Versus Flap Deflection.

$$\left(\frac{c_{m_\delta}}{c_{\ell_\delta}}\right)_{TH}$$ is the theoretical relationship accounting for flap chord (from Figure 3).

K_m is the empirical factor developed from experimental data (from Figure 10).

Thin airfoil theory gives a good approximation of moment for trailing edge flaps for which the flow remains attached. However, as flap chord and thickness are increased, factors are required to account for flow separation as shown in Figure 10.

2.1.6 Pitching Moment Curve Slope

Deflection of a trailing edge flap on a thin airfoil introduces camber to the basic airfoil. The thin airfoil theory discussed in Section 2.1.1 indicates that camber does not change the moment curve slope of the airfoil. Experimental data verify that there is no change in slope for the angle of attack and flap deflection ranges of plain flaps for which flow is attached. At angles of attack above the linear range, the flow over the flap separates and the additional loading from the flap is lost and pitch-up results. Below the linear range, the flow separates on the underside of the airfoil, causing a forward shift in center of pressure and a resulting nose-up moment change.

This investigation only concerns itself with the linear variation of the pitching moment curve slope. For plain flaps, the assumption is that there is no change in slope. Trailing edge flaps with translating motion cause a change in moment curve slope. This change is related directly to chord extension as indicated by References 19, 22, and 27, and is described by the following expression:

$$\frac{\Delta c_m}{\Delta c_\ell} \approx -0.25 \, K_{ac} \left(\frac{c_{EXT} - c}{c}\right) \tag{29}$$

where K_{ac} is an empirical factor to account for chord extension (from Figure 11).

c_{EXT} is the extended chord which is defined as c_1 for the single-slotted flap and c_2 for the double-slotted flap (from Figure 4).

The linear range on the moment curve is reduced at higher flap deflections.

23
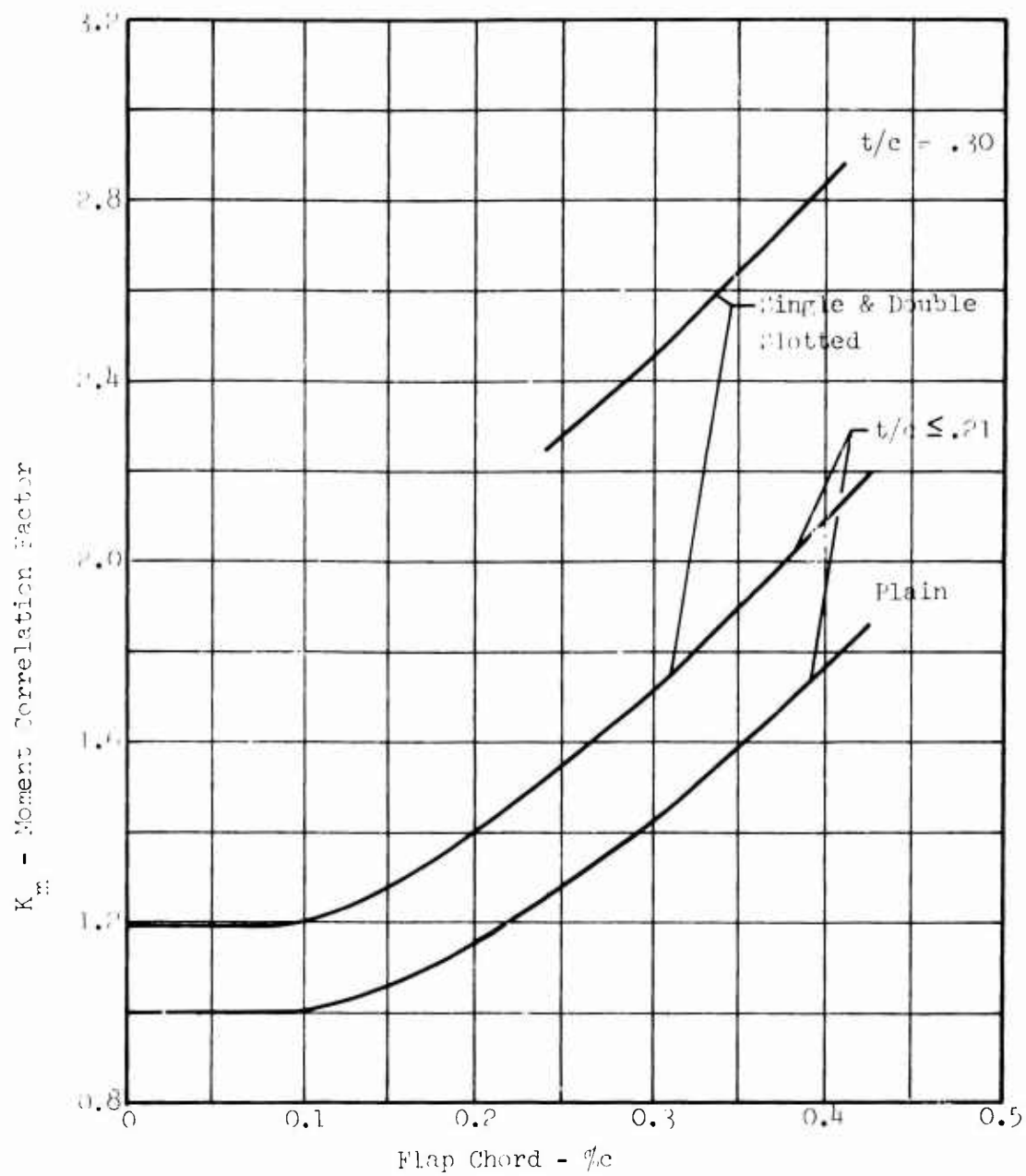
Figure 10. Moment Correlation Factor Versus Flap Chord.
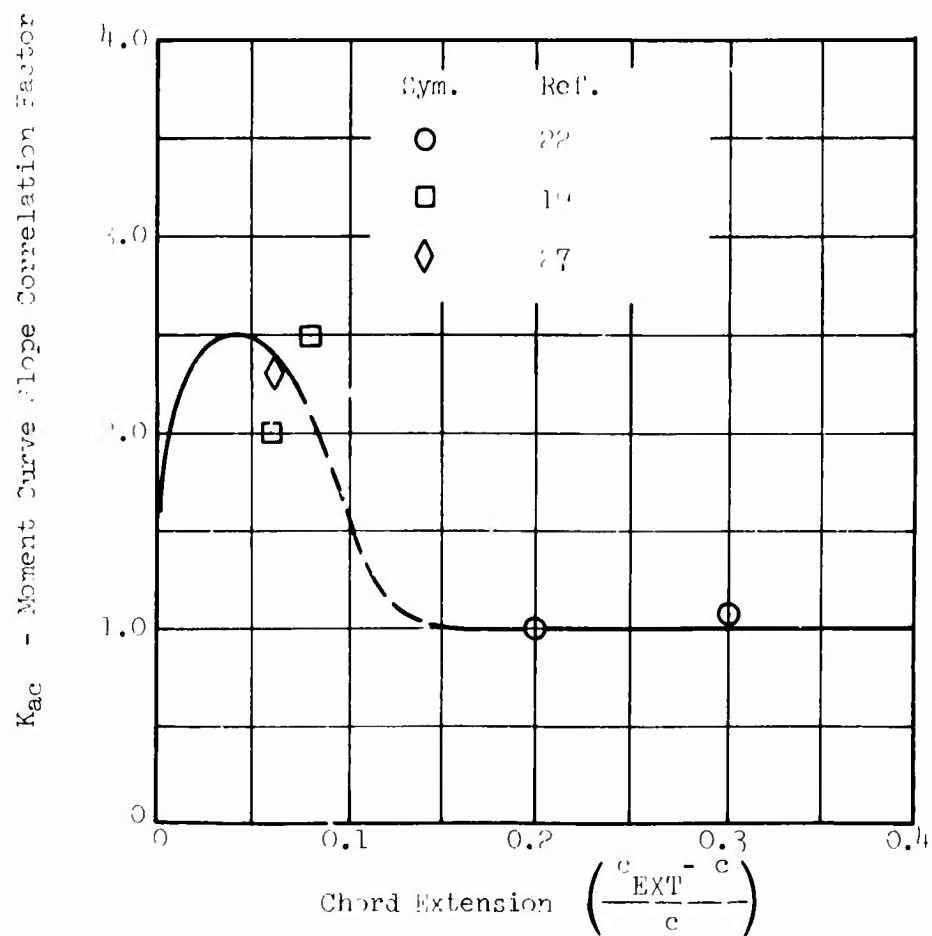
Figure 11. Moment Curve Slope Correlation Factor Versus Chord Extension.

2.1.7 Drag Increment

The approach utilized for predicting the drag of trailing edge flaps is mainly empirical. All available data utilized in Section 2.1.1 for predicting the increment of lift at $\alpha = 0$ was used in the correlation. The correlation parameter selected was the value of $\Delta c_{\ell_{\alpha=0}}$ so that any variation in drag with flap deflection was removed. This assumes that the drag is directly related to the lifting capability of the flap and indirectly related to flap deflection and flap type.

Flap drag increments at $\alpha = 0$ for plain, single- and double-slotted flaps are shown in Figures 12, 13, and 14.

2.2 LEADING EDGE DEVICES

2.2.1 Theory

Thin airfoil theory for trailing edge flaps is covered in Section 2.1.1. A further extension of this theory to cover leading edge devices is covered in this section. The aerodynamic lift and moment of leading edge flaps can be obtained from trailing edge flap theory with a geometrical transformation. Consider the flapped airfoil shown below:
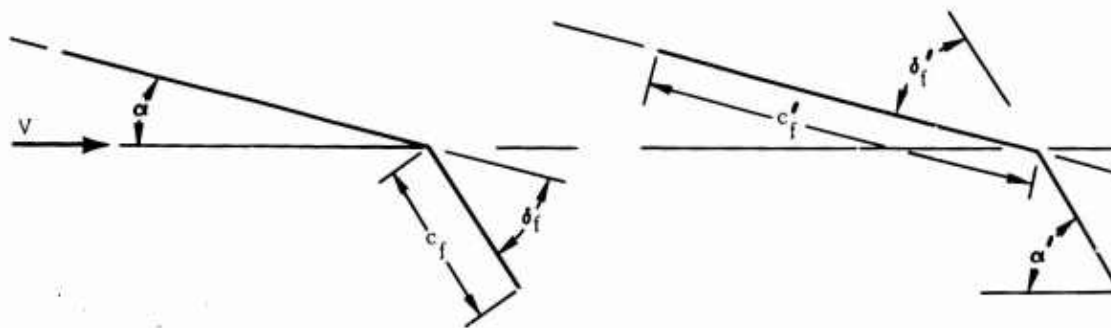
Geometry for Airfoil With   Geometry for Airfoil With
a Trailing Edge Flap   a Leading Edge Flap

26
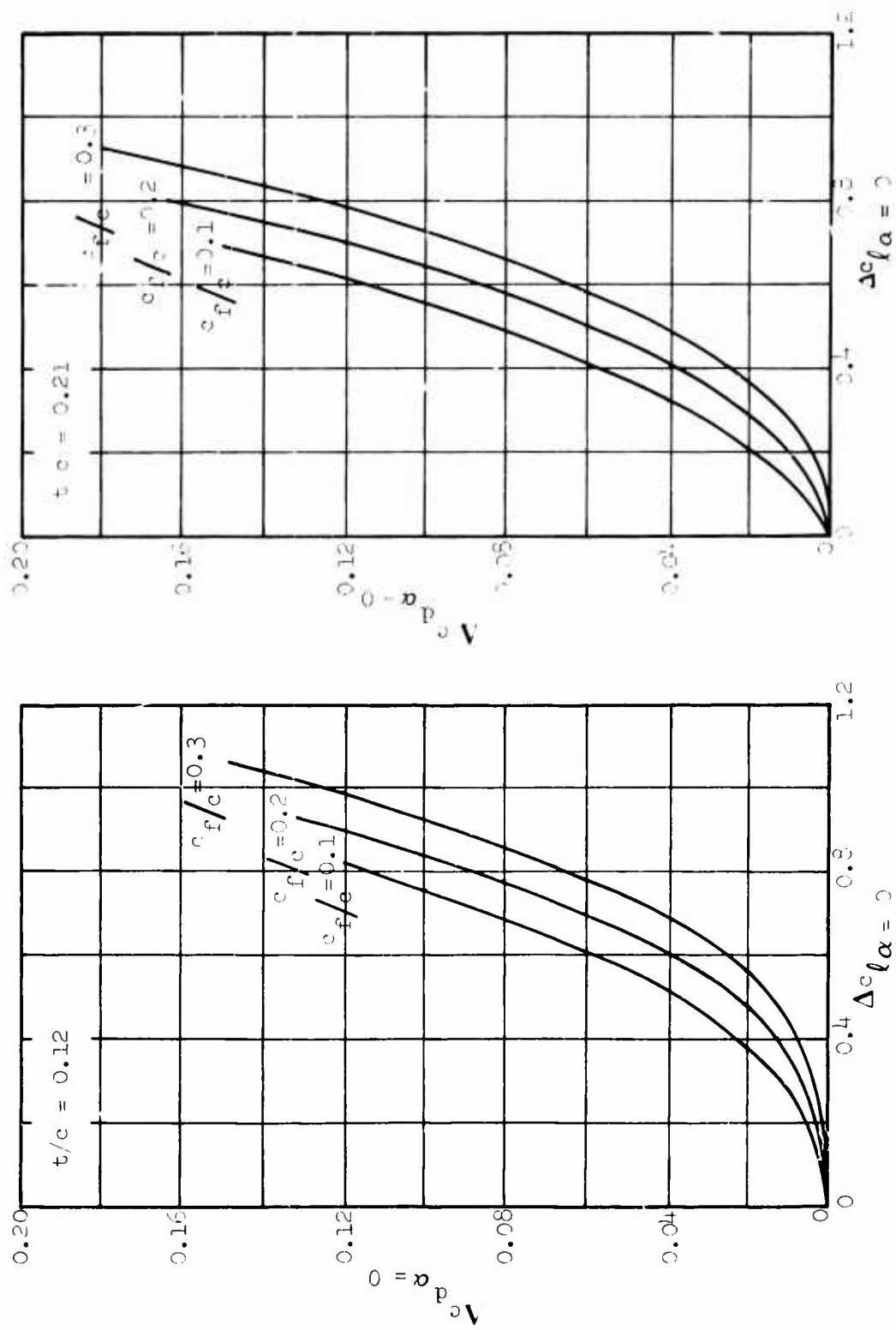
Figure 12. Drag increments for Plain Flaps Versus Lift Increment at $\alpha = 0$.

27
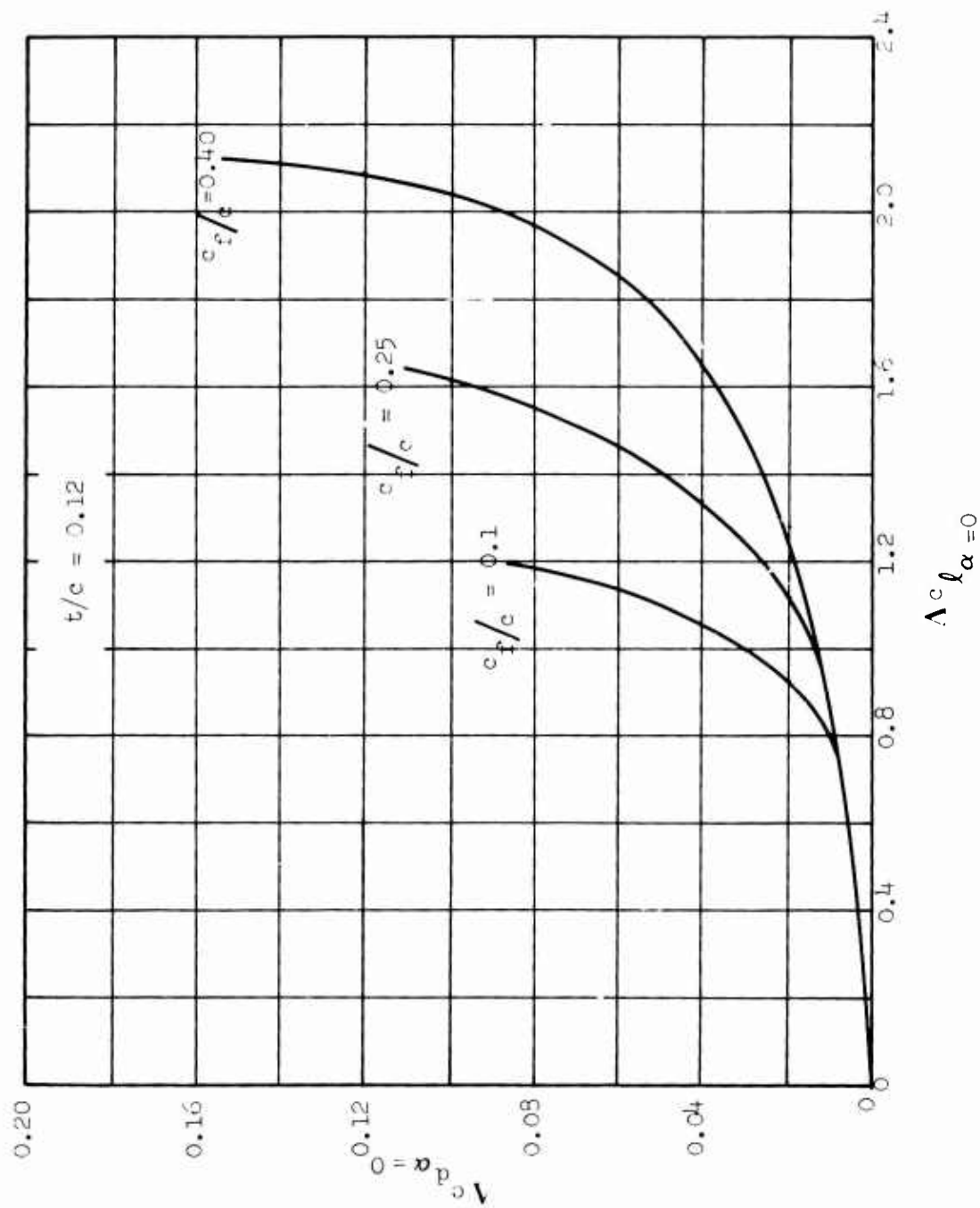
Figure 13a. Drag Increments for Single-Slotted Flaps Versus Lift Increment at $\alpha = 0$.

28
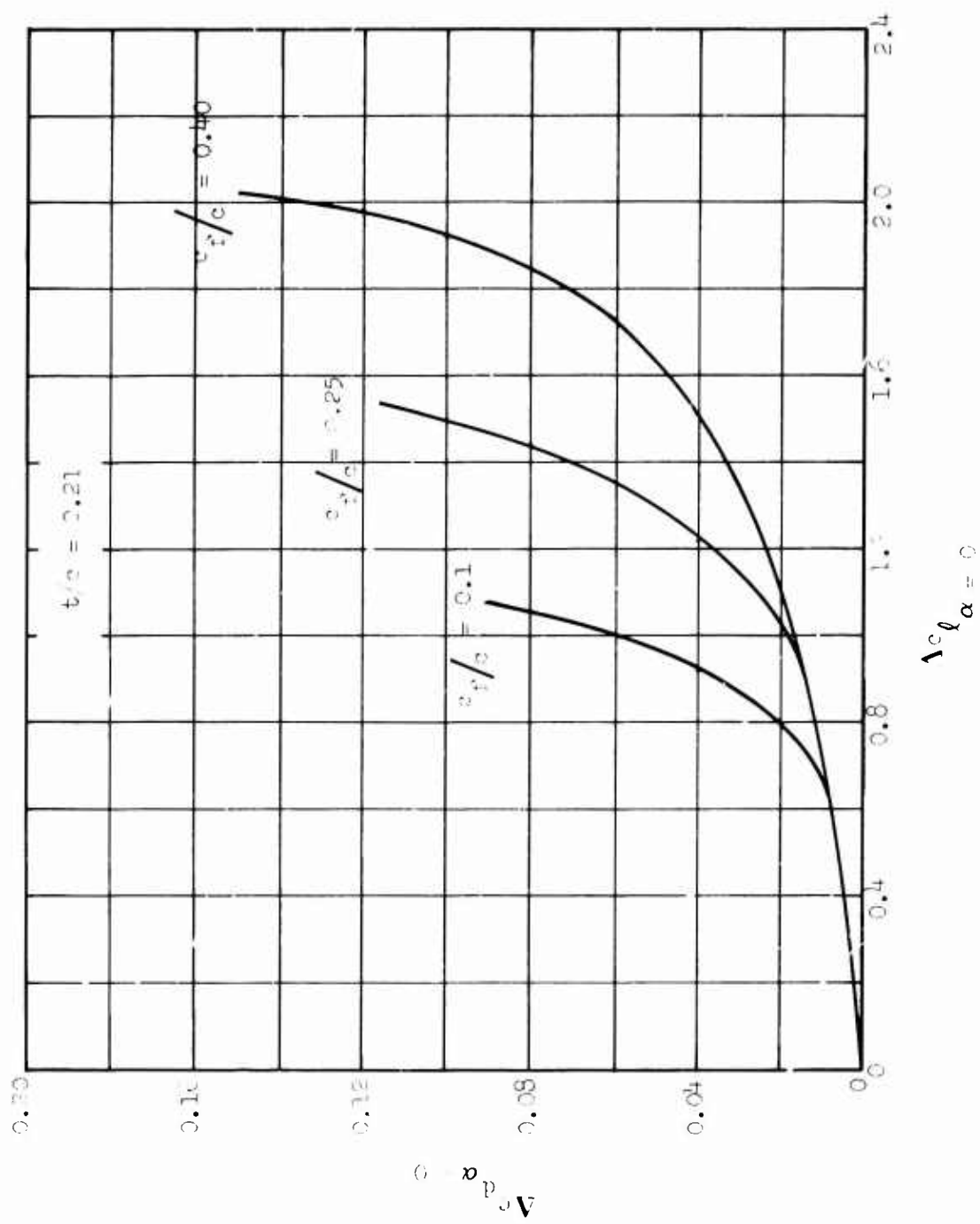
Figure 13b. Drag Increments for Single-Slotted Flaps Versus Lift Increment at $\alpha = 0$, Contd.

29
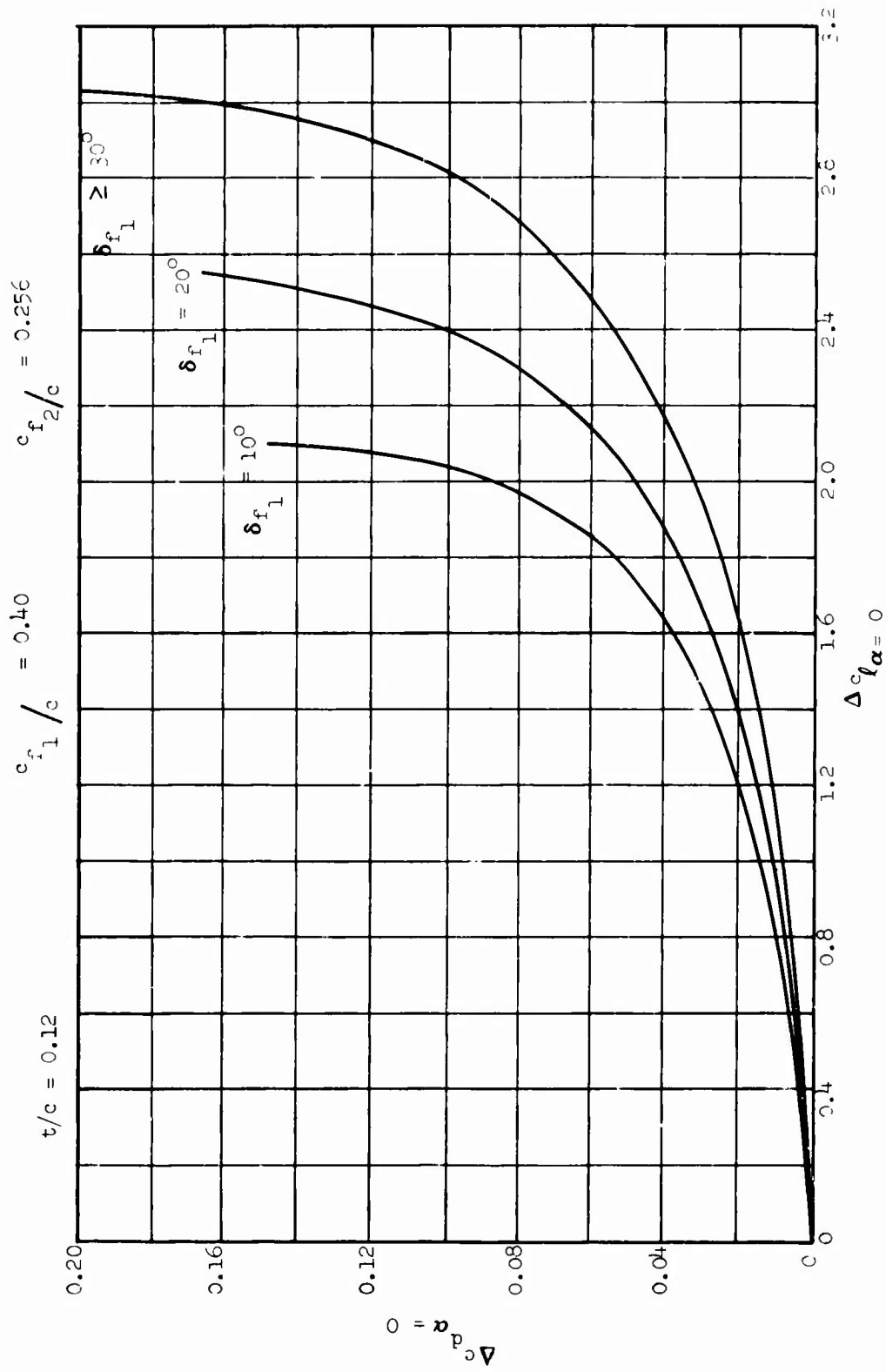
Figure 14a. Drag Increments for Double-Slotted Flaps Versus Lift Increment at $\alpha = 0$.

30
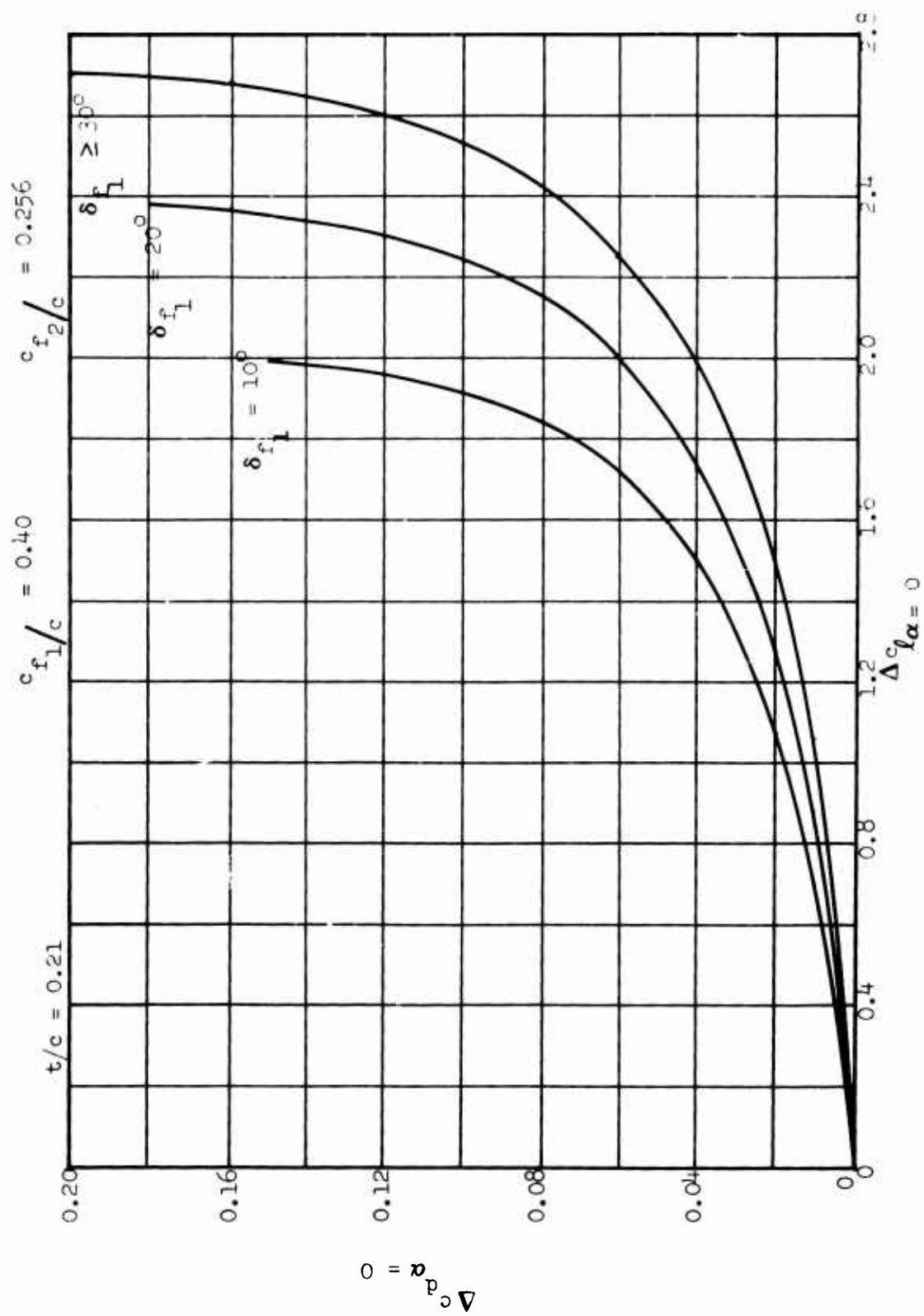
Figure 14b. Drag Increments for Double-Slotted Flaps Versus Lift Increment at $\alpha = 0$, Contd.

31
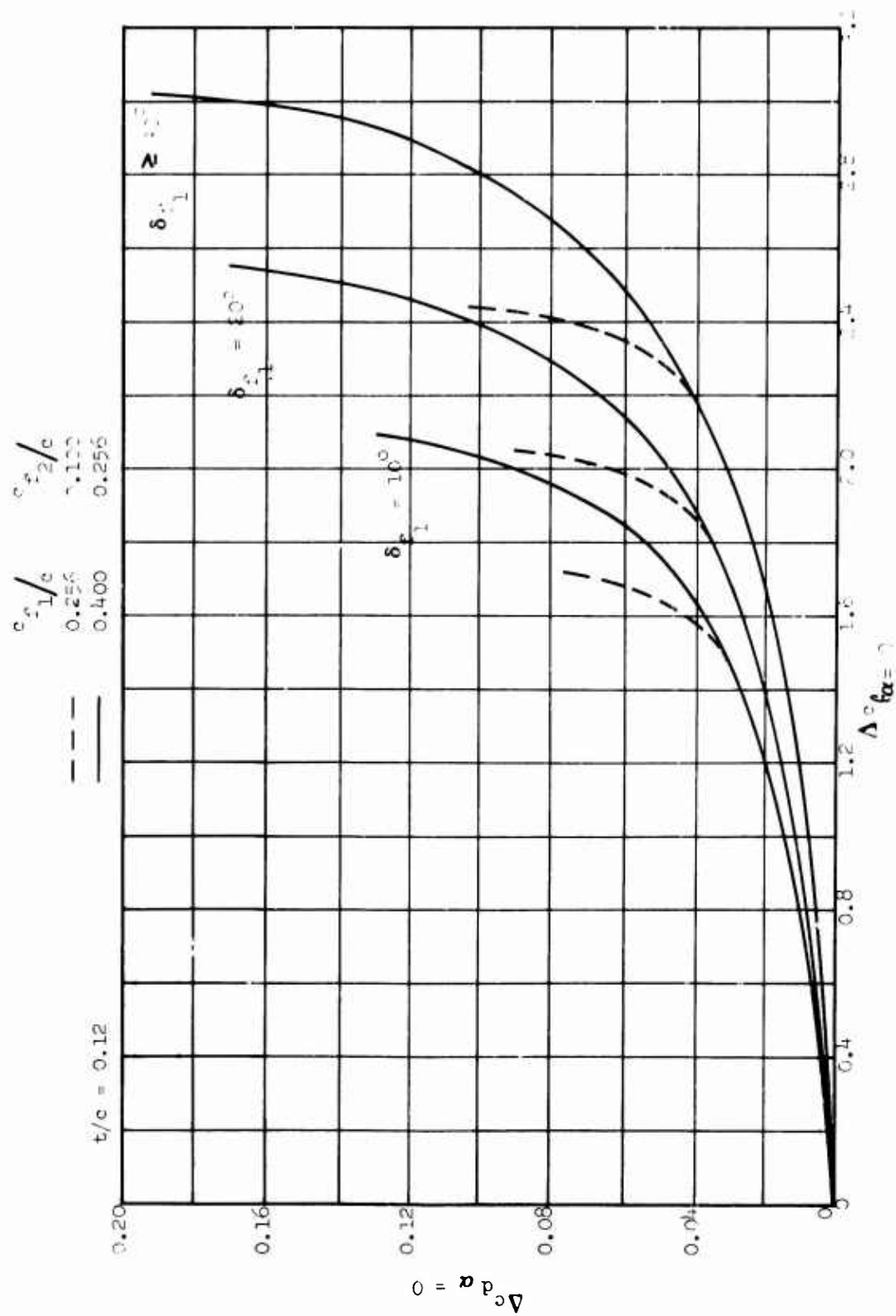
Figure 14c. Drag Increments for Double-Slotted Flaps Versus Lift Increment at $\alpha = 0$, Contd.

32

These two flapped airfoils have identical profiles to the relative velocity. The following relationship may then be written:

$$\alpha' = \alpha + \delta_f \tag{30}$$

$$\delta_f' = -\delta_f \tag{31}$$

$$\frac{c_f'}{c} = 1 - \frac{c_f}{c} \tag{32}$$

Thin airfoil theory for a trailing edge flap (Section 2.1.1) indicates that the lift coefficient is defined by Equation (6) as

$$c_\ell = 2\pi (\alpha - \alpha_\delta \delta_f)$$

Substituting the terms for the leading edge flap, we have

$$c_\ell = 2\pi [\alpha' + \delta_f' (1 + \alpha_\delta)] \tag{33}$$

Differentiating with respect to δ_f' at constant section lift,

$$\left(\frac{\partial \alpha'}{\partial \delta_f'} \right)_{c_\ell} = \alpha_\delta' = - (1 + \alpha_\delta) \tag{34}$$

Differentiating with respect to δ_f' at constant α',

$$\left(\frac{\partial c_\ell}{\partial \delta_f'} \right)_\alpha = c_{\ell_\delta}' = - \alpha_\delta' 2\pi \tag{35}$$

It can also be shown that at constant section lift,

$$c_{m_\delta}' = -c_{m_\delta} \tag{36}$$

and

$$c_{\ell_{\delta_{max}}}' = \left(c_{\ell_\delta}' - 2\pi + 2\theta_f \right) \tag{37}$$

The leading edge flap lifting effectiveness parameter is then computed using Equations (32), (34), and (35), and is shown in Figure 15.

33
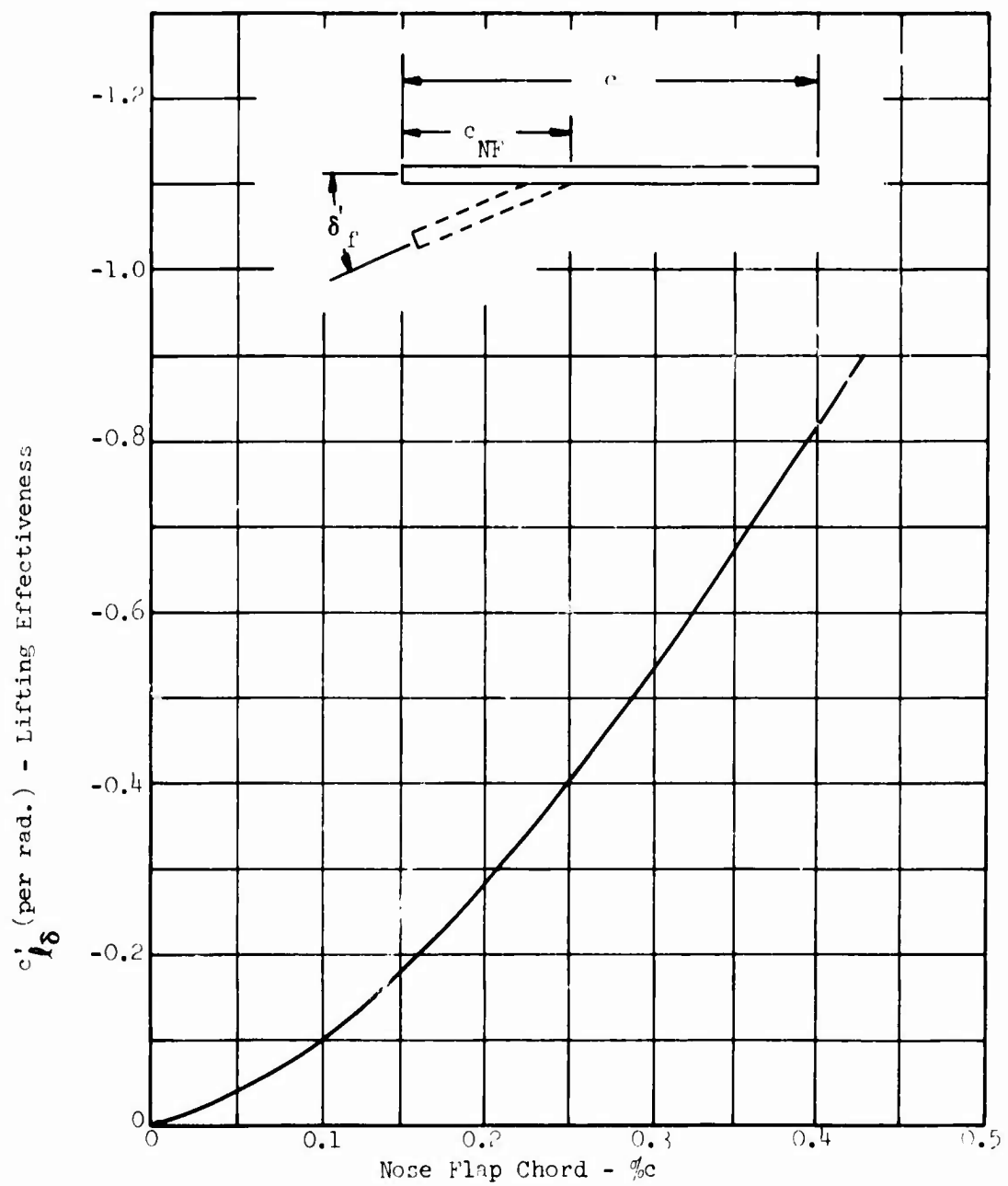
Figure 15. Theoretical Lifting Effectiveness Versus Nose Flap Chord.

34

Referring back to Figure 5, it can be seen that the lifting effectiveness of a leading edge flap is much less than that of a trailing edge flap of the same chord. The maximum lift and moment parameters are shown in Figures 16 and 17, respectively.

2.2.2   Lift Increment at α = 0 Degrees

Leading edge devices change the lift of the unflapped airfoil by changing the effective angle of attack. Unlike trailing edge flaps, the deflection of a nose flap causes a loss in lift rather than an increase at $\alpha = 0$. The effect of these devices may be determined with the following expression:

$$\Delta c_{\ell_{\alpha=0}} = c'_{\ell_\delta} \delta_{LE} \tag{38}$$

where c'_{ℓ_δ} is the theoretical lifting effectiveness for leading edge flaps (from Figure 15).

δ_{LE} is the deflection angle of the leading edge device.

The above equation is used for nose flaps. The equation is modified to account for chord extensions associated with Krueger flaps and slats as shown below:

$$\Delta c_{\ell_{\alpha=0}} = c'_{\ell_\delta} \delta_K \left(\frac{c_{EXT}}{c} \right) \tag{39}$$

and

$$\Delta c_{\ell_{\alpha=0}} = c'_{\ell_\delta} \delta_S \left(\frac{c_{EXT}}{c} \right) \tag{40}$$

where $\left(\dfrac{c_{EXT}}{c} \right)$ is the ratio of extended chord to airfoil chord (from Figure 18).

2.2.3   Section Lift Curve Slope Increment

The lift curve slope of the leading edge flap is assumed to be the same as that of the unflapped airfoil. For Krueger flaps or slats, the change in lift curve slope due to chord extension is given by

$$\Delta c_{\ell_\alpha} = c_{\ell_{\alpha_{AIRFOIL}}} \left(\frac{c_{EXT} - c}{c} \right) \tag{41}$$

35
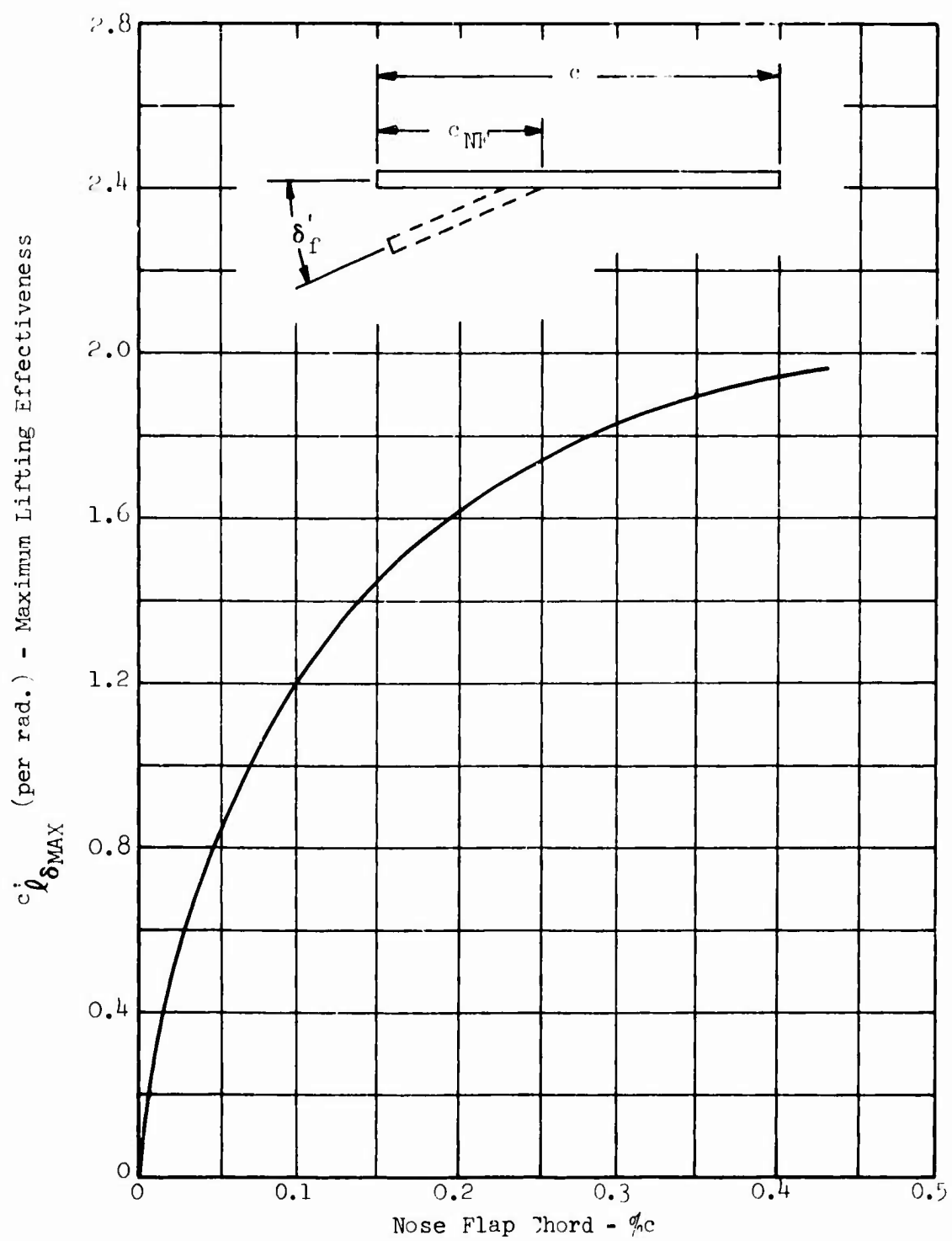
Figure 16. Theoretical Maximum Lift Effectiveness Versus Nose Flap Chord.
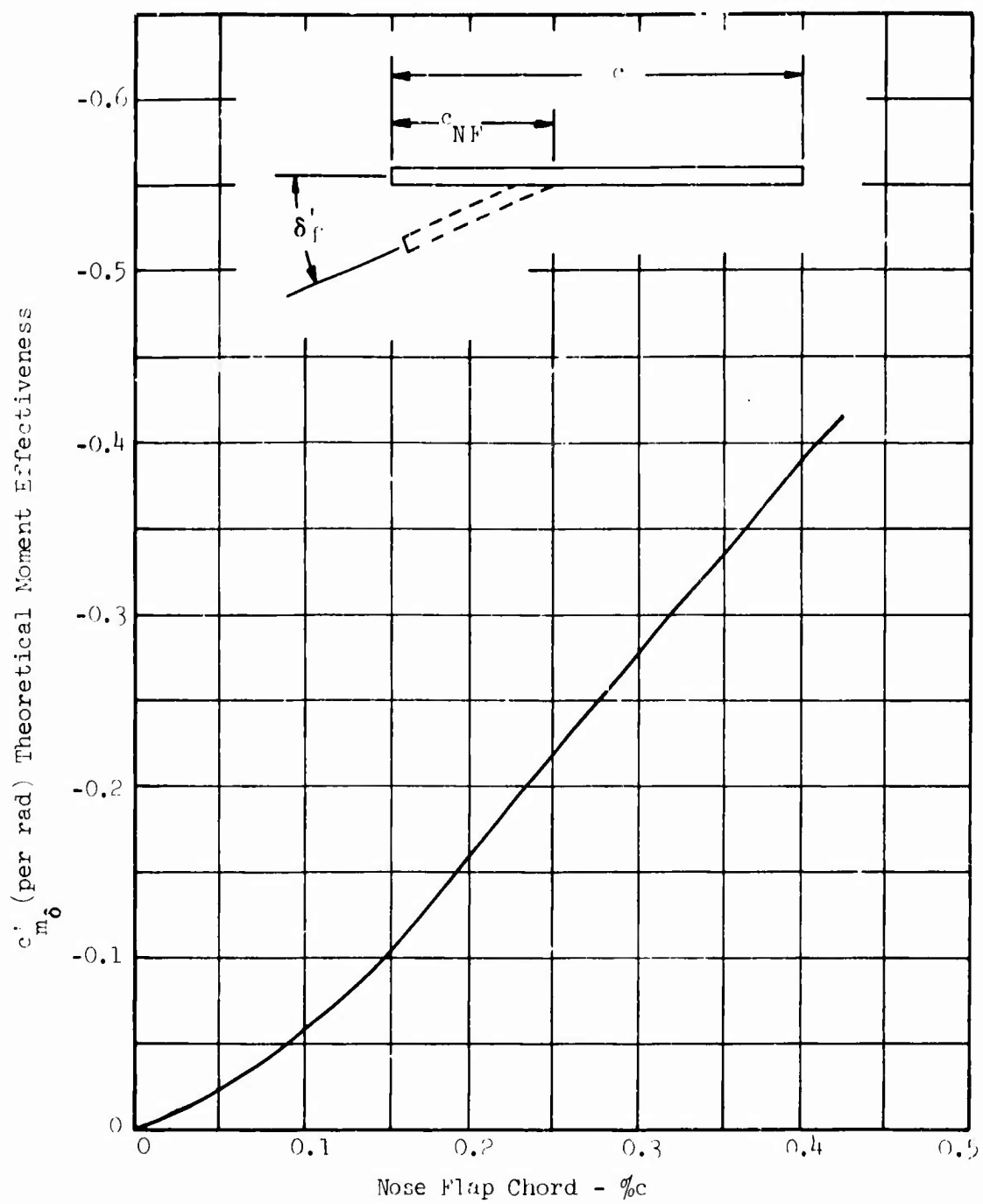
Figure 17. Theoretical Moment Effectiveness Versus Nose Flap Chord.

37

where c_{ℓ_α} is the lift curve slope of the unflapped airfoil (from Reference 1).

c_{EXT} is the extended chord (from Figure 18).

2.2.4 Maximum Lift Increment

Leading edge devices increase the maximum lift of airfoils by lowering the negative pressures (suction) near the nose and delaying leading edge flow separation. The maximum lift on the airfoil is achieved when the pressure on the nose device approximates that of the airfoil prior to stall. Leading edge devices delay flow separation at the nose without significantly affecting trailing edge flow and are most effective on thin airfoils.

The relationship from the theory developed in Section 2.2.1 was applied to the available maximum lift data on leading edge devices. The theoretical value of maximum lift increment for leading edge devices on a thin airfoil from Equation (37) is

$$\left(\Delta c_{\ell_{MAX}}\right)_{TH} = \left(c'_{\ell_\delta} - 2\pi + 2\theta_f\right)\delta_f = c'_{\ell_{\delta_{MAX}}}\delta_f$$

Empirical factors were developed to correlate all available data on leading edge devices on airfoils with finite thickness. The correlation parameter from Section 2.1.4, leading edge radius/thickness ratio, was again used to account for nose shape and thickness. The maximum lift increment at optimum deflection was determined and then related to the theoretical values shown in Figure 16.

The following expression resulted:

$$\Delta c_{\ell_{max}} = c'_{\ell_{\delta_{max}}} \eta_{max} \eta_\delta \delta_{LE}\left(\frac{c_{EXT}}{c}\right) \tag{42}$$

where η_{max} is the maximum lifting efficiency of leading edge devices (from Figure 19) (data from References 34 through 39).

η_δ is a factor accounting for changes in flap deflection from the optimum deflection (from Figure 20).

$c'_{\ell_{\delta_{max}}}$ is the theoretical maximum lifting effectiveness (from Figure 16).

38
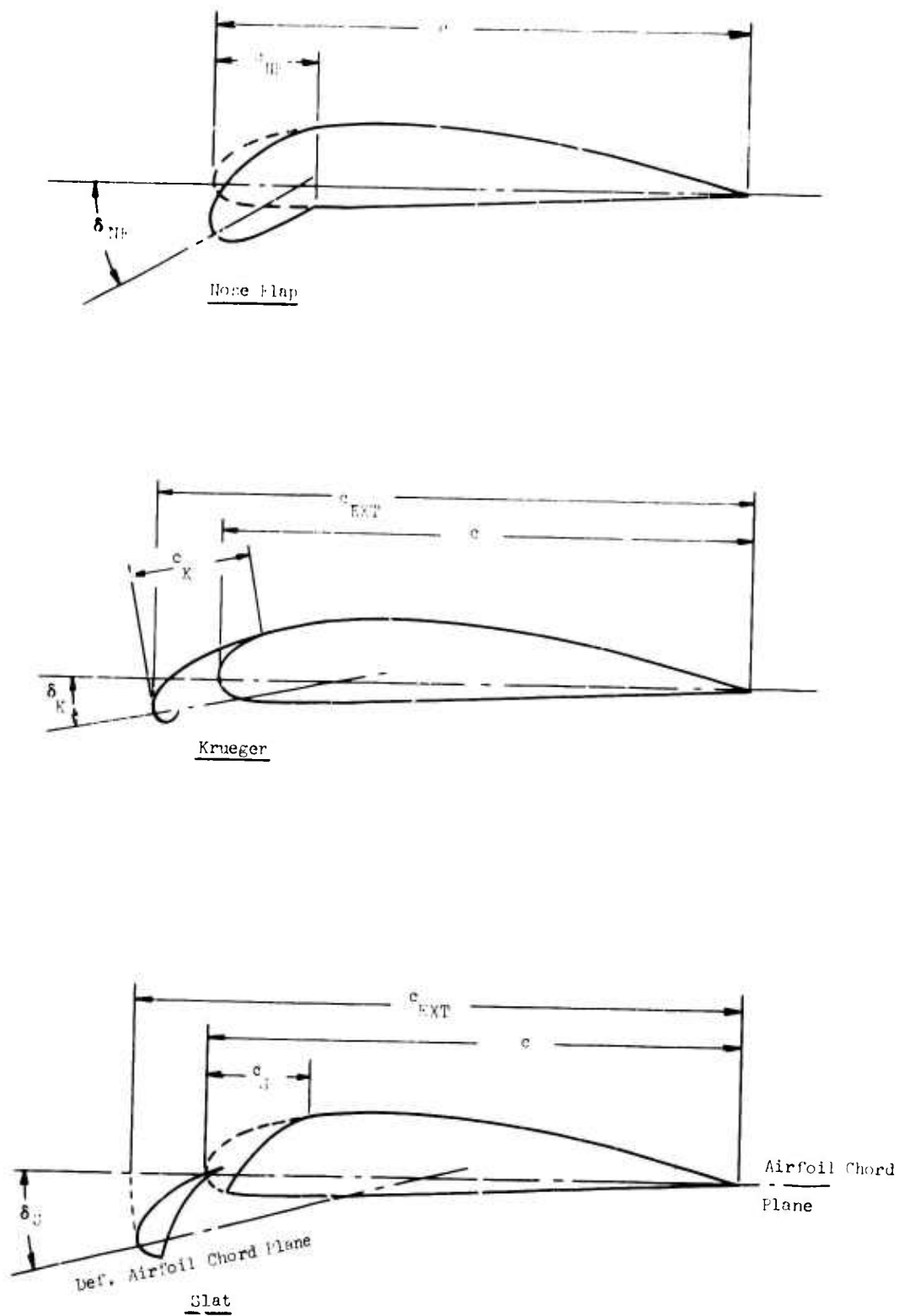
Figure 18. Geometry for Leading Edge Devices.
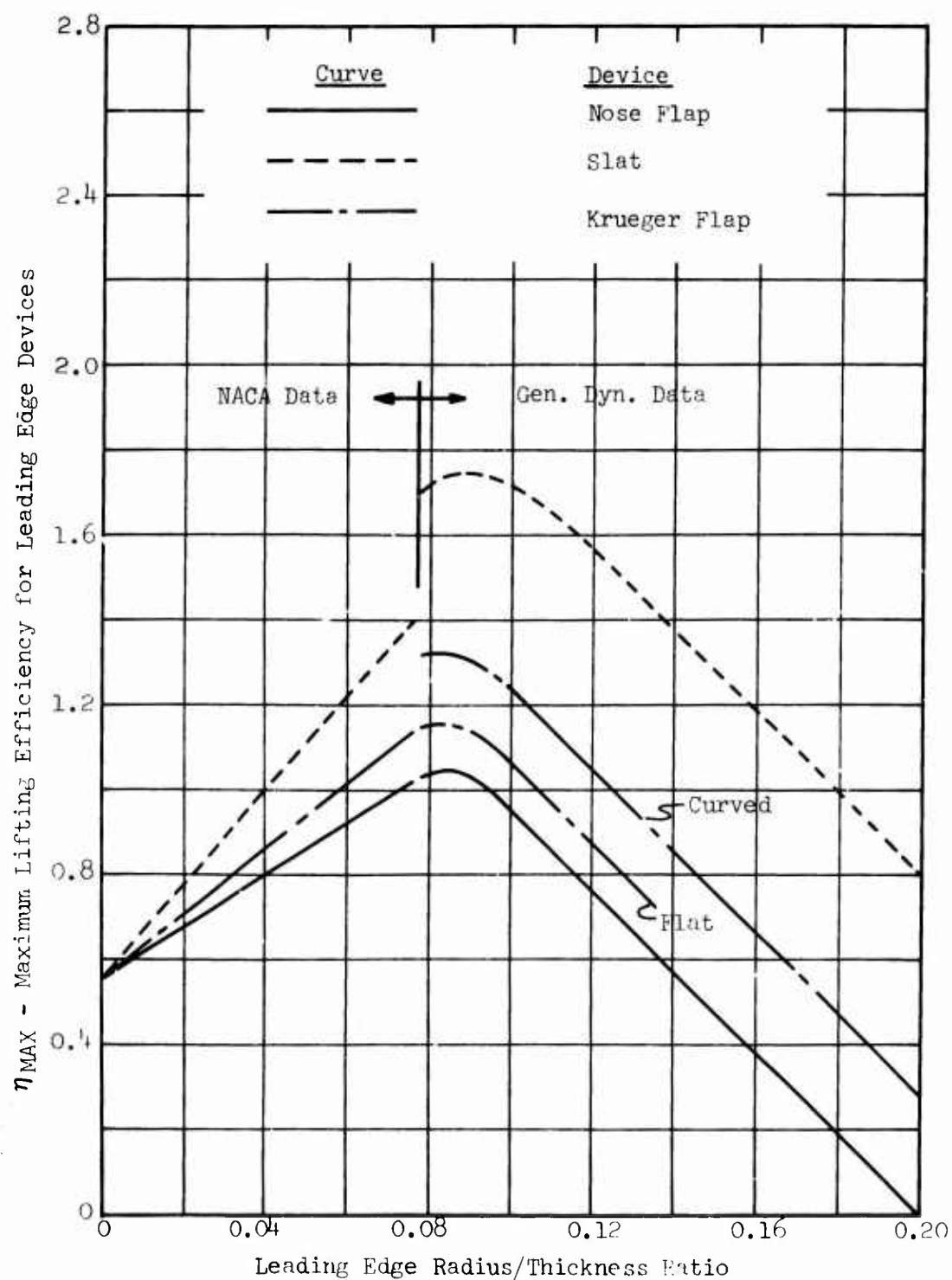
Figure 19. Maximum Lift Efficiency for Leading Edge Devices.
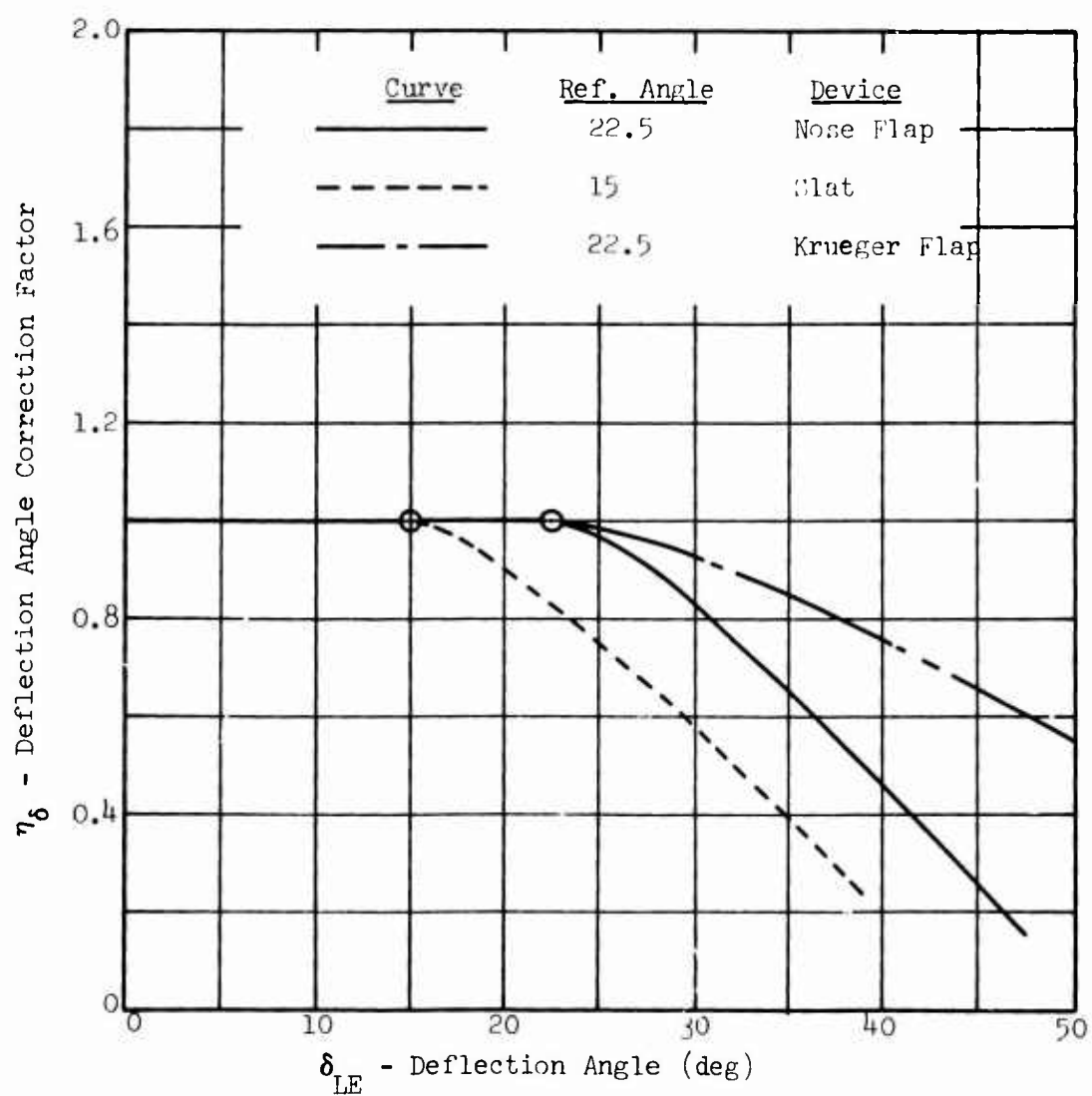
Figure 20. Deflection Angle Correction Factor.

$\left(\dfrac{c_{EXT}}{c}\right)$ is the ratio of extended chord to airfoil chord (from Figure 18).

δ_{LE} is the deflection angle of the leading edge device.

2.2.5 Pitching Moment Increment

Equation (36) shows that the pitching moment for a nose flap is

$$c'_{m_\delta} = -c_{m_\delta}$$

The c_{m_δ} term is defined by the nose flap chord which is equal to $(1 - c_f/c)$. The theoretical values of c'_{m_δ} versus nose flap chord are shown in Figure 17.

The moment increment due to nose flap deflection then becomes

$$\Delta c_{m_{LE}} = c'_{m_\delta} \delta_{LE} \tag{43}$$

where c'_{m_δ} is the theoretical moment effectiveness for leading edge devices (from Figure 17).

This expression is used for all leading edge devices.

2.2.6 Pitching Moment Curve Slope

As discussed in Section 2.1.6, the introduction of camber by either nose or trailing edge flap deflection causes no change in the moment curve slope. Leading edge devices that have translational motion produce a change in slope. The following expression should be used for slats and Kruegers:

$$\frac{\Delta c_m}{\Delta c_\ell} \approx 0.75 \, (c_{EXT} - c) \tag{44}$$

where c_{EXT} is the extended chord as defined in Figure 18.

2.2.7 Drag Increment

There is insufficient experimental data to empirically determine the effect of leading edge devices on drag. Quantitatively speaking, leading edge devices cause an upward shift in minimum drag with small changes in drag level. For the purposes of this study, it is assumed that leading edge devices cause no change in drag level.

42

3.0 PROFILE DRAG OF FUSELAGE, NACELLES, WING AND TAIL SURFACES

The profile drag is predicted by a build-up method that calculates the flat plate skin friction drag of each component and accounts for three-dimensional effects (interference and roughness). This approach, mainly empirical, is more accurate than wind tunnel test data because of Reynolds number effects and other items which normally cannot be represented on a wind tunnel model.

3.1 Wetted Area

The profile drag estimation is directly related to the ability to determine wetted areas. The wetted area of the wing and tail surfaces is readily obtained from the planform area and a factor to account for thickness:

$$S_{WET} = K_F \times \text{(planform area)} \tag{45}$$

where K_F is the planform area factor (from Figure 21).

The fuselage and nacelle wetted areas are determined by simplified formulas or solved graphically. One approach is to measure the top and side planview area, and to measure the circumference, height and width at the constant section. The wetted area is given by

$$S_{WET} = \frac{\text{CIRCUMFERENCE}}{H_B + W_B} (S_{TOP} + S_{SIDE}) \tag{46}$$

3.2 Profile Drag

The profile drag of each component is defined as the flat plate skin friction drag plus three-dimensional, interference, and roughness effects. The skin friction drag is equal to the wetted area multiplied by the skin friction coefficient. The coefficient with fully turbulent flow is based on Reynolds number and roughness effects and is given in Figure 22. A roughness factor value of 1.2 is considered representative for propeller-driven V/STOL aircraft and is used to determine the value of flat plate skin friction coefficient from Figure 22.

The three-dimensional profile drag for wing, horizontal, and vertical tail surfaces is determined from the following equation from Reference 40:

$$C_{D_{o_{\substack{WING \\ OR\,TAIL}}}} = \frac{C_f \times S_{WET}}{S} [1 + K_S(t/c) + K_p(t/c)^4] \tag{47}$$

43
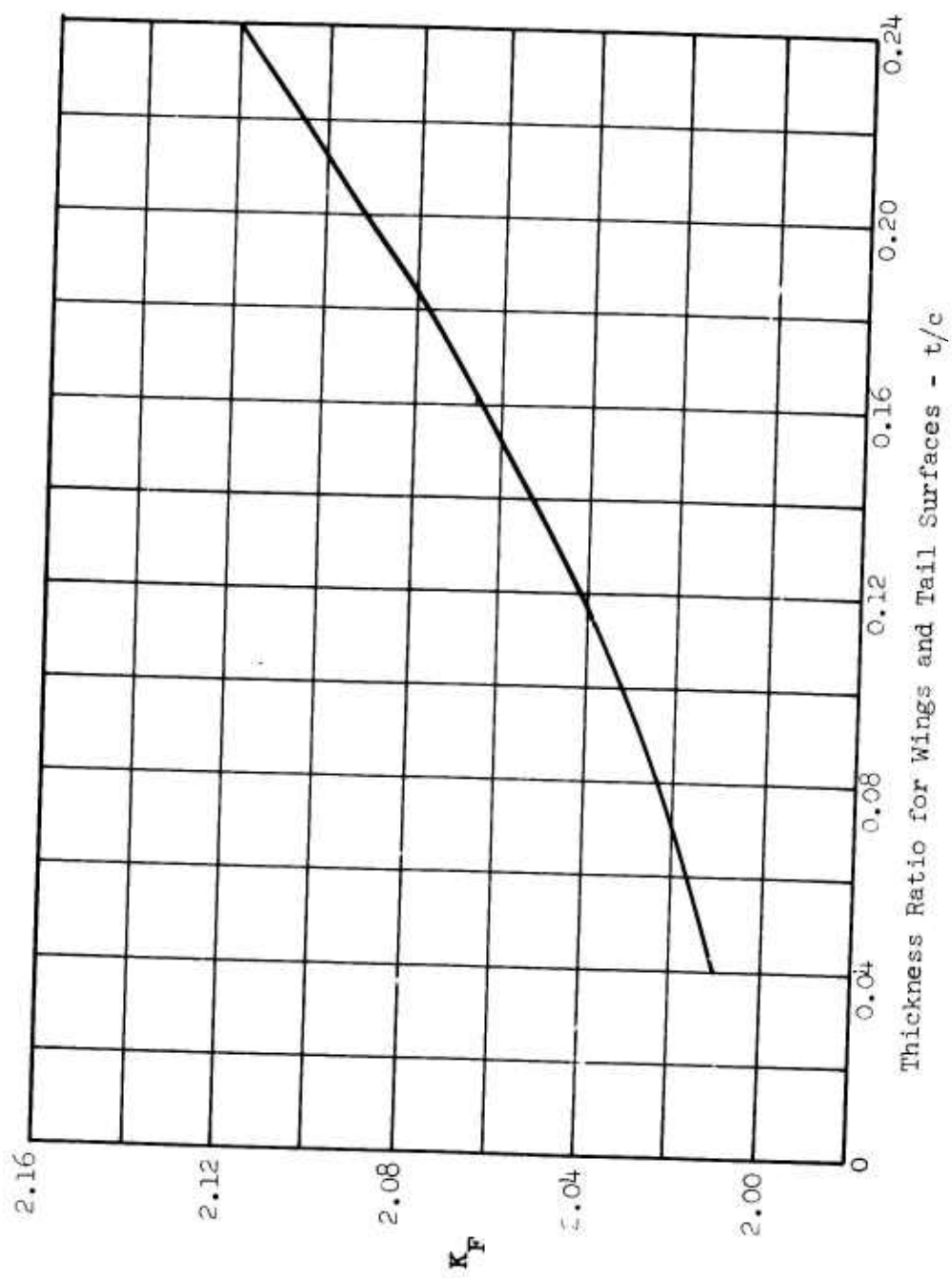
Figure 21. Thickness Correction to Wetted Area.

44
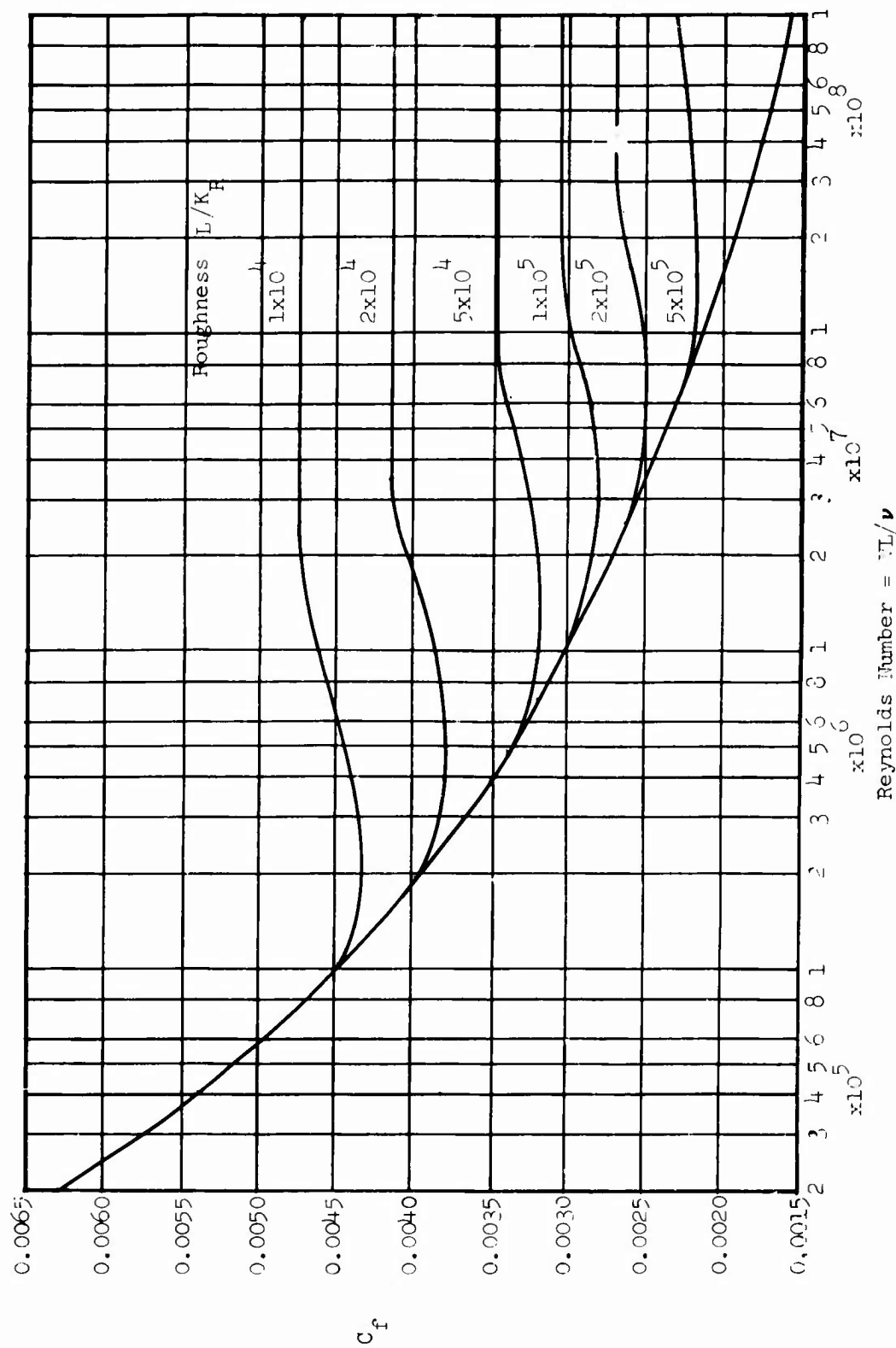
Figure 22. Turbulent Skin Friction Coefficient Versus Reynolds Number.

45

where K_S = supervelocity term from Figure 23.

K_P = 60 for airfoils with max t/c located at 30 percent chord.

K_P = 100 for airfoils with max t/c located at 40 to 50 percent chord.

The profile drag of three-dimensional streamlined bodies of revolution is calculated with the following equation from Reference 40:

$$C_{D_{o_{BODY}}} = \frac{C_f \times S_{WET}}{S} \left[1 + 0.001(\ell/D_B) + 1.5(D_B/\ell)^{3/2} + 7(D_B/\ell)^3 \right] \quad (48)$$

The second term in the above equation accounts for the boundary layer thickness increase for wrapping a flat plate into a cylinder. The third term accounts for supervelocity and the fourth term pressure drag. The equation is used for fuselages and nacelles. Deviations from the streamline shape should be accounted for in the fineness ratio term (ℓ/D_B) determined from the length and equivalent diameter.

$$\ell/D_B = \frac{\ell}{2\sqrt{\dfrac{S_B}{\pi}}} \quad (49)$$

where S_B is the frontal area.

On nacelles or fuselages where the aft end is truncated, the fineness ratio is determined from an effective length measured to a faired point.
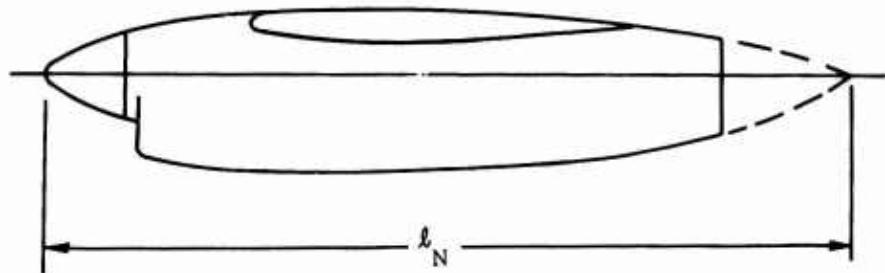
Nacelle Geometry
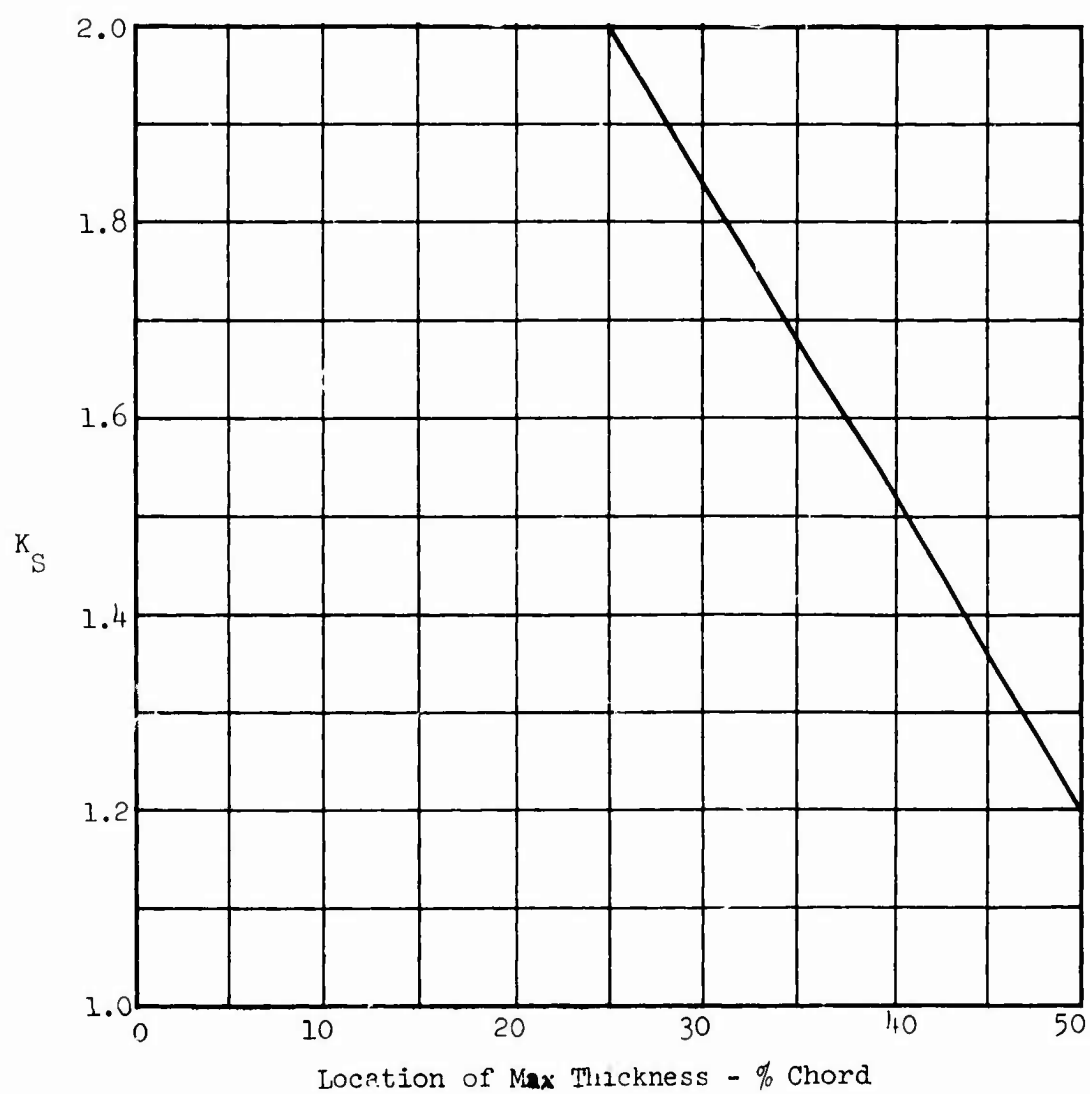
Figure 23. Supervelocity Factor for Airfoils.

The drag of V/STOL aircraft fuselages with rear loading ramps is not adequately predicted by Equation (48). Reference 41 shows correlations of these type fuselages which resulted in new terms for the fuselage drag. These terms replace the pressure drag term $7 (D_B/\ell)^3$ in Equation (48) which is valid for streamlined bodies. The resulting equations are indicated below:

$$C_{D_{o_{FUSELAGE}}} = \frac{C_f \times S_{WET}}{S} [1 + 0.001(\ell/D_B) + 1.5(D_B/\ell)^{3/2}]$$

$$+ 0.0070 \left(\frac{\frac{\pi}{4} D_B^2}{S} \right) \{ [6(D_B/\ell)^{5/2} - 1] + 5.2(y_a/D_B) [1.4 - (D_B/\ell_a)^4] \}$$

$$(50)$$

For fuselages with afterbodies that contract laterally as well as longitudinally, the last term in the equation drops out.
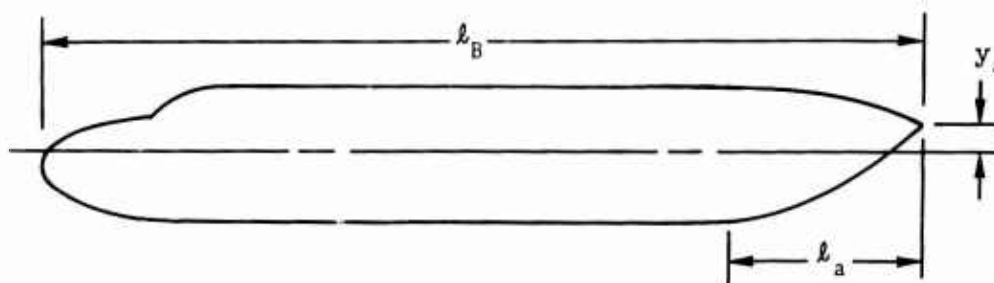
$$D_B = 2\sqrt{S_F/\pi}$$

Fuselage Geometry

3.3 Interference Drag

The interference drag between components is estimated with the following equation:

$$C_{D_{o_{INT}}} = K_1 C_{D_{o_{WING+FUS}}} + K_2 C_{D_{o_{TAIL+FUS}}} + C_{D_{o_{NAC}}} (K_3 K_4 - 1) \qquad (51)$$

where K_1 accounts for wing–body interference (from Figure 24).

K_2 accounts for horizontal tail–body interference (from Figure 24).
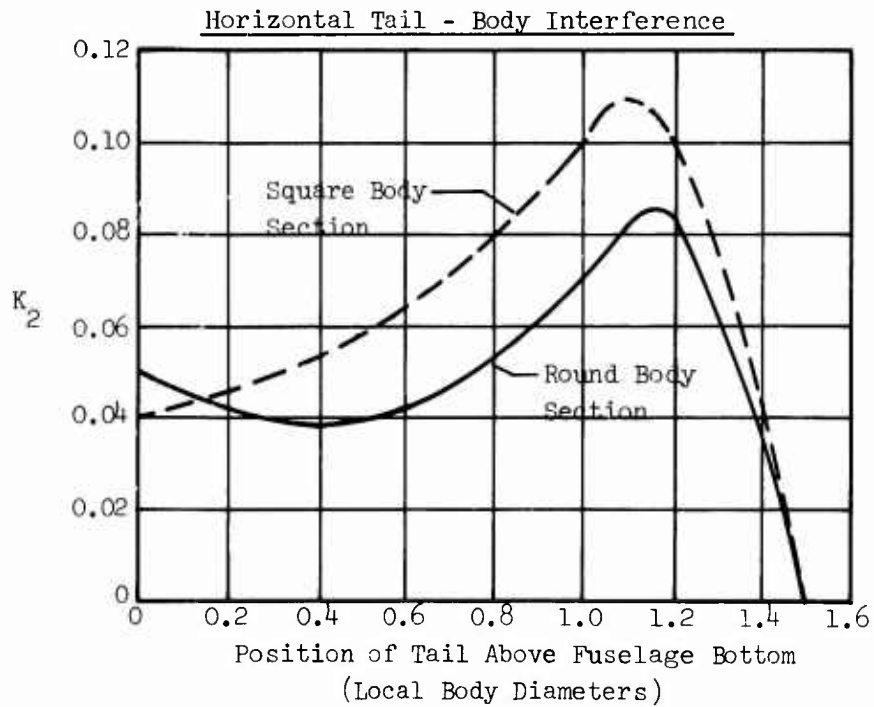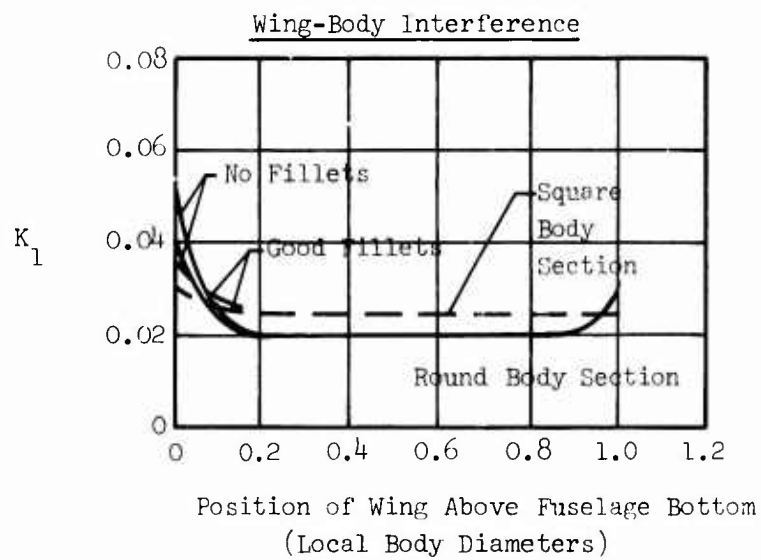
Figure 24. Wing-Body or Tail-Body Interference Drag Factors.
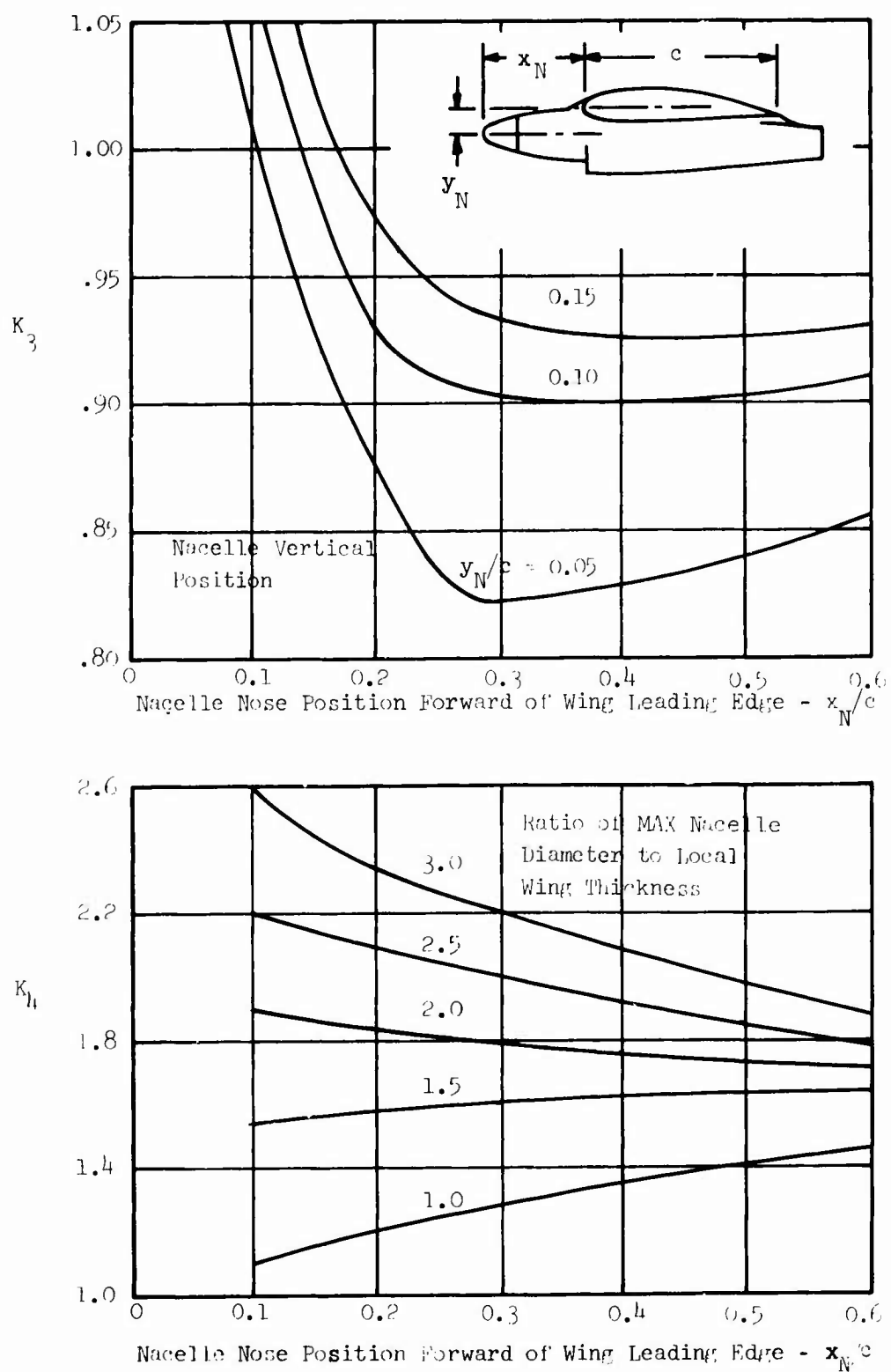
Figure 25. Nacelle-Wing Interference Drag Factors.

50

K_3 accounts for position of nacelle nose with respect to leading edge of wing (from Figure 25).

K_4 accounts for vertical position of the nacelle (from Figure 25).

If the nacelle is on the wing tip, the interference is taken to be one-half the value used for inboard nacelles.

The drag of three-dimensional bodies at angle of attack is given by

$$C_D(\alpha_{FUS}) = C_{D_{o_{BODY}}} + \left[\frac{\pi}{2}\sin\alpha_{FUS}\tan\frac{\alpha_{FUS}}{2} + 1.5\sin^3\alpha_{FUS}\frac{S_{TOP}}{S_F}\right]\frac{S_F}{S} \quad (52)$$

where S_F is the frontal area of the fuselage.

4.0 SPAN LOAD PROGRAM

The procedures developed in Sections 2 and 3 are used with the basic airfoil char-
acteristics in a span load digital computer program. This program was written
at Convair and uses linear and nonlinear flapped airfoil section data to predict the
three-dimensional flapped wing characteristics. The span load program, original-
ly set up to use two-dimensional experimental data from the Convair wind tunnel,
has been modified to use the predicted characteristics for this study.

The program is based on the modified Weissinger L-method described by Gray and
Schenk (Reference 42) and by Holt (Reference 43). The method represents the wing
with a system of horseshoe vortices extending aft from the quarter-chord line.
The strengths of the vortices, and the corresponding load distribution, are ex-
pressed in terms of the downwash angles at the three-quarter-chord points for a
set of spanwise control stations. Using one control station for each horseshoe
vortex leads to a set of simultaneous algebraic equations which can be solved for
the vortex strengths required to produce a specified set of downwash angles. The
coefficients in these equations are calculated from the geometry of the wing plan-
form. The planform parameters required by the program are the wing span, as-
pect ratio, taper ratio, and quarter-chord-line sweep angle.

This basic span load distribution program is used in an iterative procedure to
calculate the spanwise variation of lift satisfying angle of attack relationships at
each wing section, as illustrated in the following sketch.
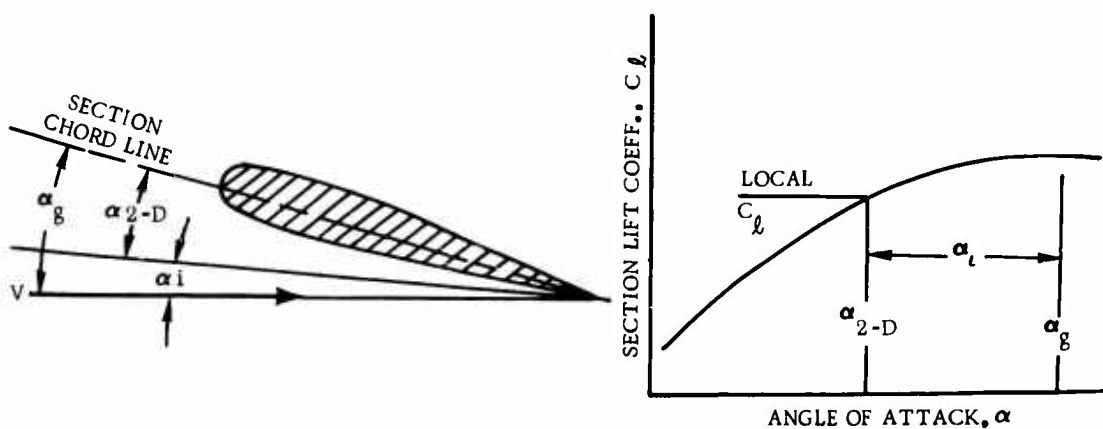
Airfoil Angles of Attack   Airfoil Lift Curve

52

Nonlinear section lift curves (two-dimensional data) are specified for each span-
wise control station, and the spanwise variation of geometric angle of attack is
known from basic wing geometry. The basic set of algebraic equations represent-
ing the horseshoe vortex simulation of the lifting wing is used to extract the induced
angles for an assumed initial load distribution for equality. This process is cycled
through a controlled iterative procedure until the equality is satisfied within an
acceptable tolerance.

The span load program in essence accepts the two-dimensional lift curves and pre-
dicts not only the linear region of the three-dimensional lift curve but also the stall
characteristics. The program accepts as additional input two-dimensional drag
and pitching moment data. From these data and the calculated local lift coefficients,
the program determines the spanwise moment and profile drag distributions. The
local drag and pitching moment are integrated numerically to obtain the coefficients
for segments of the wing which are subsequently used to determine the lift, longi-
tudinal force and moment coefficients of a wing immersed in a slipstream.

5.0 DEVELOPMENT OF LIFT AND LONGITUDINAL FORCES ON A WING-NACELLE-FLAP COMBINATION IMMERSED IN A PROPELLER SLIPSTREAM

Due to the limitations imposed by the existing semiempirical and theoretical methods for estimating the lift and longitudinal force coefficients for a wing partially immersed in a propeller slipstream, a program was initiated at Convair to investigate a more basic approach to the problem. This approach depends on a method of predicting two-dimensional data and was, in part, first conceived by Canadair Limited in the early 1960's for use on the proposed CL-62 aircraft. Although an attempt was made in Reference 44 to summarize the Canadair approach, a rigorous analysis has never been published. This section documents, in detail, the analytical reasoning behind the method and describes the improvements which have been incorporated in it during this effort.

There are basically four terms which contribute to the lift and longitudinal force coefficients of an interacting wing/propeller configuration:

1. Forces due to the inclination of the thrust vector to the free-stream flow (herein defined as direct thrust forces).

2. Forces due to the free-stream flow acting on the portion of the wing outside the propeller slipstream (herein defined as free-stream forces).

3. Forces due to the superimposed slipstream/free-stream flow acting on the portion of the wing inside the propeller slipstream (herein defined as slipstream forces).

4. Forces due to the engine nacelle located in the superimposed slipstream/ free-stream flow (herein defined as nacelle forces).

In the present analysis, it is assumed that these four items can be analyzed independently, being functions only of configuration geometry, thrust vector, T, and thrust inclination angle, α_T. The relative orientation of these quantities is presented in Figure 26.

5.1 Direct Thrust Forces

It is apparent from Figure 26 that the inclination of the thrust vector to the free stream results in a direct contribution of this vector to the lift and longitudinal force terms. The contributions are, respectively,

54
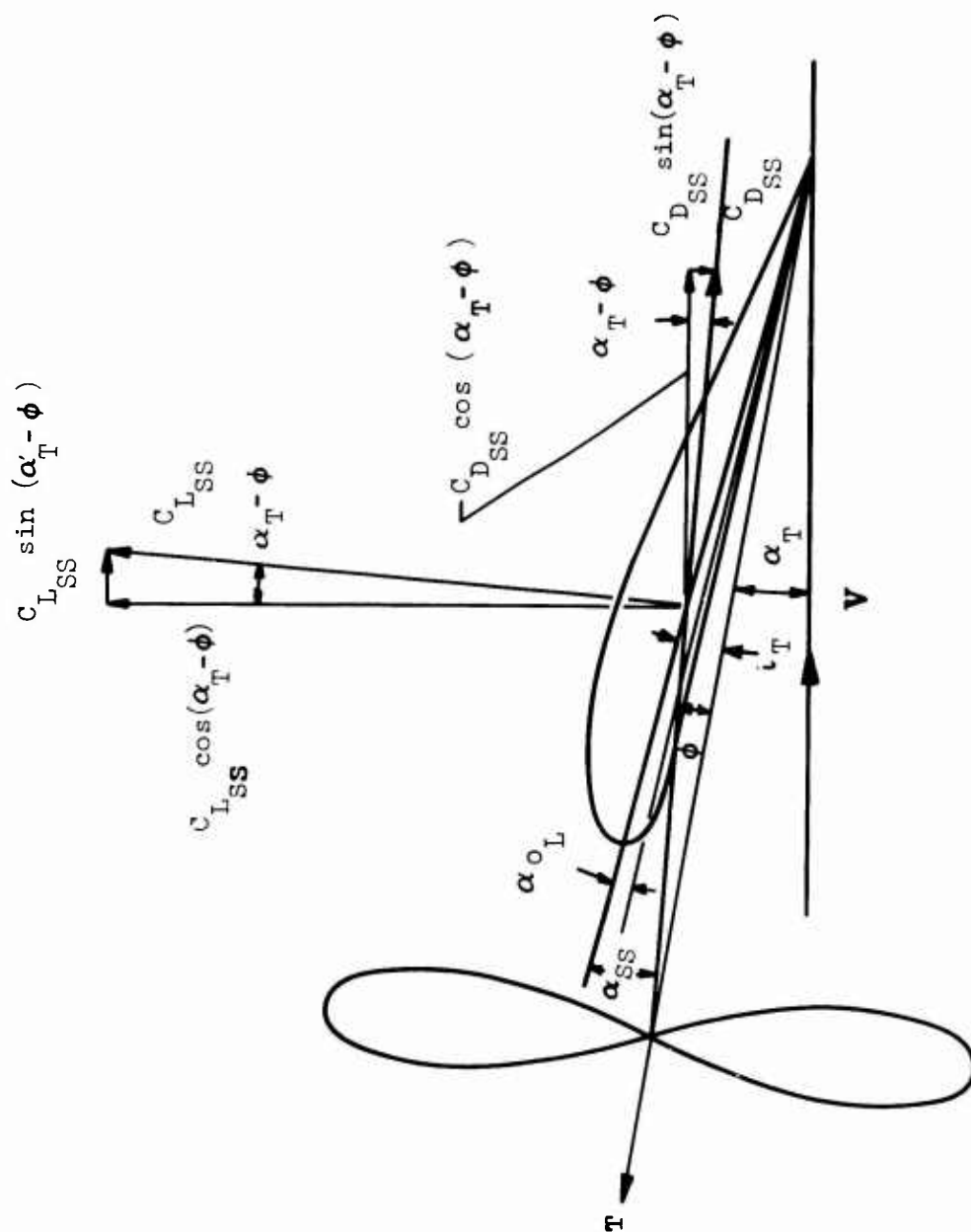
Figure 26. Propeller Slipstream Notation.

$$L_{DT} = NT \sin \alpha_T$$

$$X_{DT} = NT \cos \alpha_T \tag{53}$$

where N = number of propellers.

T = thrust of one propeller, $C_{T_S} S_P q_S$.

C_{T_S} = thrust coefficient based on q_S and S_P.

q_S = slipstream dynamic pressure.

S_P = propeller disk area, $\pi D^2/4$.

D_P = propeller diameter.

α_T = angle between the thrust line and the free stream.

Expressing Equation (53) in coefficient form yields

$$C_{L_{DT}} = \frac{L_{DT}}{q_S S} = \frac{N \pi D^2}{4S} C_{T_S} \sin \alpha_T \tag{54}$$

and

$$C_{X_{DT}} = \frac{X_{DT}}{q_S S} = \frac{N \pi D^2}{4S} C_{T_S} \cos \alpha_T \tag{55}$$

where S = reference wing area.

It should be mentioned here that all coefficients will be referenced to slipstream dynamic pressure, q_S, to eliminate the problem of infinite values in the hover condition where the free-stream dynamic pressure, q, goes to zero.

5.2 Free-Stream Forces

Since the lift and drag characteristics on the free-stream segment of the wing are assumed to be independent of the slipstream flow (and hence thrust coefficient), these forces may be determined quite easily knowing the spanwise variation of the power-off section lift and drag characteristics of the wing in question.

56

One simply applies an integration technique to these spanwise variations over the free-stream segment of the wing. Typical spanwise variations of power-off lift and drag coefficients (c_ℓ and c_d from the span load program described in Section 4.0) are shown in Figures 27 and 28 respectively at an arbitrary angle of attack. The quantities ($c_\ell c$) and ($c_d c$) are considered to be weighted in the sense that the section lift and drag coefficients are multiplied by the local wing chord, c, at each section. Also included on these figures is a representative model showing how the flow over the wing might be divided between the free-stream and slipstream regions. The shaded areas on both figures represent the free-stream segments. This model will be used in the derivation of the expressions for determining the lift and drag coefficients on the two segments of the wing.

The quantity η shown on Figures 27 and 28 is a nondimensional spanwise quantity defined as

$$\eta = \frac{y}{\dfrac{b}{2}} \tag{56}$$

where   y = spanwise distance measured from the wing root section.

b = wing span.

During the course of the analysis, η_ℓ will be assumed constant and located at the inboard tip of the most inboard propeller. In effect, this assumes that the slipstream tube remains tubular rather than contracting with increasing thrust coefficient, as is normally the case. The primary purpose of making this assumption was to reduce computer time. Thus, future improvement in the method might make use of the relationship

$$d = 0.707\,D \sqrt{\frac{1}{\sqrt{1 + \dfrac{C_{T_S}}{1 - C_{T_S}}\,\dfrac{1}{\cos^2 \alpha_T}}} + 1} \tag{57}$$

where   d is the contracted stream-tube diameter.

The model is further simplified by assuming that the outboard boundary of the fully developed slipstream extends beyond the wing tip to eliminate the necessity of including additional terms in the free-stream solution.

The integration of the shaded area in Figure 27 and the resultant calculation of the lift coefficient on the free-stream segment is carried out within the operation of the span load program. The result can be expressed mathematically as
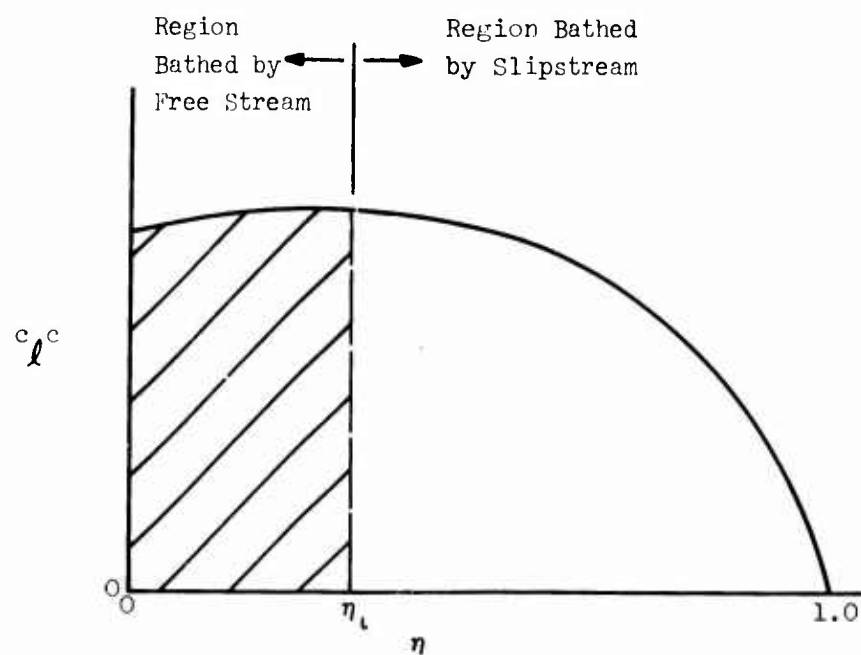
Figure 27. Spanwise Distribution of Weighted Section Lift Coefficient.
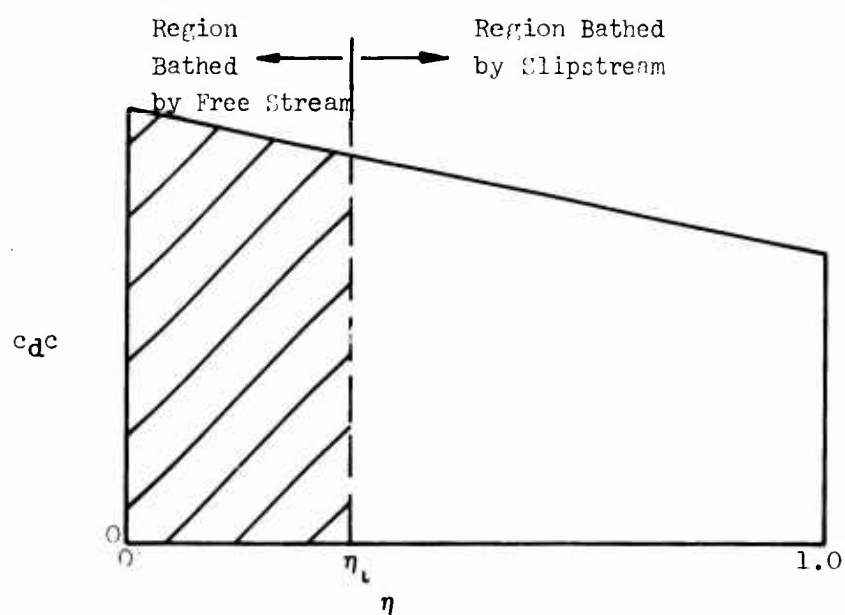
Figure 28. Spanwise Distribution of Weighted Section Drag Coefficient.

58

$$C_{L_{FS}} = \frac{b}{S} \int_0^{\eta_\ell} c_\ell c \, d\eta \tag{58}$$

This operation is carried out at several angles of attack throughout the entire lift curve. Using the results obtained in the linear portion of the lift curve yields the following solution for the lift curve slope of the free-stream segment:

$$\left(C_{L_\alpha}\right)_{FS} = \frac{\Delta C_{L_{FS}}}{\Delta \alpha} \tag{59}$$

where α = wing angle of attack relative to the root chord.

Finally, the lift coefficient on the free-stream section at any angle of attack α_{FS} can be found from the relation

$$C_{L_{FS}} = \left(C_{L_\alpha}\right)_{FS} (\alpha_{FS}) \tag{60}$$

where

$$\alpha_{FS} = \alpha_T + i_T - \alpha_{o_L}$$

i_T = angle between thrust line and local wing chord (see Figure 26).

α_{o_L} = angle between local wing chord and wing zero lift line.

To determine the drag coefficient of the free-stream section, it is necessary to express the lift curve slope of Equation (60) in terms of an effective geometric aspect ratio. Basically, this means determining an aspect ratio which, when used in conventional finite aspect ratio theory, yields a three-dimensional lift curve slope equal to the slope found in Equation (59). From finite aspect ratio theory,

$$a_w = \frac{a_o}{\dfrac{a_o}{\pi AR} + 1} \tag{61}$$

where $a_w = C_{L_{\alpha_W}}$ = wing three-dimensional lift curve slope.

AR = wing geometric aspect ratio.

$a_o = c_{\ell_\alpha}$ = wing two-dimensional lift curve slope.

Note here that the wing section is assumed to be constant across the span so that the section lift curve slope of the wing remains constant.

Note that Equation (61) assumes an elliptical lift distribution over the wing span. Modification of this equation for use on the wing section in the free stream yields

$$a_{FS} = \frac{a_o}{\dfrac{a_o}{\pi AR_{FS}} + 1} \tag{62}$$

where $a_{FS} = \left(C_{L_\alpha}\right)_{FS}$ = lift curve slope on free-stream segment of the wing.

Finally, solving Equation (62) gives the expression for the effective geometric aspect ratio of the free-stream section as

$$AR_{FS} = \frac{a_o}{\pi \left(\dfrac{a_o}{a_{FS}} - 1\right)} \tag{63}$$

The drag coefficient of the free-stream segment can now be described by the equation

$$C_{D_{FS}} = C_{D_{P_{FS}}} + C_{D_{i_{FS}}} \tag{64}$$

where $C_{D_{P_{FS}}}$ = the profile drag coefficient of the free-stream section.

$C_{D_{i_{FS}}}$ = the induced drag coefficient of the free-stream section.

Following the same approach used in the lift expression of Equation (58),

$$C_{D_{P_{FS}}} = \frac{b}{S} \int_o^{\eta_\iota} c_d c \, d\eta \tag{65}$$

As in the lift case, the integration of the shaded area of Figure 28 and resultant calculation of $C_{D_{P_{FS}}}$ is carried out in the span load program. Now, by referencing the value of $C_{L_{FS}}$ to free-stream area S_{FS} rather than total wing area, the induced drag term can be expressed as

60

$$C_{D_{i_{FS}}} = \frac{\left(C_{L_{FS}} \frac{S}{S_{FS}}\right)^2}{\pi \, AR_{FS}} \qquad (66)$$

The usefulness of the free-stream effective geometric aspect ratio term (AR_{FS}) is readily apparent. This referencing of $C_{L_{FS}}$ to free-stream area is necessary to remain consistent with the effective geometric aspect ratio terminology.

The resultant value of $C_{D_{i_{FS}}}$ must now be referenced back to total wing area to remain consistent with the profile drag term determined by Equation (65),

$$C_{D_{i_{FS}}} = C_{D_{i_{FS}}} \left(\frac{S_{FS}}{S}\right) \qquad (67)$$

One additional correction must be made to the results of Equations (60) and (64). Since the two-dimensional lift and drag coefficients are referenced to free-stream dynamic pressure (q), and since all coefficients are to be referenced to q_S, Equations (60) and (64) must be modified to

$$C_{L_F} = C_{L_{FS}} \left(\frac{q}{q_S}\right) = C_{L_{FS}} (1 - C_{T_S}) \qquad (68)$$

$$C_{X_F} = -C_{D_{FS}} \left(\frac{q}{q_S}\right) = -\left[C_{D_{FS}} (1 - C_{T_S})\right] \qquad (69)$$

where

$$\frac{q}{q_S} = (1 - C_{T_S})$$

5.3 Slipstream Forces

The estimation of the aerodynamic characteristics of a wing segment immersed in a propeller slipstream is by far the most difficult area of analysis associated with a wing/propeller configuration. The basic difficulty lies in the fact that the slipstream and free-stream flow characteristics over this segment are superimposed in a manner which varies throughout transition from hover ($C_{T_S} = 1.0$) to high-speed flight ($C_{T_S} = 0.0$).

The procedures discussed in the following paragraphs make use of the effective geometric aspect ratio terminology for each of these two end conditions of the flight regime, and suggest a total equivalent aspect ratio concept for bridging the gap to include the intermediate thrust coefficients.

From Figure 26, it is seen that in the general case of intermediate thrust coefficients, the superposition of the free-stream and slipstream velocities results in an effective slipstream flow which approaches the wing at an angle α_{SS}. This is the angle between the resultant slipstream velocity vector and the zero lift line of the wing. In equation form,

$$\alpha_{SS} = \phi + i_T - \alpha_{o_L} \tag{70}$$

where ϕ = the angle through which the slipstream velocity vector is rotated due to the superposition of the free-stream and slipstream flows.

From geometry relations, ϕ can be expressed as

$$\phi = \sin^{-1}\left[\sqrt{1 - C_{T_S}} \sin\alpha_T\right] \tag{71}$$

In the hover condition ($C_{T_S} = 1.0$), where the free-stream velocity is zero, Equation (71) yields the result $\phi = 0$, so that $\alpha_{SS} = i_T - \alpha_{o_L}$. Under these conditions, the effective aerodynamic lift on the slipstream segment can be approximated by a term which amounts to a turning of the thrust through the angle $\alpha_{SS} = i_T - \alpha_{o_L}$. This term may be thought of as a supplement to the previously defined direct thrust term and may be expressed as

$$L_H = NT \sin\alpha_{SS} \tag{72}$$

Assuming α_{SS} to be a small angle ($\sin\alpha_{SS} \simeq \alpha_{SS}$) and reducing to coefficient form, Equation (72) becomes

$$C_{L_H} = \frac{L_H}{q_S S_{SS}} = \frac{N\pi D^2}{4S_{SS}} C_{T_S} \alpha_{SS} \tag{73}$$

But, in the hover case, $C_{T_S} = 1.0$, so that

$$C_{L_H} = \frac{N\pi D^2}{4S_{SS}} \alpha_{SS} \tag{74}$$

62

Differentiation of Equation (74) with respect to α_{SS} yields

$$a_H = \left(C_{L_\alpha}\right)_H = \frac{N\pi D^2}{4S_{SS}} \tag{75}$$

Note that the slipstream area S_{SS} is used as a reference area to again remain consistent with the effective geometric aspect ratio terminology.

Finally, the effective geometric aspect ratio of the slipstream section in hover can be derived from finite aspect ratio theory:

$$AR_H = \frac{a_o}{\pi\left(\dfrac{a_o}{a_H} - 1\right)} \tag{76}$$

Considering the other end condition of high-speed flight ($C_{T_S} = 0.0$) where the slipstream velocity increment is negligible compared to the free stream, Equation (71) yields the result $\epsilon = \alpha_T$, so that $\alpha_{SS} = \alpha_T + i_T - \alpha_{o_L}$. This end condition thus reduces to a problem similar to that of Section 5.2 where the wing is subjected to flow coming at it from the free-stream direction. The lift coefficient on this slipstream segment for the high-speed flight condition may now be determined by integrating the power-off span load distribution over the slipstream area.

Mathematically, the integration of the span load distribution and the resulting calculation of lift coefficient on the slipstream section, $C_{L_{HS}}$, can be expressed by the relation

$$C_{L_{HS}} = \frac{b}{S} \int_{\eta_L}^{1.0} c_\ell\, c\, d\eta \tag{77}$$

As in the free-stream segment of the wing, carrying out this span load solution at several angles of attack gives results both in the linear and nonlinear portions of the lift curve. The linear results are again useable in determining the lift curve slope on the slipstream segment of the wing as follows:

$$a_{SS} = \left(C_{L_\alpha}\right)_{SS} = \frac{\Delta C_{L_{SS}}}{\Delta\alpha} \tag{78}$$

63

This lift curve slope of the slipstream segment in the high-speed flight condition is converted to an effective geometric aspect ratio as follows:

$$AR_{HS} = \frac{a_o}{\pi \left(\dfrac{a_o}{a_{SS}} - 1 \right)} \tag{79}$$

There now exist two effective geometric aspect ratios AR_H and AR_{HS} which satisfy the end conditions of hover and high-speed flight respectively. In the transition region between these two extremes, a total equivalent aspect ratio is assumed to have the form

$$AR_{EQ} = AR_H + \frac{V}{V_S} (AR_{HS} - AR_H) \tag{80}$$

where V = free-stream velocity.

V_S = resultant slipstream velocity.

However, since

$$\frac{V}{V_S} = \sqrt{\frac{q}{q_S}} = \sqrt{1 - C_{T_S}}$$

Equation (80) may be rewritten as

$$AR_{EQ} = AR_H + \sqrt{1 - C_{T_S}} (AR_{HS} - AR_H) \tag{81}$$

This equivalent aspect ratio may be converted to an equivalent lift curve slope for the slipstream segment, using the relationship

$$a_{EQ} = \left(C_{L_\alpha} \right)_{EQ} = \frac{a_o}{\dfrac{a_o}{\pi AR_{EQ}} + 1} , \tag{82}$$

and the total lift coefficient on the slipstream segment may be calculated from the equation

$$C_{L_{SS}} = (a_{EQ}) (\alpha_{SS}) \tag{83}$$

64

where
$$\alpha_{SS} = \phi + i_T - \alpha_{o_L}$$

The drag coefficient on the slipstream segment is found from the expression

$$C_{D_{SS}} = C_{D_{P_{SS}}} + C_{D_{i_{SS}}} \qquad (84)$$

where $C_{D_{P_{SS}}}$ = the profile drag coefficient of the slipstream section.

$C_{D_{i_{SS}}}$ = the induced drag coefficient of the slipstream section.

Similar to the free-stream section, the mathematical expression

$$C_{D_{P_{SS}}} = \frac{b}{S} \int_{\eta_L}^{1.0} c_d c \, d\eta \qquad (85)$$

represents the span load integration of the slipstream section of Figure 28 and the resultant calculation for the profile drag term, $C_{D_{P_{SS}}}$, which is carried out within the span load program. Referencing the slipstream lift coefficient $C_{L_{SS}}$ to the slipstream area S_{SS} rather than the total wing area S, the induced drag term $C_{D_{i_{SS}}}$ can be expressed as

$$C_{D_{i_{SS}}} = \frac{\left(C_{L_{SS}} \dfrac{S}{S_{SS}}\right)^2}{\pi AR_{EQ}} \left(\frac{S_{SS}}{S}\right) \qquad (86)$$

making use of the total equivalent aspect ratio term.

Since in the general case the lift and drag terms in the slipstream section are respectively perpendicular and parallel to the resultant slipstream velocity vector, they must be transferred into the free-stream coordinate system. Thus, according to Figure 26, the final lift and drag coefficients for the slipstream segment become

$$C_{L_S} = C_{L_{SS}} \cos(\alpha_T - \phi) - C_{D_{SS}} \sin(\alpha_T - \phi) \qquad (87)$$

$$C_{X_S} = - \left[C_{L_{SS}} \sin(\alpha_T - \phi) + C_{D_{SS}} \cos(\alpha_T - \phi) \right] \qquad (88)$$

65

5.4 Nacelle Forces

The lift curve slope of the nacelle has been estimated to be 0.0349 per degree based on the cross-sectional area of the nacelle. Since all coefficients are to be referenced to total wing area S, the following relation is used:

$$C_{L_{\alpha_N}} = 0.0349 \, \frac{\pi D_N^2}{4S} \tag{89}$$

where D_N = nacelle diameter.

The lift on the nacelle can now be found from the relationship

$$C_{L_N} = C_{L_{\alpha_N}} \phi \tag{90}$$

since the nacelle is located in the slipstream flow.

The drag on the nacelle is determined from the methods of Section 3.0. This value must be corrected for thrust coefficient by the relation

$$C_{D_N} = C_{D_{o_{NAC}}} (1 - C_{T_S}) \tag{91}$$

Finally, since the nacelle lift and drag terms are respectively perpendicular and parallel to the resultant slipstream velocity vector, they must be put into the free-stream coordinate system. Thus,

$$C_{L_N} = N \left[C_{L_N} \cos (\alpha_T - \phi) - C_{D_N} \sin (\alpha_T - \phi) \right] \tag{92}$$

$$C_{X_N} = -N \left[C_{L_N} \sin (\alpha_T - \phi) + C_{D_N} \cos (\alpha_T - \phi) \right] \tag{93}$$

where N = total number of propellers.

5.5 Summary Equations

Summarizing the results of the previous sections yields the following total equations for the lift and longitudinal forces on a wing/propeller-nacelle configuration:

66

$$\underline{\text{Direct Thrust}} \qquad\qquad \underline{\text{Wing in Free Stream}}$$

$$C_{L_T} = \frac{L}{q_S S} = \frac{N\pi D^2}{4S} \quad C_{T_S} \sin \alpha_T + (1 - C_{T_S}) \ C_{L_{FS}}$$

$$\underline{\text{Wing in Slipstream}}$$
$$+ \left[C_{L_{SS}} \cos (\alpha_T - \phi) - C_{D_{SS}} \sin (\alpha_T - \phi) \right]$$

$$\underline{\text{Nacelle}}$$
$$+ N \left[C_{L_N} \cos (\alpha_T - \phi) - C_{D_N} \sin (\alpha_T - \phi) \right]$$

$$(94)$$

$$\underline{\text{Direct Thrust}} \qquad\qquad \underline{\text{Wing in Free Stream}}$$

$$C_{X_T} = \frac{X}{q_S S} = \frac{N\pi D^2}{4S} \quad C_{T_S} \cos \alpha_T - (1 - C_{T_S}) \ C_{D_{FS}}$$

$$\underline{\text{Wing in Slipstream}}$$
$$- \left[C_{L_{SS}} \sin (\alpha_T - \phi) + C_{D_{SS}} \cos (\alpha_T - \phi) \right]$$

$$\underline{\text{Nacelle}}$$
$$- N \left[C_{L_N} \sin (\alpha_T - \phi) + C_{D_N} \cos (\alpha_T - \phi) \right]$$

$$(95)$$

The two-dimensional stall characteristics as determined from Section 2.0 for the airfoil section or high-lift devices being investigated are used in the span load program to calculate the maximum lift coefficients of the free-stream and slipstream segments of the wing. Once these values are reached, a flat plate theory is applied which calculates the lift and drag on the wing at angles of attack past stall. These equations for the free-stream forces are

$$C_{L_{FS}} = C_{N_{FS}} \cos \alpha_{FS} \qquad\qquad (96)$$

$$C_{D_{FS}} = C_{N_{FS}} \sin \alpha_{FS} \qquad\qquad (97)$$

where $\quad C_{N_{FS}} \quad$ is calculated at

$$C_{L_{FS}} = C_{L_{MAX_{FS}}}$$

$$\alpha_{FS} = \alpha_{MAX_{FS}}$$

In the same manner, the slipstream forces are found to be

$$C_{L_{SS}} = C_{N_{SS}} \cos \alpha_{SS} \qquad (98)$$

$$C_{D_{SS}} = C_{N_{SS}} \sin \alpha_{SS} \qquad (99)$$

where $C_{N_{SS}}$ is calculated at

$$C_{L_{SS}} = C_{L_{MAX_{SS}}}$$

$$\alpha_{SS} = \alpha_{MAX_{SS}}$$

These summary equations and stall limits have been programmed using standard FORTRAN IV language. A program description, listing, and required input are presented in Reference 45.

6.0 MOMENTS ON A WING-NACELLE-FLAP COMBINATION IMMERSED IN A PROPELLER SLIPSTREAM

The methods currently available for estimating the lift and drag characteristics of propeller-wing-flap V/STOL configurations do not predict the effects of propeller slipstream on pitching moments. Methods are presented herein for predicting power effects on zero-lift pitching moments and the pitching moment curve slope of a wing immersed in a slipstream. These methods, developed at Convair, are described in References 46 and 47 where the backup data correlations are shown. Use is made of the span load program to obtain the basic power-off characteristics of the wing-flap system being analyzed, and analytical expressions are presented to correct these terms for power effects.

There are three basic contributions to the moment of a wing immersed in a propeller slipstream:

1. Forces due to the basic wing.

2. Forces due to the inclination of the thrust vector (herein defined as direct thrust forces).

3. Forces due to the lift augmentation.

This analysis assumes that these forces can be analyzed separately, being functions only of configuration geometry and thrust coefficient.

6.1 ZERO LIFT PITCHING MOMENT

The individual contributions to the zero lift pitching moment of a flap immersed in a propeller slipstream are shown in Figure 29 and described below.

6.1.1 Power-Off Contribution

The power-off contribution is

$$\left(\Delta C_{m_o}\right)_{PO} = \left(1 - C_{T_S}\right)\left(\Delta C_{m_o}\right)_F \tag{100}$$

where $\left(\Delta C_{m_o}\right)_F$ is the zero lift pitching moment increment of the flap, determined from the span load program.
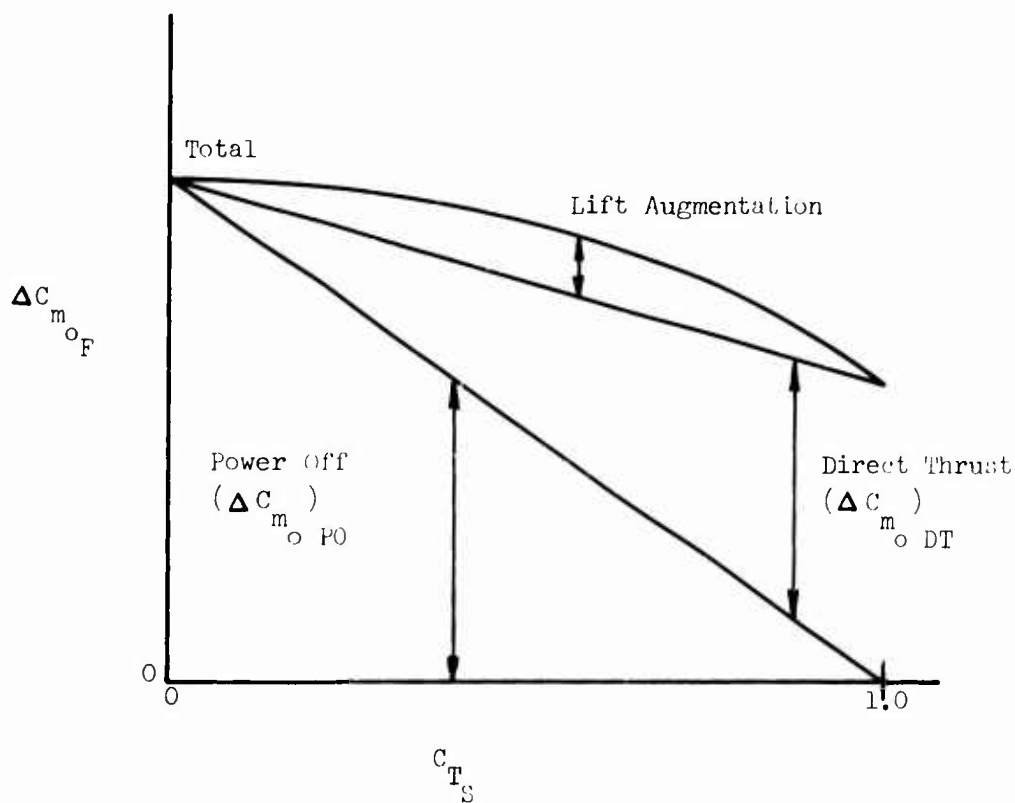
Figure 29.   Power Effects on Zero Lift Pitching Moment.

6.1.2   Direct Thrust Contribution

The direct thrust contribution is

$$\left(\Delta C_{m_o}\right)_{DT} = \frac{C_{T_S}}{2} \left(\Delta C_{m_o}\right)_{SS} \tag{101}$$

where $\left(\Delta C_{m_o}\right)_{SS}$ is the zero lift pitching moment increment of that portion of the flap which is immersed in the propeller slipstream, determined by the span load program.

The spanwise locations of the flap ends are shown in Figure 30 and defined below:

$$\eta_\iota = \frac{2y_n - d}{b} \tag{102}$$

$$\eta_o = 1.0 \tag{103}$$

70
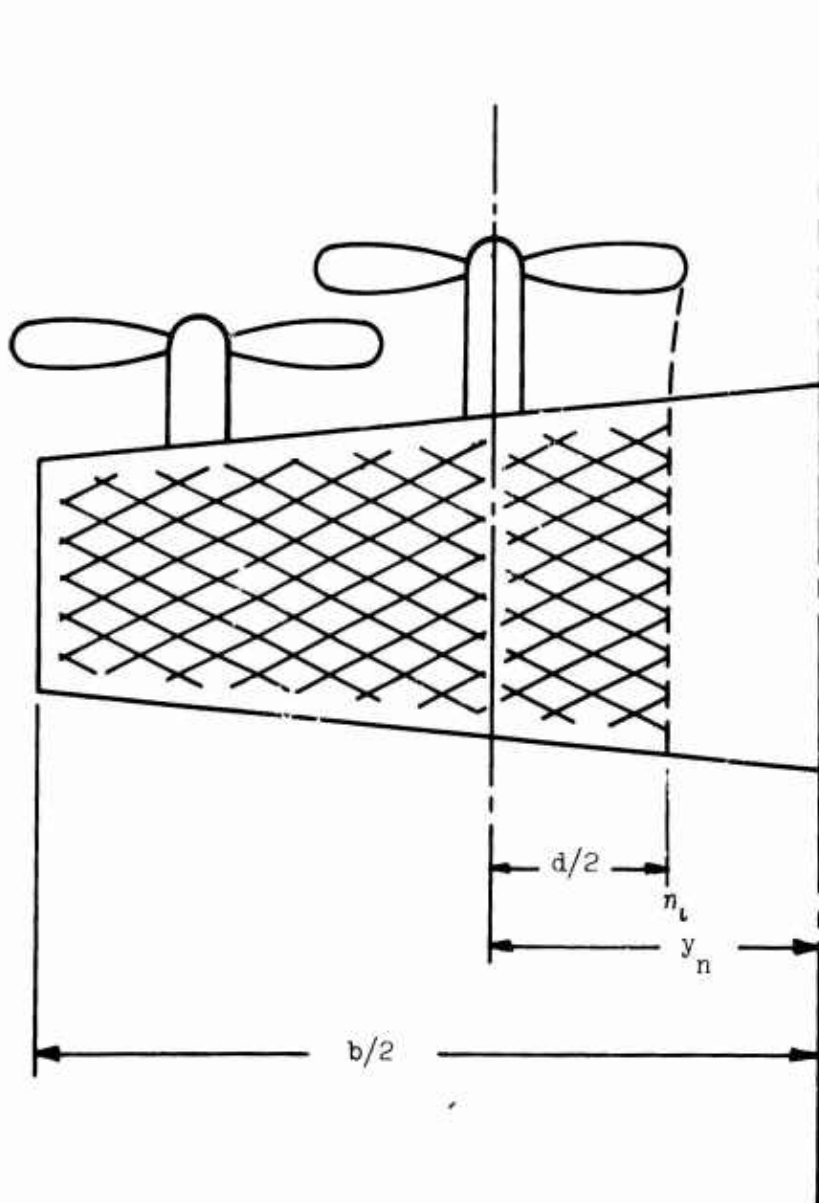
Figure 30. Geometry for Flaps in Propeller Slipstream.

As in Section 5.0, η_ι will be assumed constant and located at the inboard end of the propeller.

There is an additional thrust contribution from the geometrical relationship between the thrust line and the moment reference center:

$$\left(\Delta C_{m_0}\right)_{DT} = \frac{\pi ND^2}{4S\bar{c}} L_P C_{T_S} \tag{104}$$

where $\bar{c}$ = mean aerodynamic chord.

L_P = moment arm from quarter chord of the MAC to the propeller plane.

6.1.3   Lift Augmentation Contribution

The lift augmentation contribution is

$$\left(\Delta C_{m_0}\right)_{LA} = \frac{C_{T_S}}{2} \sqrt{1 - C_{T_S}} \left(\Delta C_{m_0}\right)_{SS} \tag{105}$$

6.2   PITCHING MOMENT CURVE SLOPE

The calculation of the effects of propeller slipstream on the pitching moment curve slope resolves itself into determining power effects. The approach used in the method is to estimate power-off lift curve slope and the direct thrust and lift augmentation contributions. The power-on lift curve slope is resolved into the individual terms shown in Figure 31 and described in the following paragraphs.

6.2.1   Power-Off Contribution

The power-off pitching moment curve slope is corrected to slipstream dynamic pressure in the following manner:

$$\left(C_{m_\alpha}\right)_{PO} = \left(1 - C_{T_S}\right) C_{m_{\alpha_W}} \tag{106}$$

where $C_{m_{\alpha_W}}$ is the pitching moment curve slope of the basic wing, determined by the span load program.

6.2.2   Direct Thrust Contribution

The direct thrust contribution due to propeller normal force and effective thrust line displacement has been determined from empirical correlations. This variation is shown in Figure 32 and is assumed applicable for all configurations.

72
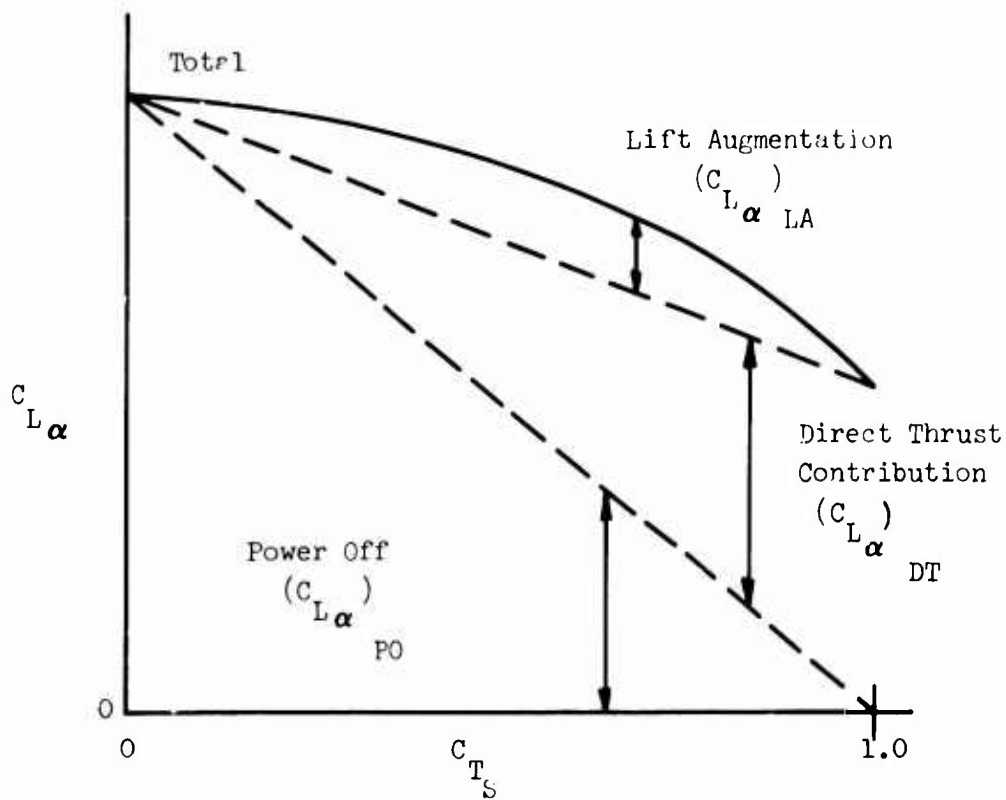
Figure 31. Power Effects on the Lift Curve Slope.

6.2.3 Lift Augmentation Contribution

Since the lift augmentation is a result of the increased mass flow in the wing stream tube due to the higher velocity in the propeller slipstream, the pitching moments are determined from the geometry of that portion of the wing immersed in the slipstream.

$$\left(C_{m_\alpha}\right)_{LA} = \left(C_{m_{C_L}}\right)_{SS} \left(C_{L_\alpha}\right)_{LA} \tag{107}$$

where

$$\left(C_{m_{C_L}}\right)_{SS} = \left(C_{m_\alpha}\right)_{SS} / \left(C_{L_\alpha}\right)_{SS}$$

The $\left(C_{m_\alpha}\right)_{SS}$ and $\left(C_{L_\alpha}\right)_{SS}$ terms are respectively the power-off pitching moment curve slope and the lift curve slope on the slipstream segments of the wing, determined by the span load program.

73
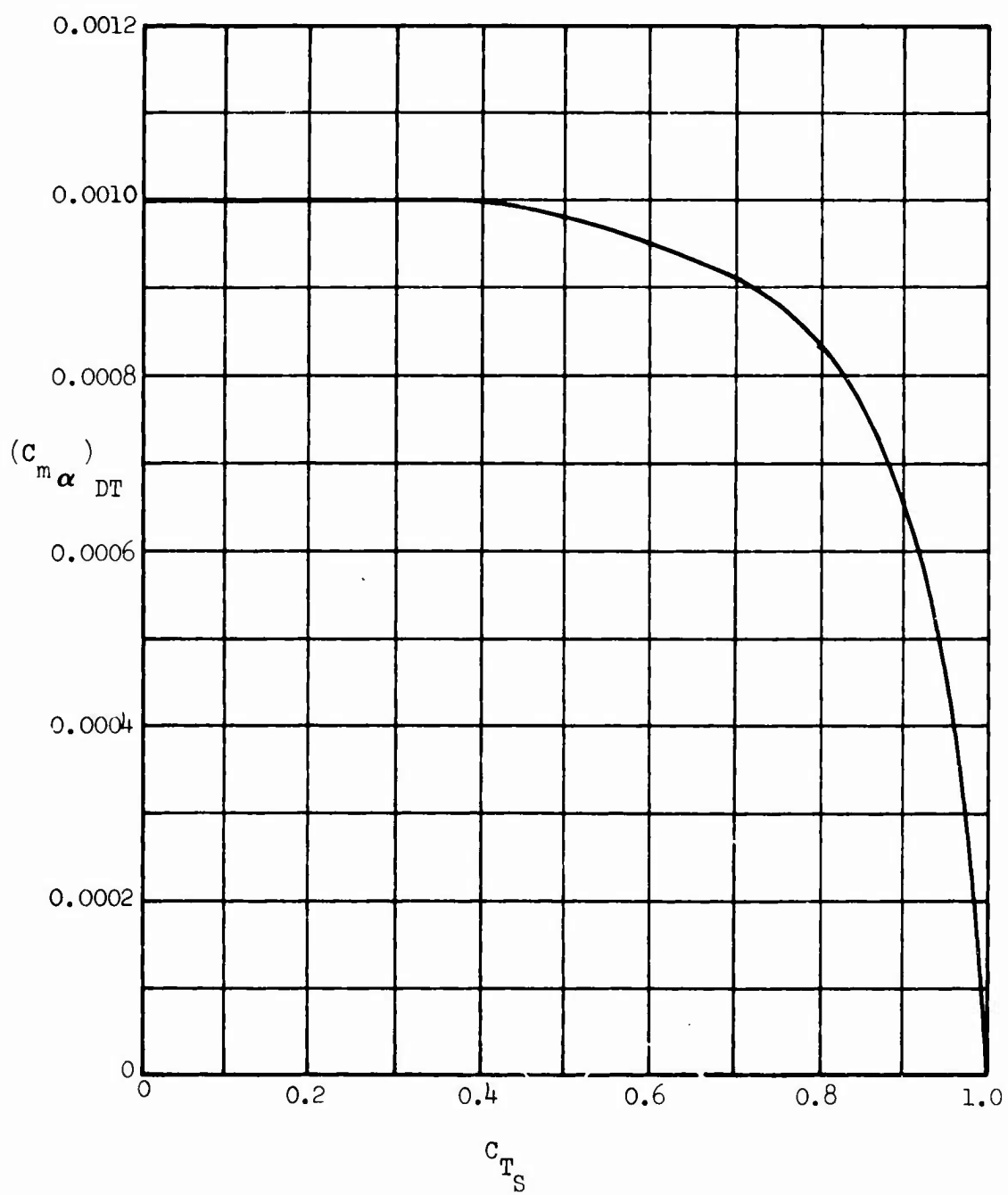
Figure 32. Direct Thrust Contribution From Propeller and Thrust Line Offset.

6.2.4 Nacelle and Fuselage Contributions

Since the nacelles are in the presence of the slipstream, both the power-off
and lift augmentation contributions to the lift curve slope are used to obtain
the nacelle pitching moment curve slope. Also, an additional multiplying term
has been included because it is expected that the destabilizing effect of the na-
celles would increase in direct proportion to the increase in lift curve slope
arising from the lift augmentation term. The reason for including this term is
intuitive, but it is needed to achieve correlation, and physically, the nacelle
stability contribution is related to the wing upwash field in the vicinity of the
nacelle, which in turn is related to the aerodynamic contributions to lift curve
slope. The contribution of the nacelles is then given by

$$\left(C_{m_\alpha}\right)_N = \left(C_{m_{C_L}}\right)_N \left[\left(C_{L_\alpha}\right)_{PO} + \left(C_{L_\alpha}\right)_{LA}\right]\left[1 + \frac{\left(C_{L_\alpha}\right)_{LA}}{\left(C_{L_\alpha}\right)_{PO}}\right] \tag{108}$$

where

$$\left(C_{m_{C_L}}\right)_N = \frac{N K_N W_N^2 \ell_N}{S c C_{L_{\alpha_W}}} \tag{109}$$

$$\left(C_{L_\alpha}\right)_{PO} = \left(C_{L_\alpha}\right)_W \left(1 - C_{T_S}\right) \tag{110}$$

$$\left(C_{L_\alpha}\right)_A = \left(C_{L_\alpha}\right)_T - \left(C_{L_\alpha}\right)_{PO} - \left(C_{L_\alpha}\right)_{DT} \tag{111}$$

and N = number of propellers.

K_N = nacelle stability coefficient (from Figure 5-16 in Reference 48).

W_N = nacelle width.

ℓ_N = nacelle length.

c = wing chord at nacelle location.

$$\left(C_{L_\alpha}\right)_{DT} = \frac{\pi N D^2}{4S} C_{T_S} \ (RAD^{-1}) \text{ for small } \alpha\text{'s}.$$

$$\left(C_{L_\alpha}\right)_T = \text{total power-on lift curve slope}.$$

The pitching moment contribution due to the body is found from the relation

75

$$\left(C_{m_\alpha}\right)_B = \frac{K_B W_B^2 L_B}{Sc} \tag{112}$$

where K_B = fuselage stability coefficient (from Figure 5-16 in Reference 48).

W_B = fuselage width.

L_B = fuselage length.

6.3   SUMMARY EQUATIONS

The power effects on the total zero lift pitching moment coefficient increments due to flap deflection are given by the following equation:

<div align="center"><u>POWER OFF</u>   <u>DIRECT THRUST</u></div>

$$\Delta C_{m_{o_F}} = \left(1 - C_{T_S}\right)\left(\Delta C_{m_o}\right)_F + \frac{C_{T_S}}{2}\left(\Delta C_{m_o}\right)_{SS}$$

<div align="center"><u>LIFT AUGMENTATION</u></div>

$$+ \frac{C_{T_S}}{2}\sqrt{1 - C_{T_S}}\left(\Delta C_{m_o}\right)_{SS} \tag{113}$$

These increments were patterned after the relationships of Reference 49.

The total pitching moment curve slope at any thrust coefficient is calculated with the following equation:

<div align="center"><u>POWER OFF</u>   <u>DIRECT THRUST</u>   <u>LIFT AUGMENTATION</u></div>

$$C_{m_\alpha} = \left(1 - C_{T_S}\right)C_{m_{\alpha_W}} + \left(C_{m_\alpha}\right)_{DT} + \left(C_{m_{C_L}}\right)_{SS}\left(C_{L_\alpha}\right)_{LA}$$

<div align="center"><u>NACELLE</u>   <u>FUSELAGE</u></div>

$$+ \left(C_{m_{C_L}}\right)\left[\left(C_{L_\alpha}\right)_{PO} + \left(C_{L_\alpha}\right)_{LA}\right]\left[1 + \frac{\left(C_{L_\alpha}\right)_{LA}}{\left(C_{L_\alpha}\right)_{PO}}\right] + \frac{K_B W_B^2 L_B}{Sc} \tag{114}$$

The combination of Equations (113) and (114) provides values of pitching moment for any value of C_{L_T}, α, or C_{T_S}. These equations and the lift and longitudinal force equations have been incorporated into the computer program described in Reference 45 to supply tail-off aerodynamic data to the performance program.

7.0 DOWNWASH CHARACTERISTICS

The basic approach of this procedure is to develop equations for calculating downwash velocities in the plane of symmetry, at the longitudinal and vertical stations of the horizontal tail, as given by the Biot-Savart equation. The span load distributions necessary to carry out the computations can be obtained from the existing computer program (described in Section 4.0) based on the method of Reference 42. Finally, the downwash thus obtained is modified to account for the effects of a slipstream by a procedure similar to that given in Reference 50.

As a starting point in the analysis, equations are developed for calculating downwash angle in the plane of symmetry for any longitudinal or vertical position of the horizontal tail. An undeflected, undistorted wake is assumed. Since span load distributions are obtained from Reference 42, the same conceptual model of horseshoe vortices which replace the circulation distribution of the actual wing will be considered in calculating the induced velocities at the tail plane. Also, the same general form of the Biot-Savart equation is used for calculating the downwash velocity at a point P induced by an elemental vortex filament:

$$w_P = \frac{\Delta \Gamma (\cos \alpha - \cos \beta)}{4 \pi R} \cos \omega$$

The angles and distances in the above equation are defined in Figure 33. The component q_P is the total tangential velocity component induced at point P by the vortex element, and w_P is the downwash velocity component.

The planform geometry and typical arrangements of the horseshoe vortices (corresponding to those in Reference 42) are shown in Figure 34. The tail length is defined in the usual sense, i.e., distance from the quarter chord of the wing mean aerodynamic chord to the quarter chord of the horizontal tail mean aerodynamic chord. In deriving the equations, the origin of the x axis is at the quarter chord of the wing root chord, so that the tail length is defined by the following equation:

$$\ell_H' = \ell_H + \frac{1}{3}\left(\frac{1 + 2\lambda}{1 + \lambda}\right)\tan \Lambda_{c/4} \tag{115}$$

On Figure 34, η_i refers to the spanwise location of the midpoint of the bound vortex for any chosen number of spanwise stations, and $\Delta \eta$ is the bound vortex span of each elemental horseshoe vortex system.

77

End View   Plan View
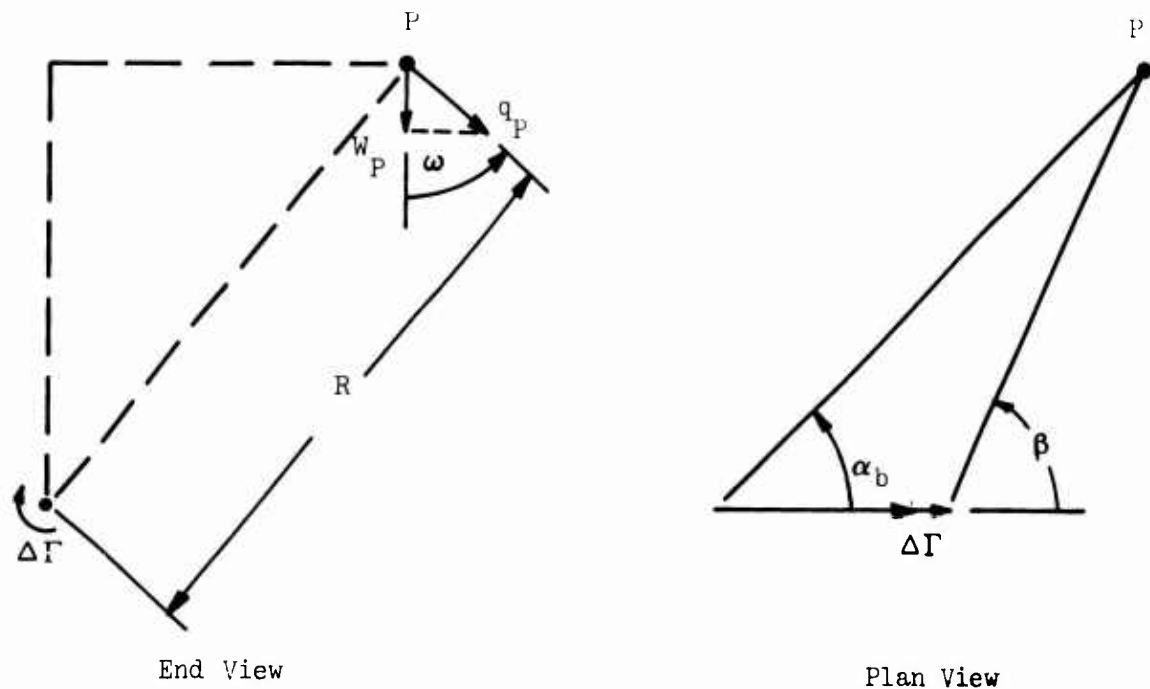
Figure 33. Vortex Element Geometry.

From the geometry for the tilt-wing in Figure 35, it is seen that the problem becomes that of calculating the downwash at a point aft of the wing root quarter chord and above the wing wake. These distances vary as a function of the wing tilt angle, angle of attack, and wake location. The longitudinal distance can be written directly in terms of tilt angle, angle of attack, and airplane geometry as follows:

$$\ell_H'' = \left[\ell_H + \frac{1}{3}\left(\frac{1+2\lambda}{1+\lambda}\right)\tan\Lambda_{c/4} - (1 - \cos i_W)x_{PIV}\right]\cos(\alpha_W - i_W)$$

$$+ (z_H - z_{PIV} - x_{PIV}\sin i_W)\sin(\alpha_W - i_W)$$

(116)

The vertical distance is given by

$$z_H'' = z_H' + h_o + h$$

(117)

The first two te.ms in the above equation are dependent only on the tilt angle, angle of attack, and airplane geometry, as follows:

78
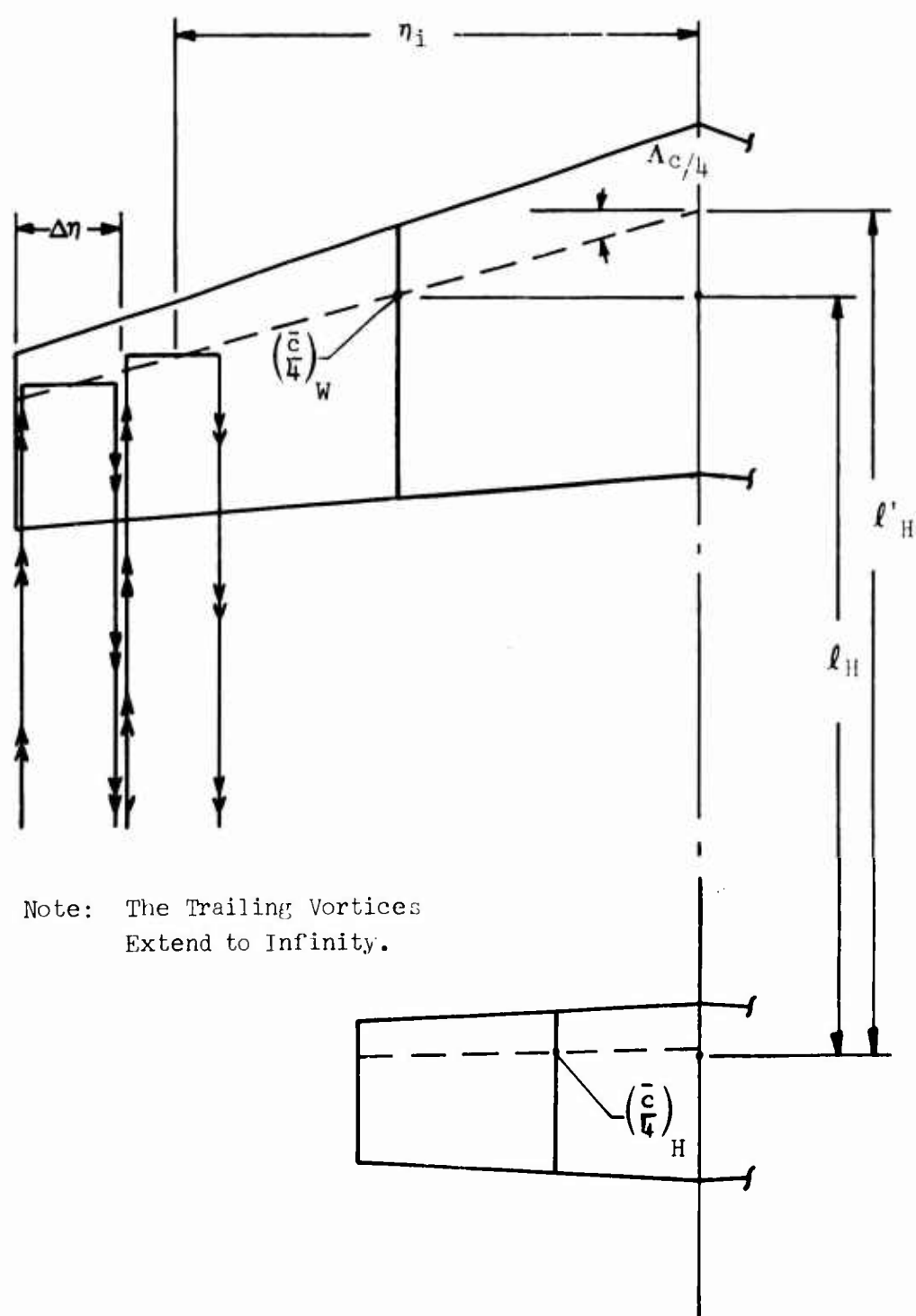
Note: The Trailing Vortices
Extend to Infinity.

Figure 34. Planform Geometry and Typical Arrangements
of the Horseshoe Vortices.

79

Figure 35. Side View of Wake Geometry for Tilt-Wing Configuration.

$$z_H' = (z_H - z_{PIV} - x_{PIV}\sin i_W)\cos(\alpha_W - i_W)$$
$$- \left[\ell_H + \frac{1}{3}\left(\frac{1+2\lambda}{1+\lambda}\right)\tan\Lambda_{c/4} - (1 - \cos i_W)x_{PIV}\right]\sin(\alpha_W - i_W)$$

$$\text{(118)}$$

$$h_o = .75\, c_r \sin i_W \tag{119}$$

The last term is the wake displacement, which requires an auxiliary calculation. The equations for calculating wake displacement are developed in subsequent paragraphs.

The next step in the analysis is to apply the Biot–Savart equation to an element of the horseshoe vortex system. With all distances measured on semispans, the total downwash contribution of two elemental bound vortices at equivalent spanwise stations on the left and right wing panels is given by the following equation:

$$\tan\epsilon_{b_i} = \left(\frac{\Delta\Gamma_i}{\pi Vb}\right)\frac{\left(\ell_H'' - \eta_i\tan\Lambda_{c/4}\right)}{\left[\left(z_H''\right)^2 + \left(\ell_H'' - \eta_i\tan\Lambda_{c/4}\right)^2\right]}\left[\frac{\left(\eta_i - \frac{\Delta\eta}{2}\right)}{\sqrt{\left(\eta_i + \frac{\Delta\eta}{2}\right)^2 + \left(\ell_H'' - \eta_i\tan\Lambda_{c/4}\right)^2 + (z_H'')^2}}\right.$$
$$\left. - \frac{\left(\eta_i - \frac{\Delta\eta}{2}\right)}{\sqrt{\left(\eta_i - \frac{\Delta\eta}{2}\right)^2 + \left(\ell_H'' - \eta_i\tan\Lambda_{c/4}\right)^2 + (z_H'')^2}}\right]$$

$$\text{(120)}$$

Contribution of the trailing vortices of the left and right wing panels is

$$\tan\epsilon_{t_i} = \left(\frac{\Delta\Gamma_i}{\pi Vb}\right)\frac{\eta_i + \frac{\Delta\eta}{2}}{\left[\left(\eta_i + \frac{\Delta\eta}{2}\right)^2 + (z_H'')^2\right]}\left[1 + \frac{\left(\ell_H'' - \eta_i\tan\Lambda_{c/4}\right)}{\sqrt{\left(\eta_i + \frac{\Delta\eta}{2}\right)^2 + \left(\ell_H'' - \eta_i\tan\Lambda_{c/4}\right)^2 + (z_H'')^2}}\right]$$

$$\text{(121)}$$

Then the total downwash is obtained as the summation of Equations (120) and (121) for any specified number, i, of elemental horseshoe vortices. All of the terms in Equations (120) and (121) are defined except the distance from the wake displacement at the longitudinal station of the horizontal tail. The effects of vertical

81

displacement of the wake are approximated by assuming that its inclination at every point is the downwash angle of the wake. Starting with zero inclination at the wing trailing edge, the wake displacement is

$$h = \int_{\left[x_o \cos(\alpha_W - i_W)\right]}^{\left[\ell_H{''} - x_o \cos(\alpha_W - i_W)\right]} \tan \epsilon_o \, dx \tag{122}$$

To perform the wake displacement calculations, Equations (120) and (121) reduce to the following form:

$$\tan \epsilon_{o_i} = \left(\frac{\Delta \Gamma_i}{\pi V b}\right) \left\{ \frac{1}{\left(x - \eta_i \tan \Lambda_{c/4}\right)} \left[\frac{\left(\eta_i + \frac{\Delta \eta}{2}\right)}{\sqrt{\left(\eta_i + \frac{\Delta \eta}{2}\right)^2 + \left(x - \eta_i \tan \Lambda_{c/4}\right)^2}} \right. \right.$$

$$\left. - \frac{\left(\eta_i - \frac{\Delta \eta}{2}\right)}{\sqrt{\left(\eta_i - \frac{\Delta \eta}{2}\right)^2 + \left(x - \eta_i \tan \Lambda_{c/4}\right)^2}} \right] + \frac{1}{\left(\eta_i + \frac{\Delta \eta}{2}\right)} \left[1 + \frac{\left(x - \eta_i \tan \Lambda_{c/4}\right)}{\sqrt{\left(x - \eta_i \tan \Lambda_{c/4}\right)^2 + \left(\eta_i + \frac{\Delta \eta}{2}\right)^2}} \right] \right\}$$

$$\tag{123}$$

where x is the distance behind the wing root chord trailing edge.

These equations determine the downwash in the plane of symmetry at the longitudinal and vertical location of the quarter chord of the mean aerodynamic chord of the horizontal tail. A partial assessment of the validity of these equations was obtained by a comparison with some test data from Reference 51. The downwash measurements in Reference 51 were obtained from vanes which were at fixed locations in the tunnel, and therefore did not completely simulate a horizontal tail on an actual configuration. However, the data do provide a partial check and, of more importance, provide information on the effect of the propeller slipstream on downwash characteristics. Since the test data did not represent a horizontal tail at angle of attack, the comparison with calculated values was made at zero angle of attack. The comparison is shown in Figure 36 where the downwash angle at zero angle of attack and thrust coefficient is shown as a function of vertical distance above and below the wing quarter chord. As background information,
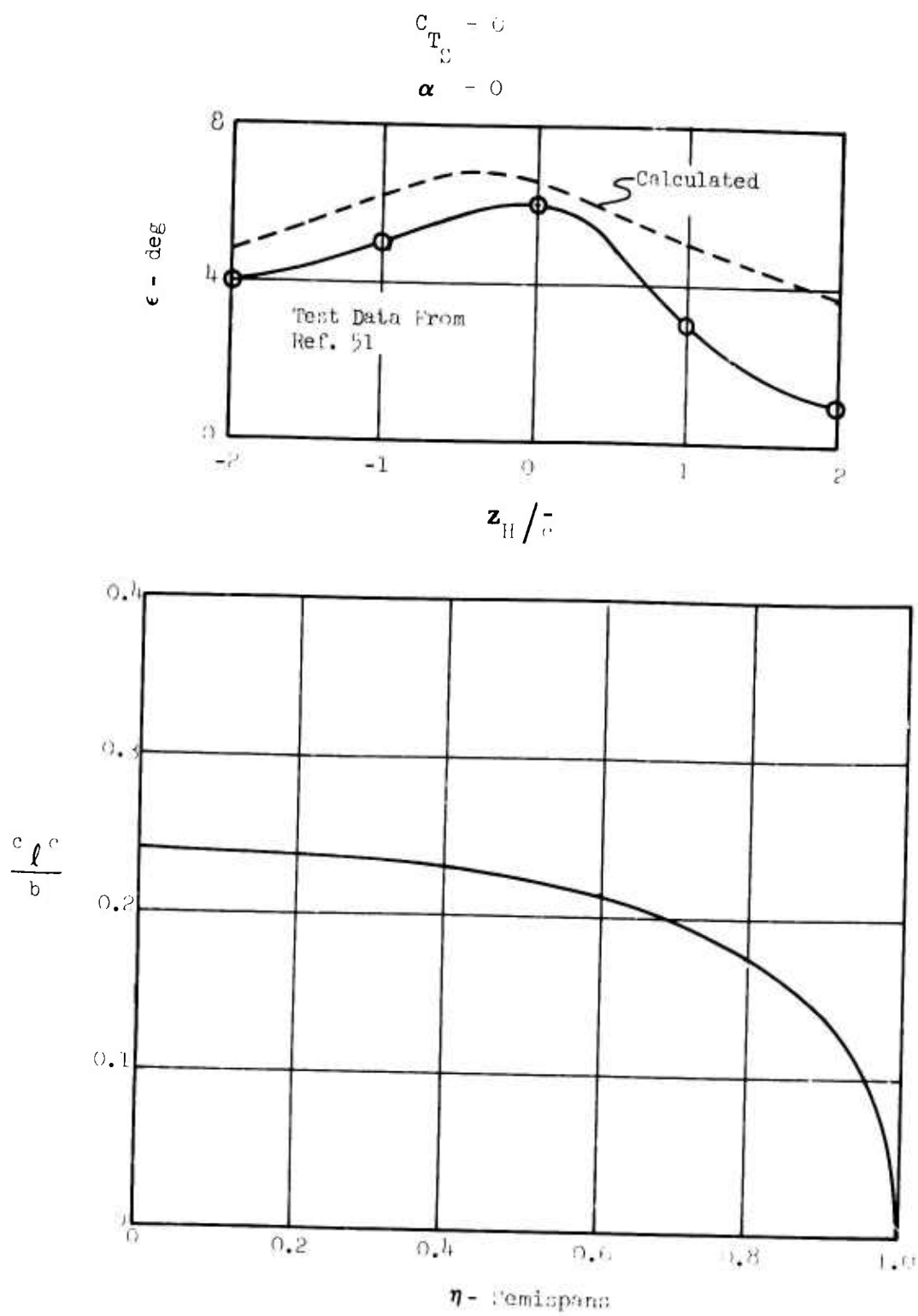
82

Figure 36. Span Load Distributions and Downwash for Model.

83

the span loading from which the calculated downwash angles were obtained is also included on Figure 36. There is good trend agreement between calculated and test downwash angles for locations below the center line. The test data are notably unsymmetrical about the center line and result in calculated downwash values that are significantly higher than the test values for locations well above the center line. The agreement is considered to be generally satisfactory for trends, but adjustments appear to be required for absolute levels.

As noted in the introductory paragraphs, power effects are accounted for by modification of the downwash calculated at zero thrust coefficient by a procedure similar to that given in Reference 42. In essence, the method states that the tangent of the downwash angle at any thrust coefficient is proportional to the lift coefficient at that thrust coefficient. The calculated downwash angles will thus have a limiting value of 90 degrees at a thrust coefficient of one. In equation form, the tangent of the downwash angle at any thrust coefficient is simply

$$(\tan \epsilon)_{C_{T_S}=x} = (\tan \epsilon)_{C_{T_S}=0} \, (C_L)_{C_{T_S}=x} \tag{124}$$

Or, for the test condition of Figure 36,

$$\tan \epsilon = .0449 C_L \tag{125}$$

A comparison of the downwash calculated from the above equation with the test data from Reference 51, at zero angle of attack, is shown on Figure 37. The proper trend is predicted, but the calculated values are higher than test data throughout the thrust coefficient range. It was found that improved correlation could be obtained by determining a constant of proportionality based on an average value obtained from all of the available test points. The equation becomes

$$\tan \epsilon = .0319 C_L \tag{126}$$

The above equation is also plotted on Figure 37. Constants of proportionality were determined for test conditions in Reference 51 other than those given on Figures 36 and 37, and it was found that the average values determined for all the other configurations did not differ greatly from .0319. It would therefore seem likely that a constant of proportionality exists which would apply satisfactorily to all configurations.
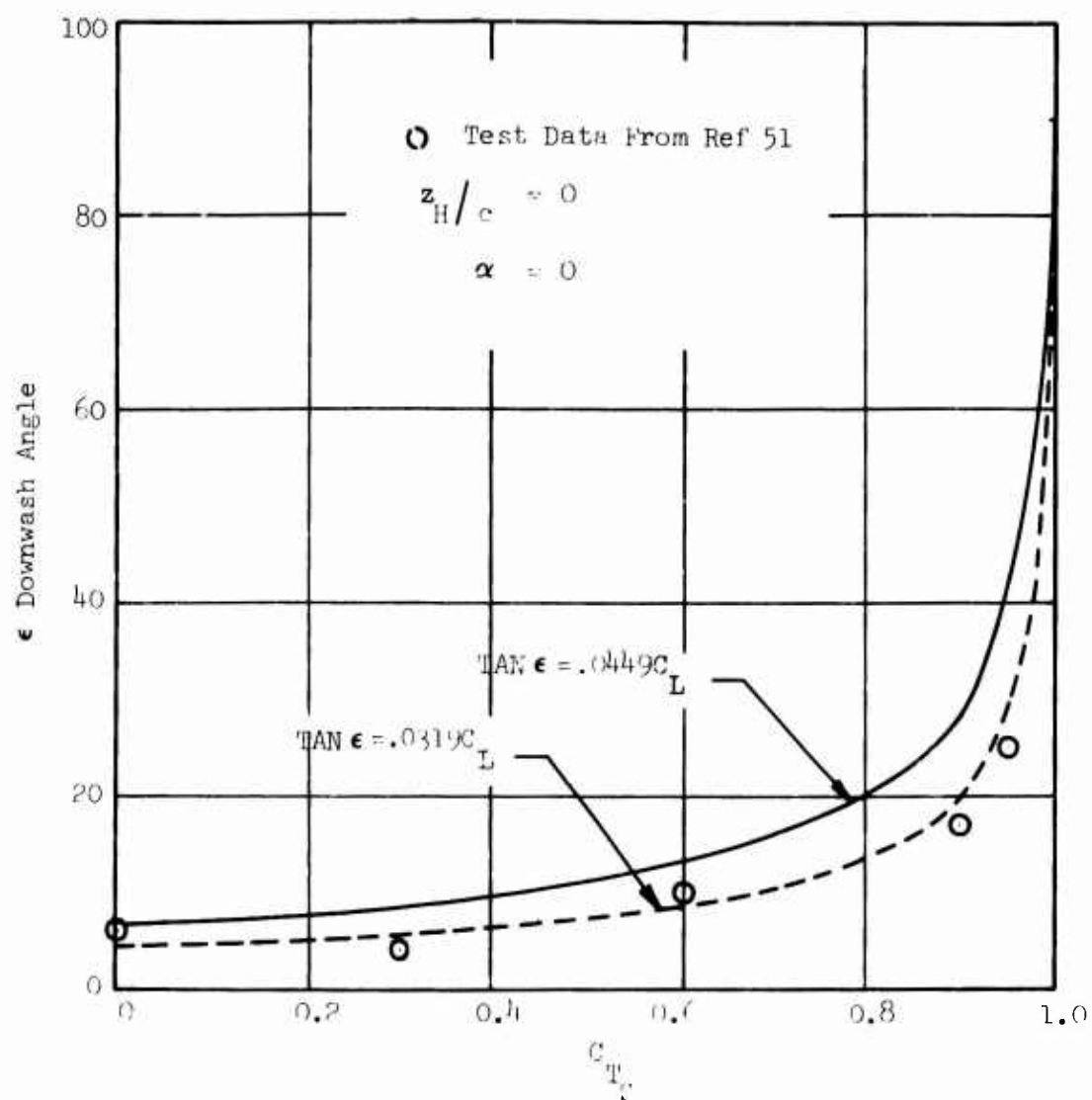
84

Figure 37. Effect of Thrust Coefficient on Downwash Angle.

8.0   WIND TUNNEL WALL CORRECTIONS

A study was performed to investigate the validity and accuracy of wind tunnel wall
corrections as applied to models of tilt-wing and deflected-slipstream V/STOL
configurations. It was hoped that a significant amount of wind tunnel and flight test
data on the same configuration would be available to insure a reasonable conclu-
sion. However, a rigorous literature search revealed that useful flight test data
were essentially nonexistent on these types of configurations. In spite of this, the
study was continued to gain a basic familiarity with the available correction proce-
dures in terms of their relative complexity and the relative magnitude of the re-
sulting corrections.

A continuation of the literature search indicated two basic correction procedures
which were considered worthy of further investigation:

1.   The standard wind tunnel wall correction procedure first proposed by
     H. Glauert in the 1920's.

2.   A more recent procedure developed by Mr. H. Heyson of NASA's
     Langley Research Center.

The discussion which follows deals with the theoretical justification of each of these
procedures as well as provides a description of the steps required in their numeri-
cal calculation. The procedures are then applied to uncorrected wind tunnel data
from models of tilt-wing and deflected-slipstream configurations.

8.1   STANDARD WALL CORRECTIONS

A complete description of the standard wall correction theory is presented in
Reference 52 and will not be duplicated herein. However, enough information will
be presented to provide a general understanding of the theory.

8.1.1   Theoretical Justification

It is well known in fluid theory that a solid boundary near a vortex may be simu-
lated by the introduction of a second vortex of opposite sign at some finite distance
away. This is the basis for the so-called Method of Images in which the solid
boundary corresponds to the zero streamline produced between the two interacting
vortices. Since the flow characteristics about a wing may be closely represented
mathematically by a simple vortex system, it is reasonable to assume that the
simulation of wind tunnel walls around a model configuration may be appropri-
ately carried out using this Method of Images.

86

This is precisely the approach taken in the standard wall correction procedure. Once the image system is established, its effect on the model is theoretically identical to that of the solid boundary it represents. Thus, the problem is reduced to one of finding the effect of the image system on the flow characteristics in the neighborhood of the model.

For an image vortex located at a distance from the model, the induced upwash velocity at the model as predicted by vortex theory becomes

$$w = \frac{\Gamma}{4 \pi r} \tag{127}$$

In addition, the circulation for a uniformly loaded wing may be expressed as

$$\Gamma = \left(\frac{S V}{2 b}\right) C_L \tag{128}$$

where   S   = wing area

   V   = free-stream velocity

   b   = wing span

   C_L = lift coefficient

Combining Equations (127) and (128) and expressing the distance in general terms as a constant times the tunnel height yields

$$w = \left(\frac{S V}{8 \pi k h_T b}\right) C_L \tag{129}$$

Now, rearranging terms and introducing the tunnel width (B) such that the product of height times width is the tunnel test section area (C) gives

$$\frac{w}{V} = \left(\frac{S}{\left(\frac{8 \pi k b}{B}\right) C}\right) C_L \tag{130}$$

Finally, defining the correction factor

$$\delta = \frac{B}{8 \pi k b} \tag{131}$$

and applying the small angle assumption to Equation (130), the boundary induced upwash angle at the model becomes

87

$$\Delta\alpha_i = \tan\Delta\alpha_i = \frac{w}{V} = \delta\frac{S}{C}C_L \tag{132}$$

Also, since the induced drag coefficient may be approximated by

$$C_{D_i} = C_L\,\alpha_i \tag{133}$$

the change in the induced drag caused by the boundary induced upwash becomes

$$\Delta C_{D_i} = C_L\Delta\alpha_i = \delta\frac{S}{C}C_L^{\,2} \tag{134}$$

Equations (132) and (134) are assumed to be applicable for all test conditions, even though they were strictly defined for the case of a small wing and uniform load distribution. This assumption is validated by the fact that δ is varied to account for the type of span load distribution, the ratio of model span to tunnel width, the shape of the test section, and even the position of the wing relative to the tunnel center line. The determination of δ is facilitated by the many charts presented in Reference 52.

8.1.2 Calculation Procedure

The use of Equations (132) and (134) for all test conditions is made possible by appropriately varying the correction factor δ. Once this factor is determined for a given set of test conditions, it remains constant, and the calculation of the boundary induced upwash angles and resulting changes in induced drag at various values of lift coefficient becomes a straightforward procedure. Therefore, because of the importance of this δ term, it is instructive to understand its derivation using the charts presented in Reference 52.

A quick examination of Reference 52 indicates the existence of charts covering only elliptically or uniformly loaded wings. Since most wings exhibit neither of these loading conditions, it would appear, at first, that the whole theory is rather academic. Closer examination, however, reveals that by using an effective vortex span rather than the total wing span, the use of the uniform load distribution curves is quite proper. This is because the shed vortices of an arbitrary planform wing rapidly roll up into a single pair of vortices which exactly duplicate the trailing vortex pattern of a uniformly loaded wing. Thus, most planforms to be studied can take advantage of the uniform loading charts of Reference 52 as long as the effective vortex span notation is used.

Given the taper ratio and aspect ratio of any wing in question, Figure 6.25 of Reference 52 yields the value of b_v/b, where b_v is the vortex span downstream of the model. The effective vortex span is then determined from the relation

88

$$b_e = \frac{b + b_v}{2} \tag{135}$$

Now, calculating the ratio of tunnel height to tunnel width

$$\lambda_T = \frac{h_T}{B} \tag{136}$$

along with the parameter

$$k = \frac{b_e}{b} \tag{137}$$

and assuming the model to be located in the center of a closed rectangular tunnel, the value of δ can be found directly from Figure 6:32 of Reference 52.

A similar procedure may be followed for the case of an open rectangular tunnel, an open and closed circular tunnel, an open and closed square tunnel, an open and closed elliptic tunnel, and an open and closed circular arc tunnel. In addition, corrections are also presented for conditions where the model is not located in the ce	er	f these various tunnels.

Basically, the application of the standard wall correction theory to wind tunnel data is a straightforward task, the greatest problem being the determination of the factor δ. Results of sample calculations on various sets of wind tunnel data are presented in Section 8.3.

8.2 HEYSON'S CORRECTIONS

A complete description of the basic Heyson wall correction theory is presented in Reference 53. Only that information deemed pertinent to a general understanding of the theory is presented here.

8.2.1 Theoretical Justification

The theoretical justification of the Heyson method depends on the application of the Method of Images to the mathematical representation of the model wake by a uniform distribution of point doublets located along the wake axis. Note that in the standard procedure of Section 8.1.1, the wake was represented mathematically by a vortex system which was assumed to trail horizontally down the tunnel, neglecting any interference with the tunnel floor. Heyson's method accounts for the downward deflection of the model wake through the superposition of both vertical and longitudinal doublets. The magnitude of this deflection is defined by a

89

so-called wake skew angle which, as shown in Figure 38, is the compliment of the more commonly used wake deflection angle θ.

Since both longitudinal and vertical velocities are induced from each of these types of doublets, four separate interference factors result for each wake skew angle:

$$\delta_{w,L} = \frac{\Delta w_L}{w_o} \cdot \frac{A_T}{A_M}$$ = the interference factor associated with the vertical velocity induced by the vertical doublet

$$\delta_{u,L} = \frac{\Delta u_L}{w_o} \frac{A_T}{A_M}$$ = the interference factor associated with the longitudinal velocity induced by the vertical doublet

$$\delta_{w,D} = \frac{\Delta w_D}{u_o} \frac{A_T}{A_M}$$ = the interference factor associated with the vertical velocity induced by the longitudinal doublet

$$\delta_{u,D} = \frac{\Delta u_D}{u_o} \frac{A_T}{A_M}$$ = the interference factor associated with the longitudinal velocity induced by the longitudinal doublet

where

A_T = wind tunnel cross-sectional area (same as C in the standard method).

$A_M = \dfrac{\pi b^2}{4}$ = model momentum area.

The terms w_o and u_o are the vertical and longitudinal induced velocities respectively, as determined from momentum theory.

Heyson's original theory, as defined in Reference 53, assumed the model to be vanishingly small so that only one line of doublets was necessary to accurately represent the model wake. He has since extended the theory to cover several specific model configurations including the finite span swept wing. The method of determining the interference factors for these various configurations is discussed in detail in Reference 54. For the case of the finite span swept wing, the basic procedure is to divide the wing into several segments and then represent the wake of each segment by its own doublet distribution. The resulting interference factors for each segment are then averaged over the model span to determine a total interference factor for the wing in question.

Mr. Heyson has made one additional modification to his original theory which warrants mention: the introduction of an effective wake skew angle in place of
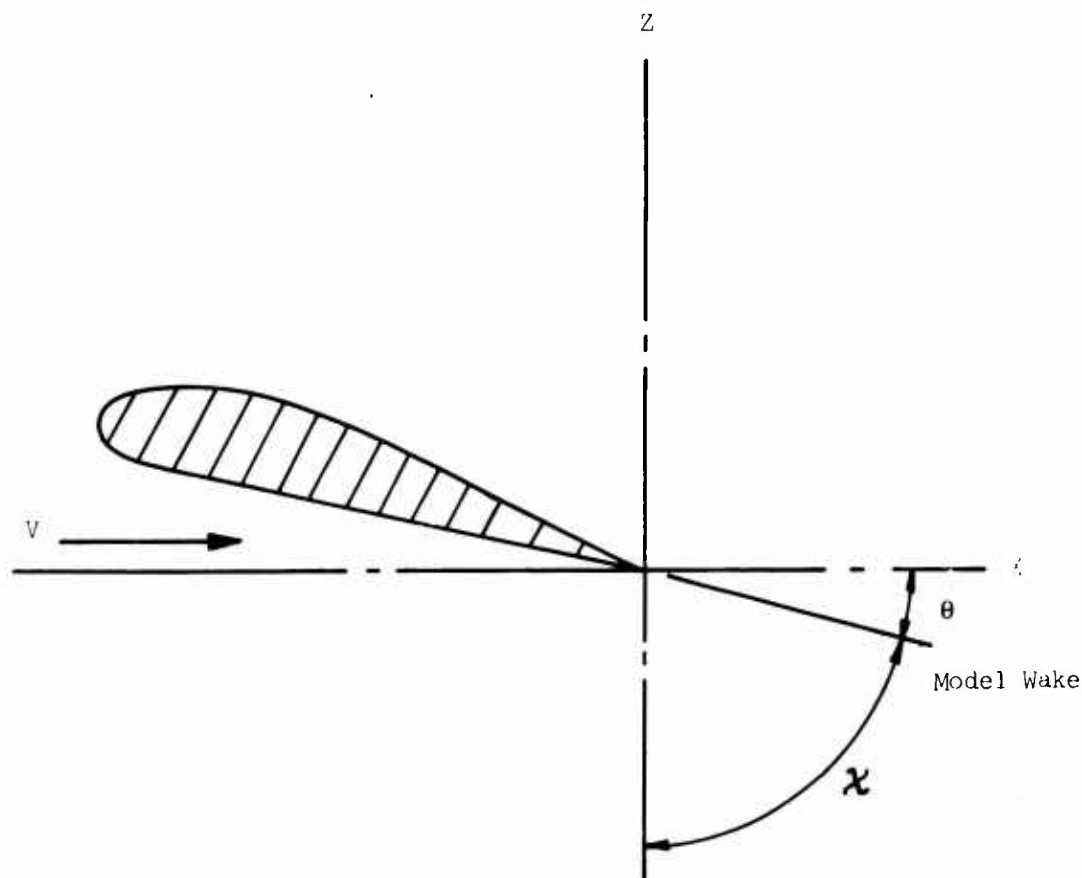
90

Figure 38. Wake Skew Angle Definition.

the old wake skew angle shown in Figure 38. This effective wake skew angle was originally defined in Reference 55 as

$$X_{eff} = \frac{X + 90}{2} \tag{138}$$

and was incorporated primarily to account for the roll-up of the model wake. This roll-up results in an effective wake deflection angle which is approximately one-half of that predicted at the center of lift.

Throughout the remainder of this section, all interference factors calculated by Heyson's method will be averaged values over the model span and will be based on the effective wake skew angle definition. A discussion of the use of these interference factors in determining the final corrected lift and drag coefficients of an arbitrary model is found in the following section.

8.2.2 Calculation Procedure

The general procedure for applying Heyson's wind tunnel wall correction theory to uncorrected wind tunnel data is presented in Appendix C of Reference 53. The remainder of this section deals with the basic equations contained in the calculation procedure and includes a description of the mathematical techniques required in its computerization.

The basic equations in Heyson's method, as given in Reference 53, are shown below:

$$w_h = -\sqrt{\frac{L}{n\,\rho\,A_M}} \tag{139}$$

$$\frac{V}{w_h} = \frac{V}{w_o}\frac{w_o}{w_h} \tag{140}$$

$$\left(\frac{w_o}{w_h}\right)^4 = \frac{1}{1+\left(\dfrac{V}{w_o}+\dfrac{D_i}{L}\right)^2} \tag{141}$$

where w_h = reference velocity

L = lift force

D_i = induced drag force

ρ = tunnel density

n = ratio of final induced velocities in the far wake to the initial induced velocities u_o and w_o at the model ($n = 2$ for a wing/propeller configuration).

A close examination of Equations (139), (140), and (141) revealed the possibility of expressing the equations in a more usable form. For example, with $n = 2$ and $A_M = \pi b^2/4$, Equation (139) may be written as follows:

$$\frac{w_h}{V} = \frac{-\sqrt{\dfrac{L}{n\,\rho A_M}}}{V} = -\sqrt{\frac{C_L\dfrac{\rho}{2}V^2 S}{2\rho\dfrac{\pi b^2}{4}V^2}}$$

92

$$\frac{w_h}{V} = -\sqrt{\frac{C_L S}{\pi b^2}} = -\sqrt{\frac{C_L}{\pi AR}} \tag{142}$$

or

$$\frac{V}{w_h} = -\sqrt{\frac{\pi AR}{C_L}} \tag{143}$$

Now, writing Equation (140) as

$$\frac{V}{w_o} = \frac{\dfrac{V}{w_h}}{\dfrac{w_o}{w_h}} \tag{144}$$

and substituting into Equation (141) yields

$$\left(\frac{w_o}{w_h}\right)^4 = \frac{1}{1 + \left(\dfrac{\dfrac{V}{w_h}}{\dfrac{w_o}{w_h}} + \dfrac{D_i}{L}\right)^2} \tag{145}$$

Finally, for simplicity, it is normally assumed that

$$\frac{D_i}{L} = \frac{D}{L} = \frac{C_D}{C_L} \tag{146}$$

so that Equation (145) may be written as

$$\left(\frac{w_o}{w_h}\right)^4 = \frac{1}{1 + \left(\dfrac{\dfrac{V}{w_h}}{\dfrac{w_o}{w_h}} + \dfrac{D}{L}\right)^2} \tag{147}$$

The problem is thus reduced to one of finding the values of w_o/w_h which satisfy Equation (147) for values of V/w_h and D/L as determined from Equations (143)

93

and (146), respectively. Actually, according to Reference 56, only one root of Equation (147) is needed: that between 0 and 1. For this case, it becomes possible to use the Newton-Raphson iteration scheme. V/w_0 is then calculated from Equation (144) and the value of the wake skew angle is found from the expression

$$\chi = \frac{\pi}{180} \, \text{arc tan} \left[-\frac{V}{w_0} - \frac{D}{L} \right] \tag{148}$$

which eliminates the problem of determining the proper sign of the wake skew angle. Finally, the effective wake skew angle is determined from Equation (138).

With the proper value of the effective skew angle known, it becomes necessary to determine the four interference factors $\delta_{w,L}$, $\delta_{w,D}$, $\delta_{u,L}$, and $\delta_{u,D}$. The procedure followed in the computer program listed in Reference 53 was to parametrically determine the interference factors at 10-degree increments of χ_{eff} between 20 and 90 degrees. The resulting values are then used in a slope intercept routine to determine the correct values which correspond with the value of χ_{eff}.

The remainder of the calculation procedure is a straightforward task, and the following equations resulted:

$$\Delta\alpha = \text{arc tan} \left[\frac{\frac{\Delta w}{V}}{1 + \frac{\Delta u}{V}} \right] \tag{149}$$

$$\frac{q_c}{q} = \left(1 + \frac{\Delta u}{V} \right)^2 + \left(\frac{\Delta w}{V} \right)^2 \tag{150}$$

$$L_c = L \cos\Delta\alpha - D \sin\Delta\alpha \tag{151}$$

$$D_c = L \sin\Delta\alpha - D \cos\Delta\alpha \tag{152}$$

$$q_c = \frac{q_c}{q} \, q \tag{153}$$

$$\alpha_c = \alpha + \Delta\alpha \tag{154}$$

$$C_{L_c} = \frac{L_c}{q_c \, S} \tag{155}$$

94

$$C_{D_c} = \frac{D_c}{q_c S} \qquad (156)$$

$$C_{T_c} = C_T \frac{q}{q_c} \qquad (157)$$

A visual picture of the effect of these corrections is shown in Figure 39. Since the corrected thrust coefficient varies throughout a given wind tunnel run, as does C_{L_c} and C_{D_c}, some cross-plotting must be done to obtain a valid representation of the corrections at a constant corrected thrust coefficient.
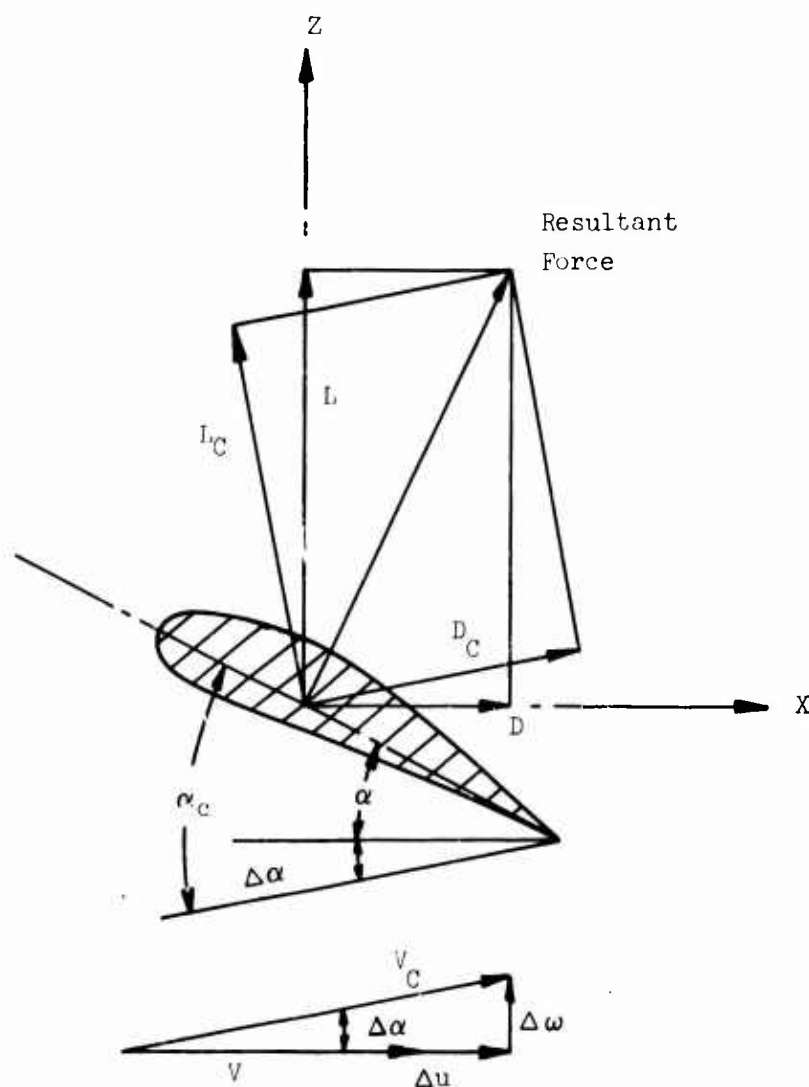

Figure 39. Geometry for Heyson's Wall Corrections.

95

8.3 RESULTS

The first data to which the standard and Heyson wall corrections were applied are presented in Reference 56. In that report a study is described concerning an investigation on the effects of Heyson's wall corrections as applied to a tilt-wing model (without fuselage) tested in three different size tunnels: (1) the Langley 7- X 10-foot tunnel, (2) the 17-foot diffuser section of this 7- X 10-foot tunnel, and (3) the Langley full-scale 30- X 60-foot tunnel.

The model tested had a 4.23-foot wing span with two symmetrically located non-overlapping propellers, each having a diameter of 2 feet. In addition, the model was equipped with a 30-percent-chord trailing edge flap which could be deflected to an angle of 40 degrees. All tests were run at the same slipstream Reynolds number. The same sting attachment was used on the model to eliminate these items from the correlation.

The data used in this study were for the flaps-down configuration, and were obtained in the 7- X 10-foot and 30- X 60-foot tunnels only. None of the 17-foot diffuser section data is presented because of the questionable application of Heyson's corrections to these data. This diffuser section converges quite rapidly downstream of the model and thus negates that aspect of Heyson's theory which requires the doublet distribution to flow in a straight line along the floor following its downward deflection. In addition, a close inspection of the basic uncorrected data showed the 17-foot diffuser section data to be inconsistent with those of the other sections.

Most of the corrections applied to the data of Reference 56 assumed the model to be vanishingly small, and did not include the new definition of effective wake skew angle. This analysis corrects for both of these deficiencies in the application of Heyson's method to the 7- X 10-foot tunnel data. The 30- X 60-foot tunnel data are assumed to be free of wall effects due to the small ratio of model to tunnel size.

The increments in induced upwash angle and induced drag coefficient, as calculated by the standard procedure of Section 8.1.2, are applied to the test data of Reference 56. The final corrected lift and drag curves obtained from these standard corrections are shown in Figures 40 and 41 respectively.

The calculation of Heyson's corrections for the data of Reference 57 proved to be considerably more difficult th . the standard correction method. The basic corrections themselves were determined fairly easily using the computer program listed in Reference 54. However, a problem arose in reducing the corrected values of lift, drag and angle of attack to a constant thrust coefficient basis. This procedure was necessitated by the fact that Heyson's procedure corrects the tunnel dynamic pressure and hence the thrust coefficient of every data point. Cross plots

of the corrected values of lift, drag and angle of attack were required. Data at constant values of corrected thrust coefficient ($C_{T_C} = 4$, 8 and 14) and uncorrected angle of attack (α_u) are plotted on the lift and drag curves of Figures 40 and 41.

From the data on Figures 40 and 41, it is seen that both the correction procedures tend to decrease the correlation with the so-called correction-free 30- × 60-foot tunnel data. Therefore, from this information, it would be hard to justify the need for any wall corrections. It is unfortunate that there are not more correction-free data available to substantiate this finding.

Another interesting result of Figures 40 and 41 is that as the uncorrected lift co-efficient (C_{L_u}) increases, the standard corrections become significantly larger than those of Heyson's method. This is primarily due to the large decrease in corrected dynamic pressure (q_c) with increasing C_{L_u}, which occurs in Heyson's method. The reduction in q_c caused an increase in both C_{L_c} and C_{D_c}, which in effect decreases the magnitude of Heyson's corrections. For a true comparison of the relative magnitudes of the two corrections, some sort of q correction should be incorporated in the standard procedure.

Since the above correlation was performed on a configuration which has a fairly small ratio of model to tunnel area ($A_M/A_T = 0.20$), it was considered important to check this discrepancy with that obtained on a configuration having a larger value of A_M/A_T. Therefore, the two correction procedures were applied to the data presented in Reference 54 on a 0.6 scale model of the Brequet 941 aircraft tested in the NASA Ames 40- × 80-foot tunnel. The model to tunnel area ratio of this configuration is 0.63 (medium span wing).

The data presented in Reference 57 had already been corrected by the standard procedure. Therefore, it was necessary to remove the standard corrections before applying Heyson's corrections. The final corrected lift and drag data from the two methods are presented in Figures 42 through 45. Data are presented at two values of corrected thrust coefficient and for two different combinations of trailing edge flap deflection.

The standard wall corrections become significantly higher than Heyson's as the uncorrected lift coefficient is increased. It is therefore assumed that this situation will exist regardless of the ratio of model area to tunnel area.
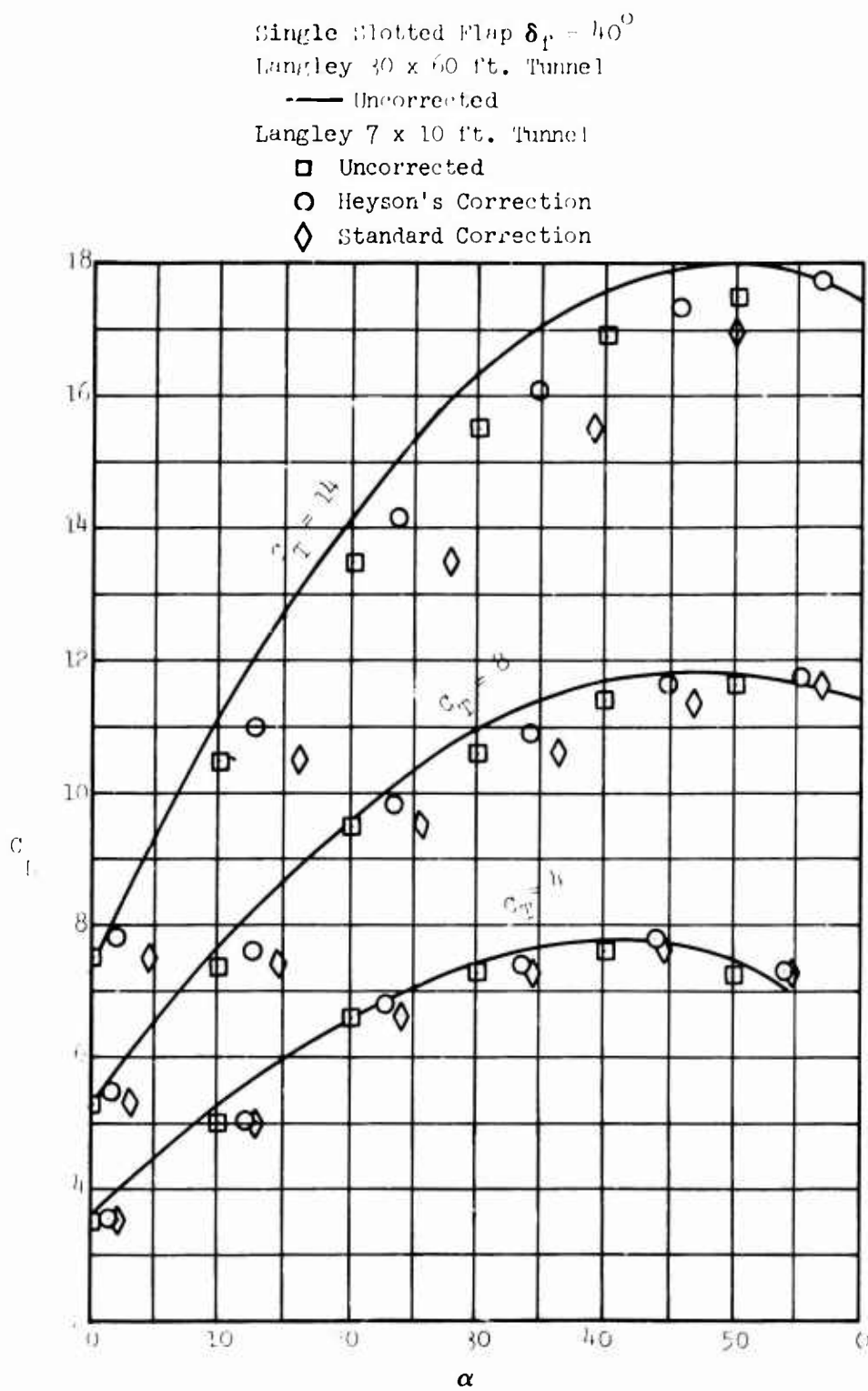
97

Figure 40. The Effect of Wind Tunnel Wall Corrections
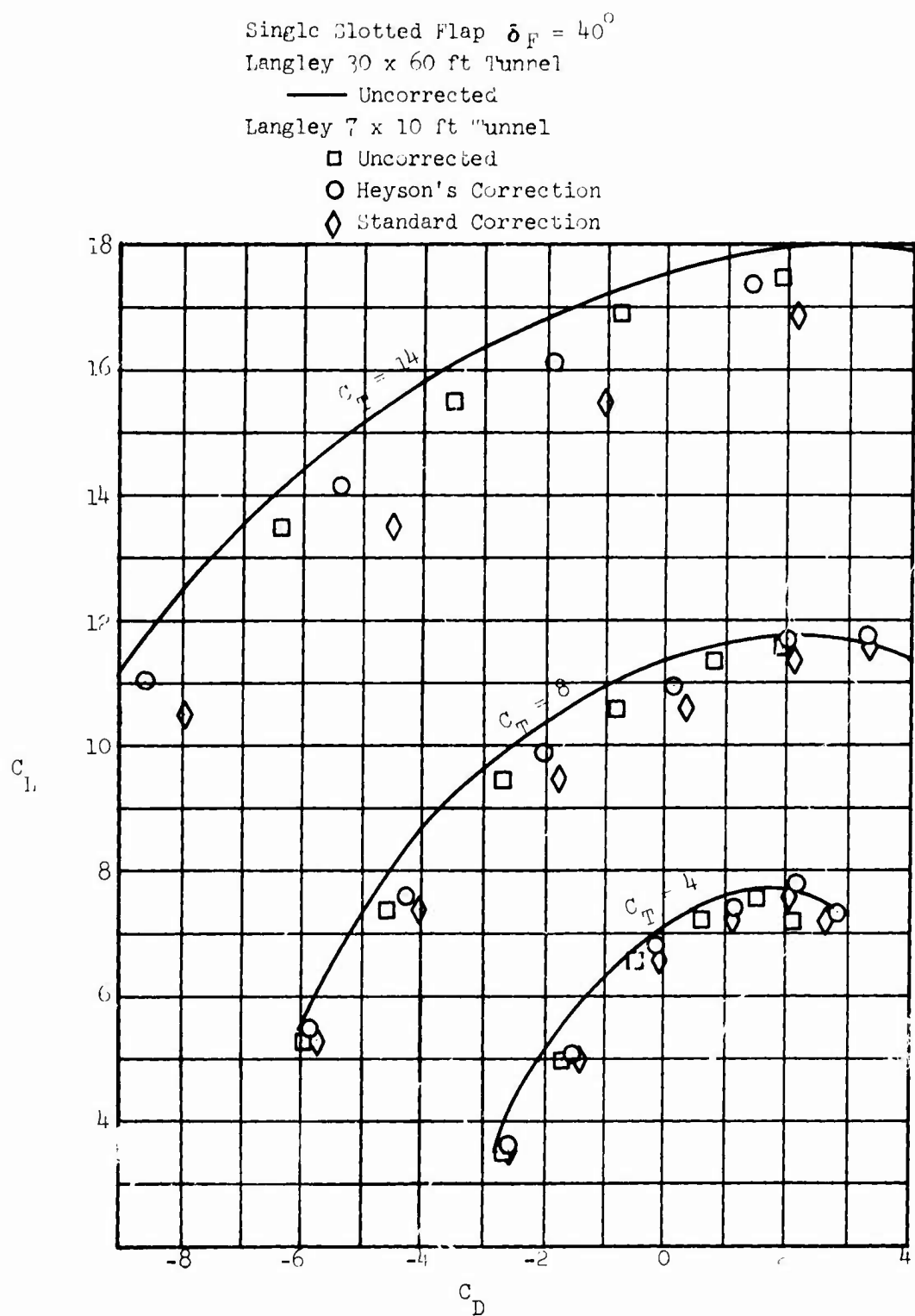to Lift Coefficient Data From Reference 56.

Figure 41. The Effect of Wind Tunnel Wall Corrections
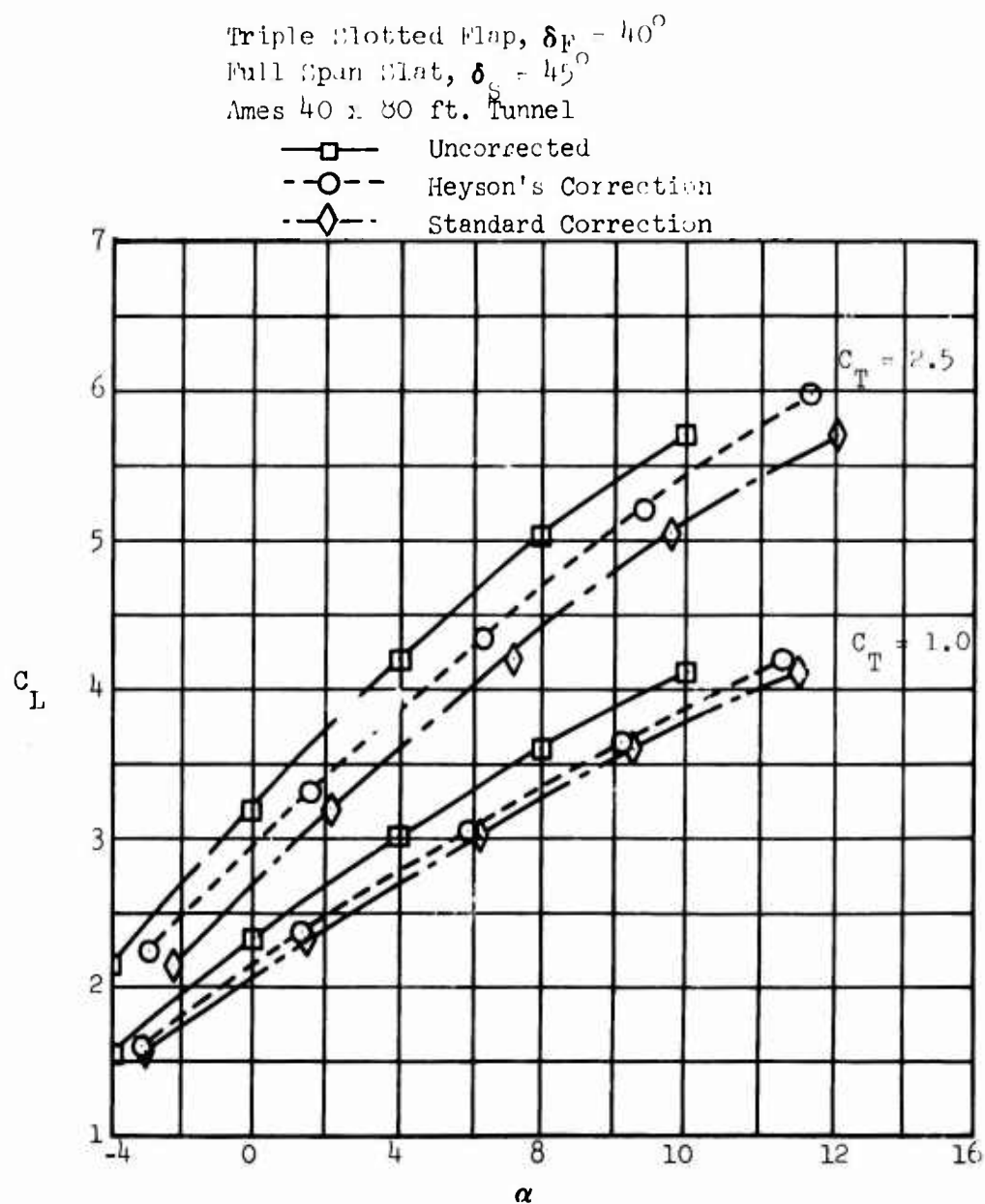to Drag Coefficient Data From Reference 56.

Figure 42. The Effect of Wind Tunnel Wall Corrections to Lift Coefficient Data From Reference 57.
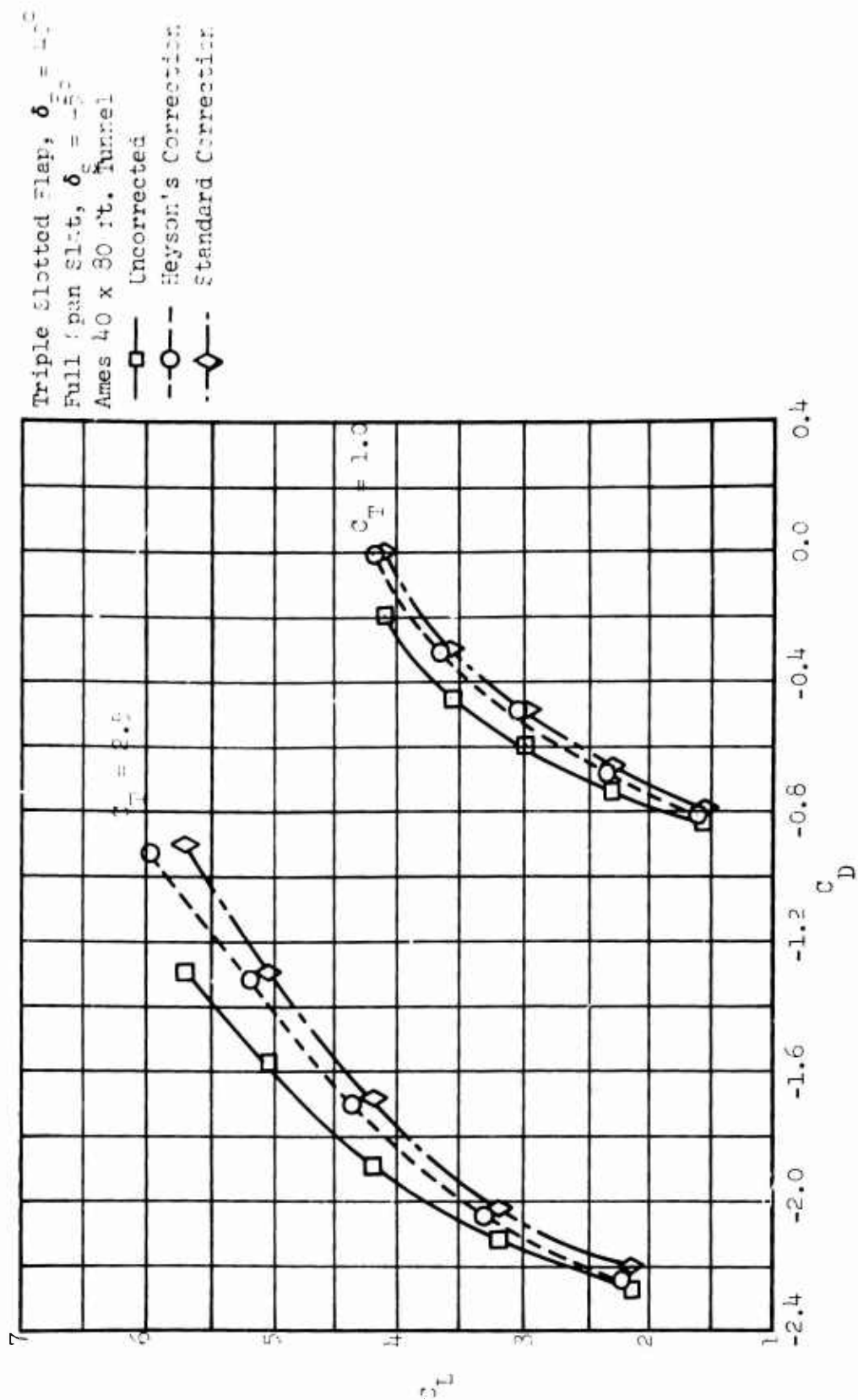
100

Figure 43. The Effect of Wind Tunnel Wall Corrections to Drag Coefficient Data From Reference 57.

101

Full Span Slat, δ_s = 45°
Triple Slotted Flap
δ_f = 100° Inboard/60° Outboard
Ames 40 x 80 ft. Tunnel

—□— Uncorrected
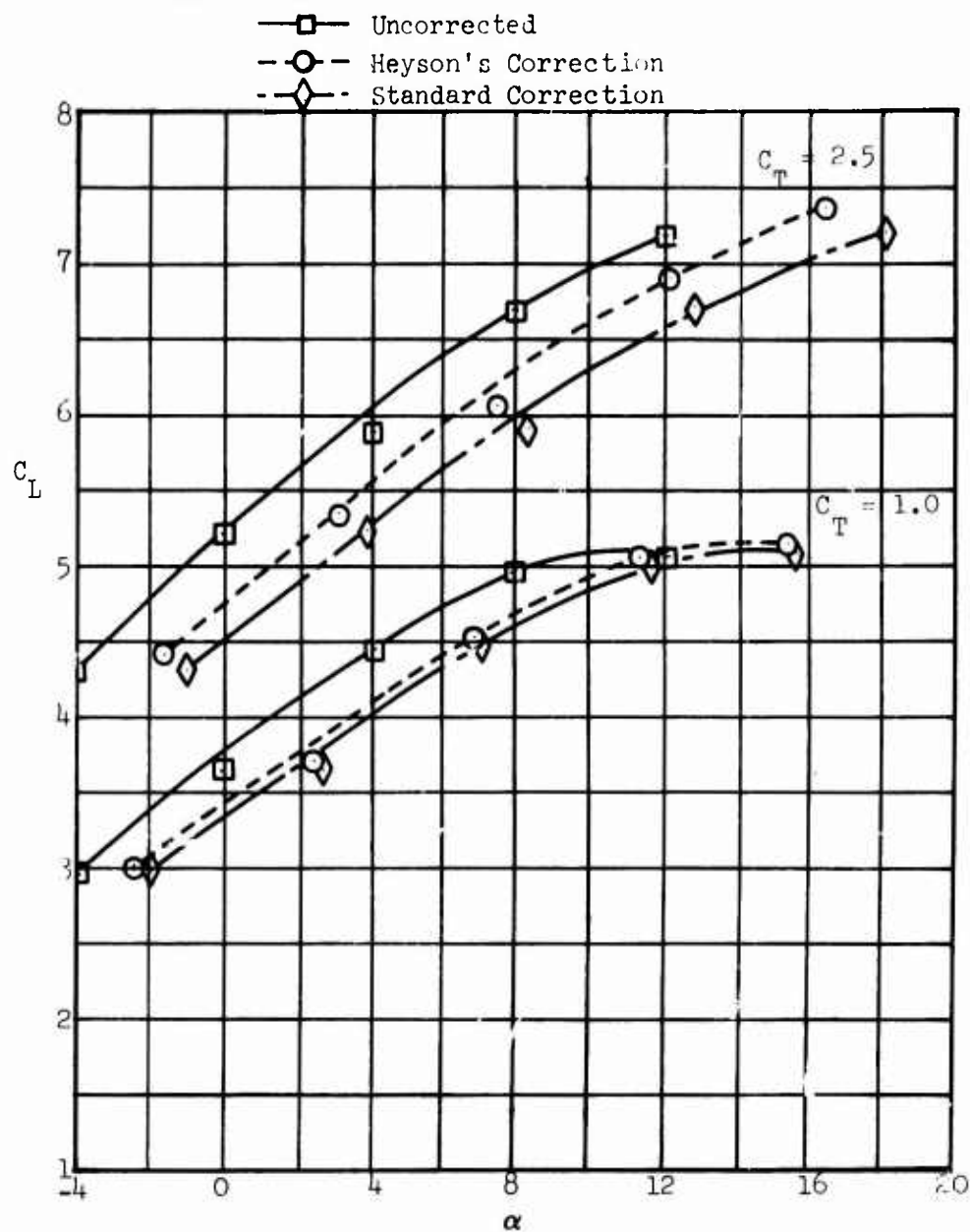—○— Heyson's Correction
—◇— Standard Correction

Figure 44.   The Effect of Wind Tunnel Wall Corrections
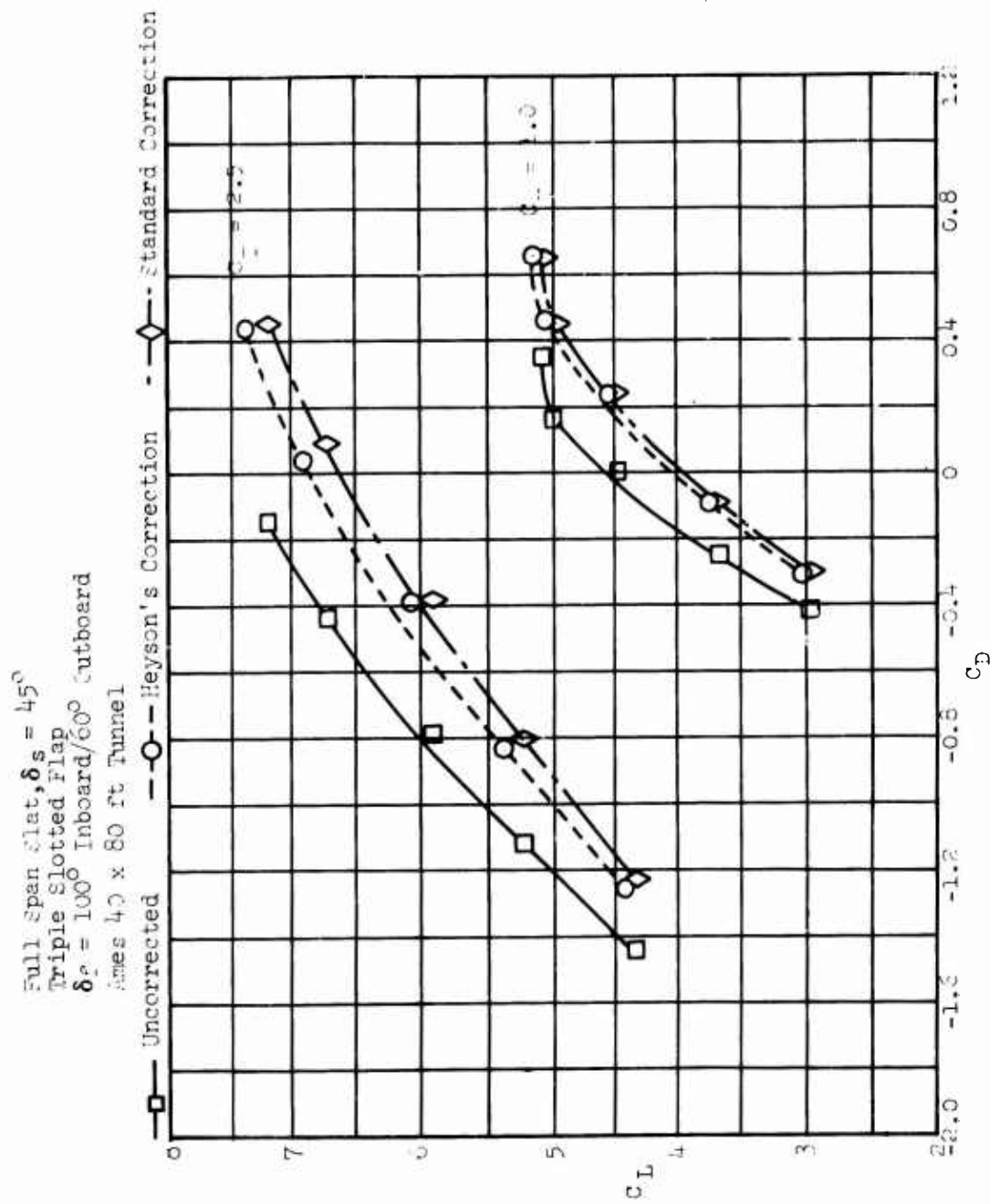to Lift Coefficient Data From Reference 57.

102

Figure 45. The Effect of Wind Tunnel Wall Corrections to Drag Coefficient Data From Reference 57.

9.0 CORRELATION OF THEORY WITH TEST DATA

In order to determine the general accuracy of the aerodynamic estimation procedures for lift, longitudinal force and pitching moment coefficients, as described in Sections 5.0 and 6.0 of this report, comprehensive data correlations have been carried out and are presented in Reference 52. The purposes of this section are to present selected correlation curves and to provide explanations for the major discrepancies. Several types of high-lift configurations were examined, which included plain, single-slotted and double-slotted trailing edge flaps, and leading edge slats. Selected results obtained on these configurations are presented for various thrust coefficients and for wing angles of attack up to 50 degrees.

Before proceeding with the discussion of the correlation curves, it is important to understand the limitations inherent in the estimation procedures because of the basic two-dimensional data which form the foundation of the procedures. This two-dimensional data base was obtained from selected two-dimensional model tests, and therefore represents only an average of the vast amount of data available. It is therefore logical to assume that the estimation procedures will provide correlation only to the same degree of accuracy found in the basic two-dimensional data, and will not correlate with every set of data examined. The important thing to note is that the two-dimensional data base has been consistently derived for all types of high-lift systems, and should thus provide a satisfactory basis for selecting one high-lift system over another.

Correlations of a single-slotted trailing edge flap configuration are presented in Figures 46 through 54 for flap deflections of 0, 20, and 50 degrees. Thrust coefficients of 0, 0.6, 0.9, and 1.0 are shown for each of these flap deflections. With the exception of the pitching moment curves for the 20- and 50-degree flap deflections, all of the correlations are quite good. A detailed analysis of this pitching moment discrepancy indicated that the two-dimensional increment in C_{m_0} due to flap deflection, as determined from Section 2.0, appears to be too large. Comparison of the predicted two-dimensional C_{m_0} increment with the experimental data of References 20 and 28 for large chord trailing edge flaps shows the predicted level to be correct. However, a similar comparison with the two-dimensional data of Reference 2 shows poor agreement for flap chord to wing chord ratios greater than 35 percent. Therefore, it is possible that the aerodynamic estimation procedure should have factors for large values of flap chord to wing chord ratio in order to provide the necessary correlation tolerance.

The double-slotted trailing edge flap correlations are presented in Figures 55 through 57 for a flap deflection of 40 degrees at thrust coefficients of 0.6, 0.8,

104

and 0.9. The significant discrepancy in this data again lies in the area of C_{m_ρ} prediction. In this case, the two-dimensional estimate is conservative rather than overpredicted. This further points out the strong need of additional work in this area of the moment estimation procedure.

The correlation data for the leading edge slat configuration in conjunction with the 50-degree single-slotted trailing edge flap are shown in Figures 58 through 60. Once again, thrust coefficients of 0, 0.6, 0.9, and 1.0 are presented. In addition to the pitching moment discrepancy, which was discussed in the previous paragraph, there is a large discrepancy in the lift curves at the low angles of attack. This discrepancy results from the typical problem of leading edge devices: flow separation at low angles of attack. The estimation procedure, as it now exists, does not treat the separated flow phenomena which are predominant on this type of configuration. According to the test data, the addition of this leading edge slat actually decreases the available maximum lift coefficient of the total system. This is the primary reason for the rather poor $C_{L_{MAX}}$ correlation on this configuration.
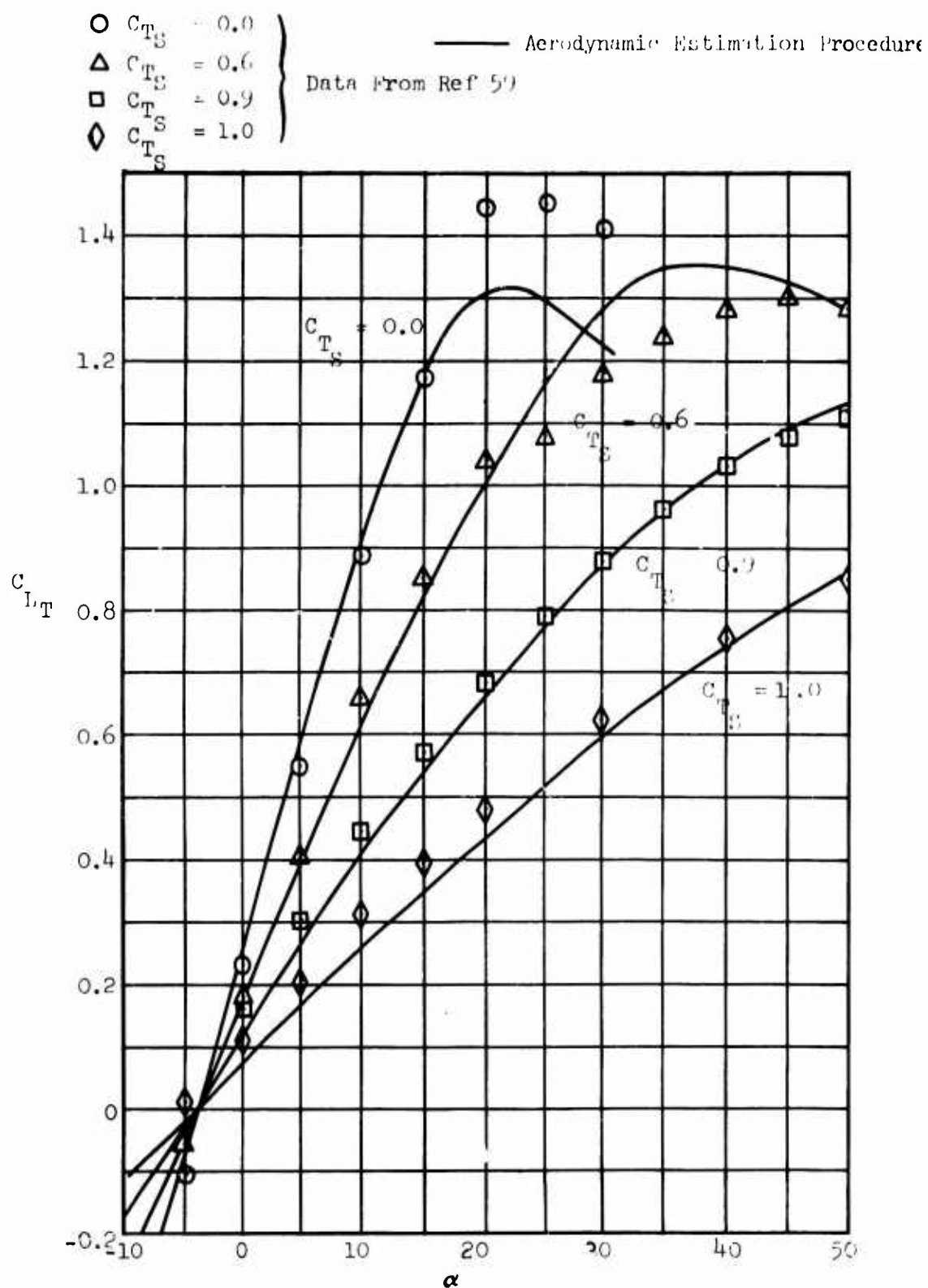
105

Figure 46. Total Lift Coefficient Versus Wing Angle of Attack, $\delta_f = 0°$.

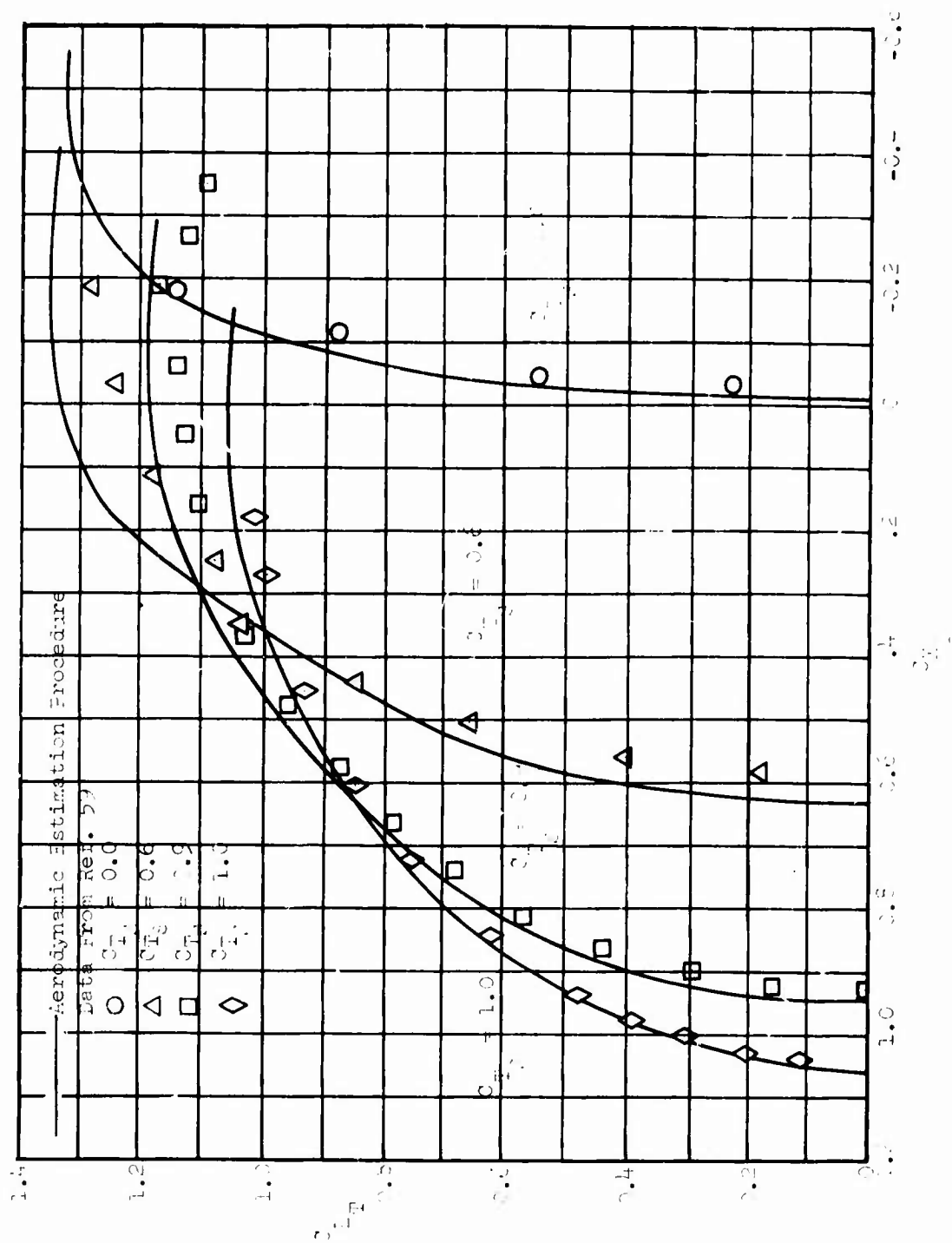106

Figure 47. Total Lift Coefficient Versus Total Drag Coefficient, $\delta_f = 0°$.

Figure 48. Total Pitching Moment Versus Wing Angle of Attack, $\delta_f = 0°$.

Figure 49. Total Lift Coefficient Versus Wing Angle of Attack, $\delta_f = 20°$.

Figure 50. Total Lift Coefficient Versus Total Drag Coefficient, $\delta_f = 20°$.

110

Figure 51. Total Pitching Moment Versus Wing Angle of Attack, $\delta_f = 20°$.

Figure 52. Total Lift Coefficient Versus Wing Angle of Attack, $\delta_f = 50°$.
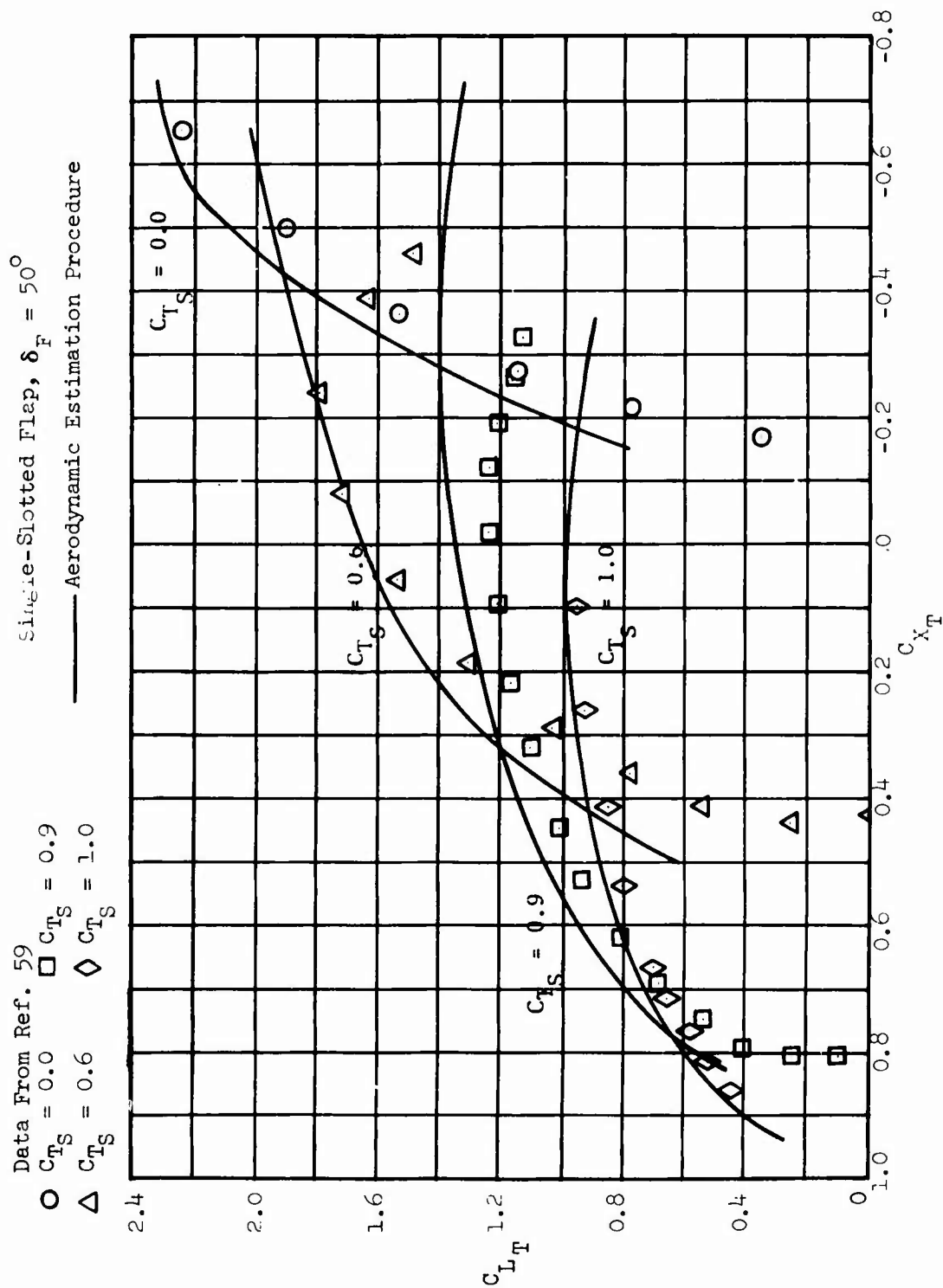
Figure 53. Total Lift Coefficient Versus Total Drag Coefficient, $\delta_f = 50°$.

Single-Slotted Flap, $\delta_F = 50^\circ$
———— Aerodynamic Estimation Procedure
Data From Ref. 59
O $C_{T_S} = 0.0$
△ $C_{T_S} = 0.6$
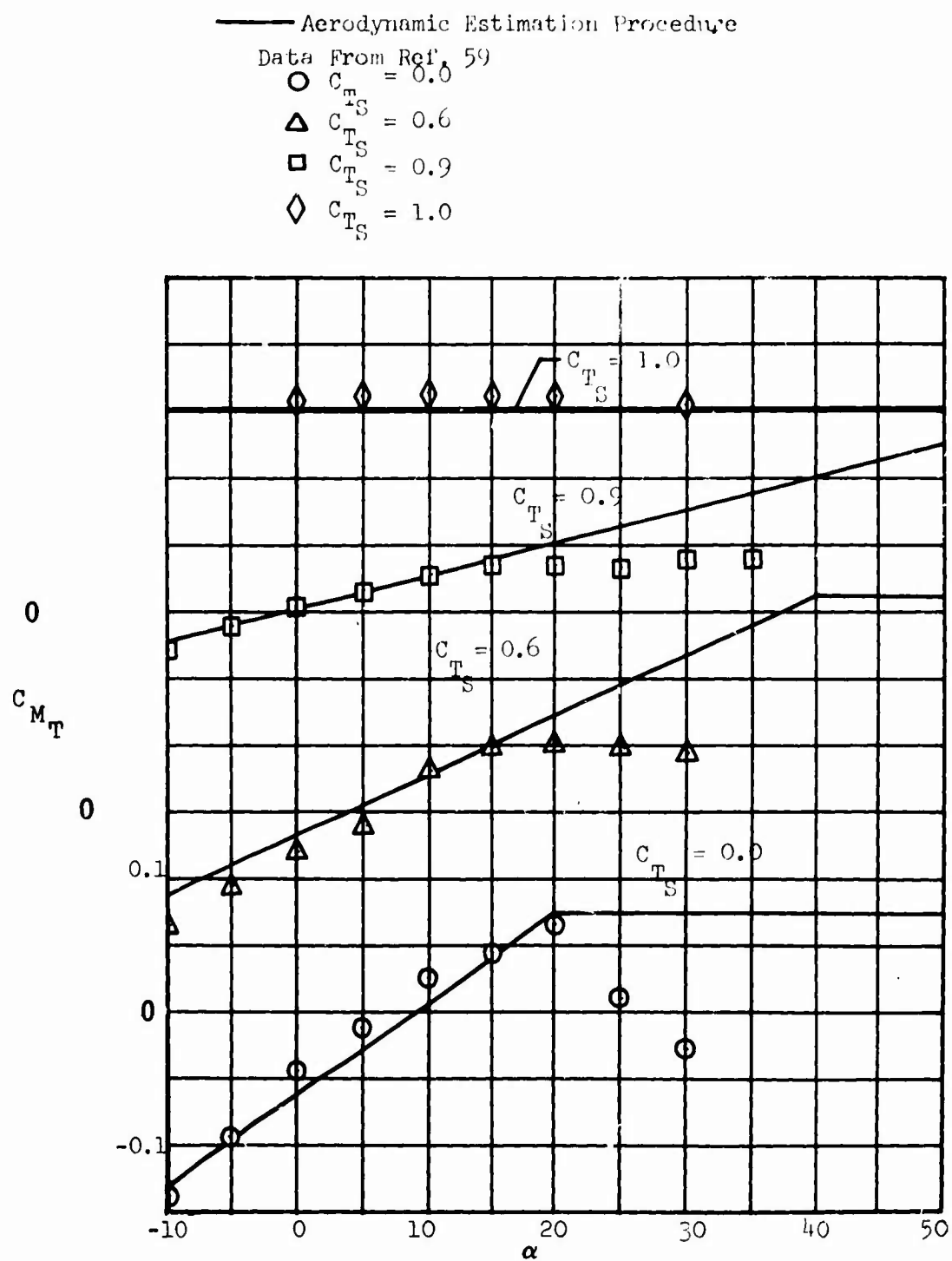□ $C_{T_S} = 0.9$
◊ $C_{T_S} = 1.0$
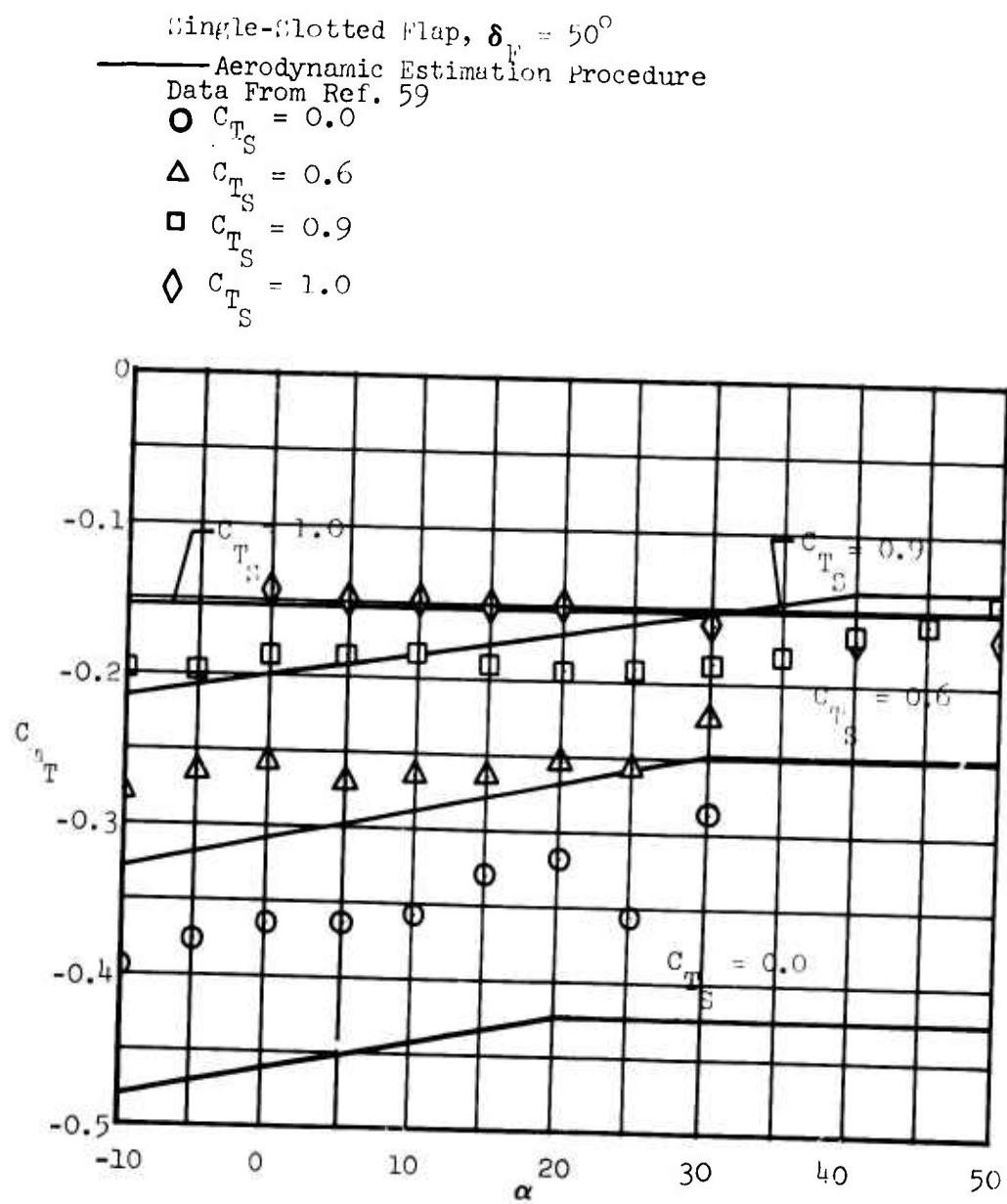
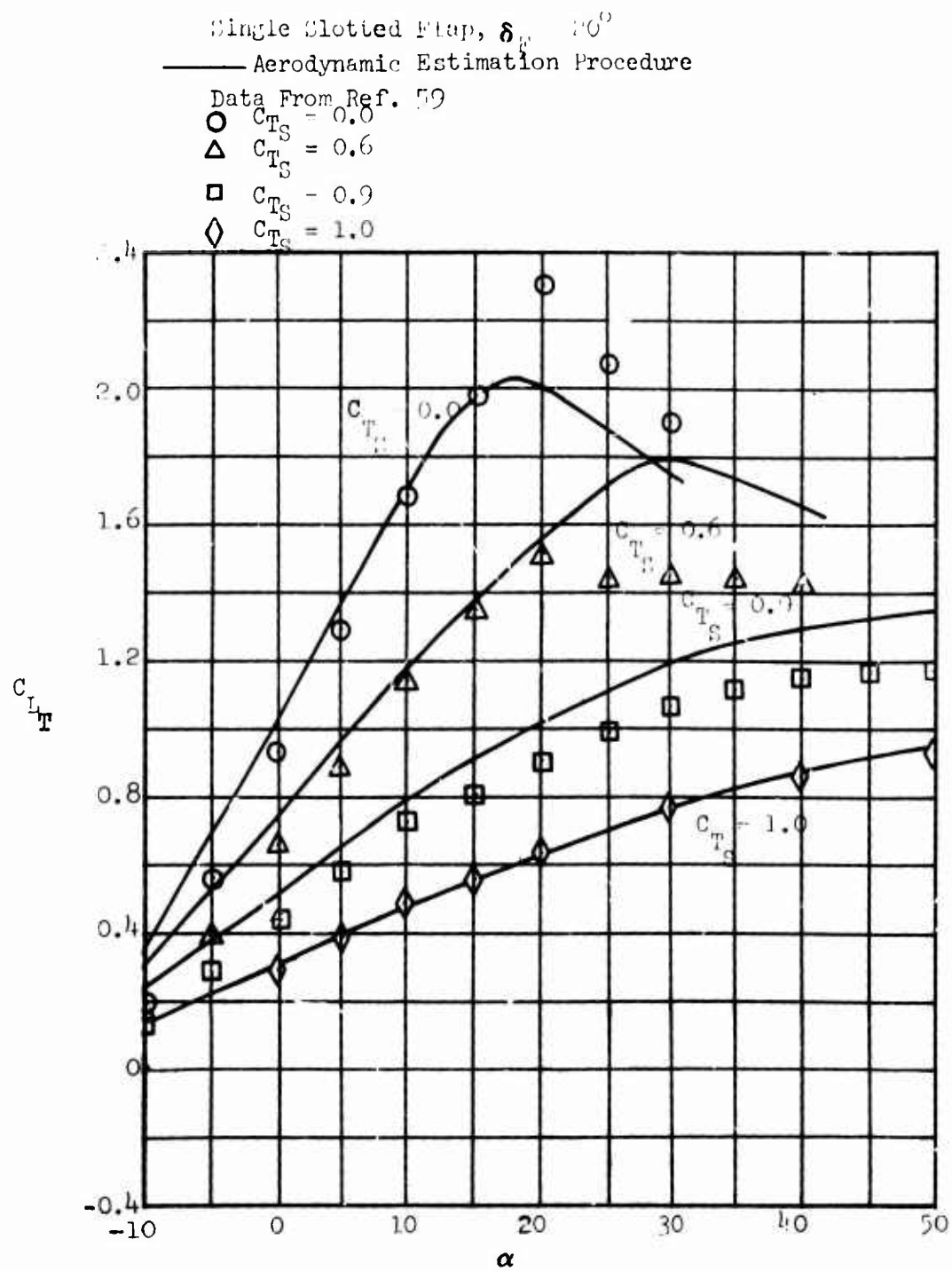Figure 54. Total Pitching Moment Versus Wing Angle of Attack, $\delta_f = 50^\circ$.

114
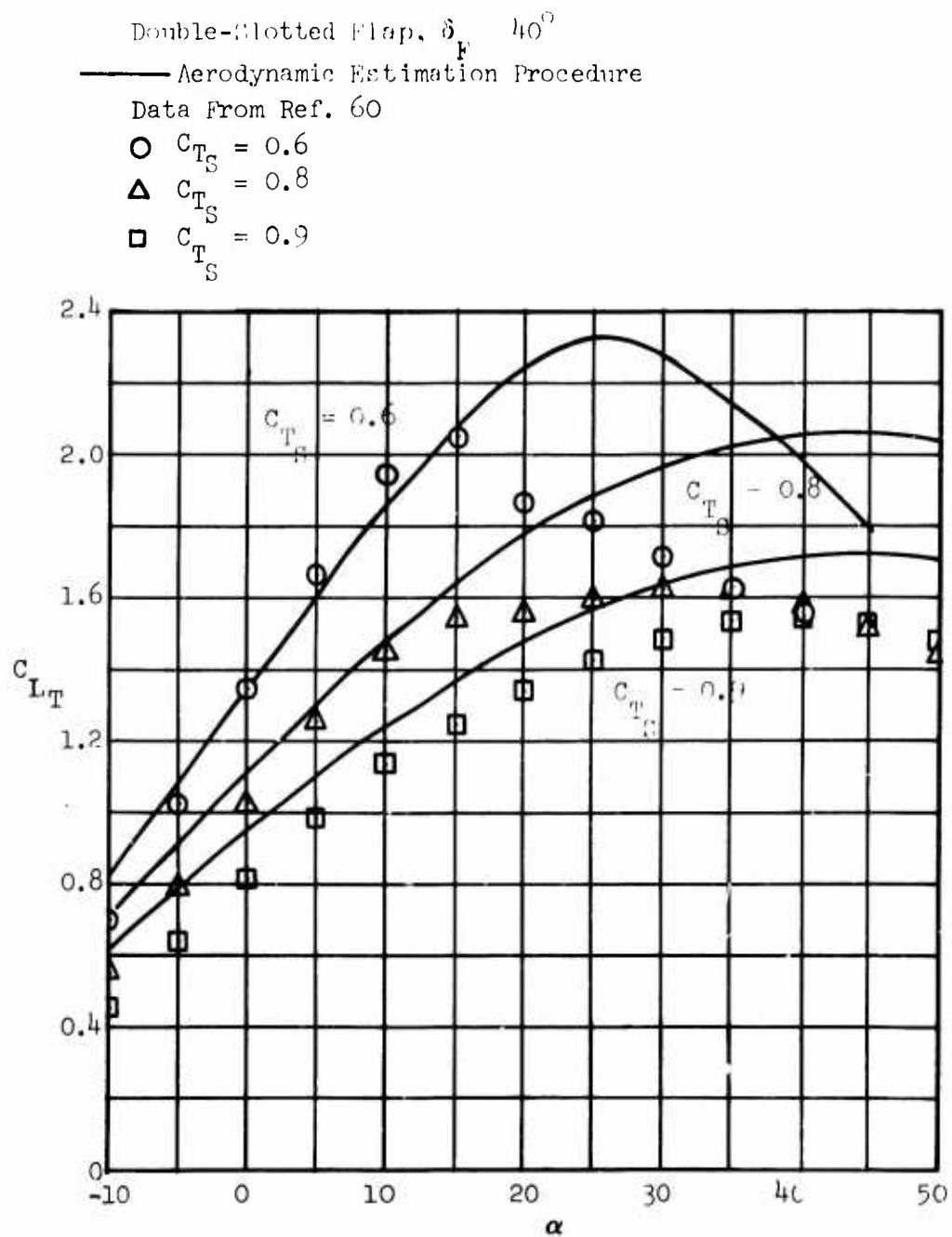
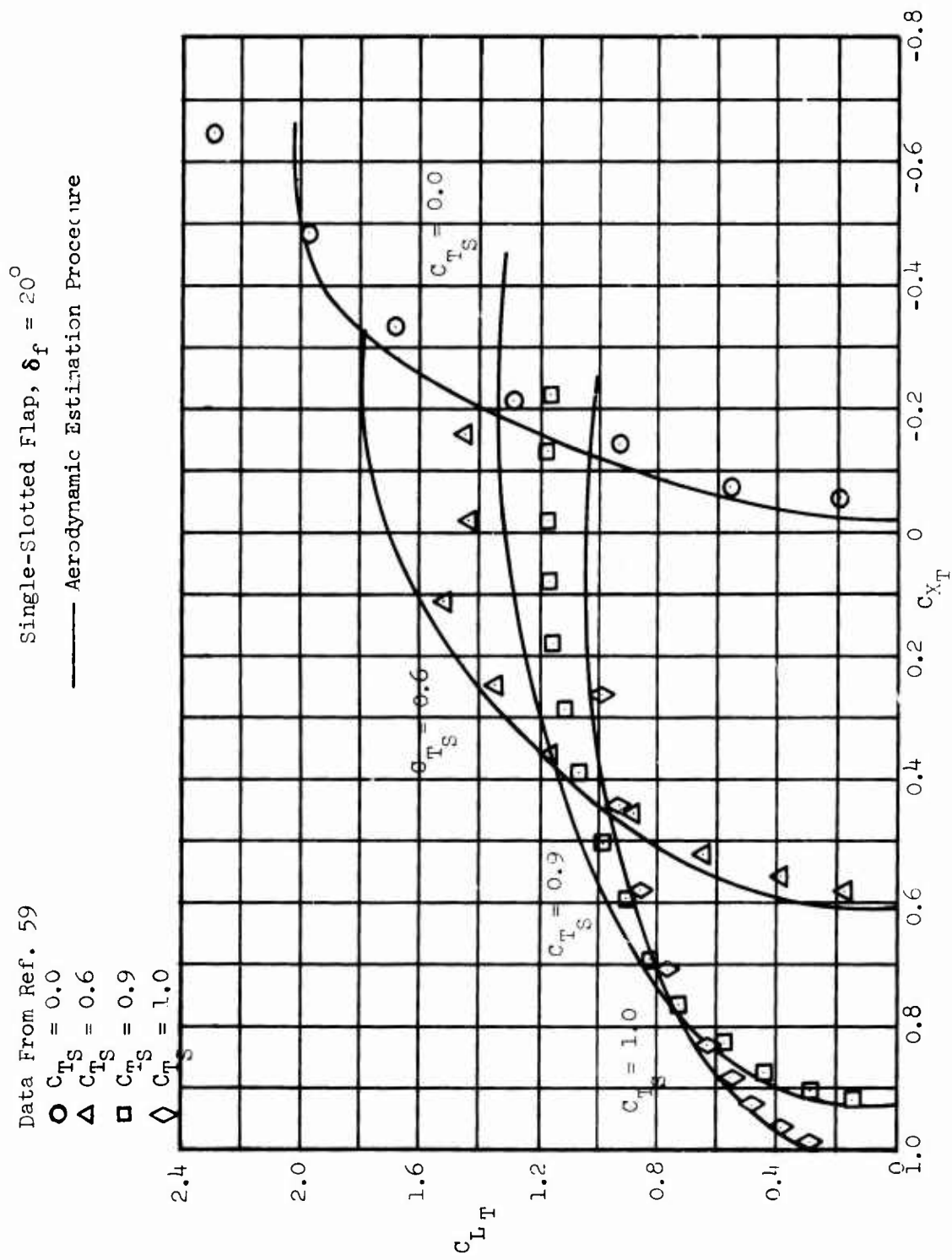Figure 55. Total Lift Coefficient Versus Wing Angle of Attack, $\delta_f = 40°$.
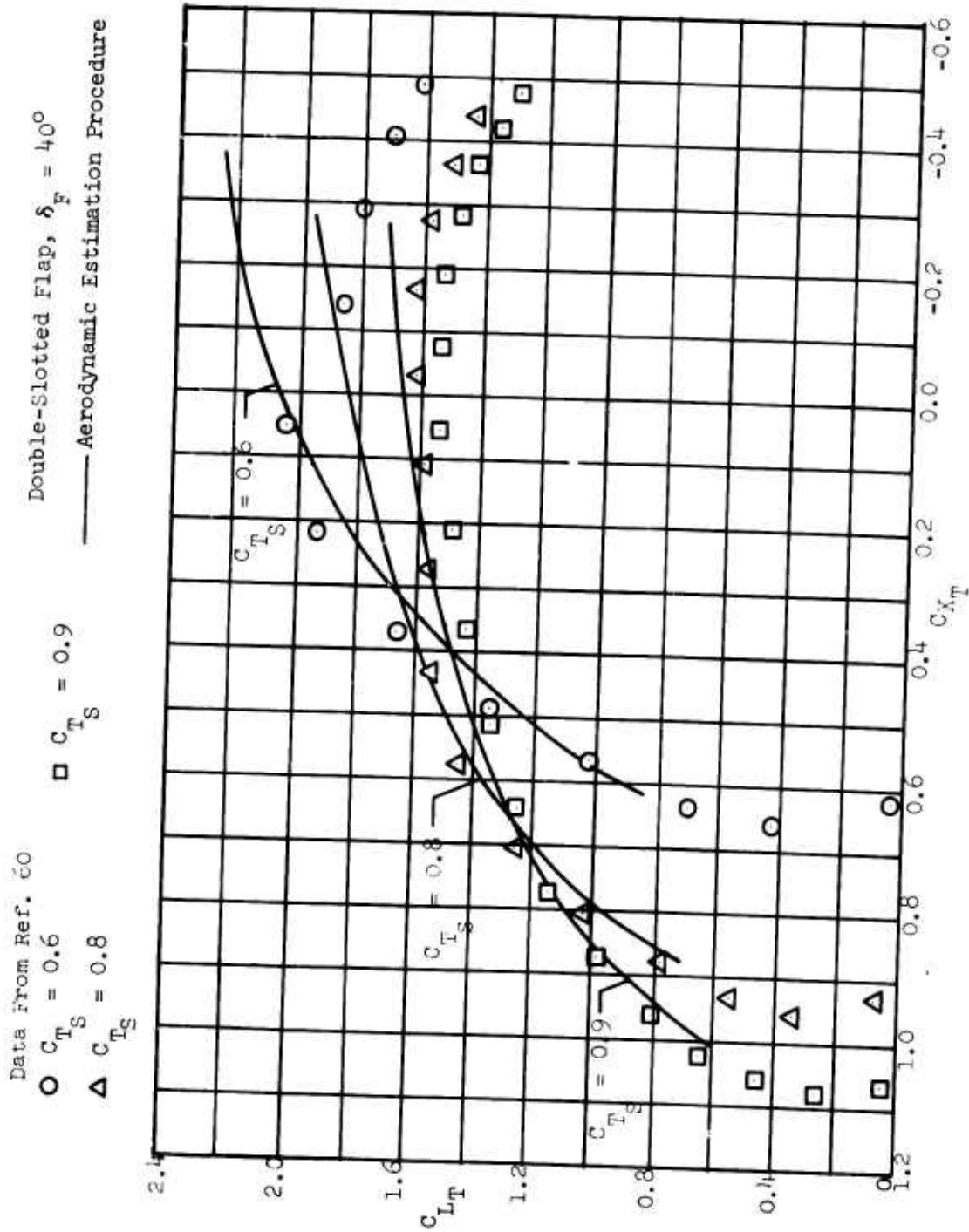
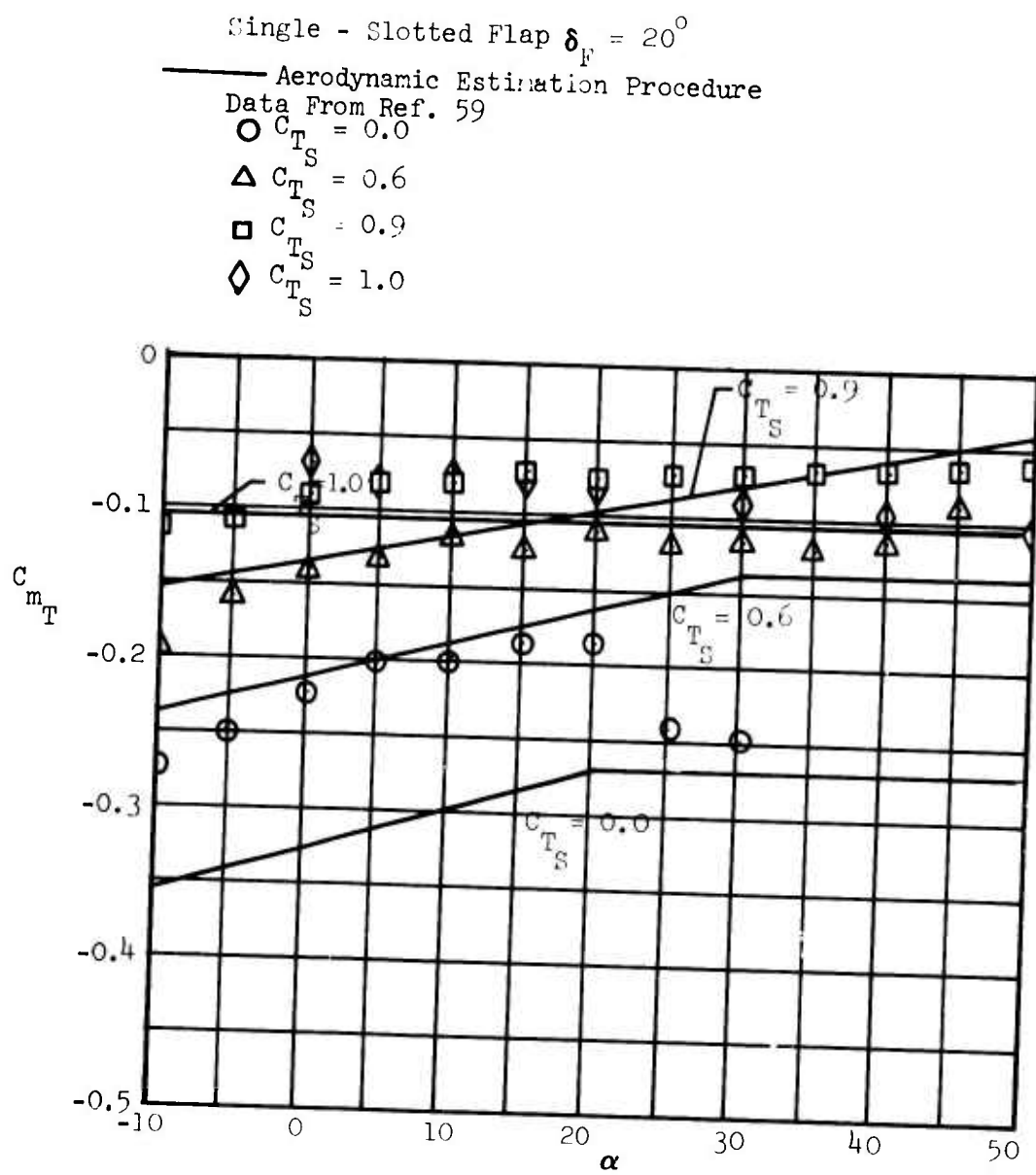Figure 56. Total Lift Coefficient Versus Total Drag Coefficient, $\delta_f = 40°$.

116

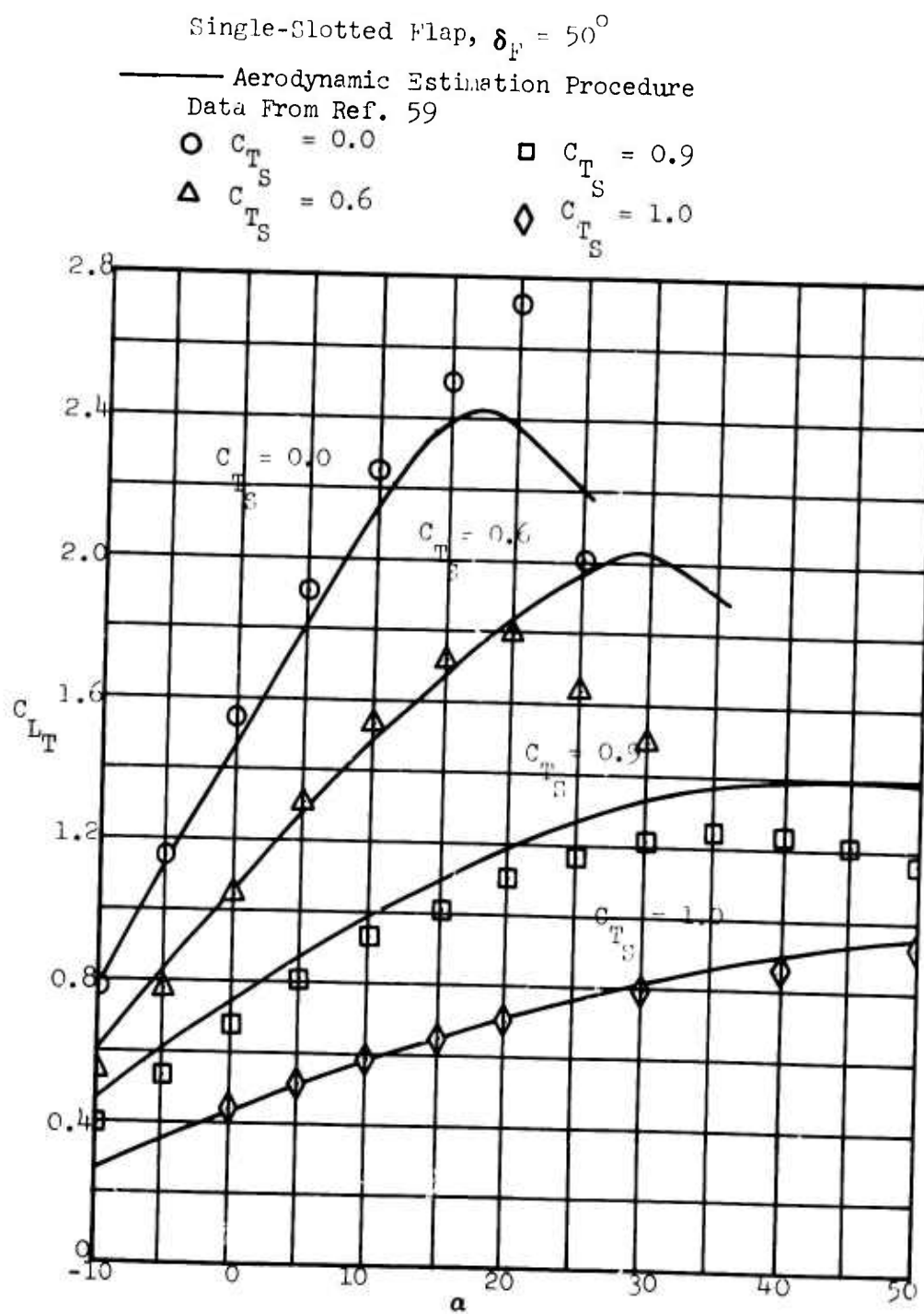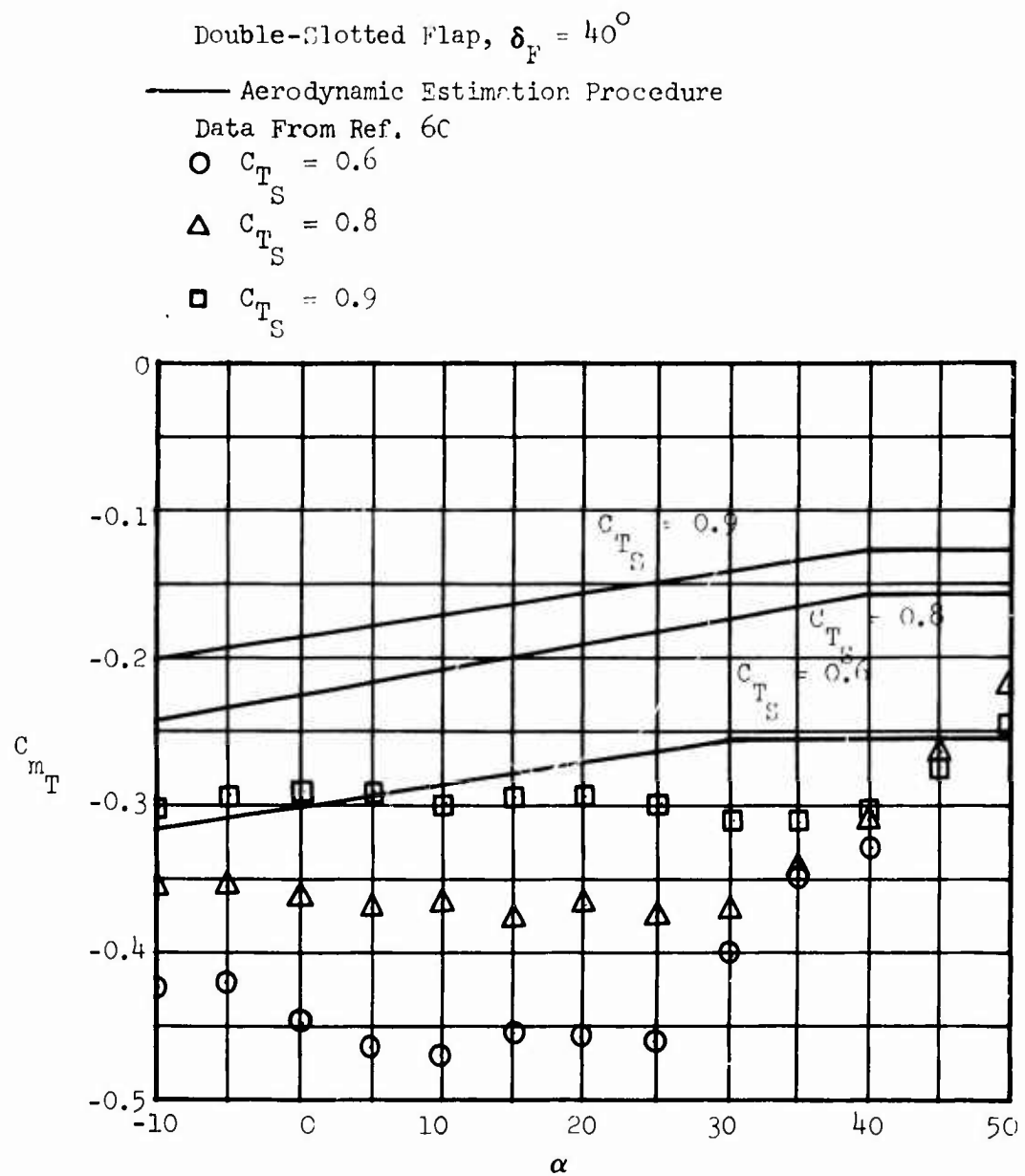Figure 57. Total Pitching Moment Versus Wing Angle of Attack, $\delta_f = 40°$.
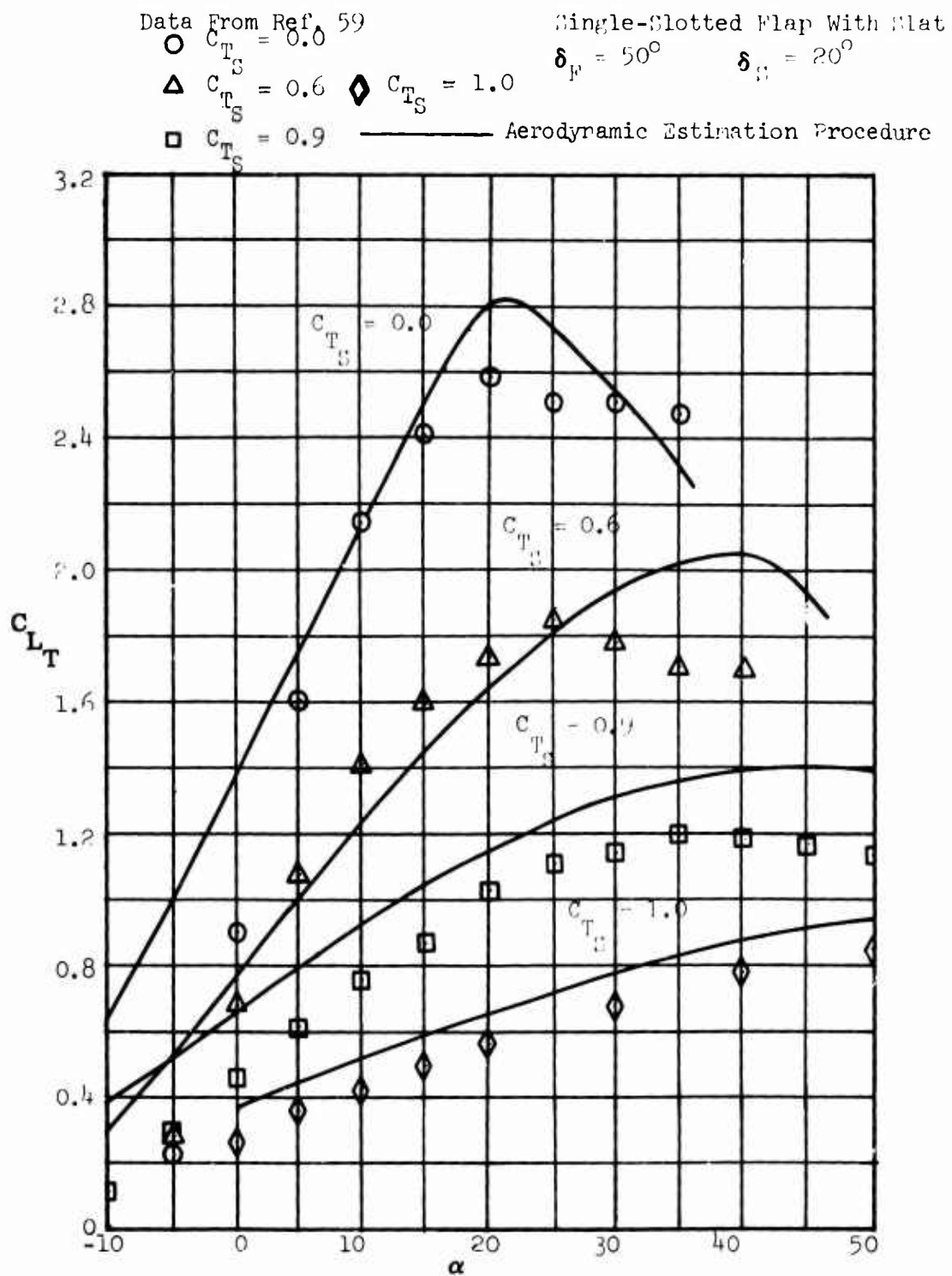
Figure 58. Total Lift Coefficient Versus Wing Angle of Attack, $\delta_f = 40°$, $\delta_s = 20°$.

118
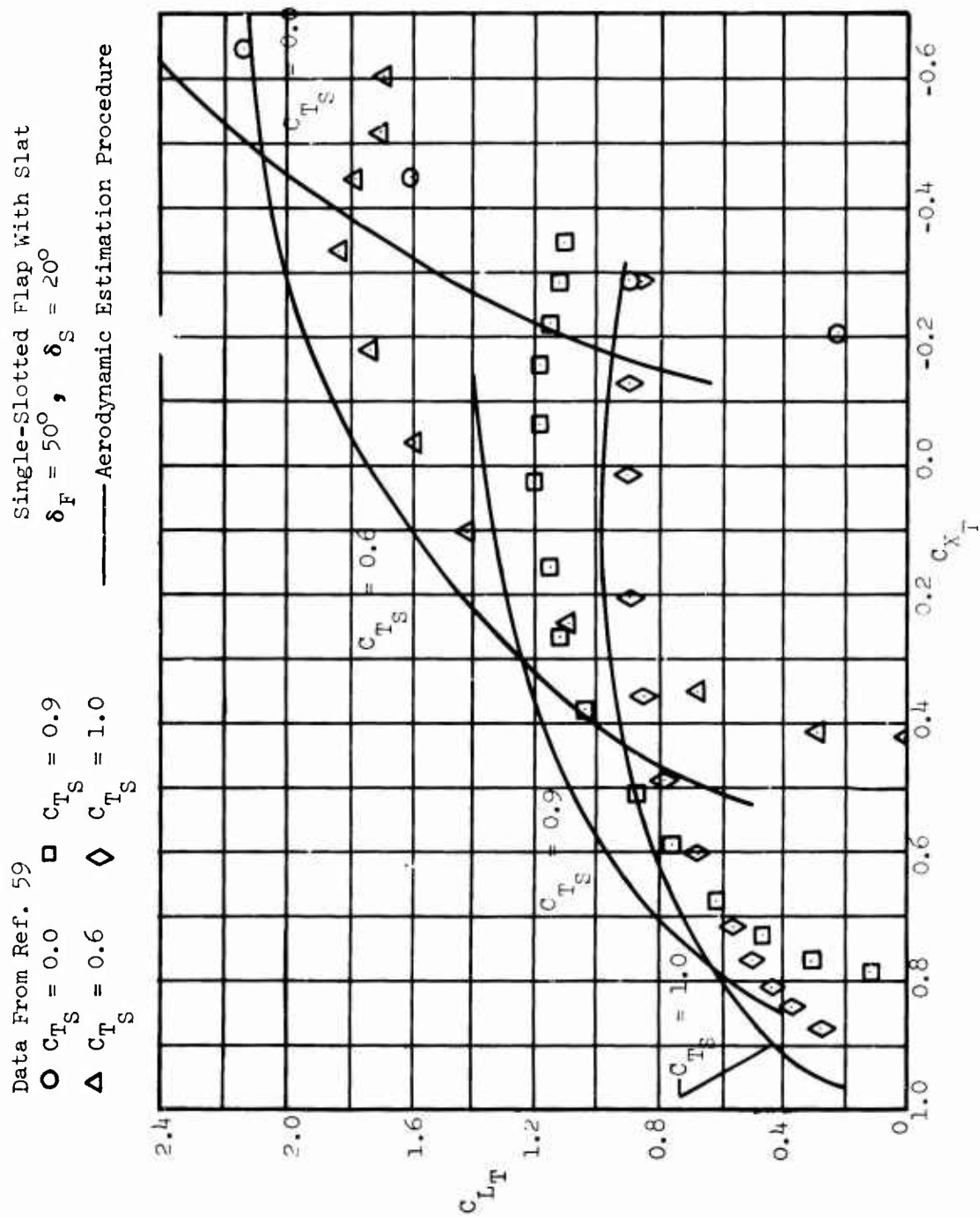
Figure 59. Total Lift Coefficient Versus Total Drag Coefficient, $\delta_f = 40°$, $\delta_s = 20°$

Single Slotted Flap With Slat
——— Aerodynamic Estimation Procedure
Data From Ref. 59
O $C_{T_S} = 0.0$
△ $C_{T_S} = 0.6$
□ $C_{T_S} = 0.9$
◊ $C_{T_S} = 1.0$
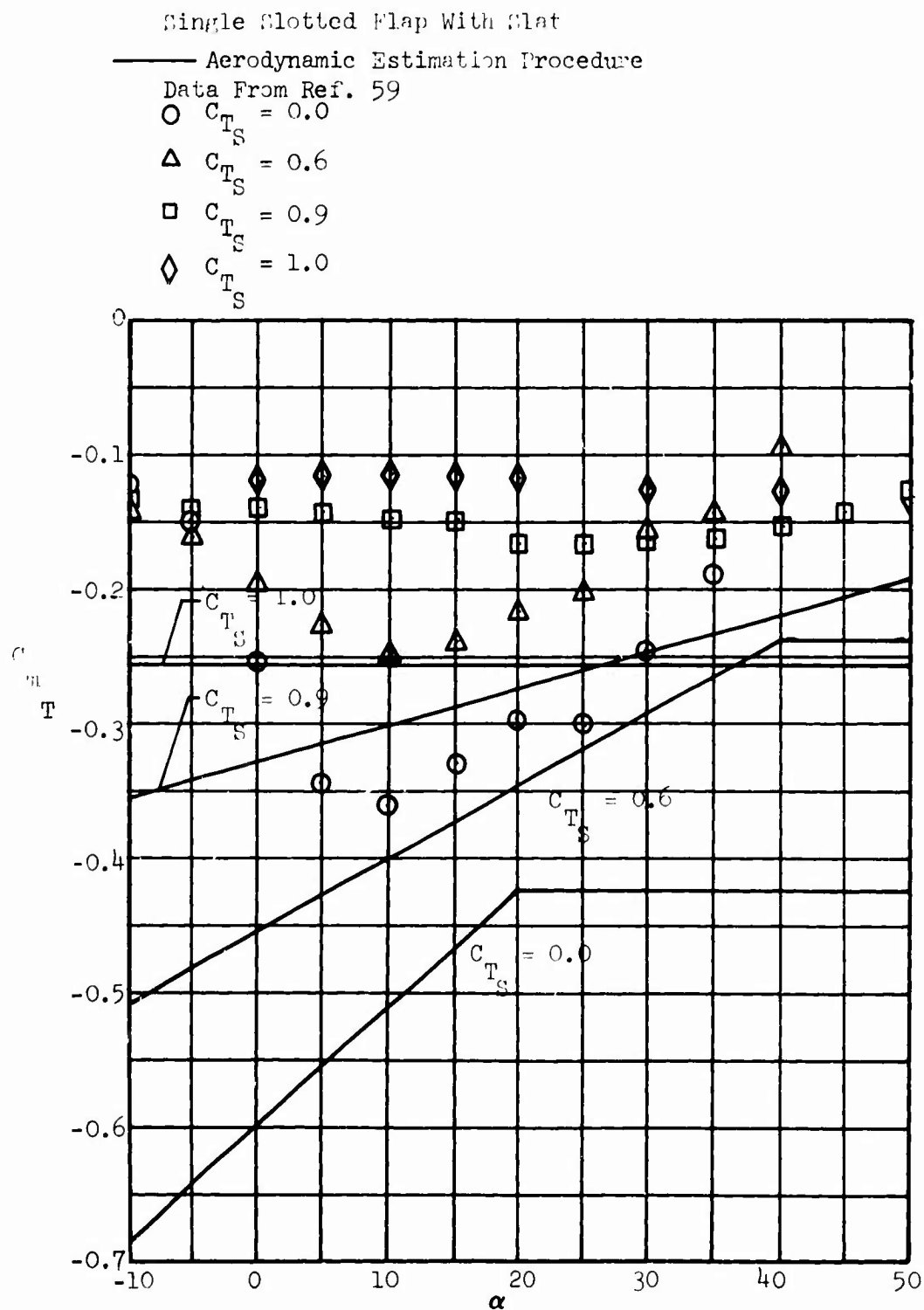
Figure 60. Total Pitching Moment Versus Wing Angle of Attack, $\delta_f = 40°$, $\delta_s = 20°$.

120

10.0 PERFORMANCE PROGRAM TO CALCULATE TAKEOFF, LANDING AND TRANSITION OF V/STOL AIRCRAFT

The digital computer program described herein was developed to evaluate the effect of various high-lift systems on takeoff, landing and transition performance. Complete sets of program listings, program flow charts, and input data for a sample case are included in Reference 61. The summary equations in Sections 4.0 and 5.0 have been programmed (Reference 45) to supply aerodynamic data input to the performance program.

10.1 EQUATIONS OF MOTION

The equations used in this calculation system are derived for an earth axis motion system (ground speed, vertical speed). Acceleration in the vertical speed direction is given by

$$A_Z = (g/W) \left[\text{Lift} \cos \gamma + \text{Drag} \sin \gamma - W - (EQ)T \sin (\alpha_w + i_T + \gamma) \right] \tag{158}$$

and acceleration in the ground speed direction is given by

$$A_X = (g/W) \left[\text{Drag} \cos \gamma - \text{Lift} \sin \gamma - (EQ)T \cos (\alpha_w + i_T + \gamma) \right] + A_Z \mu \tag{159}$$

where A_X = horizontal acceleration

A_Z = vertical acceleration

Drag = summation of drag and thrust forces along the free-stream velocity vector (positive forward)

EQ = flight condition index

= -1.0 for hovering or descending flight
= +1.0 for thrust reversal
= 0 for all other conditions

g = acceleration due to gravity

i_T = thrust incidence

Lift = summation of lift and thrust forces perpendicular to the free-stream velocity vector (positive up)

T = thrust

W = weight

121

α_w = wing angle of attack

γ = flight path angle

μ = coefficient of friction (ground roll portions only)

The forces and angles are shown in Figure 61.
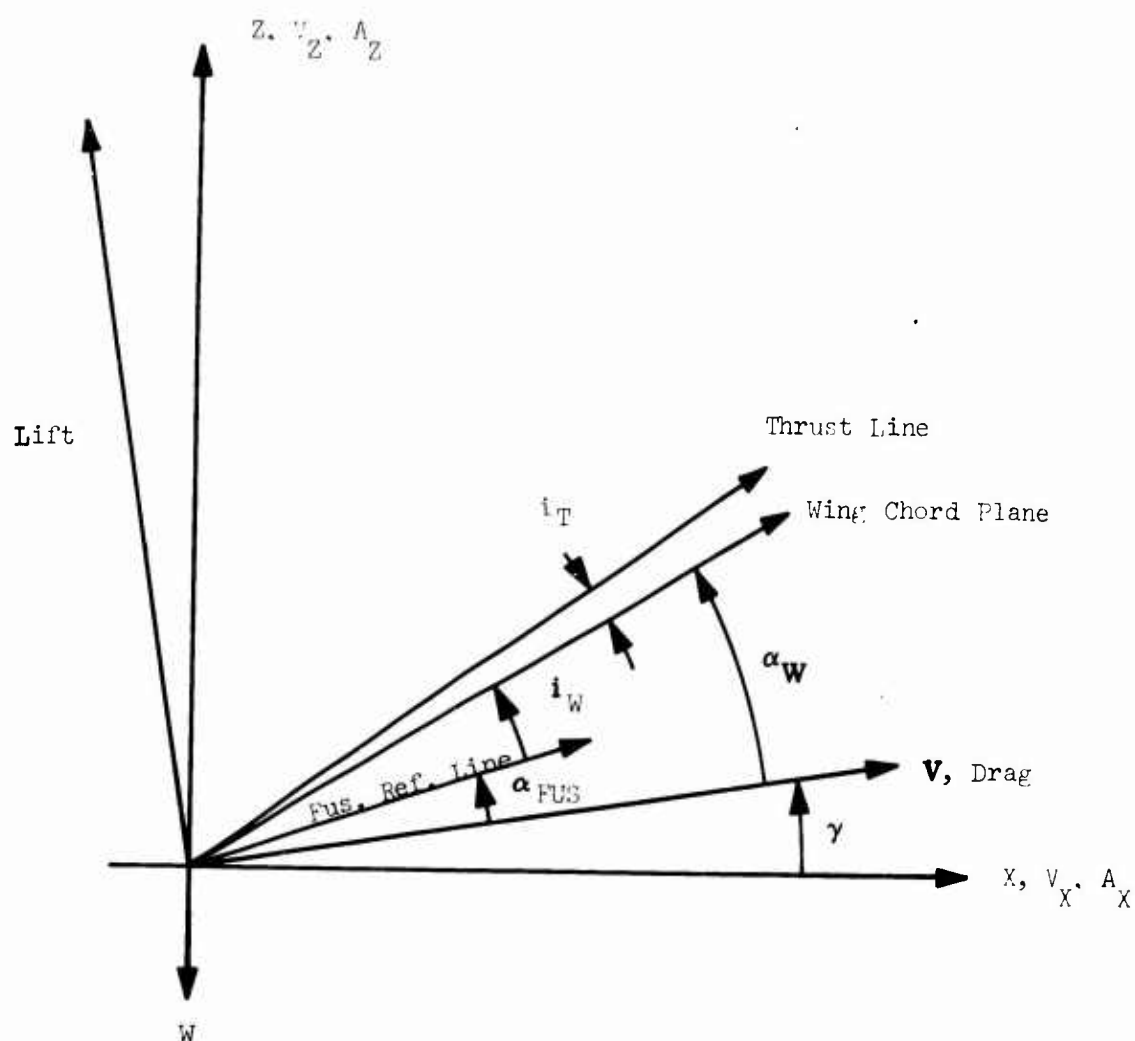
Figure 61. Force and Angle Diagram for Equations of Motion.

10.2 PROGRAM DESCRIPTION

The primary objectives during the development of this calculation system were:

1. Minimum input data generation

2. Reasonable piloting techniques

3. Ability to refine the subroutines with minimum interfacing problems

These objectives were satisfied by designing a modular program with the five following functional groups:

1. The main program (direct) is the executive routine and controls the reading of inputs, initializing weights, altitudes, and temperatures, and the executing of the configuration subprograms for a given weight, altitude and temperature matrix.

2. The configuration subprograms are designed to "drive" and monitor the particular calculation desired, e.g., deflected-slipstream short takeoff, tilt-wing vertical landing.

3. The physical data subroutines are used to store and retrieve aerodynamic data, propulsion characteristics, and atmospheric properties. In addition, an aerodynamic subroutine calculates accelerations acting on the aircraft.

4. The general use subroutines provide calculations or timing cues used in one or more of the configuration subroutines.

5. The support subroutines do table look-ups and evaluate curve fits.

The program can perform calculations for deflected-slipstream takeoffs and landings and tilt-wing short takeoffs, vertical takeoffs, vertical landings, and transitions. Tilt-prop V/STOL and tilt-wing short landing calculation subprograms have not been included in this system. Provisions have been made, however, in the physical data and general use subroutines to support calculations for any propeller-driven V/STOL aircraft.

In addition to the calculation system, a trimming program was written. A schematic of the program flow and structure is given in Figure 62.
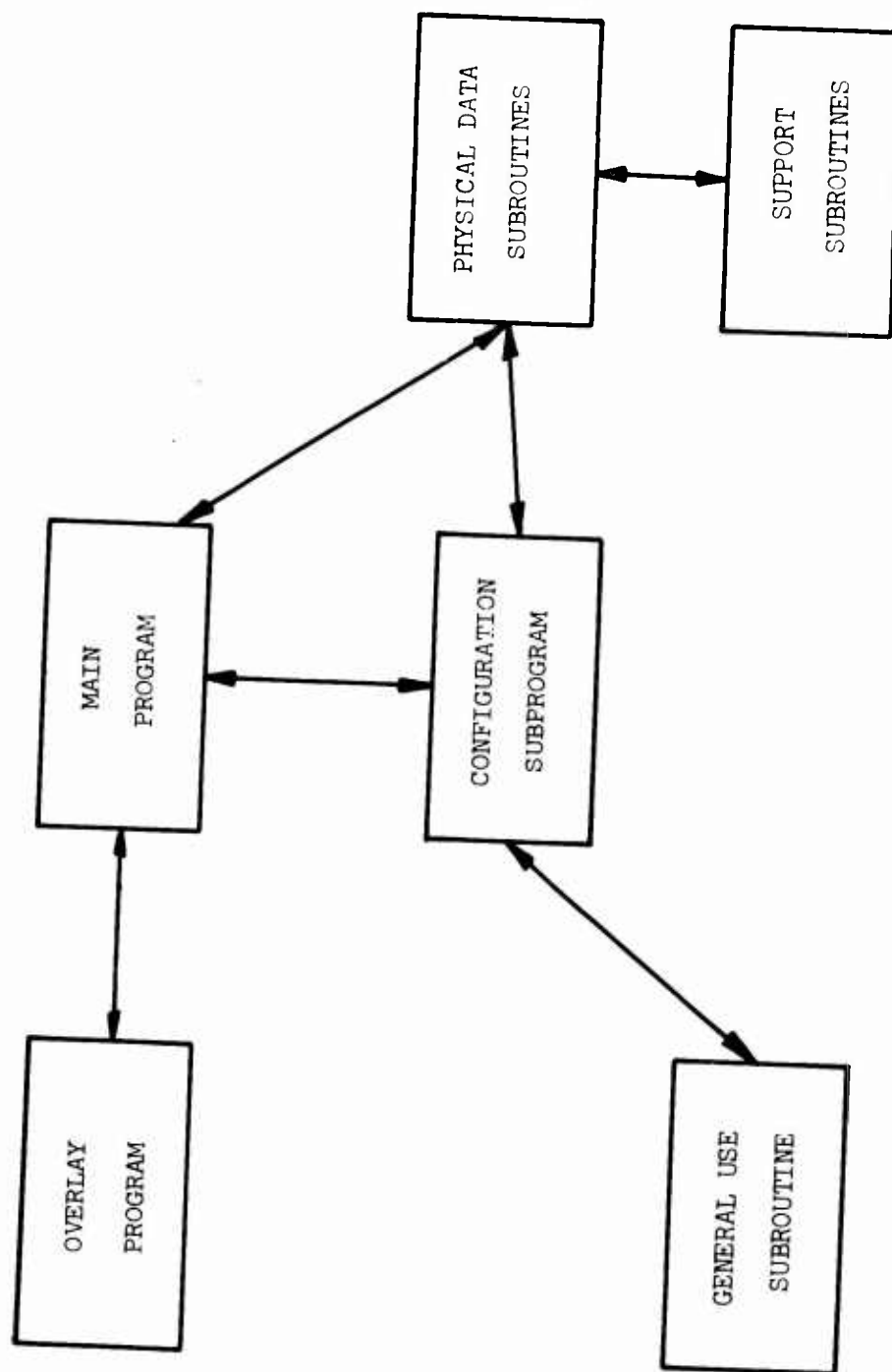
Figure 62. Performance Program Structure by Functional Group.

10.3 SIMPLIFYING ASSUMPTIONS

The major assumptions made to simplify the calculations and trajectories are listed by subroutine or program name. The assumptions reflect reasonable piloting technique and reduce a three-degree-of-freedom problem to a more manageable two-degree-of-freedom problem. In all cases the assumptions can be eliminated by substituting a more refined subroutine for the routine presently in the system.

10.3.1 Main Program

The assumptions in the main program are:

1. The tail-off pitching moment is trimmed using the expression

$$C_{L_{TRIMMED}} = C_{L_{TAIL-OFF}} + \frac{C_{m_{TAIL-OFF}} + C_{l_{TAIL-OFF}}(0.25-CG)}{\ell_{H/\bar{c}}}$$

(160)

   where $\ell_{H/\bar{c}}$ is the nondimensional tail arm.

   CG is the location of the center of gravity in relation to the mean aerodynamic chord.

   $C_{m_{TAIL-OFF}}$ is referenced to the 0.25 $\bar{c}$ station.

2. Incremental drag due to trimming is several orders of magnitude smaller than the total aircraft drag and is considered to be negligible.

3. All trimming on the tilt-wing configuration is with the tail rotor.

4. Atmospheric properties are not recomputed during the problem. Due to the small altitude changes encountered, runway altitude and ambient temperature are used in all density expressions.

5. Aircraft gross weight is not reduced as fuel is used. The time involved in any of the maneuvers is short, and even at maximum power, fuel used is less than 0.5% of the aircraft gross weight.

6. Zero wind conditions are assumed by all routines in this system.

125

10.3.2 Configuration Subprograms

The assumptions in the configuration subprograms are:

Deflected-Slipstream Short Landing — The trajectory assumed for this configuration is represented in Figure 63.

1. "Start at the Obstacle" — Airspeed at this point is a percentage of power-on stall speed. Sink speed is an input. Both airspeed and sink speed are held constant to touchdown.

2. "Touchdown" — If the aircraft attitude at touchdown will cause a "nosewheel-first" landing, the aircraft is instantaneously rotated to ground attitude at touchdown.

3. "Braking Devices On" — Braking and rolling coefficients of friction are not a function of velocity.

Deflected-Slipstream Short Takeoff — The trajectory assumed for this configuration is represented in Figure 64.

1. "Start Takeoff" — The entire maneuver is performed at a constant power setting. Rolling coefficient of friction is not a function of velocity.

2. "Rotation and Lift-Off" — Rotation speed is a percentage of power-on stall speed. The aircraft is rotated at a constant angular rate until the maximum angle of attack is attained.

3. "Clear the Obstacle" — If the maximum angle of attack is attained before the obstacle height is reached, the maximum angle is held over the obstacle.

Tilt-Wing Short Takeoff — The trajectory assumed for this configuration is represented in Figure 65.

1. "Start Takeoff" — Wing tilt angle is set at the beginning of the maneuver. Flap deflection is a sine function of wing tilt angle (e.g., wing tilt = 0, flap = 0; wing tilt = 45 deg, flap is at the maximum deflection; wing tilt = 90 deg, flap = 0). Coefficient of rolling friction is not a function of velocity.

2. "Airborne" — Fuselage angle of attack and wing tilt angle are constant throughout the maneuver. Tail rotor thrust is in the lift direction for all wing tilt angles. (This is a predetermined percentage of total power as a function of tilt angle and is used to replace the trim equation of 10.3.1).

1. START AT THE OBSTACLE

2. TOUCHDOWN

3. BRAKING DEVICES ON

4. STOP
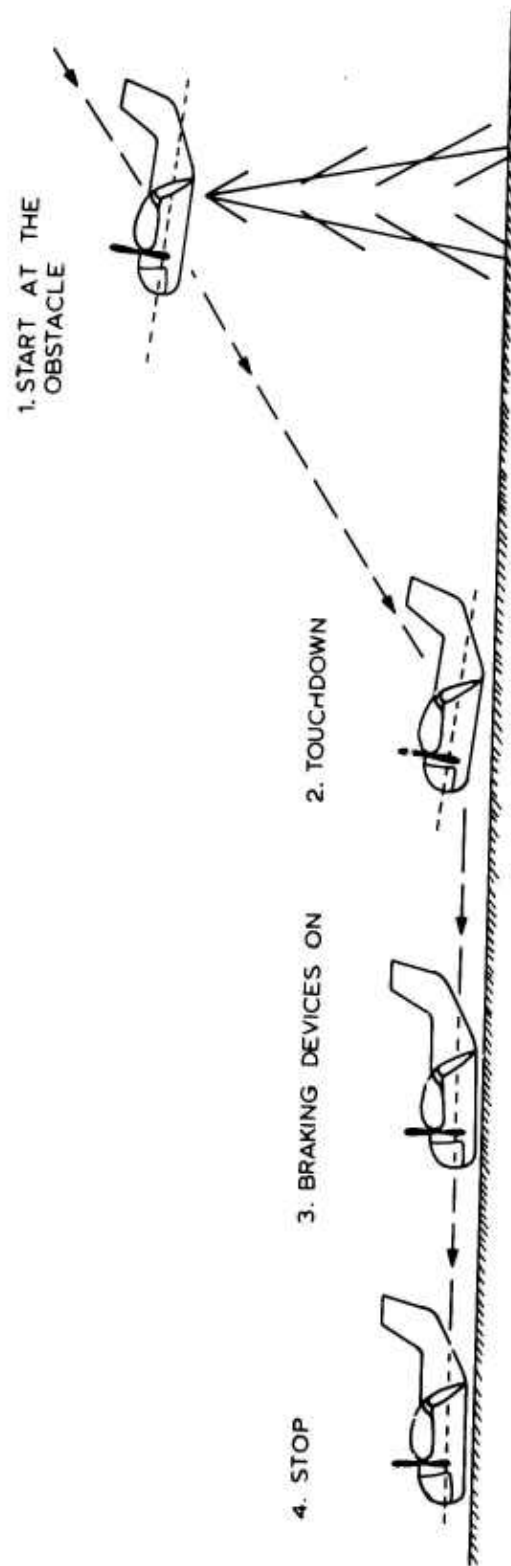
Figure 63. Illustration of the Deflected-Slipstream Short Landing.

127

3. CLEAR THE OBSTACLE

2. ROTATION & LIFT-OFF
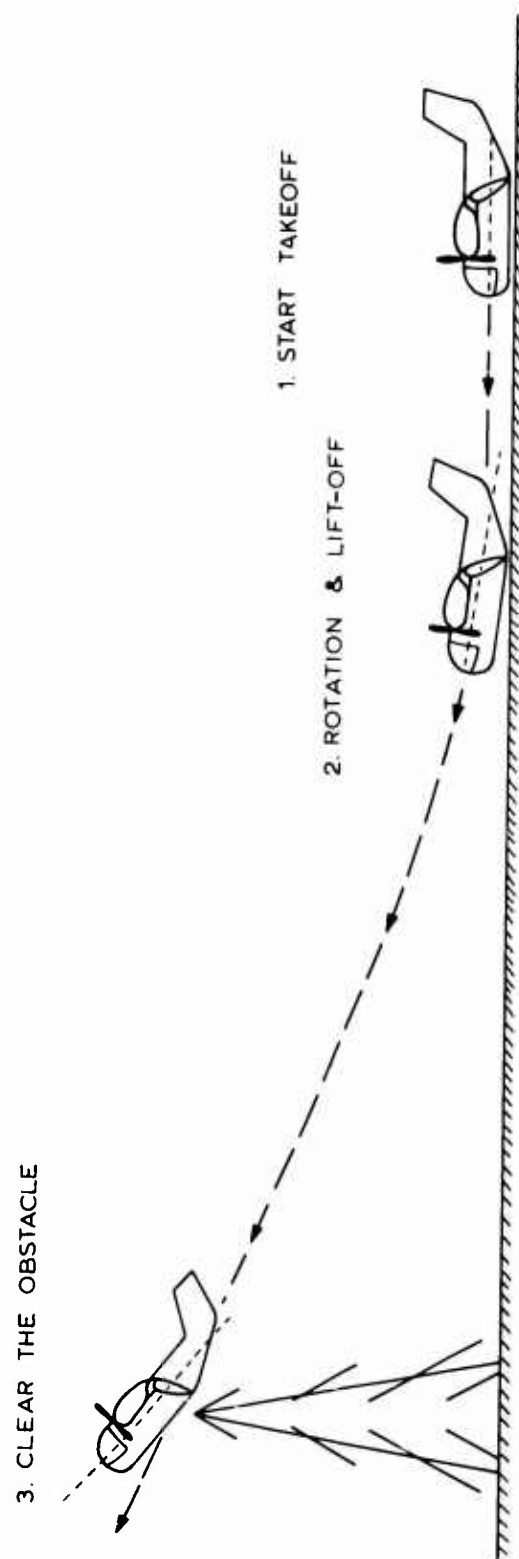
1. START TAKEOFF

Figure 64. Illustration of the Deflected-Slipstream Short Takeoff.

128

1 START TAKEOFF
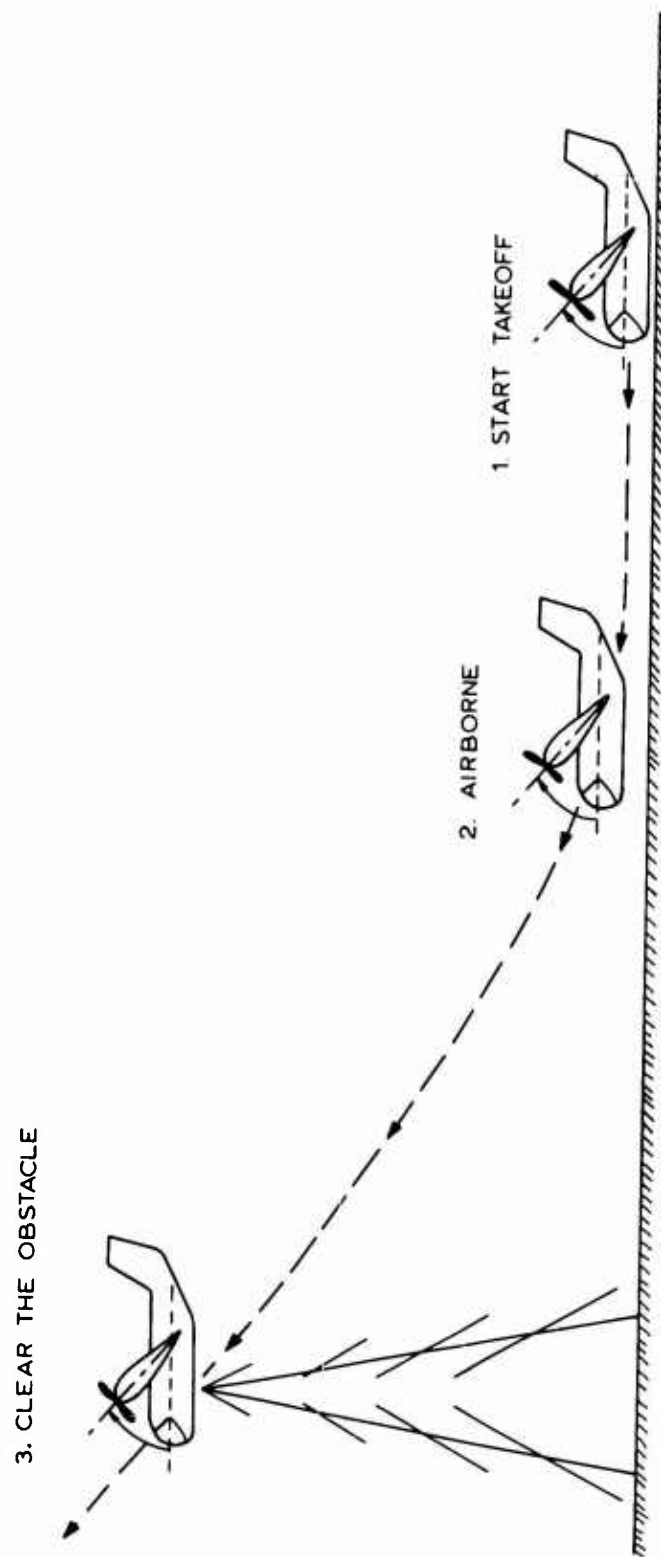
2. AIRBORNE

3. CLEAR THE OBSTACLE

Figure 65. Illustration of the Tilt-Wing Short Takeoff.

129

3. "Clear the Obstacle" — The problem is terminated at the obstacle. Once the aircraft is above the obstacle, forward speed is sufficient for an easy transition to conventional flight.

Tilt-Wing Vertical Landing — The vertical landing trajectory is shown in Figure 66. To attempt a vertical landing, the aircraft must have a thrust to weight ratio greater than 1.07 to insure an adequate maneuver margin.

1. "Conventional Flight" — The maneuver is started at a steady-state speed which is a percentage of power-off stall speed.

2. "Transition" — The wing is tilted at a constant angular rate. Flap deflection is a sine function of wing tilt angle. Zero flight path angle is maintained throughout the transition. Tail rotor thrust is in the lift direction for all wing tilt angles.

3. "Hover" — Maximum wing angle of attack during this maneuver is 90 degrees plus the angle of zero lift.

4. "Touchdown" — Input sink speed is maintained with throttle control during the vertical descent.

Tilt-Wing Vertical Takeoff — The vertical takeoff trajectory is shown in Figure 67. To attempt a vertical takeoff, the aircraft must have a thrust to weight ratio greater than 1.05 to insure an adequate maneuver margin.

1. "Start Takeoff" — Takeoff is initiated at thrust equals weight. The throttle is then advanced to maximum thrust.

2. "Vertical Ascent" — Fuselage pitch angle is held constant during this phase. Tail rotor thrust is in the lift direction for all wing tilt angles. This phase terminates when a minimum rate of climb and a minimum altitude are exceeded.

3. "Start Transition - Pitch Fuselage Down" — The fuselage nose is pitched down to a preset angle to make the transition to conventional flight quicker.

4. "Transition - Tilt Wing Down" — The wing is tilted down at a constant angular rate. Flap deflection is a sine function of wing tilt angle.

5. "Conventional Flight" — The problem terminates when wing tilt angle reaches zero.
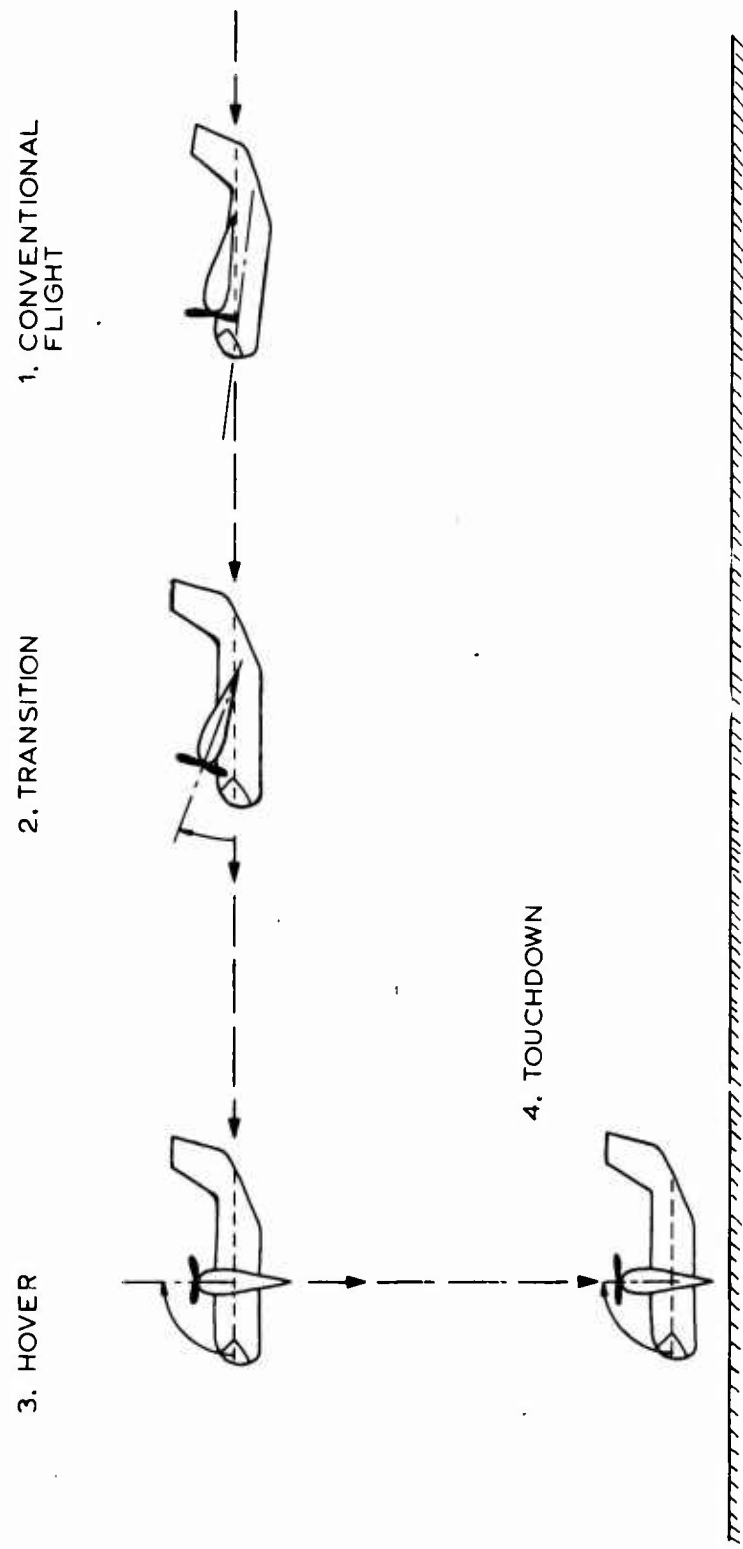
130

1. CONVENTIONAL FLIGHT

2. TRANSITION

3. HOVER

4. TOUCHDOWN

Figure 66. Illustration of the Tilt-Wing Vertical Landing.

131
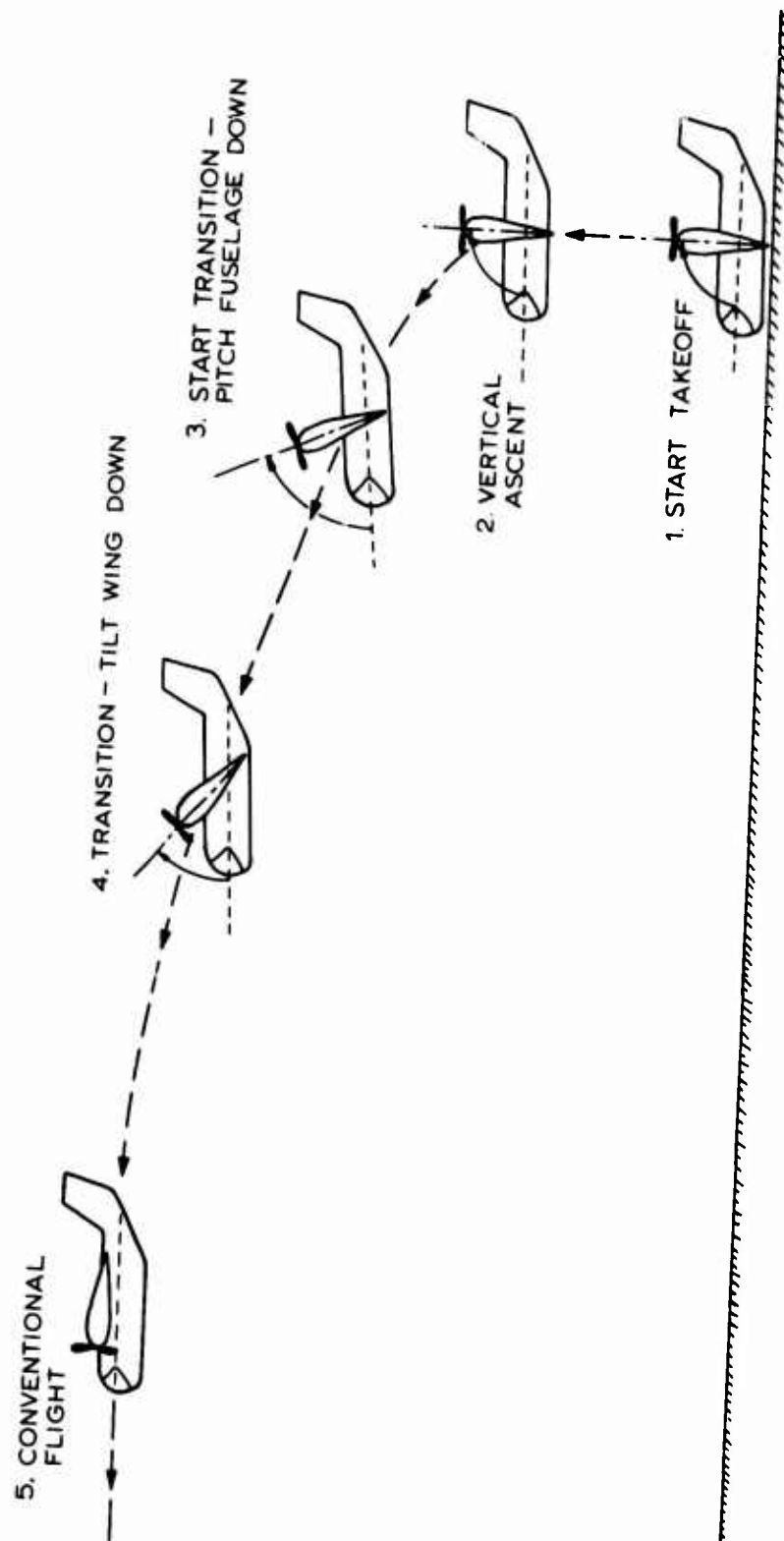
Figure 67. Illustration of the Tilt-Wing Vertical Takeoff.

5. CONVENTIONAL FLIGHT

4. TRANSITION – TILT WING DOWN

3. START TRANSITION – PITCH FUSELAGE DOWN

2. VERTICAL ASCENT

1. START TAKEOFF

10.3.3 Physical Data Subroutines

The ass'mptions in the physical data subroutines are:

Aerody:amic Data Subroutine

1. When the aircraft is in a hovering or vertical descent mode ($C_{T_S} = 1.00$), C_L and C_D equal zero.

2. Aerodynamic coefficients include both indirect and direct thrust effects.

3. For reverse thrust, wing lift equals zero.

Atmospheric Properties Subroutine

The standard day temperature lapse rate is valid for all temperature/altitude combinations to be considered.

Propulsion Characteristics Subroutine

1. One propeller per engine.

2. A constant percentage of optimum propeller efficiency is valid for the speed regime considered.

3. For tilt-wing aircraft, tail rotor power extraction is a function of wing tilt angle only.

4. Input data are valid throughout the altit..de change during the maneuver.

5. Axial inflow to the propeller. A sample calculation was made with oblique inflow and compared with the axial inflow case. The difference was negligible.

10.3.4 General Use Subroutines

The assumptions in the general use subroutines are:

Subroutine BRAKE (provides timing cues for ground roll portion of short landings)

1. Aircraft nose is rotated to a three-point attitude at a constant rate.

2. Brake application occurs 1 second after touchdown.

3. To use reverse thrust, the engines are throttled back to idle power before reverse thrust is initiated.

4. The wing is tilted down at a constant rate after touchdown for all tilt-wing and tilt-prop aircraft.

133

Integration Subroutine

Trapezoidal rule integration with a small time step (approximately 0.25 sec) is sufficiently accurate.

Power-On Stall Speed Convergence

$C_{L_{MAX}}$ occurs at an angle of attack determined by pilot comfort rather than aerodynamic separation.

134

11.0 CONCLUSIONS

1. The procedures to predict the two-dimensional aerodynamic characteristics of high-lift devices furnish reasonable estimates, generally within 10 percent of experimental results, that can be used in the span load program. The trend from General Dynamics experimental data indicates that the maximum lift levels from NACA data are approximately 10 to 20 percent lower. This may be attributed to the General Dynamics testing technique which utilizes side-wall blowing to eliminate adverse wall boundary layer interference effects.

2. The program initiated at Convair to develop a more basic approach to the problem of estimating the lift and longitudinal force coefficients was well justified. It is considerably less limited than existing empirical methods in that it requires only two-dimensional data for application to general configurations. The procedures for predicting lift and longitudinal force coefficients of a wing-flap combination give satisfactory results at all thrust coefficients. However, the procedures for predicting pitching moment coefficients result in erratic correlations for flaps-deflected cases.

3. The entire task of correlating wind tunnel data that have been corrected for wall effects with actual flight test conditions could not be accomplished due to the lack of a good set of flight test data for comparison. The evaluation of tunnel wall effects indicated that currently available correction procedures for lift and drag yield erroneous results and should not be applied.

4. The complexity of the performance program made numerous assumptions and capability restrictions desirable. For example, the equations of motion were reduced to two dimensions (i.e., no pitch dynamics), and several terms, such as pitch rates, wing tilt angular rates, and pilot braking response time, were used as predetermined inputs. These assumptions were made to expedite the development of the system; however, the accuracy of the methods employed is sufficient to reflect the impact of high-lift devices on V/STOL aircraft. The program is a viable tool for performance estimation.

135

12.0 RECOMMENDATIONS

1. The problems associated with predicting the aerodynamic forces acting on a wing immersed in a slipstream should be investigated further. To improve the basic procedures, it is necessary that (1) additional correlations of pitching moments be made with experimental data to develop improved empirical factors for large chord ratio flaps, (2) methods be developed to incorporate the pronounced nonlinear characteristics of leading edge devices at low angles of attack, (3) the downwash estimating procedure be programmed for digital computer application and correlations be made with experimental data, and (4) tilt-prop configuration methodology be developed and incorporated into the aerodynamic and performance programs.

2. Jet flap and boundary layer control devices should be investigated so that methods can be developed to describe the effects of these devices on a wing immersed in a slipstream.

3. A study should be performed to define a wind tunnel/flight test program to correlate V/STOL vehicle aerodynamic characteristics.

13.0 LITERATURE CITED

1. Abbott, I. H., and Von Doenhoff, A. E., THEORY OF WING SECTIONS, New York, Dover Publications, Inc., 1959.

2. Ellison, D. E., and Malthan, L., USAF STABILITY AND CONTROL DATCOM, McDonnell Douglas Corporation, Douglas Aircraft Division, Long Beach, California, August 1968.

3. Anon, LIFTING CAPABILITIES OF WINGS WITH AND WITHOUT HIGH LIFT DEVICES, Martin Engineering Report 8055, Martin Aircraft, 1956.

4. Young, A. D., THE AERODYNAMIC CHARACTERISTICS OF FLAPS, RAE Report Aero 2185, Royal Aeronautical Establishment, Farnborough, England, 1947.

5. Hebert, J., PROCEDURE FOR ESTIMATING THE AERODYNAMIC CHARAC-TERISTICS OF TWO-DIMENSIONAL PASSIVE HIGH LIFT DEVICES, TN-70-AVLABS-07, Convair Division of General Dynamics, San Diego, California, 1970.

6. Glauert, H., THEORETICAL RELATIONSHIPS FOR AN AIRFOIL WITH A HINGED FLAP, ARC R & M 1095, England, 1927.

7. Cahill, J. F., SUMMARY OF SECTION DATA ON TRAILING-EDGE HIGH-LIFT DEVICES, NACA TR 938, National Advisory Committee for Aeronautics, Washington, D.C., 1949.

8. Abzug, M. J., ESTIMATION OF THE LIFT AND MOMENT PARAMETERS OF LEADING EDGE FLAPS, Journal of The Aeronautical Sciences, September 1955, pp. 655-656.

9. Roshko, A., COMPUTATION OF THE INCREMENT OF MAXIMUM LIFT DUE TO FLAPS, Douglas Report SM-23626, Douglas Aircraft Company, California, 1959.

10. McCormick, B. W., AERODYNAMICS OF V/STOL FLIGHT, New York, Academic Press, 1967.

11. Racisz, S. F., TWO-DIMENSIONAL WIND-TUNNEL INVESTIGATION OF MODIFIED NACA 65 (112)-111 AIRFOIL WITH 35-PERCENT-CHORD SLOTTED FLAP AT REYNOLDS NUMBERS UP TO 25 MILLION, NACA TN 1463, National Advisory Committee for Aeronautics, Washington, D.C., 1947.

12. Sears, R. I., WIND-TUNNEL DATA ON THE AERODYNAMIC CHARACTER-ISTICS OF AIRPLANE CONTROL SURFACES, NACA WR L-663, National Advisory Committee for Aeronautics, Washington, D.C., 1943.

13. Spearman, M. L., WIND-TUNNEL INVESTIGATION OF AN NACA 0009 AIRFOIL WITH 0.25- AND 0.50-AIRFOIL-CHORD PLAIN FLAPS TESTED INDEPENDENTLY AND IN COMBINATION, NACA TN 1517, National Advisory Committee for Aeronautics, Washington, D.C., 1948.

14. Gambucci, B. J., SECTION CHARACTERISTICS OF THE NACA 0006 AIR-FOIL WITH LEADING-EDGE AND TRAILING-EDGE FLAPS, NACA TN 3797, National Advisory Committee for Aeronautics, Washington, D.C., 1956.

15. Brewer, J. D., and Polhamus, J. F., WIND-TUNNEL INVESTIGATION OF THE BOUNDARY LAYER ON AN NACA 0009 AIRFOIL HAVING 0.25- AND 0.50-AIRFOIL CHORD PLAIN SEALED FLAPS, NACA TN 1574, National Advisory Committee for Aeronautics, Washington, D.C., April 1948.

16. Wenzinger, C. J., WIND-TUNNEL INVESTIGATION OF ORDINARY AND SPLIT FLAPS ON AIRFOILS OF DIFFERENT PROFILE, NACA TR 554, National Advisory Committee for Aeronautics, Washington, D.C., 1936.

17. Rose, L. M., and Altman, J. M., LOW-SPEED EXPERIMENTAL INVES-TIGATION OF THIN, FAIRED, DOUBLE-WEDGE AIRFOIL SECTIONS WITH NOSE AND TRAILING EDGE FLAPS, NACA TN 1934, National Advisory Committee for Aeronautics, Washington, D.C., 1949.

18. Wenzinger, C. J., PRESSURE DISTRIBUTION OVER AN NACA 23012 AIR-FOIL WITH AN NACA 23012 EXTERNAL-AIRFOIL FLAP, NACA TR 614, National Advisory Committee for Aeronautics, Washington, D.C., 1938.

19. Wenzinger, C. J., and Guavain, W., WIND-TUNNEL INVESTIGATION OF AN NACA 23012 AIRFOIL WITH A SLOTTED FLAP AND THREE TYPES OF AUXILIARY FLAP, NACA TR 679, National Advisory Committee for Aero-nautics, Washington, D.C., 1939.

138

20. Harris, T. A., WIND-TUNNEL INVESTIGATION OF AN NACA 23012 AIR-FOIL WITH TWO ARRANGEMÈNTS OF A WIDE-CHORD SLOTTFD FLAP, NACA TN 715, National Advisory Committee for Aeronautics, Washington, D.C., 1939.

21. Wenzinger, C. J., and Harris, T. A., WIND-TUNNEL INVESTIGATION OF AN NACA 23021 AIRFOIL WITH VARIOUS ARRANGEMENTS OF SLOTTED FLAPS, NACA TR 677, National Advisory Committee for Aeronautics, Washington, D.C., 1939.

22. Duschik, F., WIND-TUNNEL INVESTIGATION OF AN NACA 23021 AIRFOIL WITH TWO ARRANGEMENTS OF A 40-PERCENT-CHORD SLOTTED FLAP, NACA TN 728, National Advisory Committee for Aeronautics, Washington, D.C., 1939.

23. Recant, I. G., WIND-TUNNEL INVESTIGATION OF AN NACA 23030 AIR-FOIL WITH VARIOUS ARRANGEMENTS OF SLOTTED FLAPS, NACA TN 755, National Advisory Committee for Aeronautics, Washington, D.C., 1940.

24. Lowry, J. G., WIND-TUNNEL INVESTIGATION OF AN NACA 23012 AIR-FOIL WITH SEVERAL ARRANGEMENTS OF SLOTTED FLAPS WITH EXTENDED LIPS, NACA TN 808, National Advisory Committee for Aeronautics, Washington, D.C., 1941.

25. Cahill, J. F., TWO-DIMENSIONAL WIND-TUNNEL INVESTIGATION OF FOUR TYPES OF HIGH-LIFT FLAP ON AN NACA 65-210 AIRFOIL SECTION, NACA TN 1191, National Advisory Committee for Aeronautics, Washington, D.C., February 1947.

26. Holtzclaw, R. W., and Weisman, Y., WIND-TUNNEL INVESTIGATION OF THE EFFECTS OF SLOT SHAPE AND FLAP LOCATION ON THE CHARAC-TERISTICS OF A LOW DRAG AIRFOIL EQUIPPED WITH A 0.25-CHORD SLOTTED FLAP, NACA MR A4L28 (WR A-80), National Advisory Committee for Aeronautics, Washington, D.C., December 1944.

27. Wenzinger, C. J., and Harris, T. A., WIND-TUNNEL INVESTIGATION OF AN NACA 23012 AIRFOIL WITH VARIOUS ARRANGEMENTS OF SLOTTED FLAPS, NACA TR 664, National Advisory Committee for Aeronautics, Washington, D.C., 1939.

28. Harris, T. A., and Recant, I. G., WIND-TUNNEL INVESTIGATION OF NACA 23012, 23021, and 23030 AIRFOILS EQUIPPED WITH 40-PERCENT-CHORD DOUBLE SLOTTED FLAPS, NACA TR 723, National Advisory Committee for Aeronautics, Washington, D.C., 1941.

29. Fischel, J., and Riebe, J. M., WIND-TUNNEL INVESTIGATION OF AN NACA 23021 AIRFOIL WITH A 0.32-AIRFOIL-CHORD DOUBLE SLOTTED FLAP, NACA ARR L4J05, National Advisory Committee for Aeronautics, Washington, D.C., 1944.

30. Quinn, J. H., TESTS OF THE NACA 64_1 A212 AIRFOIL SECTION WITH A SLOT, A DOUBLE SLOTTED FLAP, AND BOUNDARY-LAYER CONTROL BY SUCTION, NACA TN 1293, National Advisory Committee for Aeronautics, Washington, D.C., 1947.

31. Quinn, J. H., WIND-TUNNEL INVESTIGATION OF BOUNDARY-LAYER CONTROL BY SUCTION ON THE NACA 65_3–418, a = 1.0 AIRFOIL SECTION WITH A 0.29-AIRFOIL-CHORD DOUBLE SLOTTED FLAP, NACA TN 1071, National Advisory Committee for Aeronautics, Washington, D.C., 1946.

32. Eilert, M. B., LOW-SPEED WIND-TUNNEL TESTS OF A TWO-DIMEN-SIONAL HIGH LIFT RESEARCH MODEL, CVAL 474A, Convair Division of General Dynamics Corporation, San Diego, California, 1968.

33. Boulanger, A., WIND-TUNNEL TESTS ON A 2-D MODEL OF A NACA 4418 (Mod) SECTION, ERR-CL-RAA-228-100, Canadair Limited, Subsidiary of General Dynamics Corporation, Montreal, Canada, 1960.

34. Rose, L. M., and Altman, J. M., LOW-SPEED INVESTIGATION OF A THIN, FAIRED, DOUBLE-WEDGE AIRFOIL SECTION WITH NOSE FLAPS OF VARIOUS CHORDS, NACA TN 2018, National Advisory Committee for Aeronautics, Washington, D.C., 1950.

35. Fullmer, F. F., TWO-DIMENSIONAL WIND-TUNNEL INVESTIGATION OF AN NACA 64-009 AIRFOIL EQUIPPED WITH TWO TYPES OF LEADING-EDGE FLAP, NACA TN 1624, National Advisory Committee for Aeronautics, Washington, D.C., June 1948.

36. Fullmer, F. F., TWO-DIMENSIONAL WIND-TUNNEL INVESTIGATION OF THE NACA 64-012 AIRFOIL EQUIPPED WITH TWO TYPES OF LEADING EDGE FLAP, NACA TN 1277, National Advisory Committee for Aeronautics, Washington, D.C., May 1947.

37. Hunton, L. W., and James, H. A., USE OF TWO-DIMENSIONAL DATA IN ESTIMATING LOADS ON A 45° SWEPTBACK WING WITH SLATS AND PARTIAL-SPAN FLAPS, NACA TN 3040, National Advisory Committee for Aeronautics, Washington, D.C., 1953.

38. Kelly, J. A., and Hayter, N. L. F., LIFT AND PITCHING MOMENT AT LOW SPEEDS OF THE NACA 64A010 AIRFOIL SECTION EQUIPPED WITH VARIOUS COMBINATIONS OF A LEADING-EDGE SLAT, LEADING-EDGE FLAP, SPLIT FLAP, AND DOUBLE-SLOTTED FLAP, NACA TN 3007, National Advisory Committee for Aeronautics, Washington, D.C., September 1953.

39. Gottlieb, S. M., TWO-DIMENSIONAL WIND-TUNNEL INVESTIGATION OF TWO NACA 6-SERIES AIRFOILS WITH LEADING EDGE SLATS, NACA RM L8K22, National Advisory Committee for Aeronautics, Washington, D.C., 1949.

40. Hoerner, S. F., FLUID-DYNAMIC DRAG, New Jersey, Published by Author, 1958.

41. Anon., LIT SYSTEM PLANNING STUDY (U) VOL. II, VERTOL Division, Boeing Company, Pennsylvania, 1967. (Confidential)

42. Gray, W. L., and Schenk, K. M., A METHOD FOR CALCULATING THE SUBSONIC STEADY-STATE LOADING ON AN AIRPLANE WITH A WING OF ARBITRARY PLANFORM AND STIFFNESS, NACA TN 3030, National Advisory Committee for Aeronautics, Washington, D.C., 1953.

43. Holt, R. L., APPLICATION OF LIFTING LINE THEORY TO AIRCRAFT AEROELASTIC LOADS ANALYSIS, GDC-ERR-AN-1128, Convair Division of General Dynamics Corporation, San Diego, California, 1968.

44. Anon., V/STOL MEDIUM RANGE TRANSPORT AIRCRAFT DESIGN STUDY, REPORT RAX-62-116, VOLUME II, Canadair Limited, Subsidiary of General Dynamics Corporation, Montreal, Canada, August 1962.

45. Pederson, S. K., USERS MANUAL FOR TILT-WING AND DEFLECTED SLIPSTREAM AERODYNAMICS PROGRAM, TN-70-AVLABS-09, Convair Division of General Dynamics Corporation, San Diego, California, 1970.

141

46. Laudeman, E., A METHOD OF CALCULATING ZERO-LIFT PITCHING
    MOMENTS OF A WING-NACELLE-FLAP COMBINATION IMMERSED IN A
    PROPELLER SLIPSTREAM, TN-70-AVLABS-02, Convair Division of
    General Dynamics Corporation, San Diego, California, 1970.

47. Laudeman, E., A METHOD FOR CALCULATING PITCHING MOMENT
    CURVE SLOPE OF A WING-NACELLE-FLAP COMBINATION IMMERSED
    IN A PROPELLER SLIPSTREAM, TN-70-AVLABS-01, Convair Division of
    General Dynamics Corporation, San Diego, California, 1970.

48. Perkins, C. D., and Hage, R. E., AIRPLANE PERFORMANCE STABILITY
    AND CONTROL, New York, John Wiley and Sons, Inc., 1949.

49. Kuhn, R. E., SEMIEMPIRICAL PROCEDURE FOR ESTIMATING LIFT AND
    DRAG CHARACTERISTICS OF PROPELLER-WING-FLAP CONFIGURATIONS
    FOR VERTICAL AND SHORT TAKE OFF AND LANDING AIRPLANE, NASA
    Memo 1-16-59L, National Aeronautics and Space Administration, Washington,
    D.C., 1959.

50. Martin, J. J., A PROPOSAL FOR SOLUTION OF THE TILT WING VTOL
    AIRCRAFT DOWNWASH PROBLEM BASED ON AN ANALYSIS OF NASA
    DATA, RAX-84-107, Canadair Limited, Subsidiary of General Dynamics
    Corporation, Montreal, Canada, 1960.

51. Kuhn, R. E., and Hayes, W. C., WIND TUNNEL INVESTIGATION OF
    LONGITUDINAL AERODYNAMIC CHARACTERISTICS OF THREE PRO-
    PELLER-DRIVEN VTOL CONFIGURATIONS IN THE TRANSITION SPEED
    RANGE, INCLUDING EFFECTS OF GROUND PROXIMITY, NASA TN D-55,
    National Aeronautics and Space Administration, Washington, D.C., 1960.

52. Pope, Alan, and Harper, John J., LOW SPEED WIND TUNNEL TESTING,
    New York, John Wiley and Sons, Inc., 1966.

53. Heyson, Harry H., LINEARIZED THEORY OF WIND TUNNEL JET-
    BOUNDARY CORRECTIONS AND GROUND EFFECT FOR VTOL-STOL
    AIRCRAFT, NASA TR-R-124, National Aeronautics and Space Administra-
    tion, Washington, D.C., 1962.

54. Heyson, Harry H., USE OF SUPERPOSITION IN DIGITAL COMPUTERS TO
    OBTAIN WIND TUNNEL INTERFERENCE FACTORS FOR ARBITRARY
    CONFIGURATIONS, WITH PARTICULAR REFERENCE TO V/STOL MODELS,
    NASA TR-R-302, National Aeronautics and Space Administration, Washington,
    D.C., 1969.

142

55. Heyson, Harry H., and Grunwald, Kalman J., WIND TUNNEL BOUNDARY
    INTERFERENCE FOR V/STOL TESTING, CONFERENCE OF V/STOL AND
    STOL AIRCRAFT, NASA SP-116, National Aeronautics and Space Admini-
    stration, Washington, D.C., 1966, pp. 409-434.

56. Grunwald, Kalman J., EXPERIMENTAL STUDY OF WIND TUNNEL WALL
    EFFECTS AND WALL CORRECTIONS FOR A GENERAL-RESEARCH V/STOL
    TILT-WING MODEL WITH FLAP, NASA TN-D-2887, National Aeronautics
    and Space Administration, Washington, D.C., 1965.

57. Page, V. Robert, and Dickinson, Stanley O., LARGE SCALE WIND TUNNEL
    TESTS OF A DEFLECTED SLIPSTREAM STOL MODEL WITH WINGS OF
    VARIOUS ASPECT RATIOS, NASA TN-D-4448, National Aeronautics and
    Space Administration, Washington, D.C., 1968.

58. Pederson, S. K., TILT-WING AND DEFLECTED SLIPSTREAM AERODYNA-
    MIC ANALYSIS, TN-70-AVLABS-04, Convair Division of General Dynamics
    Corporation, San Diego, California, 1970.

59. Fink, M. P., and Mitchell, R. G., AERODYNAMIC DATA ON LARGE
    SEMISPAN TILTING WING WITH 0.6-DIAMETER CHORD, SINGLE SLOTTED
    FLAP, AND SINGLE PROPELLER ROTATING UP AT THE TIP, NASA TN
    D-1586, National Aeronautics and Space Administration, Washington, D.C.,
    1964.

60. Fink, M. D., Mitchell, R. G., and White, L. C., AERODYNAMIC DATA
    ON A LARGE SEMISPAN TILTING WING WITH 0.5 DIAMETER CHORD,
    DOUBLE-SLOTTED FLAP, AND BOTH LEFT- AND RIGHT-HAND ROTA-
    TION OF A SINGLE PROPELLER, NASA TN D-3375, National Aeronautics
    and Space Administration, Washington, D.C., 1966.

61. Whitney, C. A., A DIGITAL COMPUTER PROGRAM TO CALCULATE
    TAKEOFFS, LANDINGS AND TRANSITIONS OF V/STOL AIRCRAFT,
    TN-70-AVLABS-08, Convair Division of General Dynamics Corporation,
    San Diego, California, 1970.

APPENDIX

ANALYSIS OF THE EFFECTS OF HIGH-LIFT DEVICES ON

THE PERFORMANCE OF A TILT-WING CONFIGURATION

The analysis of the effects of high-lift devices on the performance of a tilt-wing configuration similar to the CL-84 is discussed in this section. The general arrangement of the aircraft (powered by two T64-GE-7 engines) is shown in Figure 68. The geometry is listed below:

Wing

S	= 291 sq ft
AR	= 5.18
b	= 38.8 ft
c	= 7.5 ft
λ	= 1.0
Airfoil NACA 63_3 - 418	

Horizontal Tail

S	= 95 sq ft
t/c	= 0.14

Fuselage

ℓ_B	= 44 ft
D_B	= 7.7 ft
S_{WET}	= 764 sq ft

Vertical Tail

Center		Outboard	
S	= 33 sq ft	S	= 27 sq ft
t/c	= 0.14	t/c	= 0.12

Nacelle

ℓ_N	= 14.24 ft
S_B	= 13 sq ft
D_N	= 4 ft

Propeller

D_P	= 16.5 ft
Number of Blades	= 4

The methods discussed in Section 2.0 were used to estimate the two-dimensional characteristics of the 35-percent-chord trailing edge flaps shown in Figure 69. These characteristics plus wing geometry were inputs into the span load program. The results from the span load program plus the nacelle drag were then used in the summary equations of Sections 5.0 and 6.0 to generate the tail-off aerodynamic characteristics. These data, fuselage drag, vertical tail drag, horizontal tail

drag, geometry, and weights, were inputs into the performance program described in Section 10.0. The performance for the aircraft with the various high-lift devices is shown in Figures 70 through 75.

The flight paths for vertical takeoff to conversion (wing tilt angle at 4.16 degrees) for a gross weight of 20,000 pounds are shown in Figure 70. The 35-percent-chord trailing edge flaps furnished sufficient lift to allow the vehicle to perform the transition from vertical takeoff to conversion up to the maximum vertical take-off weight. The selection of a trailing edge flap has a pronounced effect on ground distance and the altitude at which the conversion is completed. Typical distances, altitudes, and velocities to conversion for a range of gross weights up to the maximum vertical takeoff gross weight of 25,000 pounds $\left(\frac{\text{max. available thrust}}{1.05} \right)$ are shown in Figure 71. The overall effect of improving the lifting capability of the trailing edge flap is to drastically reduce the distance to conversion and allow the aircraft to maintain an altitude at conversion which is almost constant with weight.

The effects of wing tilt angle on the short-field takeoff distances at a gross weight of 24,000 pounds are shown in Figure 72. Wing tilt angles of 40 degrees for the double-slotted flap and 45 degrees for the plain and single-slotted flap configurations gave the shortest distances over the obstacle. These wing tilt angles were used for the short-field takeoff analysis.

The effects of trailing edge flaps on the short-field takeoff are shown in Figure 73. The wing is tilted to a prescribed angle and the trailing edge flaps are fully deflected to keep the ground distances down to 100 feet. The results for the trailing edge flaps analyzed are pronounced. For a 500-foot total distance requirement for an overload condition, the single- and double-slotted flap configurations would allow an additional 2200 and 4100 pounds of payload respectively.

The double-slotted flap configuration was then analyzed for the vertical landing and deflected-slipstream takeoff performance to demonstrate the capability of the program. Time and distance for a typical vertical landing for the double-slotted flap are shown in Figure 74. The maximum vertical landing weight is 24,550 pounds. The major effect of reducing the gross weight is a reduction in time and total distance to hover. Typical time required for the maneuvers is 10 seconds. Another 20 seconds is required from hover to touchdown.

Deflected-slipstream takeoff performance for the double-slotted flap is shown in Figure 75. The wing is not tilted but the flap is fully deflected for this maneuver. The distances at the lower gross weights appear low when compared to the Brequet

145

and Charger takeoff data. The following table shows that the tilt-wing configuration selected for analysis has substantially higher thrust to weight ratio and wing loading than the Brequet or Charger. The analysis has served as a very satisfactory check of the performance program. A further check should be made with the Brequet or the Charger to show the full program capability.

COMPARISON OF DEFLECTED-SLIPSTREAM PERFORMANCE			
AIRCRAFT	TILT-WING	BREQUET	CHARGER
Weight (lb)	29,100	48,500	7,800
S (sq ft)	291	902	191
W/S	100	54	41
No. of Engines	2	4	2
SHP_{TOTAL}	6,870	6,000	1,300
W/SHP_{TOTAL}	4.23	8.08	6.0
Ground Distance	240	610	275
Total Distance Over 50-Ft Obstacle	640	985	610
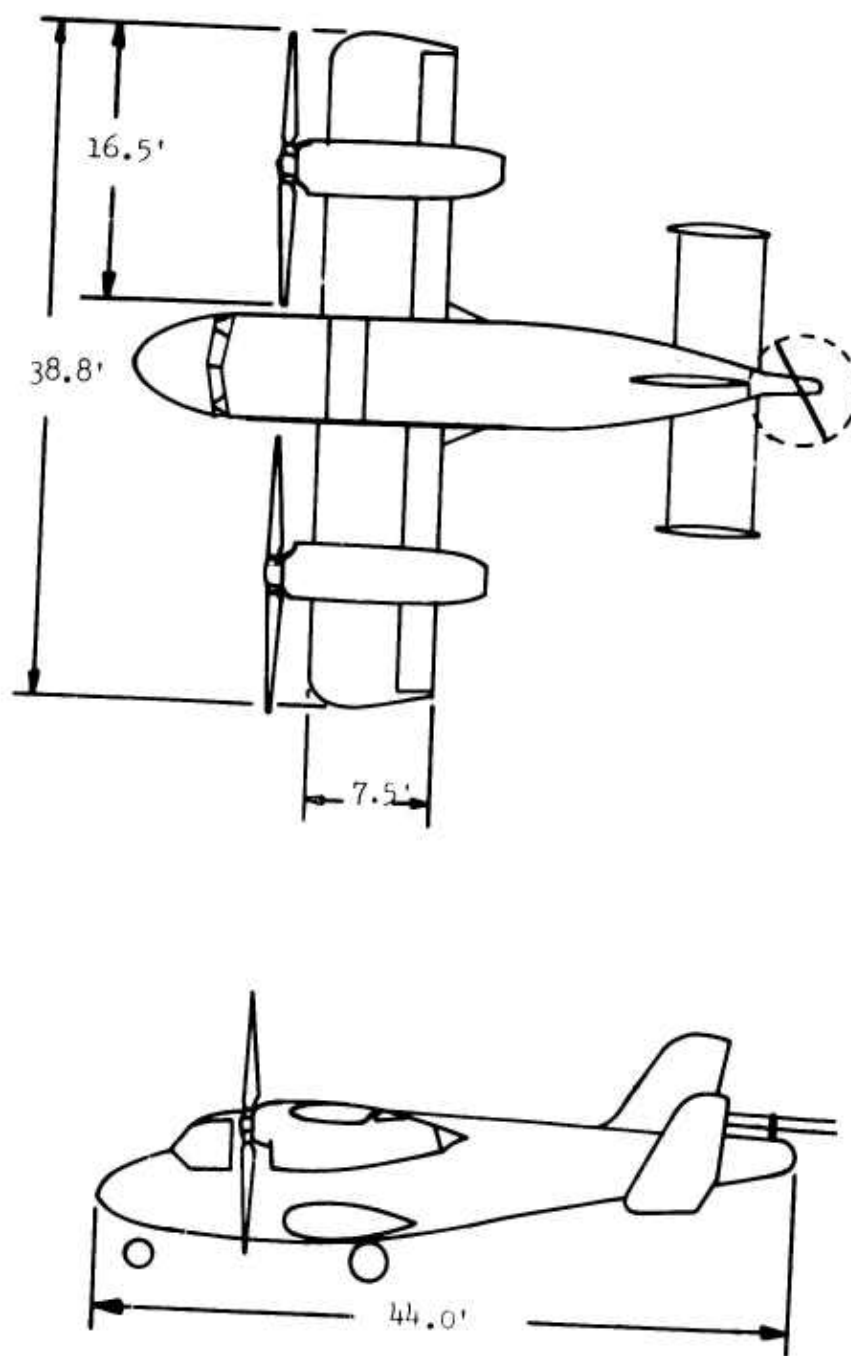
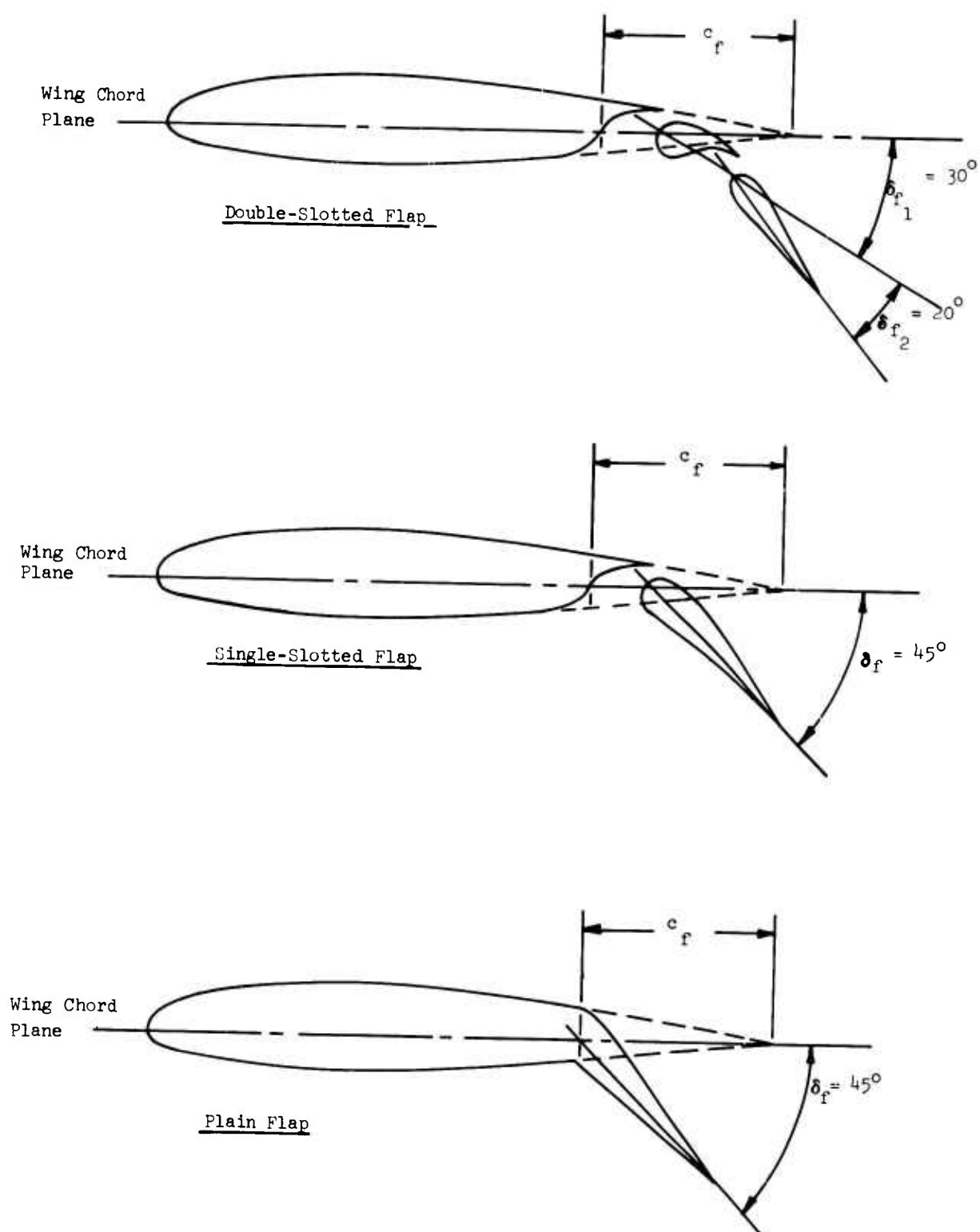Figure 68. General Arrangement of Tilt-Wing Aircraft.

147

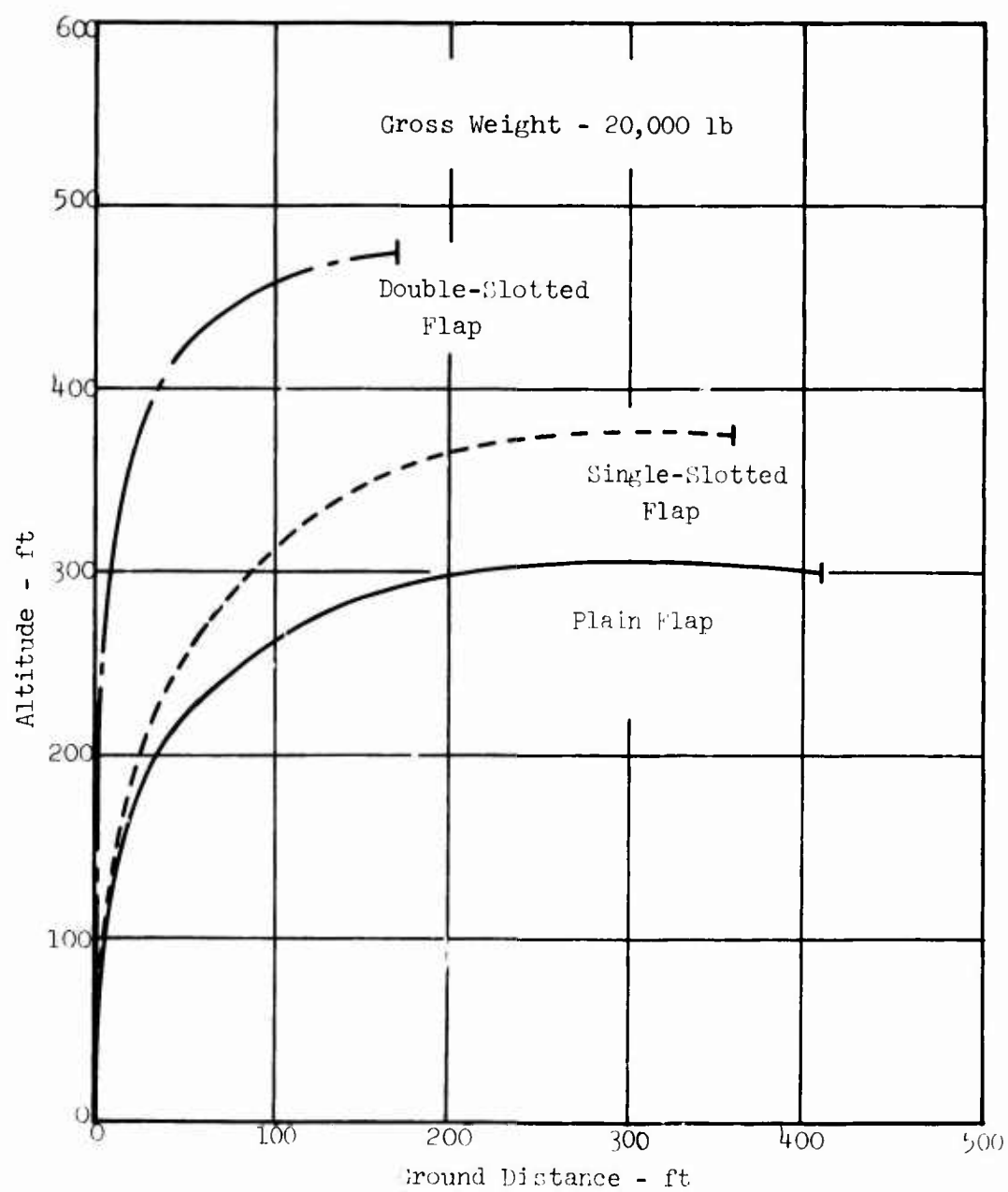Figure 69. Trailing Edge Devices for Tilt-Wing Aircraft of Figure 68.

148

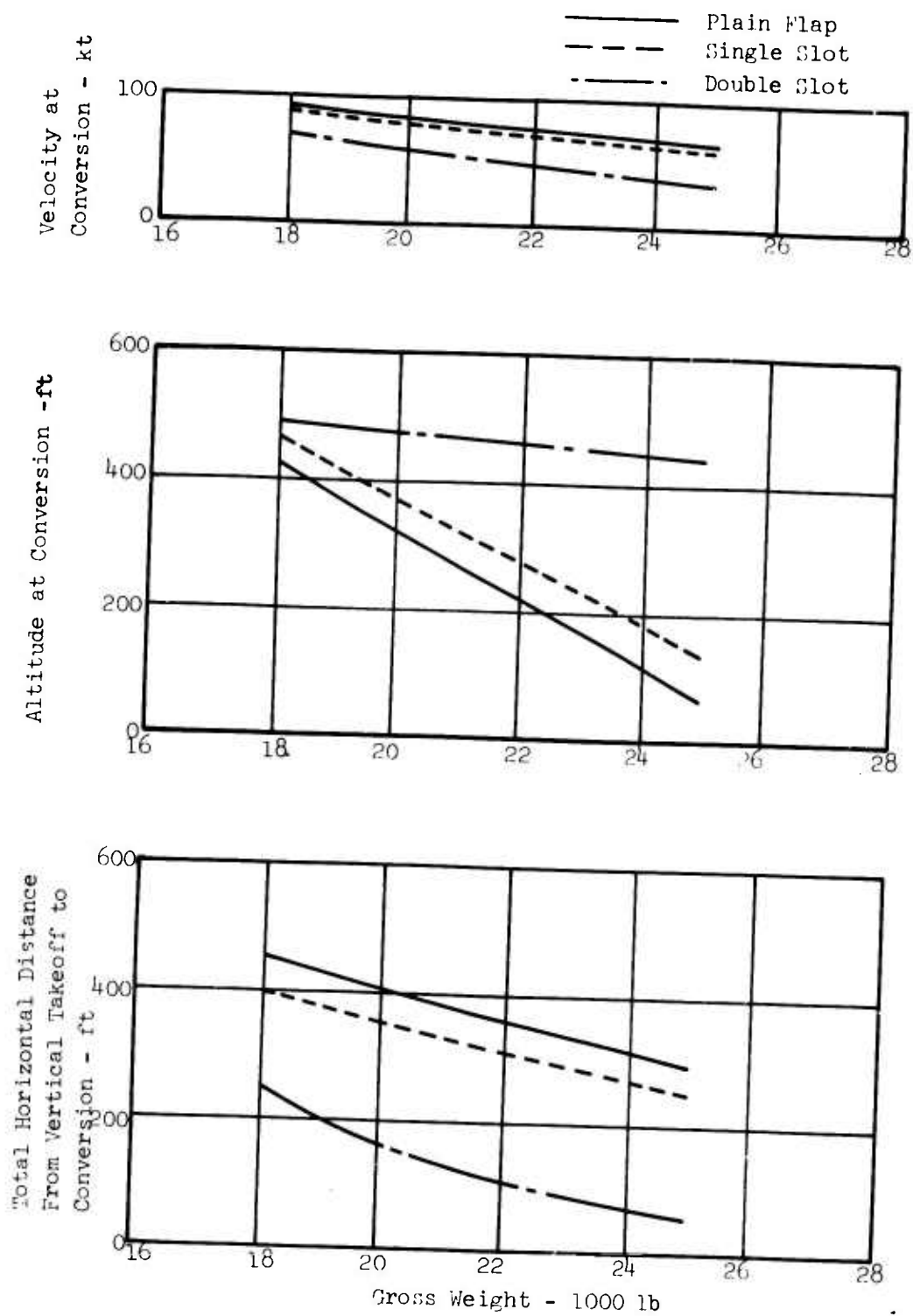Figure 70. Typical Vertical Takeoff Flight Paths.

Figure 71. Distance and Velocities at Conversion Versus Gross
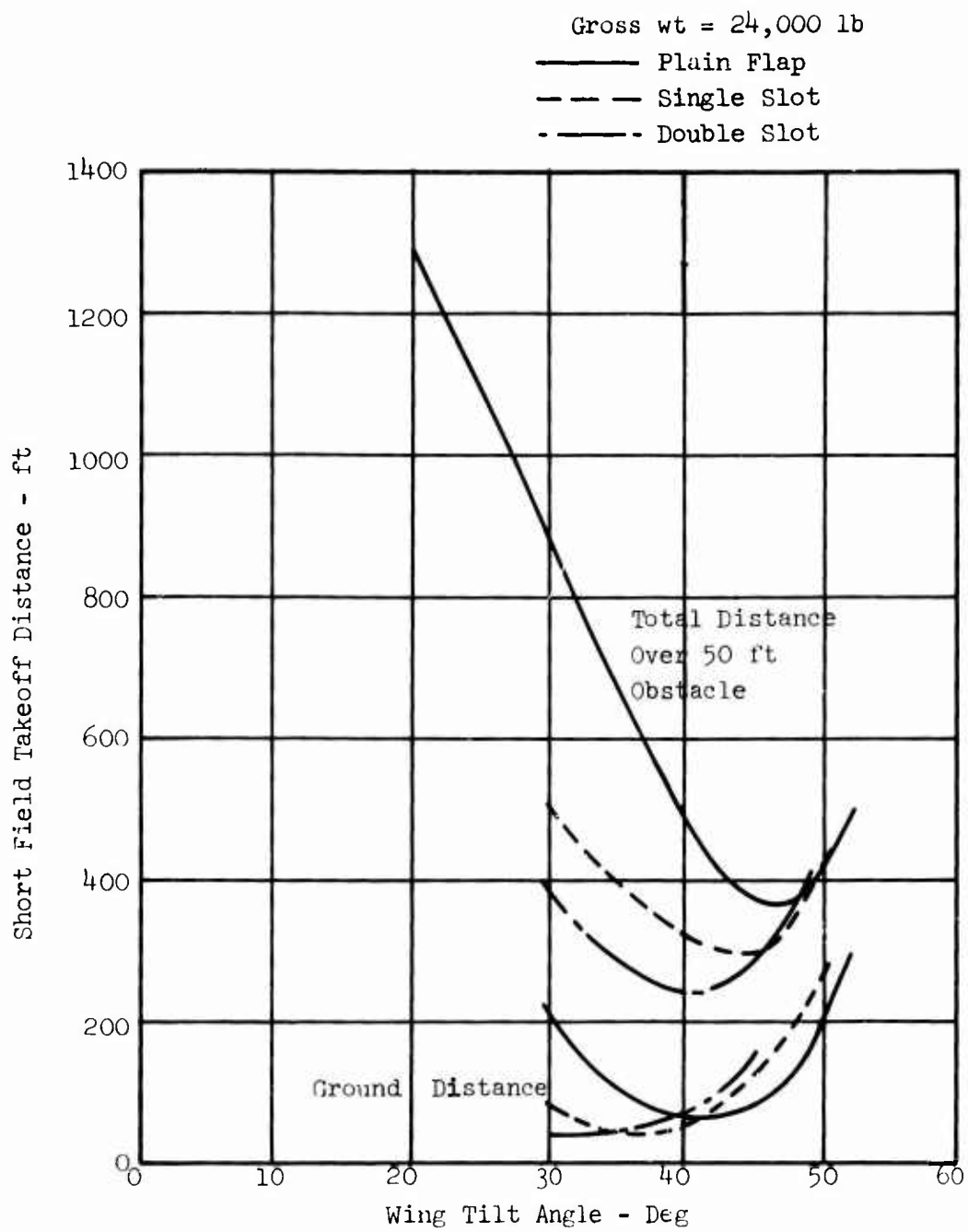Weight for a Tilt-Wing Aircraft.

150

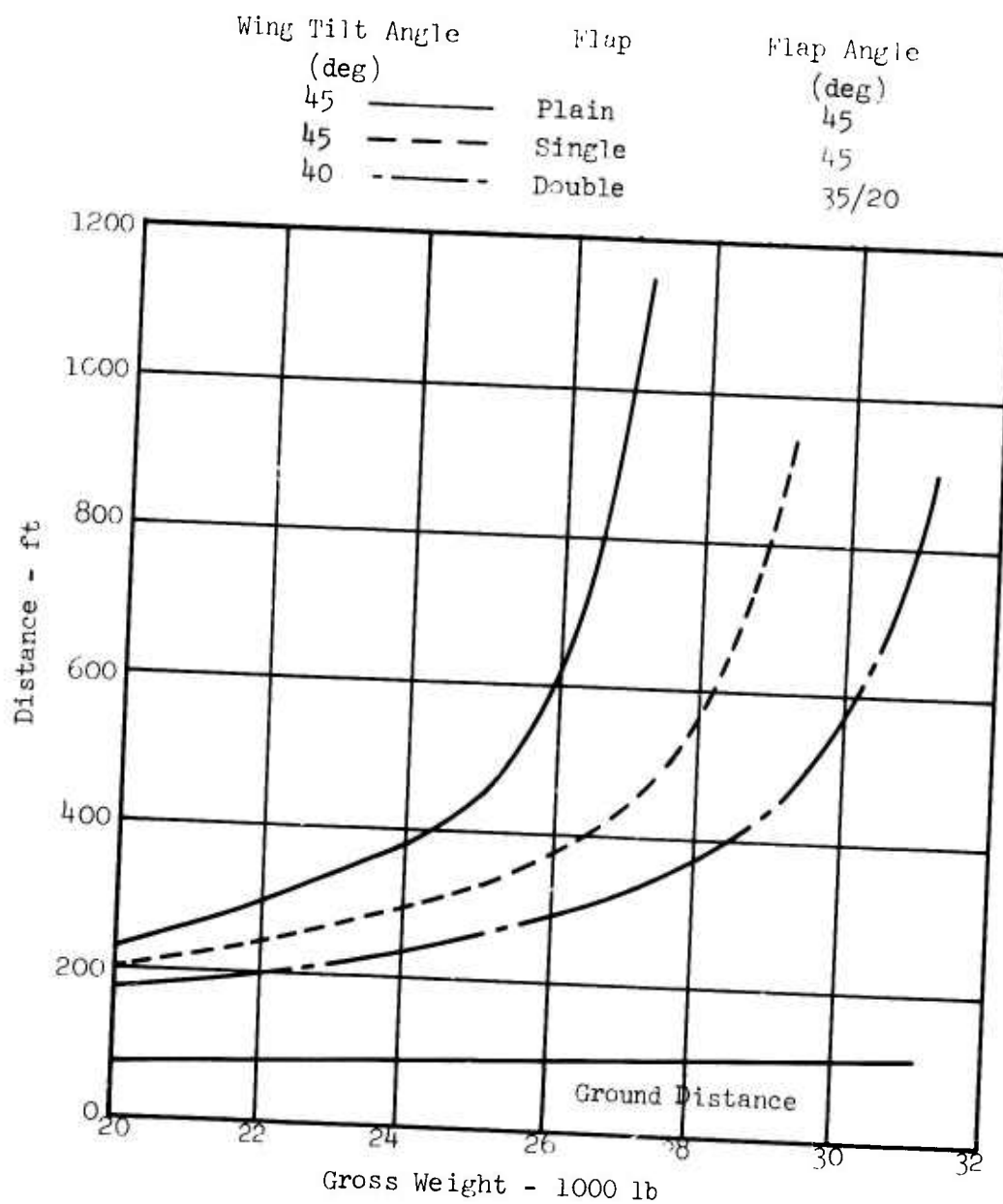Figure 72. Short-Field Takeoff Distance Versus Wing Tilt Angle.

151

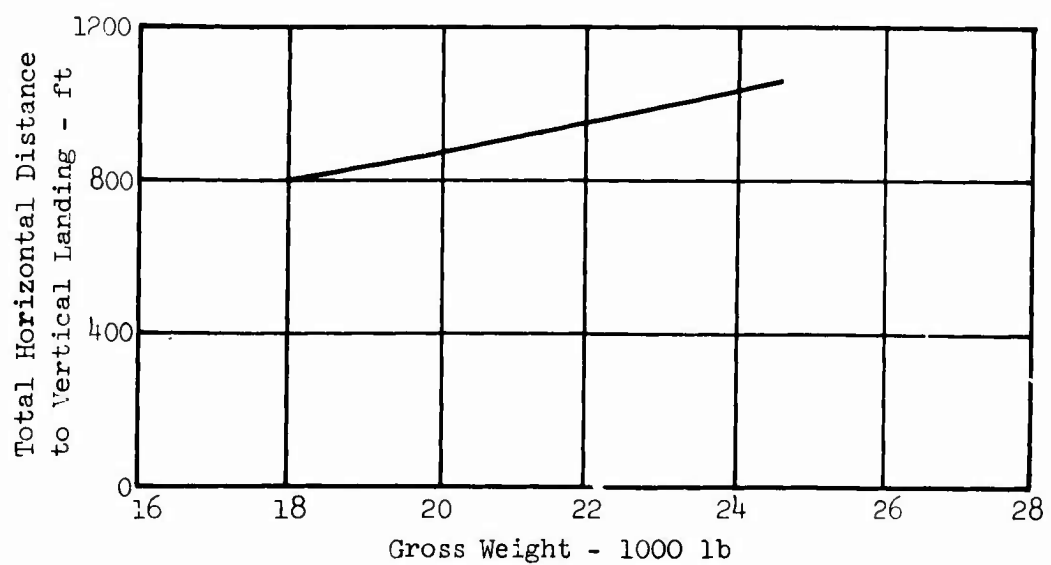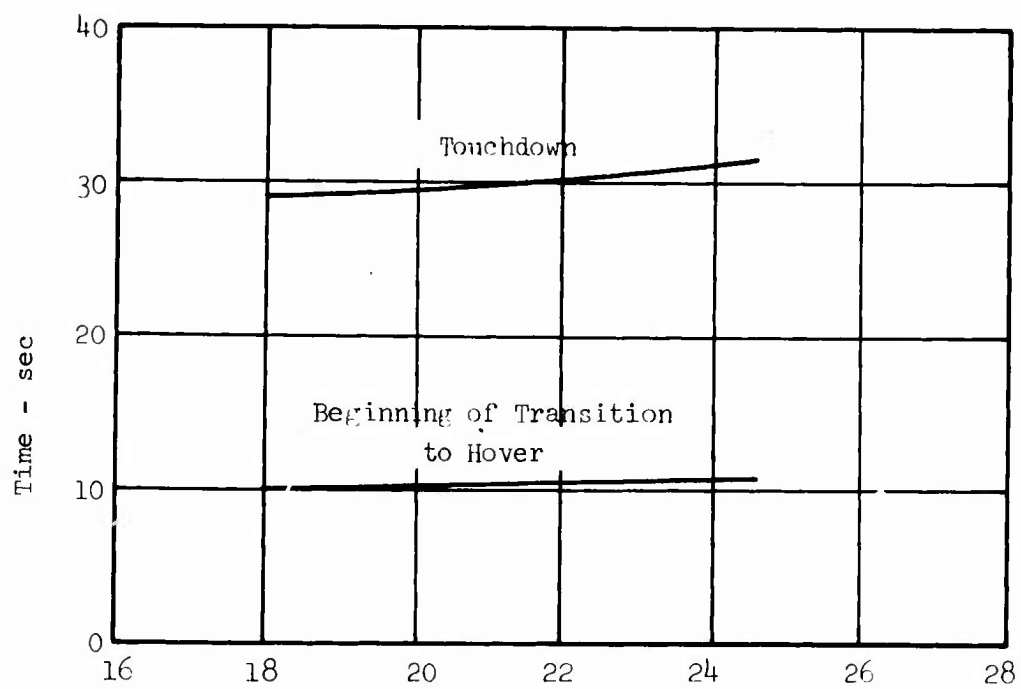Figure 73. Short-Field Takeoff Distances With Wing Tilted Versus Gross Weight.

152

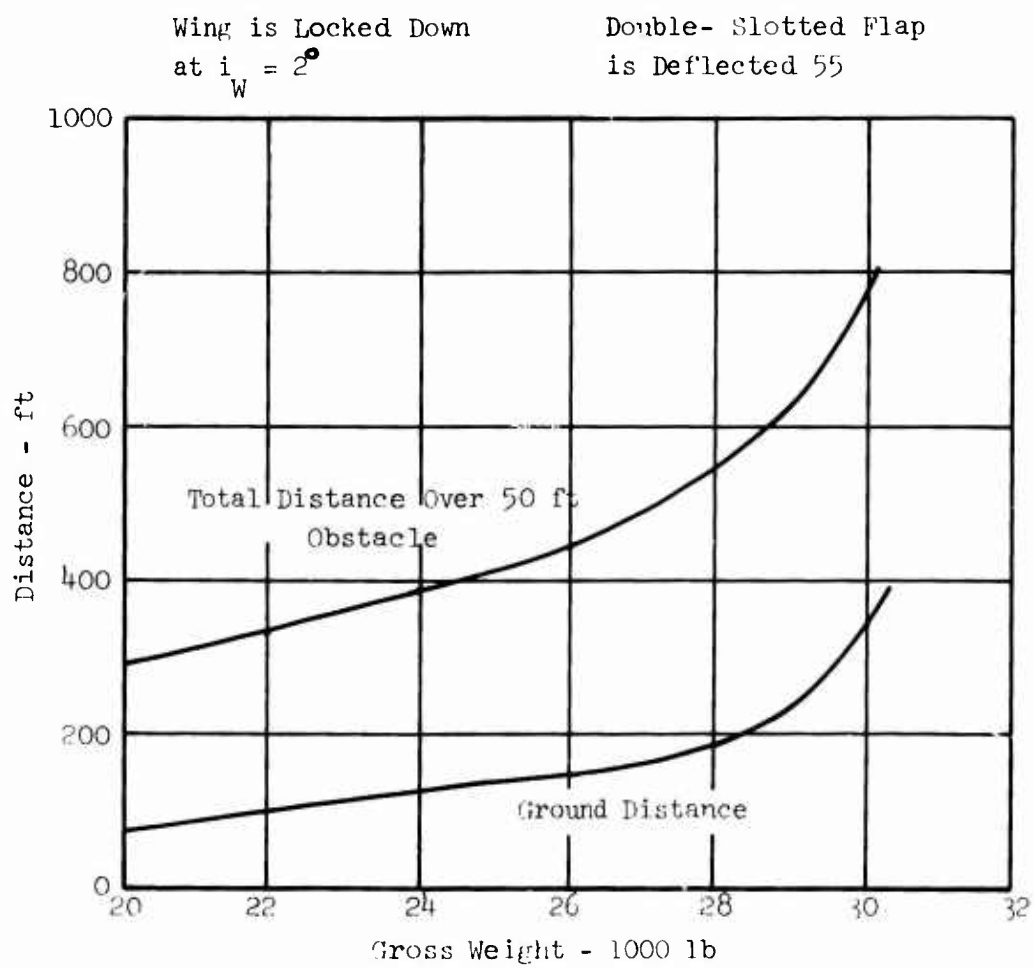Figure 74. Distance and Time for Vertical Landing Versus Gross Weight.

Figure 75. Deflected-Slipstream Takeoff Distance Versus Gross Weight.

DOCUMENT CONTROL DATA - R & D

(Security classification of title, body of abstract and indexing annotation must be entered when the overall report is classified)

1. ORIGINATING ACTIVITY *(Corporate author)*	2a. REPORT SECURITY CLASSIFICATION
Convair Division of General Dynamics San Diego, California	Unclassified
	2b. GROUP N/A

3. REPORT TITLE

EFFECTS OF HIGH-LIFT DEVICES ON V/STOL AIRCRAFT PERFORMANCE

4. DESCRIPTIVE NOTES *(Type of report and inclusive dates)*

Volume I - Final Report

5. AUTHOR(S) *(First name, middle initial, last name)*

J. Hebert et al

6. REPORT DATE	7a. TOTAL NO. OF PAGES	7b. NO. OF REFS
October 1970	182	61

8a. CONTRACT OR GRANT NO. DAAJ02-69-C-0079	9a. ORIGINATOR'S REPORT NUMBER(S)
b. PROJECT NO. Task 1F162204A14231	USAAVLABS Technical Report 70-33A
c.	9b. OTHER REPORT NO(S) *(Any other numbers that may be assigned this report)*
d.	

10. DISTRIBUTION STATEMENT

This document is subject to special export controls, and each transmittal to foreign governments
or foreign nationals may be made only with prior approval of U.S. Army Aviation Materiel
Laboratories, Fort Eustis, Virginia 23604.

11. SUPPLEMENTARY NOTES	12. SPONSORING MILITARY ACTIVITY
Volume I of a two-volume report	U.S. Army Aviation Materiel Laboratories Fort Eustis, Virginia

13. ABSTRACT

The purpose of this study was to develop a unified analytical procedure to evaluate the effects of
passive high-lift devices on deflected-slipstream or tilt-wing V/STOL configurations. Methods
were developed to predict the two-dimensional flapped airfoil characteristics to be used in a
span load program. The span load results are used in procedures for estimating the
coefficients of lift, longitudinal force, and moment for a wing partially immersed in a propeller
slipstream. These characteristics can then be used in a performance program developed to
calculate the takeoff, landing, and transition maneuvers. In addition to these tasks, investiga-
tions were made into downwash characteristics, wind tunnel wall corrections, and correlations
of flight test data with theory. An analysis of the effects of high-lift devices on the performance
of a tilt-wing V/STOL configuration is included in the appendix.

DD FORM 1473 REPLACES DD FORM 1473, 1 JAN 64, WHICH IS OBSOLETE FOR ARMY USE.

14. KEY WORDS	LINK A		LINK B		LINK C	
	ROLE	WT	ROLE	WT	ROLE	WT
V/STOL aircraft						
Aircraft performance						
High-lift devices						
Deflected slipstream						
Tilt wing						
Flapped airfoil						
Unflapped airfoil						